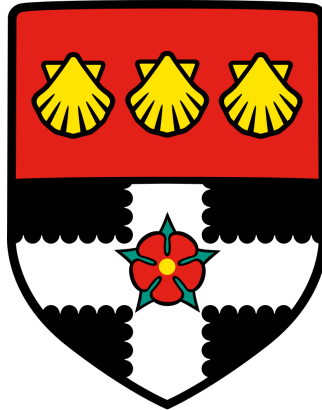


UNIVERSITY OF READING

Department of Meteorology



Available Potential Energy in Axisymmetric Tropical Cyclones

BETHAN LAURA HARRIS

A thesis submitted for the degree of Doctor of Philosophy

March 2020

Declaration

I confirm that this is my own work and the use of all material from other sources has been properly and fully acknowledged.

Bethan Harris

Abstract

Tropical cyclone (TC) intensification is challenging to represent in numerical models because it results from complex interactions between multi-scale processes, some of which are poorly understood. This thesis investigates TC development in an idealised axisymmetric model in terms of moist Available Potential Energy (APE) density, and suggests how diagnostics based on moist APE budgets could be applied to forecasting and global climate models to study the links between model parameterisations and the intensity of TCs.

The first full budget of moist APE density for the atmosphere in any context is constructed for the axisymmetric model, using the model's initial environmental sounding as a reference state. The main source of moist APE relative to the environment is the surface latent heat flux occurring in the low-level radial inflow. This APE is then transported inwards and converted into kinetic energy in the eyewall. The budget also reveals that APE density can be discontinuous in time and space in the moist atmosphere if air parcels possess multiple levels of neutral buoyancy, in which case a reservoir of latent APE may exist.

The best APE reference state for predicting the domain-integrated rate of kinetic energy generation in a TC is shown to be a vortex in thermal wind balance. Surface fluxes are still the chief source of APE when this reference state is used. Precipitation and subgrid mixing also contribute to the kinetic energy generation.

The intensification of TCs in the model, in terms of total power dissipation, is associated with an increase in the efficiency with which surface fluxes generate moist APE, even when the WISHE feedback is cut off so that the surface fluxes themselves do not increase. A two-part WISHE-efficiency feedback is proposed to drive intensification. It is also demonstrated that moist local available energetics can be used to derive a theory of potential intensity.

Acknowledgements

Firstly, thanks are due to my supervisors: Rémi Tailleux, Chris Holloway and Pier Luigi Vidale. All your advice, support and encouragement helped keep me on track, and I have learned so much from all of you over the last few years. Discussion with Maarten Ambaum and John Methven in my monitoring committee meetings was also instrumental in shaping the direction of this thesis; I am very grateful for all this feedback. I would also like to thank NERC for providing the funding that made this project possible.

The friends I made during my PhD played a huge part in making it such an enjoyable experience. Thanks to Hannah and Natalie for always being there for a tea break, Sally, Rachael and Kaja for a great trip to EGU (and also a non-negligible number of tea breaks), Jon and Josh for an excellent Florida road trip/mini golf tour, and everyone in 1U09 for making coming into the office something to look forward to. Thanks also to everyone at Phoenix and Ranelagh Hockey Club for being so welcoming and showing great enthusiasm for fun weather facts!

I am incredibly grateful to my family, whose support has got me to the position I am in today. Unfortunately, I fear this thesis lacks answers to many of the questions you've had along the way, such as, "were any apes harmed during this work?" and, "so what *is* the budget of a tropical cyclone? One million dollars?" Thanks must also go to Mrs Dunster, who refused to give up until I finally relented and agreed to study A-Level Physics.

Finally, I would like to thank James, who made this a lot easier than it would have otherwise been, and helped me keep life in perspective when I was upset about an imaginary axisymmetric vortex.

Contents

Declaration	i
Abstract	ii
Acknowledgements	iii
Contents	iv
1 Introduction	1
1.1 Introduction to tropical cyclones	1
1.2 Intensification of tropical cyclones	3
1.3 Modelling tropical cyclone intensity	5
1.3.1 Numerical Weather Prediction	5
1.3.2 Global climate models	6
1.4 Thesis aims and objectives	10
1.5 Thesis structure	11
2 Review of energetics and efficiency	13
2.1 Available Potential Energy	13
2.1.1 Lorenz APE	14
2.1.2 Local APE theory	19
2.1.3 APE relative to non-resting reference states	26
2.1.4 Summary of APE theory	28
2.2 Energetics of tropical cyclones	29
2.2.1 Total Potential Energy	30
2.2.2 Dry Available Potential Energy	35
2.2.3 Moist Available Potential Energy	37
2.3 Efficiency of tropical cyclones	43
2.3.1 Temporal variation of efficiency	43
2.3.2 Potential intensity	46
2.3.3 Summary of tropical cyclone energetics and efficiency	53
3 Assessment of algorithms for computing moist available potential energy	55
3.1 Introduction	55
3.2 Algorithms for Computing APE	58
3.2.1 Munkres algorithm	58
3.2.2 Lorenz’s algorithm	59
3.2.3 Randall and Wang’s algorithm	59
3.2.4 Top-down algorithm	60
3.2.5 Bottom-up algorithm	60

3.2.6	Divide-and-conquer algorithm	60
3.2.7	Estimation from Convective Available Potential Energy	61
3.3	Data	62
3.4	Comparison of Algorithms	64
3.5	Discussion	68
4	Model setup	73
4.1	Domain and resolution	74
4.2	Model equations	75
4.3	Initial conditions	78
4.4	Model numerics	80
4.5	Tropical cyclone characteristics	86
5	Available energetics of an axisymmetric tropical cyclone	92
5.1	Kinetic and available elastic energies	93
5.2	Available potential energy	105
5.2.1	Conserved variables	106
5.2.2	Reference height	108
5.2.3	APE density	110
5.2.4	APE production coefficients	113
5.2.5	Discontinuous behaviour of APE density	120
5.2.6	Available Potential Energy budget	126
5.3	Discussion and Conclusions	131
5.3.1	Kinetic and available elastic energy budgets	131
5.3.2	APE budget	133
6	Optimal choice of reference state for studying available energetics in tropical cyclones	138
6.1	Possible reference states	139
6.1.1	Lorenzian reference states	140
6.1.2	Environmental reference states	141
6.1.3	Balanced vortex reference state	143
6.2	Comparison of reference states	151
6.3	APE properties with respect to balanced vortex reference state	157
6.4	Discussion and Conclusions	164
7	APE efficiency in tropical cyclones	170
7.1	Definitions of APE efficiency	170
7.2	Temporal variation of surface APE efficiency	174
7.2.1	Dependence on WISHE feedback	177
7.3	Potential intensity using APE theory	181
7.4	Discussion and Conclusions	187

8	Conclusions	192
8.1	Key findings and recommendations	192
8.2	Limitations and future work	203
A	Sorting Algorithm Runtimes	207
B	Energy Budget Closures	209
B.1	Finite difference forms of energy budgets	209
B.1.1	Kinetic and elastic energy budgets	209
B.1.2	Available Potential Energy budget	211
B.2	Budget closures	212
B.2.1	Kinetic and elastic energy budgets	212
B.2.2	Available Potential Energy budget	213
C	The generalised buoyancy/inertial forces and available energy of ax- isymmetric compressible stratified vortex motions	217
	References	241

Chapter 1:

Introduction

The impacts of landfalling tropical cyclones (TCs) are severe: from 1979 to 2009, TCs caused a total of 789,000 fatalities, and Hurricane Katrina alone resulted in \$125 billion worth of damage (Peduzzi et al., 2012). TC damage is expected to increase in the future as a result of increasing TC intensities and rising populations and GDP in TC-prone areas (Pielke et al., 2008; Mendelsohn et al., 2012). A fundamental physical understanding of the processes governing TC development is therefore critical in order to produce models that can predict TC behaviour and provide a sound basis for early warning systems. However, there is still much disagreement on the mechanisms by which TCs intensify, and there remain shortcomings in the representation of TC intensity in current dynamical models. This thesis uses local Available Potential Energy (APE) theory to provide new insight into the physics of TC intensification and to develop diagnostics for process-oriented model assessment.

1.1 Introduction to tropical cyclones

A tropical cyclone is a non-frontal cyclone originating over the tropical or subtropical oceans. To be classified as a tropical cyclone, the system must have a closed cyclonic low-level circulation around a well-defined low pressure centre. The intensity of a tropical cyclone is typically measured by its maximum sustained 10 m wind speed. Very intense TCs, with wind speeds above 33 m s^{-1} , are also known as hurricanes (over the Atlantic and Northeast Pacific oceans) or typhoons (over the Northwest Pacific ocean), but the generic term *tropical cyclone* (TC) will be used throughout this thesis.

Figure 1.1 illustrates the main structural features and circulations found in a typical mature TC. Air near the ocean surface spirals cyclonically inwards towards the low pressure centre. It converges and rises in the eyewall, which is a ring of deep convection

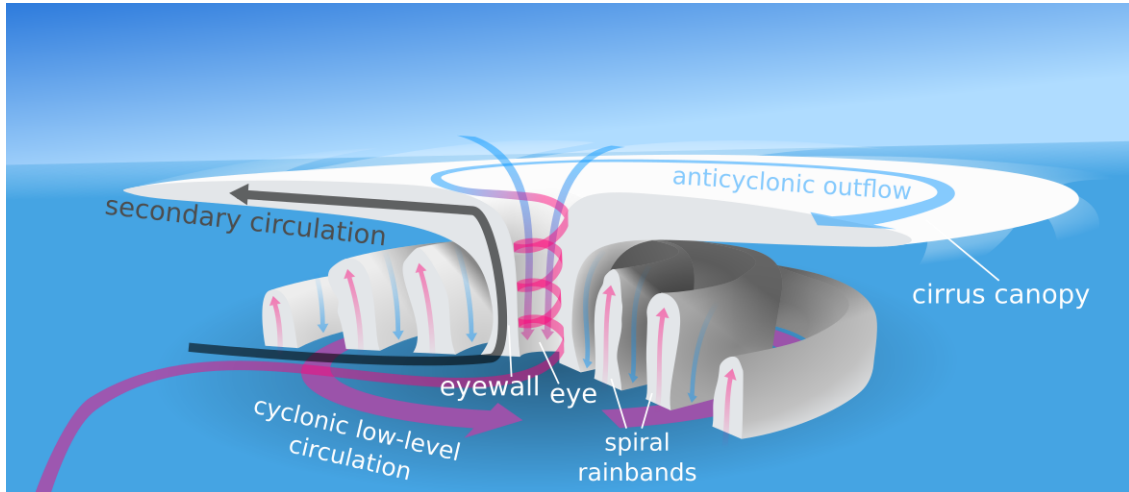


Figure 1.1: Structure of a tropical cyclone in the Northern Hemisphere. Arrows indicate wind direction, with the arrow colour representing the temperature of the air (pink=warm, blue=cold). Adapted from diagram by Kelvin Ma (<https://commons.wikimedia.org/w/index.php?curid=23226142>) under Creative Commons license CC BY 3.0.

near the TC centre that can extend through the entire depth of the troposphere. The fastest winds are usually located at the base of the eyewall. Many TCs possess an eye, which is a calm, cloud-free region of subsiding air inside the eyewall. The air outside the eyewall also subsides to balance the ascent found in the eyewall, but this large-scale subsidence is interrupted by updrafts in spiral rainbands. These are bands of precipitating cumulonimbus cloud, which may be tens of kilometres across (Emanuel, 2003). When cumulonimbus clouds (both in the eyewall and in the rainbands) penetrate a stable layer of the atmosphere, for example at the tropopause, they spread out horizontally and create a canopy of cirrus cloud above the TC (Merritt and Wexler, 1967).

The flow in a TC is often considered in terms of the *primary* and *secondary* circulations. The primary circulation is the flow in the azimuthal direction (i.e. around the central axis of the TC), which is cyclonic at lower levels but weakens with height, eventually becoming anticyclonic at upper levels. This thesis will focus on idealised axisymmetric TCs—TCs that are symmetric around their central axis. The secondary circulation, which is marked by the black arrow in Figure 1.1, comprises the radial and vertical parts of the flow: air travels inwards near the surface, upwards in the eyewall, then outwards at upper levels. The energy transfers that occur as a parcel moves around the secondary circulation are crucial for supporting the primary circulation; these energetics will be reviewed in more detail in Chapter 2.

1.2 Intensification of tropical cyclones

An early theory for TC intensification developed by Charney and Eliassen (1964), called Conditional Instability of the Second Kind (CISK), described a feedback between moist convection and a developing cyclonic vortex. Above the boundary layer, the vortex is in approximate gradient wind balance, with the radial pressure gradient force opposed by the sum of the Coriolis and centrifugal forces. However, in the boundary layer, surface friction reduces the Coriolis and centrifugal forces, resulting in a net force towards the centre of the vortex. This would cause moisture to converge near the vortex centre, leading to convection. The convection would result in latent heat release due to the condensation of water vapour. This diabatic heating would then lower the vortex's central pressure, enhancing the frictional convergence and providing further moisture convergence to fuel the convection.

The key novelty of the CISK theory was the suggestion that surface friction could play a dual role in a TC. Friction had previously been considered only to reduce wind speeds by dissipating kinetic energy. However, Charney and Eliassen (1964) showed that it also promotes intensification by supplying latent energy to fuel convection in the core (via the frictional convergence of moisture), and that this effect can dominate over the kinetic energy dissipation to intensify a TC. Rather than acting against intensification, from the CISK viewpoint surface friction is essential to TC spin-up. The CISK theory assumes that there is a pre-existing reservoir of Convective Available Potential Energy (CAPE) in the atmosphere, which allows deep convection to occur as moisture converges.

However, criticisms of CISK noted that CAPE is generally low over the tropical oceans (Emanuel et al., 1994), and that Charney and Eliassen (1964) assume latent heat release to be proportional to the convergence of moisture; this assumes that convection is limited by the environmental supply of water, rather than energy (Raymond and Emanuel, 1997). CISK also ignores the contribution of moisture to the boundary layer by surface fluxes, which had been established as an important moisture source by Kleinschmidt (1951) and Malkus and Riehl (1960). Ooyama (1982) developed CISK into the theory of *cooperative intensification* by including surface moisture fluxes and parameterising the convection based on mass rather than moisture convergence.

The role of frictional convergence has also been emphasised by recent studies outside the context of CISK, which have shown that the spin-up of winds in the inner core of a TC is associated with a convergence of angular momentum in the boundary layer (Smith and Vogl, 2008; Smith et al., 2009; Montgomery and Smith, 2014).

An alternative theory, established by Emanuel (1986), suggested that intensification instead relies upon Wind-Induced Surface Heat Exchange (WISHE). In this theory, the TC intensifies due to a positive feedback between surface wind speed and surface enthalpy fluxes, without the need for pre-existing atmospheric conditional instability. The WISHE feedback relies on surface fluxes being proportional to the surface wind speed. Surface fluxes increase the equivalent potential temperature of boundary layer air, triggering convection, which leads to latent heat release in the eyewall and therefore tropospheric warming throughout the TC core. This decreases the central pressure of the TC, so surface winds must accelerate to maintain approximate gradient wind balance. Higher surface wind speeds result in higher surface fluxes, which result in higher surface wind speeds and so on.

From the WISHE viewpoint, the fundamental source of energy for the TC is the surface enthalpy flux. CAPE is generated by surface fluxes and subsequently consumed by convection, but pre-existing environmental CAPE is not required for intensification. The WISHE and cooperative intensification theories are similar in that they both regard surface fluxes and convection as necessary ingredients for intensification, but WISHE does not consider the organisation of convection by frictional convergence to be a crucial part of the process (Smith, 1997); convergence occurs above the boundary layer due to the buoyancy gradient driven by radially-varying surface fluxes.

Axisymmetric numerical simulations performed by Craig and Gray (1996) supported WISHE over CISK or cooperative intensification as the mechanism of TC intensification, showing that the modelled intensification was much more sensitive to changes in the surface transfer coefficients for heat and moisture than for momentum. Rotunno and Emanuel (1987) used a numerical model to show that a TC could intensify in a convectively neutral environment, demonstrating that the pre-existing reservoir of CAPE required by CISK is not necessary. There is ongoing discussion regarding the importance of WISHE: simulations with a capped surface wind speed in the equations for surface flux demonstrate that a TC may still intensify without the WISHE feedback, but will do so more slowly and reach a lower maximum intensity (Montgomery et al., 2009, 2015; Zhang and Emanuel, 2016). This implies that the WISHE feedback plays an important role in intensification, but that some other mechanism or mechanisms must also contribute.

Three-dimensional effects may also be crucial for intensification. The rotating convection paradigm (Smith et al., 2009; Montgomery and Smith, 2014, 2017) proposes a move away from the axisymmetric viewpoint of CISK and WISHE and emphasises the role

of deep convective updrafts in providing localised centres of vorticity. These updrafts—sometimes referred to as Vortical Hot Towers (Hendricks et al., 2004; Van Sang et al., 2008)—have their vorticity amplified by vortex tube stretching and tilting, and then merge into a central cyclonic “monolith” (Montgomery and Smith, 2017). The existence and merging of VHTs have been observed in some developing TCs (Reasor et al., 2005; Sippel et al., 2006; Houze Jr et al., 2009; Bell and Montgomery, 2010; Raymond and López Carrillo, 2011).

Other recent avenues of research into TC intensification include the possible effect of small-scale mixing in the outflow (Emanuel, 2012; Persing et al., 2013; Montgomery et al., 2019), the changes in intensity associated with eyewall replacement cycles (Houze Jr et al., 2007; Kossin and Sitkowski, 2012; Kossin, 2015) and the intensity response of the TC to microphysical processes occurring in its spiral rainbands (Wang, 2009; Didlake et al., 2018). The interaction between so many physical processes, and the lack of consensus on which intensification mechanisms are most important, makes it challenging to understand the best routes to developing numerical models that can accurately represent the intensification and maximum intensity of TCs for the correct physical reasons. A combination of model assessment and the development of theoretical understanding are required in order to decide whether particular configuration choices are appropriate—for example, whether to use a convective parameterisation, and with which closure, at a certain resolution—based on the physical fundamentals of intensification, in order to hopefully produce models with improved statistical representations of TC intensification and intensity.

1.3 Modelling tropical cyclone intensity

1.3.1 Numerical Weather Prediction

Whereas operational forecasts of TC track have vastly improved in recent decades, improvements in intensity forecasts have been much slower (DeMaria et al., 2014; Yamaguchi et al., 2017; Cangialosi, 2019). The National Hurricane Centre (NHC) reduced 2-day track forecast errors by three quarters in the Atlantic over the period 1990-2018, during which time the 2-day intensity forecast errors were cut by less than one third (Cangialosi, 2019). The track of a TC is less challenging to forecast because it is mostly determined by the large-scale flow in which the TC is embedded, whilst its intensity is influenced by processes at many scales, from inner-core mixing to convection to the

interaction of the core with its environment (Marks et al., 1998).

The intensity of TCs in dynamical models is sensitive to resolution (Davis et al., 2008; Jin et al., 2014) as well as model physics configurations such as the cloud microphysics scheme (Lord et al., 1984; Zhu and Zhang, 2006; Chan and Chan, 2016), the parameterisation of surface fluxes (Braun and Tao, 2000; Andreas and Emanuel, 2001; Green and Zhang, 2013, 2014; Nystrom et al., 2020), and the parameterisation of vertical boundary layer mixing (Braun and Tao, 2000; Zhang et al., 2017). Such parameterisations often have an uncertain physical basis and poorly constrained parameters due to the difficulty of obtaining observations in the inner core or boundary layer of a TC; for example, measurements from a field campaign studying major hurricanes were only able to estimate the surface exchange coefficients for enthalpy and momentum to within 50% (Bell et al., 2012).

Particularly large intensity forecast errors occur in cases of rapid intensification (RI) (Kaplan and DeMaria, 2003; Davis et al., 2008; Judt and Chen, 2016; Magnusson et al., 2019). RI is usually defined as an increase of at least 30 kt (15 m s^{-1}) in 10 m winds over a period of 24 h (Kaplan and DeMaria, 2003). TCs that undergo RI shortly before making landfall are particularly dangerous, since forecasters are likely to underestimate the threat to the local population (Emanuel, 2017). Understanding the conditions and processes leading to RI and improving the representation of RI in operational forecast models have therefore been highlighted as priorities for the TC research community (Rappaport et al., 2009, 2012; Gall et al., 2013; Hendricks et al., 2019).

1.3.2 Global climate models

Current high-resolution global climate models (also known as general circulation models, or GCMs) are capable of reproducing to a reasonable degree the global frequency of TCs and the spatial distribution of TC track density (Shaevitz et al., 2014; Roberts et al., 2015, 2020). GCMs also capture the interannual variability in TC numbers to a sufficient extent to provide skilful seasonal forecasts on a regional scale (Chen and Lin, 2011, 2013; Vecchi et al., 2014; Camp et al., 2015; Murakami et al., 2016).

GCMs generally cannot simulate TCs of the highest observed intensities, due to their insufficient horizontal resolution: Davis (2018) showed that it is unrealistic to expect a model with resolution coarser than 0.25° ($\approx 28 \text{ km}$) to represent storms achieving Category 4 or 5 on the Saffir-Simpson wind scale, and this is borne out by most GCM simulations.

In general, GCMs are able to produce more intense TCs and therefore more realistic

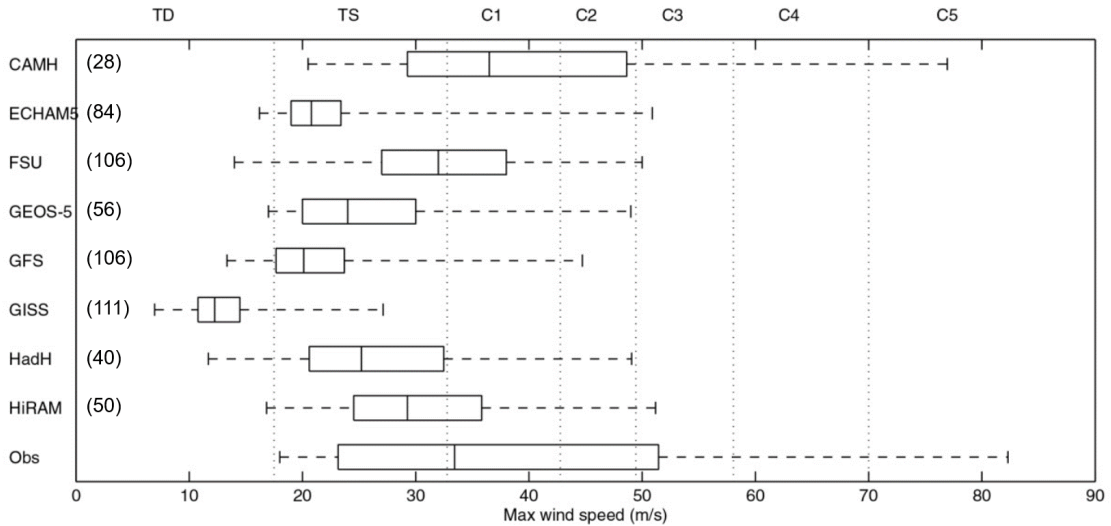


Figure 1.2: Distributions of the maximum intensity of TCs in GCMs and observations (Obs). The numbers in brackets next to the name of each GCM give its approximate nominal resolution in km. The boxes span the 25th to 75th percentiles of maximum intensity, and the line in each box marks the median. The whiskers mark the minimum and maximum values of maximum intensity. The dotted vertical lines demarcate the TC classifications: tropical depression (TD), tropical storm (TS), Category 1-5 hurricane (C1-C5). Adapted from Shaevitz et al. (2014).

intensity distributions as their horizontal resolution increases, to a typical highest resolution of 25 km (Manganello et al., 2012; Shaevitz et al., 2014; Roberts et al., 2015, 2020). However, this is not the case for every GCM (Shaevitz et al., 2014; Roberts et al., 2015). Figure 1.2 compares the distributions of maximum intensity produced in simulations by a range of atmosphere-only GCMs, as studied by Shaevitz et al. (2014), to the observed distribution. Whilst the highest-resolution model is also the one that produces the best match to the observed distribution (CAMH, the high-resolution run of the Community Atmosphere Model CAM5.1), a higher resolution does not always correspond to a better simulation of intensity. The 40 km-resolution run of HadGEM3 (HadH) produces TCs that are too weak, and even weaker on average than those from the 50 km HiRAM model. Two different TD models with the same resolution may generate markedly different distributions of TC intensity: the FSU and GFS models are both run with a resolution of 106 km, but the GFS model TCs are much weaker on average.

Part of the reason for this is that the resolution usually quoted for a GCM is its *nominal resolution*, which is simply a measure of grid box size, but models with the same nominal resolution may have different *effective resolutions*; this refers instead to the smallest scale the model can plausibly represent, based on the kinetic energy spectrum it produces, and is typically 3–5 times larger than the nominal resolution (Klaver et al., 2020). The effective resolution of a dynamical core is affected by factors such as the order

of accuracy of the advection scheme and the type of numerical diffusion implemented (Kent et al., 2014); these can therefore be expected to influence the representation of TCs. Model physics configurations, such as the choice of convective parameterisation, do not impact the effective resolution but cause additional differences in TC intensity.

It is difficult to ascertain precisely why GCMs of similar nominal resolution differ in their representation of TC intensity, since the ultimate intensity distribution is the result of interactions between many aspects of model structure and parameterisations—the intensification of the model’s TCs being affected by all the processes and parameterisations mentioned in Sections 1.2 and 1.3.1—and is influenced by any differences in the large-scale climate simulated by the model. It has been confirmed that model differences do not just change this large-scale environment, but alter the structure of TCs themselves and their interactions with the environment (Camargo et al., 2007; Kim et al., 2018; Vecchi et al., 2019). Aspects of model configuration (other than nominal resolution) that have been shown to affect TC intensity in GCMs include the convective parameterisation (Reed and Jablonowski, 2011; Kim et al., 2012; Murakami et al., 2012a,b; Stan, 2012; Zhao et al., 2012; Lim et al., 2015) the dynamical core (Reed et al., 2015) and atmosphere-ocean coupling (Zarzycki, 2016).

GCMs are often used to investigate the behaviour of TCs under future climate scenarios. Generally, studies of this kind predict a decrease in the global frequency of TCs, but an increase in precipitation rates near TC centres and an increase in the frequency of the most intense TCs (Gualdi et al., 2008; Held and Zhao, 2011; Bell et al., 2013; Rathmann et al., 2014; Kim et al., 2014; Roberts et al., 2015; Wehner et al., 2015; Bacmeister et al., 2018). However, the 25 km HiFLOR model, which is able to simulate Category 4 and 5 hurricanes and their interannual variability (Murakami et al., 2015), has recently been shown to predict either no significant change or an *increase* in overall TC frequency under climate change, along with increases in the probability of higher intensities and higher intensification rates (Bhatia et al., 2018; Vecchi et al., 2019). The magnitude of changes is also uncertain in many cases. For example, estimates of the increase in TC-associated rainfall range from 3% to 37% (Scoccimarro et al., 2017).

Yoshida et al. (2017) emphasised that very large ensembles are required to reduce uncertainty in the projected behaviour of TCs, since they occur so infrequently and are subject to large internal variability—this particularly applies in the case of Category 4 and 5 hurricanes. Using 90 ensemble members to simulate future climate conditions (based on different SST warming patterns and perturbed initial atmospheric values) and

100 members for the current climate, Yoshida et al. (2017) found that Category 4 and 5 storms would decrease in frequency globally, but increase by 88% in the Northeast Pacific. Although the rarity of the highest-intensity TCs means that it may take a long time for any statistically significant changes in their frequency to be seen in the real world, these ensembles help to understand the changing probabilities of extreme events under future climate conditions.

Understanding how TCs will change in the future is vital in order to assess and mitigate the risks posed to vulnerable populations. Climate change is expected to heighten flood risks from TCs, partly due to rising sea levels (Walsh et al., 2016; Marsooli et al., 2019), and changes in TCs themselves are projected to cause a 50% increase in TC damage from now to 2070–2090 (with a further 300% increase due to increasing assets in the path of TCs, assuming no adaptation) (Gettelman et al., 2018). If intensification rates increase, occurrences of RI prior to landfall may become more common, rendering intensity forecasting even more difficult (Emanuel, 2017).

However, the uncertain aspects of TC physics in climate models make it difficult to assess which future projections should be taken most seriously. The fact that HiFLOR is more capable of representing high-intensity storms in the current climate does not necessarily mean its TCs respond more realistically to increases in CO₂ on a multi-decadal timescale than the TCs of other models (Vecchi et al., 2019). Changes to different aspects of model configuration lead to changes in projected TC distributions for different physical reasons. For example, introducing stochastic physics to a GCM can result in an increase in TC frequency that is approximately equivalent to a doubling in resolution; whereas the higher frequency in the case of increased resolution is primarily due to reduced vertical wind shear, the stochastic physics increases the frequency by moistening the mid-troposphere (Vidale et al., 2019). There has therefore been a recent effort to design process-oriented diagnostics for TCs in GCMs (Kim et al., 2018; Wing et al., 2019; Moon et al., 2019). These diagnostics are designed to be closely connected to model parameterisation choices in order to investigate the mechanisms by which these choices lead to differences in the intensity of the model’s TCs.

Kim et al. (2018) used process-oriented diagnostics based on the azimuthally-averaged dynamic and thermodynamic properties of TCs to show that a model’s treatment of moisture, convection and the coupling between them is key to the intensity of the TCs it produces. Examining three models at 50 km resolution, they found that the convection scheme used in the model that produced the most intense TCs resulted in convection

with the highest sensitivity to moisture. This model produced more precipitation and column-integrated diabatic heating than the others (for a TC of the same intensity), resulting in more favourable conditions for intensification. This demonstrates how process-oriented diagnostics can give insight into how parameterisations affect the representation of physical processes influencing TC intensity, rather than simply assessing models based on their TC frequency and intensity statistics.

1.4 Thesis aims and objectives

More advanced process-oriented diagnostics are required in order to understand the processes affecting intensity in numerically-modelled TCs. Energy budgets provide a possible basis for useful diagnostics, since they link processes involving moisture and convection, which were identified as important by Kim et al. (2018), to intensification in terms of kinetic energy. Previous energy budgets of TCs have been mostly based on total potential energy, dry APE or entropy frameworks. This thesis uses local APE theory for the moist atmosphere as the basis for its energy budgets, because it provides a closer link between the production of available energy by diabatic processes and the ultimate development of the TC via the generation of kinetic energy. APE theory and TC energetics will be reviewed fully in Chapter 2, which will explore the advantages of using APE theory over alternative thermodynamic approaches.

The overall aims of this thesis are:

- (1) To produce a full budget of moist APE for a model of the atmosphere.
- (2) To understand TC intensification and maintenance in terms of APE theory.
- (3) To identify specific aspects of APE or APE-related quantities that could be usefully applied as process-oriented diagnostics for TCs in NWP or global climate models.

A complete budget of moist APE in the atmosphere has not previously been created, so a significant part of the work here must be dedicated to developing the budget and addressing some outstanding questions in APE theory. A key problem is that APE is measured relative to a reference state, but there is no consensus on which reference state should be used. The aims listed above will be achieved by accomplishing the following objectives:

- (a) Constructing a budget of local moist APE for an idealised axisymmetric TC model.

- (b) Developing a method to assess the suitability of reference states for studying available energetics in the model, and identifying which reference state(s) should be used.
- (c) Using the APE budget to identify the key sources and sinks of APE in a TC.
- (d) Relating the APE efficiency of the modelled TC to traditional concepts of efficiency, which have been previously identified as important to TC development.

Since this will be the first full budget of moist APE for the atmosphere, it is most practical to use a simple idealised TC model, so that the fundamental properties of the budget can be established in a setting where all processes can be accounted for to ensure budget closure. The chosen axisymmetric model, which will be described fully in Chapter 4, is used because it facilitates development of the APE budget, rather than because it provides the highest-fidelity simulation of a TC possible.

1.5 Thesis structure

Chapter 2 provides a background on theories of TC energetics. This includes a review of previous energetic analyses of TCs, an account of the fundamentals of APE theory, and an explanation of why moist APE theory can provide an advantageous viewpoint of TC development. This chapter also reviews concepts of TC efficiency, so that these can later be linked to the concepts of efficiency appearing in APE theory.

Chapter 3 investigates the accuracy of the sorting algorithms that are currently used to compute moist atmospheric APE and compares them to a novel algorithm based on CAPE. The purpose of this chapter is to explore the shortcomings of existing studies of the moist atmosphere based on APE theory, and to motivate a move towards the more physical approach of local APE theory for the rest of the thesis.

Chapter 4 details the configuration of the axisymmetric TC model for which the APE budget will be constructed.

Chapter 5 explores the energetics of the axisymmetric model. In particular it details the construction of a local moist APE budget for the model—the first full budget constructed for the moist atmosphere in any context—and explores the sources and sinks of APE relative to a simple reference state. This addresses objectives (a) and (c).

Chapter 6 develops an objective method for assessing the suitability of reference states and compares the performances of several possible reference states, fulfilling objective (b).

Objective (c) is also revisited by questioning whether the sources and sinks identified in Chapter 5 are sensitive to the choice of reference state.

Chapter 7 explores the links between the APE efficiency of a TC and traditional established notions of efficiency, which have been identified as key intensification- and intensity-related diagnostics—these are the overall energetic efficiency of a TC, and the Carnot efficiency used to predict the maximum intensity of a TC. This accomplishes objective (d).

Chapter 8 discusses the major findings of the thesis in the context of Aims (1)–(3). In particular, a section is devoted to suggesting how the results of Chapters 5–7 could be parlayed into practical diagnostics to enhance the understanding of processes affecting TC intensification and intensity in NWP and climate models.

Chapter 2:

Review of energetics and efficiency

2.1 Available Potential Energy

The intensification of a tropical cyclone (TC) is primarily driven by the creation of potential energy by surface enthalpy fluxes, which is subsequently converted into kinetic energy. However, only a fraction of the generated potential energy is available to be reversibly converted into kinetic energy; the contribution of the surface enthalpy fluxes must be split between the available part and the unavailable part. Theories of available energy, such as Lorenz’s Available Potential Energy (APE) theory or the exergy-based available enthalpy, aim to quantify this available part of the potential energy and predict its sources and sinks.

The concept of APE was originally introduced by Margules (1903)—though he referred to it as *available kinetic energy*—to quantify the maximum kinetic energy a storm could achieve under any adiabatic redistribution of mass. The theory was later popularised by Lorenz (1955), who applied it to the general circulation. Later developments by Andrews (1981) and Holliday and McIntyre (1981) introduced a locally-defined APE theory, which will be the focus of this thesis. The most recent advances in local APE theory have yielded a generalised theory for multi-component compressible stratified fluids (Tailleux, 2018), which will be used in this thesis to link diabatic processes in TCs to their intensification through the generation of kinetic energy.

This section provides a background on the APE theory developed by Lorenz (1955), highlights the reasons that APE theory is the best energetic framework to use for the purpose of investigating TC intensification, and discusses the difficulties of applying the theory to a moist atmosphere. This is followed by an outline of the local theory of APE, which will form the basis for the work in Chapters 5, 6 and 7. Finally, theories of APE

for symmetric flows, which permit the use of non-resting reference states, are discussed; these form the background to the work in Chapter 6, where the APE of a TC relative to a balanced vortex is computed. Previous work that has applied APE theory to TCs will not be addressed here, but is left to Section 2.2, in which TC energetics in general will be reviewed.

2.1.1 Lorenz APE

Margules (1903) and Lorenz (1955) sought to identify the portion of the total potential energy (TPE) in the atmosphere that can be converted into kinetic energy by adiabatic motions, which Lorenz termed the APE. The specific TPE, e_{tp} , is defined as the sum of the specific internal and gravitational potential energies. For a dry atmosphere, this is

$$e_{tp} = c_v T + gz, \quad (2.1)$$

where $c_v = 717.5 \text{ J kg}^{-1} \text{ K}^{-1}$ is the specific heat capacity at constant volume of dry air, T is temperature in K, $g = 9.81 \text{ m s}^{-2}$ is gravitational acceleration, and z is height above the Earth's surface. TPE is not uniquely defined, since the internal energy is only defined up to a constant (Marquet, 2015; Marquet and Geleyn, 2015), and the gravitational potential energy also depends on the choice of reference level $z = 0$. The definition given in Equation (2.1) assumes that the internal energy is zero at a temperature of absolute zero. The issue becomes more pronounced for moist air, where the differences between the constants for the various constituents appear in the full expression, but this subtlety is usually ignored in studies of atmospheric TPE (e.g. Hogsett and Zhang, 2009).

It can be seen that not all TPE is APE by considering a stable atmosphere with a horizontal density stratification. In this case, no atmospheric motion is expected, so the APE is zero. However, the atmosphere must still contain TPE: it possesses both gravitational potential energy, since it has mass, and internal energy, since the air has some temperature above absolute zero.

Lorenz defined the APE of the atmosphere as the difference in TPE between its actual state and the state of minimum TPE that could be achieved by rearranging it through adiabatic motion. This minimised potential energy state is known as the *reference state*. The TPE contained in the atmosphere in its reference state is the Background Potential Energy (BPE); Lorenz's method partitions the TPE into APE and BPE.

The utility of considering atmospheric energetics in terms of APE instead of TPE

can most clearly be seen by thinking about the effects of warming and cooling a stable atmosphere. This example, illustrated in Figure 2.1, is known as the “cooling paradox”. If a small region of the atmosphere is heated (Figure 2.1a), it will no longer be stable. The warmer air will rise, leading to low pressure and convergence below the heating source and divergence aloft. In this case, the heating increases the TPE of the atmosphere, so it is easy to see that it can supply the energy required for motion. If instead this same region of the atmosphere is cooled (Figure 2.1b), consideration of the TPE might suggest that there will be no motion, since cooling decreases the TPE. However, it is clear that instability will still occur, so motion must result. This apparent contradiction is resolved by introducing the concept of APE: the stable atmospheric configuration is the reference state, and any process that moves the actual atmospheric state away from the reference state will make energy available for motion, regardless of its effect on the TPE. The cooling increases the APE, which is converted into kinetic energy in the downward motion at the location of the cooling, low-level divergence and upper-level convergence.

APE therefore provides a more useful quantification than TPE of the energy that could be converted into kinetic energy in the atmosphere. The majority of TPE is unavailable for conversion—Lorenz (1955) found that the APE is typically less than 1% of the TPE—and the cooling paradox demonstrates that the sign of change in APE corresponds to the sign of the change in kinetic energy in a way that the sign of change in TPE does not.

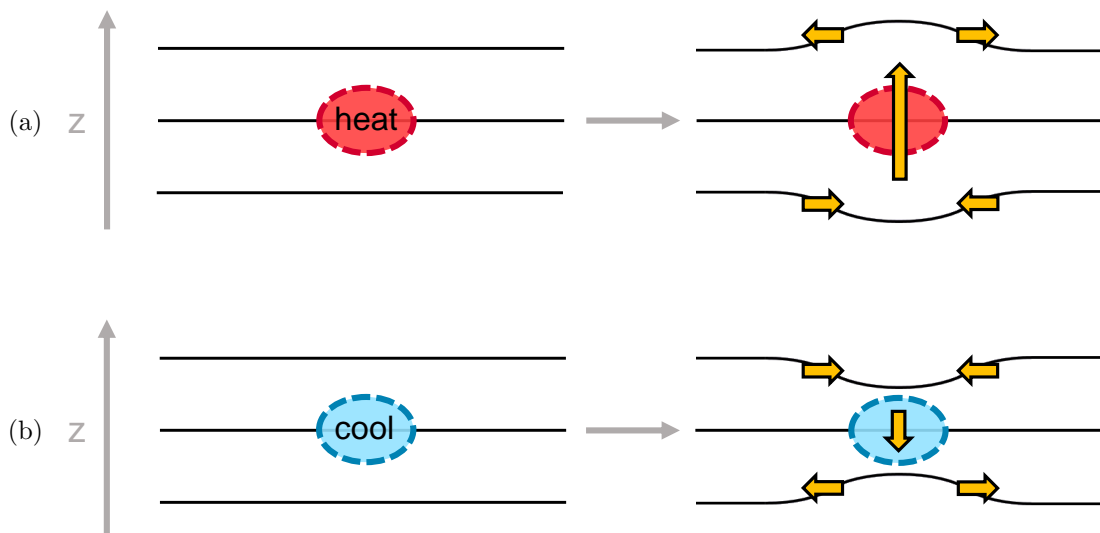


Figure 2.1: Illustration of the cooling paradox in a stable, horizontally stratified atmosphere to demonstrate the usefulness of APE theory. Black lines indicate isobars and orange arrows denote atmospheric motion. (a) Effect of localised heating. (b) Effect of localised cooling.

For a dry hydrostatic atmosphere, ignoring any topography, Lorenz (1955) expressed the average APE per unit area of the Earth's surface as

$$\overline{\text{APE}} = \frac{c_p}{g(1+\kappa)p_{00}^\kappa} \int_0^\infty \left(\overline{p^{1+\kappa}} - \overline{p}^{1+\kappa} \right) d\theta, \quad (2.2)$$

where overbars denote an average over an isentropic surface, $c_p = 1004.5 \text{ J kg}^{-1} \text{ K}^{-1}$ is the specific heat capacity at constant pressure of dry air, $R_d = 287 \text{ J kg}^{-1} \text{ K}^{-1}$ is the specific gas constant for dry air, $\kappa = \frac{R_d}{c_p}$, p is pressure, $p_{00} = 1000 \text{ hPa}$, and θ is potential temperature.

The global Lorenz energy cycle is characterised by the budgets

$$\frac{d\text{APE}}{dt} = G - C_{\text{APE} \rightarrow \text{KE}} \quad (2.3)$$

$$\frac{d\text{KE}}{dt} = C_{\text{APE} \rightarrow \text{KE}} - D, \quad (2.4)$$

where G is the rate of diabatic APE generation, $C_{\text{APE} \rightarrow \text{KE}}$ is the rate of conversion from APE to kinetic energy, and D is the rate of viscous dissipation of kinetic energy. Note that although kinetic energy is defined locally for any air parcel, Lorenz's APE is only defined globally, and therefore these equations concern the volume integrals of the energies and their conversions.

Lorenz APE can also be formulated for a limited region, for example a cylinder around a tropical cyclone (Dutton and Johnson, 1967; Johnson, 1970; Smith et al., 1977; Edmon Jr, 1978). For a limited region of area σ , extending vertically from a surface pressure p_s to an upper pressure p_u , Edmon Jr (1978) formulated the regional APE as

$$\text{APE} = \frac{c_p}{\sigma g} \int_\sigma \int_{p_u}^{p_s} NT dp d\sigma, \quad (2.5)$$

where T is temperature, the efficiency N is

$$N = \frac{p^\kappa - p_r^\kappa}{p^\kappa} = \frac{T - T_r}{T}, \quad (2.6)$$

and the reference pressure is defined as an isentropic average over the region:

$$p_r(\theta, t) = \frac{1}{\sigma} \int_\sigma p(x, y, \theta, t) d\sigma, \quad (2.7)$$

where x and y are the horizontal spatial coordinates and t is time. The generation of

APE by diabatic heating in the region is

$$G(\text{APE}) = \frac{1}{\sigma g} \int_{\sigma} \int_{p_u}^{p_s} N \dot{Q} dp d\sigma, \quad (2.8)$$

where \dot{Q} is the rate of diabatic heating. If heating occurs in locations with high positive efficiency N , the increase in APE will be higher than if it occurred in locations with low (or negative) efficiency.

Lorenz's theory of APE has been used to study dry atmospheric energetics in climate models and reanalysis datasets (Hu et al., 2004; Li et al., 2007; O'Gorman and Schneider, 2008; Schneider and Walker, 2008), showing for example that the Lorenz energy cycle is expected to weaken under increasing greenhouse gas concentrations (Veiga and Ambrizzi, 2013). The dry framework is only able to account for latent heat release by treating it as an external source of APE (as a contributor to G in Equation (2.3)), rather than viewing it as an internal energy conversion in the atmosphere; this means that computing dry APE budgets requires full knowledge of the distribution of latent heat release.

Pauluis (2007) derived a budget of Lorenz APE that fully accounts for processes occurring in a moist atmosphere, treating latent heat release as an internal energy conversion. For an idealised tropical atmosphere in radiative-convective equilibrium, Pauluis (2007) found that surface energy fluxes provide a large source of APE that must be compensated by a sink due to the diffusion of water vapour between parcels.

However, a significant obstacle to applying Lorenz's theory to a moist atmosphere is the difficulty of obtaining the moist reference state, since no analytical method exists to calculate it. For a single column of dry air parcels, the reference state can be found by simply ordering the parcels such that potential temperature θ increases with height. This provides an adiabatic rearrangement that minimises the TPE of the column and ensures that density decreases upwards, so that the column is statically stable. For a single column of moist air parcels, in which rearrangements are made conserving entropy and total water content of the parcels (Lorenz, 1978), the situation is complicated by the possibility of latent heat release due to condensation. One parcel may be denser than another at a certain height, but then less dense if they are lifted to a height where the first parcel condenses but the second one does not. An attempt to find the reference state using an reversible adiabatic re-ordering of the parcels will produce varying results depending on the exact procedure used. The presence of moisture makes it possible for stable, adiabatically rearranged states that are local TPE minima to exist, in addition to the global minimum usually defined as the Lorenz reference state (Stansifer et al., 2017;

Turner and Norbury, 2020).

Practical implementations of Lorenz APE theory for a moist atmosphere have relied on a variety of sorting algorithms to compute the reference state. Hieronymus and Nycander (2015) established that it is possible to find the globally minimal TPE rearrangement of a set of discrete moist air parcels using the Munkres algorithm (Munkres, 1957), but obtaining this exact global minimum is very computationally expensive. Many cheaper heuristic algorithms have therefore been developed, using procedures to move parcels to different pressure levels and sort them by their density in an attempt to approximate the minimal TPE state (Lorenz, 1979; Randall and Wang, 1992; Wong et al., 2016; Stansifer et al., 2017).

Sorting algorithms have been used to study moist atmospheric APE in extratropical storm tracks (O’Gorman, 2010; Gertler and O’Gorman, 2019) and tropical cyclones (Wong et al., 2016). However, it is not clear that sorting procedures will always compute the most physically useful value of APE. For example, Wong et al. (2016) suggested that their top-down sorting algorithm tended to release too much Convective Available Potential Energy (CAPE), which was not released in practice in the tropical cyclone due to the presence of Convective Inhibition (CIN). This could be an indicator that a local TPE minimum may sometimes be a more appropriate reference state than the global minimum, contrary to the usual assumption, or it could be a result of the sorting algorithm providing a poor approximation to the global minimum.

Assessment of the performance of sorting algorithms that aim to approximate the Lorenz APE in the moist atmosphere has so far been restricted to a few soundings (Stansifer et al., 2017). The work presented in Chapter 3 will improve upon this by comparing the results of existing algorithms over a wider range of atmospheric data, and investigating the possibility of estimating single-column APE directly from CAPE, as suggested by Emanuel (1994). This work aims to highlight the loss of physical insight that occurs when sorting algorithms are employed to compute moist APE.

An alternative to Lorenz’s APE theory, which makes it possible to use a computationally cheaper reference state, and makes the link between APE and CAPE clearer, is the local APE theory originally developed by Andrews (1981) and Holliday and McIntyre (1981). The next section outlines local APE theory, describes how it is linked to Lorenz’s APE, and explains why the local form is chosen for the TC budgets in this thesis.

2.1.2 Local APE theory

Andrews (1981) and Holliday and McIntyre (1981) realised that it was possible to construct an *APE density* for a parcel in a stratified fluid. APE density is defined as the work that must be done by buoyancy forces on the fluid parcel to bring it (reversibly and adiabatically) from its position in the reference state to its actual position.

In the context of local APE theory, any hydrostatically-balanced reference state may be used as an alternative to the adiabatically rearranged Lorenzian reference state. The Lorenz and local APE theories are equivalent in the sense that if the local APE is integrated over a closed domain, and the Lorenzian reference state is used, the result will be identical to the Lorenz APE for that domain. The flexibility to use an alternative reference state is a particular advantage of the local theory for the moist atmosphere, where the Lorenz reference state is difficult to obtain. This section outlines the existing theories of local APE and their applications, highlighting in particular the aspects of the theories that are relevant to their application to a compressible moist atmosphere and therefore to the investigation of tropical cyclone energetics.

The APE density as defined by Andrews (1981) or Holliday and McIntyre (1981) is advantageous for studying available energetics because it provides a quantity that is positive definite, integrates to the Lorenz APE when considered over a closed domain using the Lorenz reference state, and is locally defined. Although some studies have examined the spatial distributions of the integrand in the expression for Lorenz APE (Li et al., 2007; Ahbe and Caldeira, 2017), this is not obviously meaningful for the spatial distribution of kinetic energy production, since the Lorenz theory relies on a global definition. The local definition means that budgets of APE density can be constructed to investigate local energy production and conversion.

These properties of APE density have made it attractive for studying the energetics of mixing in turbulent stratified fluids (Winters and Barkan, 2013; Scotti and White, 2014). However, the theories of Andrews (1981) and Holliday and McIntyre (1981) are only designed to account for the energetics of a single-component fluid. Whilst a single-component fluid may suffice for an investigation of turbulent mixing, and local APE theory has been successfully applied to a dry atmosphere (Novak and Tailleux, 2018), it is necessary to consider a binary fluid in order to make a full account of the local available energetics of a salty ocean or a moist atmosphere.

The APE density of a salty water parcel in the ocean is the work done against buoyancy forces to bring it from its position in the reference state to its actual position,

whilst conserving potential temperature θ (i.e. conserving specific entropy) and salinity S (Tailleux, 2013b; Saenz et al., 2015). To simplify the local APE framework, studies of ocean energetics have typically used its form under the Boussinesq approximation, and neglected non-linearities in the equation of state (Scotti et al., 2006; Zemsikova et al., 2015; MacCready and Giddings, 2016).

Tailleux (2013b) presented a budget of APE density for a Boussinesq ocean, which allowed for a non-linear equation of state. This work also used climatological ocean data to demonstrate that using the horizontal mean density as the density profile of the reference state provides a reasonable approximation to the APE density computed using the Lorenz reference state.

This version of local APE theory allows budgeting of the generation and dissipation of APE density due to diabatic processes affecting θ and S , and is generally applicable to any multi-component Boussinesq fluid. For a moist atmosphere, the conserved quantities during reversible adiabatic parcel motion are specific entropy s (or some potential temperature variable acting as a proxy for entropy) and total specific humidity q_t , following the definition of Lorenz (1978) for the global APE theory for a moist atmosphere.

Local APE theory has been fully generalised to a compressible multi-component fluid (Tailleux, 2018). The aspects of this generalised theory that will be relevant for the energy budgets in this thesis are now detailed. Where necessary, the notation of Tailleux (2018) is adapted to suit the moist atmospheric application and to match the notation that will be used in the rest of the thesis.

The starting points for the derivation of the energetics for a moist atmosphere are the Navier-Stokes equation, the continuity equation, the equation of state, and equations for the evolution of specific moist entropy and total specific humidity:

$$\frac{D\mathbf{v}}{Dt} + 2\boldsymbol{\Omega} \times \mathbf{v} = -\frac{1}{\rho}\nabla p - \nabla\Phi + \mathbf{F}, \quad (2.9)$$

$$\frac{D\rho}{Dt} = -\rho\nabla \cdot \mathbf{v}, \quad (2.10)$$

$$\rho = \rho(s, q_t, p), \quad (2.11)$$

$$\frac{Ds}{Dt} = \dot{s}, \quad (2.12)$$

$$\frac{Dq_t}{Dt} = \dot{q}_t. \quad (2.13)$$

Here, $\frac{D}{Dt}$ is the Lagrangian derivative, \mathbf{v} is the velocity of moist air, $\boldsymbol{\Omega}$ is the Earth's

rotation vector, ρ is the density of moist air, \mathbf{F} represents frictional forces, and $\Phi = gz\hat{\mathbf{z}}$ is the geopotential (the gravitational acceleration g will be assumed constant throughout this thesis), with z the height above the Earth's surface and $\hat{\mathbf{z}}$ the unit vector in the z direction. Diabatic sources/sinks of entropy are represented by \dot{s} , while \dot{q}_t denotes sources/sinks of total specific humidity.

To begin, frictionless reversible adiabatic flow is assumed, so that $\mathbf{F} = \dot{s} = \dot{q}_t = 0$. In this case, multiplying Equation (2.9) by $\rho\mathbf{v}$ and rearranging with the use of (2.10) and (2.11) yields the standard energy conservation relation

$$\rho \frac{D}{Dt} \left(\frac{\mathbf{v}^2}{2} + \Phi + e_i \right) + \nabla \cdot (p\mathbf{v}) = 0, \quad (2.14)$$

where the specific internal energy e_i is defined in terms of the specific enthalpy $k = k(s, q_t, p)$ as $e_i = k - \frac{p}{\rho}$.

To cast this budget in terms of available energy, it is necessary to introduce a reference state. For now, the reference state is assumed to vary only in the vertical direction, following Tailleux (2018). Variables in the reference state will be denoted by a subscript 0. The reference state must be in hydrostatic balance,

$$\frac{dp_0(z)}{dz} = -\rho_0(z) \frac{d\Phi(z)}{dz}. \quad (2.15)$$

The *reference height* z_r of a moist air parcel with specific entropy s and total specific humidity q_t is defined using the Level of Neutral Buoyancy (LNB) equation

$$\rho(s, q_t, p_0(z_r)) = \rho_0(z_r). \quad (2.16)$$

The reference height is the height at which the parcel, when moved reversibly and adiabatically, reaches neutral buoyancy with respect to the reference state. It is possible for Equation (2.16) to have no solutions, one solution, or multiple solutions. Tailleux (2013b) details a method for determining the reference height that allows for all of these possibilities. For a parcel at height z , first the parcel's *in situ* buoyancy with respect to the reference state is computed. If this is positive, z_r is chosen as the lowest LNB satisfying $z_r > z$, or the top of the domain if no such LNB exists. If the *in situ* buoyancy is negative, z_r is the highest LNB with $z_r < z$, or the bottom of the domain if no such LNB exists.

Introducing the reference state and the reference height allows Equation (2.14) to be

rewritten as

$$\rho \frac{D}{Dt} \left(\frac{\mathbf{v}^2}{2} + \Pi \right) + \nabla \cdot [(p - p_0) \mathbf{v}] = 0, \quad (2.17)$$

where the *available energy* Π takes the form

$$\Pi = \Phi(z) - \Phi(z_r) + k(s, q_t, p) - k(s, q_t, p_r) + \frac{p_0 - p}{\rho}. \quad (2.18)$$

Here the definition $p_r = p_0(z_r)$ has been used. Equation (2.17) demonstrates that $\frac{\mathbf{v}^2}{2} + \Pi$ is conserved (this sum of kinetic and available energies is the pseudoenergy defined by (Shepherd, 1993)).

To understand the physical meaning of Π , it is useful to split it into two components $\Pi = e_e + e_a$, where e_e is the available elastic energy (AEE) density and e_a is the APE density. These energy densities are defined by

$$e_e = k(s, q_t, p) - k(s, q_t, p_0(z)) + \frac{p_0(z) - p}{\rho}, \quad (2.19)$$

$$e_a = \Phi(z) - \Phi(z_r) - k(s, q_t, p_r) + k(s, q_t, p_0(z)). \quad (2.20)$$

Note that Tailleux (2018) refers to e_e and e_a as Π_1 and Π_2 , but a more transparent notation is adopted here to aid the clarity of the energy budgets throughout the thesis.

The AEE density can be written in integral form as

$$e_e = \int_{p_0(z)}^p [\alpha(s, q_t, p') - \alpha(s, q_t, p)] dp' = \int_{p_0(z)}^p \int_{p'}^p \frac{1}{\rho^2 c^2} (s, q_t, p'') dp'' dp', \quad (2.21)$$

where $\alpha = \frac{1}{\rho}$ is specific volume, and $c = \sqrt{\frac{\partial p}{\partial \rho}}$ is the speed of sound. Hence e_e is the work done if the parcel were to adiabatically expand/contract from its actual pressure $p(x, y, z, t)$ to the reference pressure $p_0(z)$. Equation (2.21) also shows that e_e is positive definite. The AEE density is often written in its quadratic form for small-amplitude perturbations,

$$e_e \approx \frac{(p - p_0(z))^2}{2\rho^2 c^2}, \quad (2.22)$$

which is derived from Equation (2.21) by assuming constant ρ and c for pressures between p and p_0 (Andrews, 1981; Bannon, 2003; Peng et al., 2015).

The integral form of APE density, which can be obtained from Equation (2.20) using

the relationship $\alpha = \left(\frac{\partial k}{\partial p}\right)_{s, q_t}$ and the hydrostatic equation (2.15), is

$$e_a = \int_{p_0(z_r)}^{p_0(z)} [\alpha(s, q_t, p') - \hat{\alpha}_0(p')] dp'. \quad (2.23)$$

The function $\hat{\alpha}_0(p)$ returns the value of α_0 at the height where the reference pressure is p ; denoting the inverse of $p_0(z)$ by $Z_0(p)$, it is defined by $\hat{\alpha}_0(p) = \alpha_0(Z_0(p))$. Equation (2.23) can be written in terms of buoyancy by making the change of variable $p' = p_0(z')$, $dp' = -\frac{g}{\alpha_0} dz'$, to obtain

$$e_a = \int_z^{z_r} b(s, q_t, z') dz', \quad (2.24)$$

where the buoyancy b is defined as

$$b = g \frac{\alpha(s, q_t, p_0(z)) - \alpha_0(z)}{\alpha_0(z)}. \quad (2.25)$$

Equation (2.24) makes it apparent that the APE density is the work done by buoyancy forces in moving a parcel reversibly and adiabatically from its actual height z to its reference height z_r . This invites comparison with Convective Available Potential Energy (CAPE), which is also defined as an integral of buoyancy from a parcel's actual height to its LNB (e.g. Emanuel, 1994, p. 169). A key difference between CAPE and APE density is that when defining CAPE, the parcel's buoyancy is calculated relative to its local environment, whereas APE density is defined using buoyancy with respect to the reference state. The buoyancy (2.25) also requires that the parcel has undergone adiabatic expansion/compression to the reference pressure p_0 . In addition, the definition of CAPE assumes that the parcel moves upwards and is positively buoyant at some lifted height, whereas APE density can be computed for parcels of any buoyancy. The LNB used to calculate CAPE is specifically the LNB above the parcel's Level of Free Convection (LFC), whereas when calculating APE density it is whichever solution to the LNB equation (2.16) lies closest to the parcel in the direction of its buoyant motion.

Similarly to the the AEE density, the APE density may be approximated by a quadratic form:

$$e_a \approx N_r^2 \frac{(z - z_r)^2}{2}, \quad (2.26)$$

with buoyancy frequency

$$N_r^2 = -\frac{g_0}{\rho_r} \left[\frac{d\rho_0}{dz}(z_r) + \frac{g\rho_r}{c^2(s, q_t, p_r)} \right], \quad (2.27)$$

where $p_r = p_0(z_r)$ and $\rho_r = \rho(s, q_t, p_r)$. Although the quadratic approximation is easier to compute than the integral form of Equation (2.24), it is not used in this thesis because it is only valid for small-amplitude displacements, and therefore will not be appropriate in TCs, where extensive vertical motion of parcels is expected. The integral form is valid for finite-amplitude parcel displacements.

The budget of APE density may be obtained by taking the Lagrangian derivative of Equation (2.24):

$$\frac{De_a}{Dt} = G_s \frac{Ds}{Dt} + G_{q_t} \frac{Dq_t}{Dt} - b(z)w + b(z_r) \frac{Dz_r}{Dt}, \quad (2.28)$$

where the APE production coefficients have been defined by

$$G_s = \frac{\partial e_a}{\partial s}, \quad (2.29)$$

$$G_{q_t} = \frac{\partial e_a}{\partial q_t}. \quad (2.30)$$

The APE production coefficients govern the amount of e_a produced by a given change in s and q_t respectively. These derivatives are sometimes referred to as thermodynamic efficiencies (Tailleux, 2013b), but here the terminology *efficiency* is reserved for the scaled forms of the coefficients defined in Chapter 5, since these take values between -1 and 1 and are therefore more closely aligned with the traditional definition of an efficiency.

In terms of thermodynamic variables, the APE production coefficients are

$$G_s = T_h - T_r, \quad (2.31)$$

$$G_{q_t} = \mu_h - \mu_r, \quad (2.32)$$

where μ is chemical potential (Tailleux, 2018, Equation (3.4b)). The subscript h denotes a variable evaluated at $p_0(z)$ and the subscript r denotes a variable evaluated at $p_r = p_0(z_r)$ (in both cases conserving s and q_t). Similar production coefficients can be derived for the AEE density, but these will not be used in this thesis due to the simplified representation of AEE in the chosen idealised TC model. If the diabatic production of $e_e + e_a$ is considered, the production coefficients become $T - T_r$ and $\mu - \mu_r$ respectively.

The budget (2.28) establishes that changes in APE density are due to the diabatic production and dissipation of APE density, buoyancy fluxes, and changes in reference height.

The first two terms on the RHS represent the diabatic production/dissipation, and depend on the APE production coefficients. For example, a fixed change in specific entropy

will generate most APE density if it occurs in a parcel with a much higher temperature at p_0 than p_r , which is likely to occur if a near-surface parcel is very buoyant and therefore has a reference height high in the troposphere. If some moist potential temperature variable, such as equivalent potential temperature, were chosen to be the conserved variable during adiabatic transformation instead of s , the total diabatic production would remain the same but the partitioning between the two terms would change.

The third term on the RHS of (2.28) is the conversion between APE density and either AEE density or kinetic energy. Assuming $p \approx p_0$, it can be regarded as the conversion between APE density and kinetic energy due to vertical buoyancy fluxes.

The final term is typically taken to be zero (Tailleux, 2013b), since $b(z_r) = 0$ by the definition of the reference height in Equation (2.16). However, it will be shown in Chapter 5 that this assumption needs to be revisited in the event that z_r is discontinuous in time or space.

The local APE theory of Tailleux (2018) therefore provides a framework that permits the study of local energetics in a compressible moist atmosphere, linking the production of APE by diabatic processes to the conversion of APE into kinetic energy.

Other forms of local energetics, which may be applied to the moist atmosphere, have been suggested, such as the available potential energy of Peng et al. (2015),

$$E_p = \frac{1}{2} \frac{g^2}{N^2 \theta_0^2} \theta_m'^2, \quad (2.33)$$

where $N^2 = g \frac{\partial \ln \theta_0}{\partial z}$ is the Brunt-Väisälä frequency. The moist potential temperature θ_m is defined by $\theta_m = \theta (1 + 1.61 r_v)$, where r_v is water vapour mixing ratio, and the dash denotes a perturbation from the reference state. This expression for the moist APE density is attractive for its simplicity, but suffers from the fact that θ_m is not conserved during the condensation and evaporation of water. The theory is still effectively treating latent heat as an external source of energy, and as such behaves more like a dry theory of APE than a full moist one. The theory of Peng et al. (2015) is also formulated only for dry reference states. Particularly over the tropical oceans, a completely dry atmosphere may not be the most suitable reference state.

Another frequently-discussed approach is to measure local atmospheric energetics relative to an isothermal reference state (Dutton, 1973; Pearce, 1978; Karlsson, 1990; Marquet, 1991). This is based on the concept of *exergy*, which is the maximum useful work that can be extracted from a system as it reaches thermodynamic and mechanical

equilibrium (Cengel and Boles, 2015, p. 422). APE can be derived from an extended form of exergy (Kucharski, 1997; Kucharski and Thorpe, 2000; Kucharski, 2001); the links between exergy and APE are reviewed by Tailleux (2013a). Bannon (2005) derived a theory of local available energetics for compressible multi-component fluids based on an isothermal reference state with uniform chemical potential. This provides similar utility to the local APE theory of Tailleux (2018), in that the energetics are localised and it allows for phase changes and diabatic processes. However, exergy-based theories include a large part of the Lorenzian BPE in the available energy, because the isothermal reference state maximises entropy, whereas the Lorenzian reference state conserves the entropy of the actual atmosphere. This means that exergy theories typically calculate available energy and efficiencies much larger than those predicted by APE. The estimate of the generation of available energy by surface buoyancy fluxes in the ocean obtained using exergy theory is two orders of magnitude larger than the value predicted by APE theory; the prediction of APE theory appears to be the more realistic one (Tailleux, 2010).

The rest of this thesis therefore focuses on local available energetics as defined by Tailleux (2018). However, the discussion so far has only covered available energetics relative to a resting, hydrostatically-balanced atmospheric state without background flow. The portion of the potential energy that can be practically converted into kinetic energy can be additionally constrained by atmospheric dynamics. In the next section, theories of APE that account for these constraints are reviewed, and their relevance to the case of tropical cyclones is discussed.

2.1.3 APE relative to non-resting reference states

Lorenz's theory of APE, as outlined in Section 2.1.1, considers energetics relative to a horizontally stratified, statically stable reference state, in which no motion occurs (Lorenz, 1955). However, Lorenz himself noted that this might not always be the most relevant reference state, using the example of a purely zonal flow with dynamically stable mass and momentum distributions. In this case, the flow will remain in its stable zonal configuration, rather than reaching a resting state, and so not all of the Lorenz APE will be realised as kinetic energy.

This issue is pertinent to APE in tropical cyclones, which are associated with an approximately axisymmetric vortex structure close to thermal wind balance. The vortex structure contains APE, so that all the APE relative to a resting reference state could only be converted to kinetic energy if the vortex were to dissipate.

Whereas Lorenz's APE theory only constrains the mass and entropy of the fluid during rearrangement, Codoban and Shepherd (2003) constructed a theory of APE suitable for use with a non-resting reference state by constraining mass, entropy and momentum, based on the Hamiltonian structure of the dynamics. Using this theory, a symmetrically stable circulation has zero APE.

For symmetric zonal Boussinesq flow on an f -plane with a meridional circulation, Codoban and Shepherd (2003) demonstrated that using a non-resting reference state can change the apparent causality of the flow compared to using a resting reference state. With respect to the resting reference state, the circulation incorrectly appears to be thermally driven and mechanically damped for weak forcing, whereas the theory with respect to the non-resting reference state correctly diagnoses it as mechanically driven. It is therefore important to bear in mind that the apparent drivers of a tropical cyclone could vary with the choice of reference state, so it will be crucial to investigate both resting and non-resting reference states and assess which is most physically appropriate. It may also be challenging to interpret the processes driving the circulation of a highly balanced TC, since the balanced problem is described by an elliptic PDE and thus the solution at all points in the domain is influenced by the solution at all others.

Both Andrews (2006) and Codoban and Shepherd (2006) developed the theory of APE with non-resting reference states to address the specific case of an axisymmetric vortex. Whereas a traditional Lorenzian reference state minimises energy among fluid rearrangements conserving mass and entropy, a stable balanced axisymmetric vortex does so among rearrangements conserving mass, entropy and angular momentum (Cullen et al., 2015). Andrews (2006) used a local APE method similar to that of Andrews (1981) to generalise the theory to a single-component compressible stratified fluid. He obtained an APE density that is positive definite for any axisymmetric reference state in which angular momentum increases with radius along isentropes and both geopotential and entropy increase with height. However, such an angular-momentum-constraining APE theory has not been extended to a multi-component fluid such as a moist atmosphere.

The generalised multi-component APE theory of Tailleux (2018) can be deployed with a reference state that varies horizontally as well as vertically, thus permitting a non-resting reference state, although the theory does not consider the conservation of momentum. Tailleux (2018) suggested that the APE density relative to a non-resting state can be thought of as an eddy APE density, with the mean APE density of a parcel being its APE density in the non-resting state relative to the resting state. If the non-

resting state is a stable vortex, then rotation should suppress conversion from the eddy to the mean APE density. However, since the choices of the resting and non-resting reference states remain arbitrary, this does not answer any questions about which reference state in particular provides the most physically useful description of the available energetics. Whilst the use of an arbitrary non-resting reference state simplifies the theory compared to previous approaches, information about the physical constraints on fluid parcels is lost through the decision not to conserve momentum during parcel lifting. The work in Chapter 6 will develop a method to account for these momentum constraints in a particular application of the generalised theory.

2.1.4 Summary of APE theory

The original theory of APE, derived by Lorenz (1955), is designed to study the part of the potential energy in the atmosphere that can be reversibly converted into kinetic energy. It is therefore linked with the behaviour of the kinetic energy in a way that other quantities such as total potential energy or entropy are not. The benefits of using an APE budget over an entropy budget will be further discussed once potential intensity theory has been reviewed in Section 2.3.2. However, Lorenz's theory suffers from the shortcomings that it is only defined globally over a domain, so it is not possible to study local energy conversions, and that it requires the computation of a reference state, which has no analytical solution for a moist atmosphere. Current studies of Lorenz APE in the moist atmosphere rely on sorting algorithms to obtain a reference state.

Local APE theory computes an APE density for each fluid parcel, thus enabling the investigation of the local production of APE and its local conversion into kinetic energy. A parcel's APE density is the work against buoyancy forces required to move the parcel reversibly and adiabatically from its reference state position to its actual position. The local theory moves away from the Lorenz reference state, in which total potential energy is minimised, to an arbitrary hydrostatically-balanced reference state. Whilst this means that local APE theory is easier to apply to a moist atmosphere, since an easily-computed reference state can be chosen (such as a horizontal mean), the conclusions drawn may depend on the particular choice of reference state. However, there is no established procedure for determining which reference state ought to be used for any particular context.

For strongly axisymmetric flows, it may be preferable to use a non-resting, dynamically stable axisymmetric reference state rather than a traditional resting reference state.

The flow will tend to remain in this dynamically stable state and therefore not convert any further APE to kinetic energy. Such a reference state has not previously been implemented for a moist atmosphere.

The work in subsequent chapters of this thesis will seek to apply local APE theory to an axisymmetric tropical cyclone in a moist atmosphere, with the dual aims of enhancing the current understanding of local APE theory and investigating how diabatic processes are linked to TC development in terms of kinetic energy generation. Key contributions to APE theory will include an appraisal of the sorting algorithms used to compute Lorenz APE in the moist atmosphere (Chapter 3), the first full budget of moist APE density for an atmospheric model, and the first account of discontinuous behaviour in APE density (Chapter 5). A particular focus will also be placed in Chapter 6 on establishing a method for assessing the suitability of different reference states, both resting and non-resting, for studying local available energetics in TCs. Additionally, Appendix C provides a paper (Tailleux and Harris, 2020) developing a new formulation of local available energetics relative to an axisymmetric vortex for a single-component fluid; this more generalised work was inspired by the findings from the TC model in Chapter 6.

2.2 Energetics of tropical cyclones

It has long been known that surface enthalpy fluxes, driven by the disequilibrium between the ocean and atmosphere, are the key source of energy for TCs (Kleinschmidt, 1951; Emanuel, 1986). However, there are many different perspectives on how the TC converts the energy supplied by these surface fluxes into kinetic energy.

Understanding the physics of kinetic energy generation in a TC is crucial to linking diabatic processes to the ultimate damage caused by TCs, since kinetic energy provides a measure of a TC's destructive potential. For example, Powell and Reinhold (2007) developed the metric of integrated kinetic energy (IKE), which is the integral of the 10-m-level kinetic energy over the storm domain. IKE is useful for assessing the damage a TC can inflict because, unlike metrics such as the maximum wind speed v_{\max} or the minimum central pressure p_{\min} , the IKE accounts for the area over which high winds occur. It can therefore provide an estimate of regional impacts of storm surge (Bass et al., 2017).

This section describes traditional views of the TC energy cycle, which are based on total potential energy (TPE) and dry APE, highlighting the shortcomings of each for explaining TC development. It then outlines the TC energy cycle that arises from local

moist APE theory, explains why it provides a more physically satisfying view than the previous frameworks, and assesses the approaches of the limited number of studies that have so far attempted to apply moist APE theory to TCs.

2.2.1 Total Potential Energy

Many energetic studies of TCs, both observational (Palmén and Jordan, 1955; Palmén and Riehl, 1957) and numerical (Kurihara, 1975; Tuleya and Kurihara, 1975; Hogsett and Zhang, 2009), have considered kinetic energy to be converted from a reservoir of total potential energy (TPE), which is the sum of the internal and gravitational potential energies, as defined in Equation (2.1).

The pathway of energy transfers leading from surface enthalpy fluxes to kinetic energy via TPE is illustrated by the schematic in Figure 2.2a. In the first transfer, surface fluxes of moisture increase the latent energy of low-level parcels as they flow in towards the

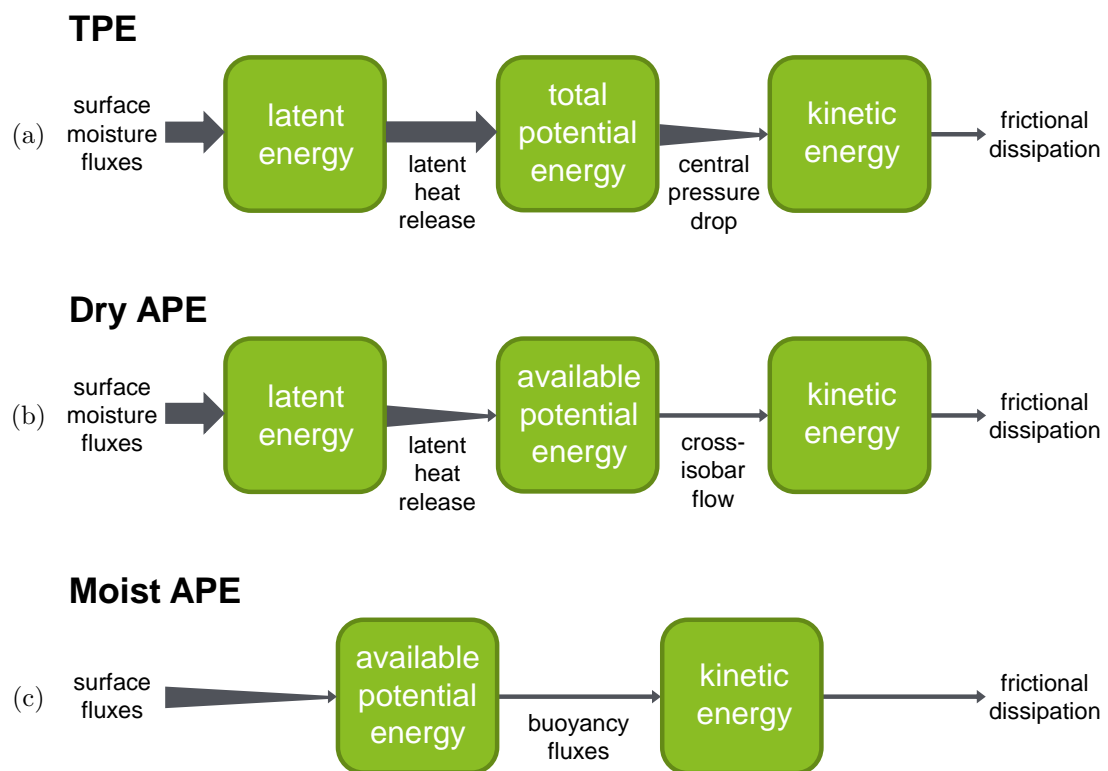


Figure 2.2: Possible views of the energy transfers through which surface enthalpy fluxes are converted to kinetic energy in a TC. The thickness of the arrows represents the relative amount of energy that feeds through a transfer process; where an arrow becomes narrower, the transfer process is inefficient, leading to a bottleneck in the energy pathway and a storage of energy.

centre of the TC. Specific latent energy is defined as

$$e_l = L_v r_v, \quad (2.34)$$

where $L_v = 2.5 \times 10^6 \text{ J kg}^{-1}$ is the latent heat of vaporisation for water (assumed constant) and r_v is the parcel's water vapour mixing ratio. The latent energy thus gives the energy that would be released in the form of latent heat if all the water vapour in an air parcel were to condense.

In the core of the TC, moisture convergence is a bigger source of latent energy than local evaporation from the surface (Kurihara, 1975; Tuleya and Kurihara, 1975; Trenberth et al., 2007; Fritz and Wang, 2014). This suggests that the conditions in the outer part of the TC may be critical in determining the total generation of kinetic energy in the system, even though the highest winds and surface fluxes are found near the eyewall.

As the inflowing parcels converge and rise in the eyewall, condensation occurs and releases latent heat; this converts latent energy into TPE (since the temperature and therefore the internal energy of parcels increases). This heating reduces the surface pressure under the eyewall, leading to a stronger radial pressure gradient in the inflow. Inflowing parcels therefore accelerate, increasing the radial kinetic energy in the TC. Through the action of the Coriolis and centrifugal forces, this also increases the azimuthal kinetic energy. Ultimately, the energy is dissipated by friction, in large part at the sea surface but also internally in turbulent eddies. The effect of dissipative heating will be ignored here for simplicity, but it should be noted that dissipative heating significantly increases the maximum intensity a TC can attain (Bister and Emanuel, 1998).

Traditionally, only the horizontal component of kinetic energy is considered as part of the energy budget, since the vertical kinetic energy is negligible in comparison (Palmén and Jordan, 1955). Although it is true that the vertical kinetic energy of a TC is a small part of the total kinetic energy, Ooyama (1969) noted that it can still be important for energy conversion and transport. Additionally, Smith et al. (2018) found that the net generation of vertical kinetic energy in an axisymmetric model was non-negligible compared to the net generation of horizontal kinetic energy, since there was significant cancellation between regions of positive horizontal kinetic energy generation in the inflow and horizontal kinetic energy destruction in the outflow. The changes in apparent energy sources and transfers that occur when vertical kinetic energy is included in the budget will be addressed as part of Chapter 5.

In his review of TC energetics, Anthes (1974) presented the budget of K , the volume

integral of horizontal kinetic energy over the cylinder bounded by heights $0 \leq z \leq H$ and radii $0 \leq r \leq r_0$, as

$$\begin{aligned} \frac{\partial K}{\partial t} = & - \int_0^H \int_0^{2\pi} r_0 (\rho u e_{kh})_{r_0} d\lambda dz \\ & + \int_0^H \int_0^{r_0} \int_0^{2\pi} (-\mathbf{v}_h \cdot \nabla p + \rho \mathbf{v}_h \cdot \mathbf{F}) r d\lambda dr dz. \end{aligned} \quad (2.35)$$

Here, u is the radial wind speed and \mathbf{v}_h the horizontal velocity vector. The specific horizontal kinetic energy e_{kh} is defined by $e_{kh} = \frac{\mathbf{v}_h^2}{2}$. The azimuthal coordinate is λ , and \mathbf{F} represents frictional forces.

Anthes (1974) noted that the contribution from the azimuthal wind in the first term in the second integral on the RHS of Equation (2.35) is negligible, because the isobars are approximately circular at lower levels, where the pressure gradient is strongest. The most important processes affecting the integrated kinetic energy K are therefore the flux of kinetic energy across the outer surface $r = r_0$ of the volume, changes in kinetic energy via work done by the radial pressure gradient force on the radial flow (i.e. the conversion of TPE into kinetic energy), and the frictional dissipation of kinetic energy.

The work done by the radial pressure gradient results in a net source of kinetic energy in the TC, because in a warm core cyclone, the pressure gradient is larger in the low-level inflow than in the upper-level outflow, so that the positive contribution to the rate of kinetic energy change from the inflow region is dominant. The boundary flux of kinetic energy due to the mean flow is only around 1% of the internal production in the TC by the radial pressure gradient (e.g. Kurihara, 1975).

However, a problem arises from the fact that the definitions of the source and boundary flux of kinetic energy are not unique. Smith et al. (2018) observed that Equation (2.35) could be rewritten as

$$\begin{aligned} \frac{\partial K}{\partial t} = & - \int_0^H \int_0^{2\pi} r_0 (\rho u e_{kh} + p u)_{r_0} d\lambda dz \\ & + \int_0^H \int_0^{r_0} \int_0^{2\pi} (-p \nabla \cdot \mathbf{v}_h + \rho \mathbf{v}_h \cdot \mathbf{F}) r d\lambda dr dz. \end{aligned} \quad (2.36)$$

In this version of the budget, the source of kinetic energy due to the work done by the radial pressure gradient is replaced by the rate of conversion between kinetic energy and internal energy due to horizontal expansion or contraction, $-p \nabla \cdot \mathbf{v}_h$. There is then an additional term in the horizontal boundary flux integral, representing the work done by expansion at the volume boundary.

This issue is part of a more general discussion, not recognised by Smith et al. (2018), on the ambiguity of energy conversions in open systems, i.e. systems with a boundary through which energy may be added or removed. Depending on which definition is chosen for the conversion between potential and kinetic energy, the boundary work may be interpreted either as a source/sink of potential energy or a source/sink of kinetic energy (Smith, 1970; Johnson and Downey, 1982).

Smith et al. (2018) concluded that it is preferable to use a kinetic energy budget of the form of Equation (2.35) because, unlike when using Equation (2.36), the boundary flux term is negligible, and so the kinetic energy budget can be considered as self-contained within the region of the TC. Equation (2.35) also yields a kinetic energy generation $-\mathbf{v}_h \cdot \nabla p$ that is more predictable in its spatial structure, with a source of kinetic energy in the inflow and a sink in the outflow. In contrast, the kinetic energy generation $-p\nabla \cdot \mathbf{v}_h$ in Equation (2.36) does not have any clear predictable spatial structure. The conclusion of Smith et al. (2018) is therefore useful for the practical application of kinetic energy budgets, but cannot eliminate the fundamental ambiguities associated with energy transfers in open systems. This issue also applies to the dry and moist APE-based energy transfer frameworks that will be discussed later in this section. The problem will be revisited, in the context of available energetics, in Chapter 5.

One major shortcoming of the TPE-based view of energy transfers is the very low efficiency of the conversion of TPE to kinetic energy, which is difficult to calculate analytically. When considering TPE, the system efficiency of the TC is commonly measured by the ratio of latent heat release to kinetic energy generation. This will henceforth be referred to as the *TPE efficiency*. The typical TPE efficiency of a TC as a whole is 2–3% (Palmén and Jordan, 1955; Palmén and Riehl, 1957; Hogsett and Zhang, 2009).

In the context of APE theory as reviewed in Section 2.1, it should perhaps be considered obvious that the TPE efficiency would be so low. Lorenz (1955) identified that the majority of TPE is not available for reversible conversion into kinetic energy, and so when latent heat release generates TPE only a small fraction of this should be expected to feed through into kinetic energy. Large amounts of TPE are exported in the upper level outflow (Palmén and Riehl, 1957; Kurihara, 1975; Hogsett and Zhang, 2009), without contributing to the development of the TC in terms of kinetic energy.

If the majority of TPE is not expected to be converted into kinetic energy, then it seems a poor choice to view it as the energy reservoir from which the TC extracts its kinetic energy. The low efficiency of the TPE to kinetic energy transfer makes it difficult

to cleanly link diabatic processes to the TC's ultimate development; even if it is possible to budget the diabatic processes that contribute to a source of TPE, this source will mostly not lead to kinetic energy generation, and it is not easy to predict the efficiency with which it does (although this can be diagnosed in a model, e.g. Hogsett and Zhang (2009)).

The TPE efficiency has been calculated analytically only under very idealised conditions, since it requires solving an elliptic equation for the secondary circulation. Hack and Schubert (1986) calculated the TPE efficiency in a dry, inviscid cyclonic vortex, to which a constant heating designed to approximate the effect of latent heat release in a TC was applied. Figure 2.3 shows the spatial distribution of TPE efficiency in the analytical balanced vortex at the end of a model run in which the maximum of the heating function occurred at 400 hPa. Figure 2.3 also includes the azimuthal wind field of the vortex, to provide context for the structure of the efficiency.

The TPE efficiency in the Hack and Schubert (1986) vortex peaks in the upper troposphere, and is of the magnitude expected from the observational evidence from TCs, with a maximum of around 6%. However, it would be difficult to generalise this analytical approach to include the effects of moisture and friction, both of which play important roles in TC development.

Most TPE generation would be expected to occur in the middle and upper troposphere, where latent heat release and the TPE efficiency are both high. This means that TPE theory is of limited use for understanding how processes in the boundary layer interact with the energy cycle. Smith and Montgomery (2016) argued that it is unsatisfactory

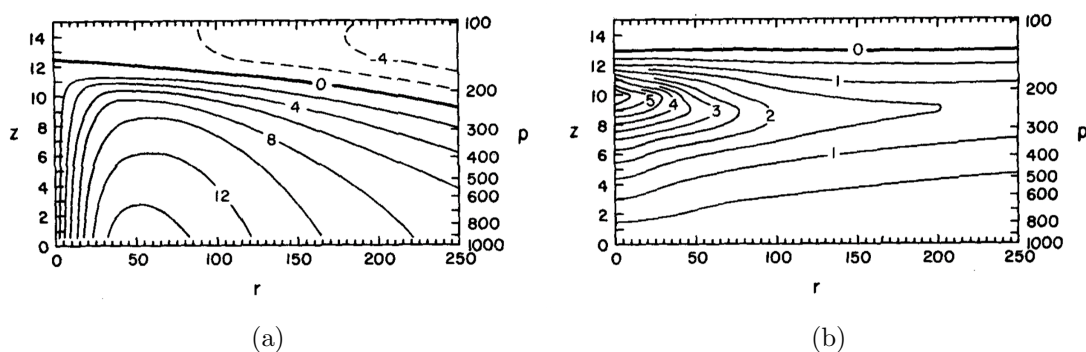


Figure 2.3: (a) Azimuthal wind speed v (ms^{-1}) and (b) TPE efficiency (%) of a balanced vortex after 120 h of constant heat forcing, with maximum heating occurring at 400 hPa. Radius r and height z are labelled in km, and pressure in hPa. The v contours are marked at intervals of 2 ms^{-1} , with negative values indicated by dashed contours. Efficiency contours are marked at intervals of 0.5%. From Hack and Schubert (1986). © American Meteorological Society. Used with permission.

to use such an efficiency, which does not account for boundary layer dynamics or thermodynamics, because boundary layer dynamics are integral to the spin-up of the maximum wind in a TC (Persing et al., 2013; Kilroy et al., 2016; Schmidt and Smith, 2016).

Some energetic studies have also used moist static energy (MSE, the sum of enthalpy, latent energy and gravitational potential energy) as a budgeted variable (Riehl and Malkus, 1961; Hawkins and Rubsam, 1968; Frank, 1977; Wing et al., 2019). This approach suffers from the same problem as the TPE framework: the efficiency of conversion from MSE to KE is very low—Wing et al. (2019) note that the kinetic energy tendency term is negligible in their MSE budget—and does not have a convenient analytical form.

If the generation of kinetic energy in a TC is to be directly attributed to the effects of particular diabatic processes, it may therefore be preferable to consider APE, rather than TPE, as the form of potential energy from which kinetic energy arises. However, as discussed in Section 2.1, it is difficult to apply APE theory to a moist atmosphere. The majority of studies of APE in TCs have therefore used theories based on dry APE. The merits and drawbacks of this are explored in the next section.

2.2.2 Dry Available Potential Energy

Energy budgets that consider dry APE in TCs have traditionally used the Lorenzian theory of APE (Anthes and Johnson, 1968; Anthes, 1974; Frank, 1977; Edmon Jr and Vincent, 1979; Bhalachandran et al., 2019). Therefore, “dry APE” refers to dry Lorenz APE in this section unless otherwise stated. The only difference between the energy transfer pathways for the Lorenz and local formulations would be that local APE theory treats vertical buoyancy fluxes as the process converting APE to kinetic energy, rather than cross-isobar flow.

From the viewpoint of dry APE theory, the key source of APE in a TC is latent heat release, which contributes approximately 80% of the APE generation (Anthes and Johnson, 1968). Other contributors include the emission of longwave radiation at upper levels and sensible heating (Anthes and Johnson, 1968; Edmon Jr and Vincent, 1979). Latent heat release remains the key source if a local theory is used, or a small-amplitude quadratic approximation to the dry APE (Nolan et al., 2007).

The energy transfers through the TC in the dry APE framework therefore look very similar to those in the TPE framework, since latent heat release is still the key source of potential energy; now, it is being considered to generate APE instead of TPE. The energy transfers described by dry APE theory are illustrated in Figure 2.2b.

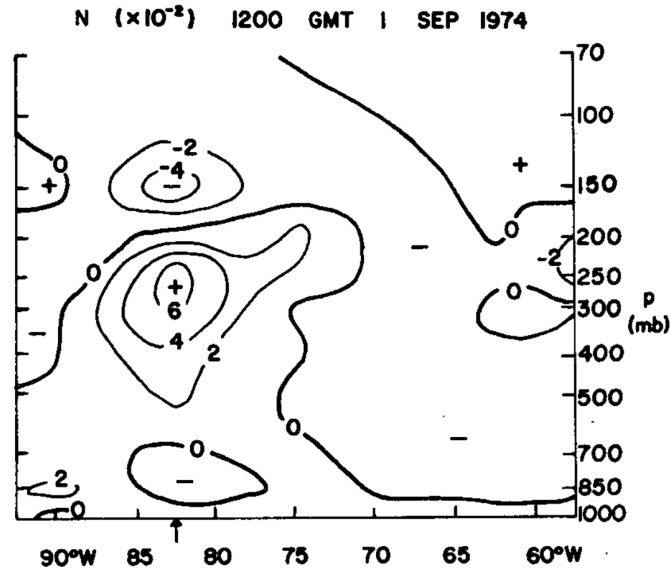


Figure 2.4: Vertical cross-section of dry APE efficiency N (%) through Hurricane Carmen (1974) at the beginning of its mature stage. The arrow beneath the x -axis marks the centre of the hurricane at the surface. From Edmon Jr and Vincent (1979). © American Meteorological Society. Used with permission.

Since APE is by definition convertible to kinetic energy by adiabatic flow, the efficiency of conversion from APE to kinetic energy is expected to be much higher than the efficiency of conversion from TPE to kinetic energy (although it will not be 100%, since the studies mentioned take no account of the effect that dynamical constraints will have on the APE). Instead, the low efficiency occurs at the point of conversion from latent energy to APE. The form of this efficiency is well-established, since it is just the efficiency N (Equation (2.6)) from Lorenzian APE theory. Edmon Jr and Vincent (1979) computed this efficiency based on observations of Hurricane Carmen; a vertical-cross section during Carmen's mature stage is shown in Figure 2.4. The maximum efficiency of 6% occurs in the upper troposphere—a similar magnitude and location to the TPE efficiency in Hack and Schubert's idealised vortex, showing that the main difference between the TPE and APE efficiencies is the point in the energy transfer pathway at which the low efficiency occurs.

If local dry APE theory were used, the efficiency would also be easy to compute, simply depending on an air parcel's temperature and reference temperature. Using dry APE theory to study the energy transfers makes it easier to understand and predict the efficiency with which latent energy will be converted into kinetic energy. The complete distribution of latent heat release must still be known in order to calculate how much APE is generated. For observational case studies this is estimated either by assuming adiabatic lifting of parcels or by parameterising the latent heat release based on large-scale moisture

convergence (Anthes and Johnson, 1968; Edmon Jr and Vincent, 1979).

However, there are still some substantial drawbacks to the dry APE-based theory of energy transfers. Using the Lorenzian theory means that it is not possible to study local transfers between APE and kinetic energy, although this could be remedied by using local APE. Another problem arises from the fact that most of the APE generation occurs in the mid-troposphere, where the latent heat release is large and the APE efficiency is highest, as seen in Figure 2.4. From observations of Hurricane Hilda, Anthes and Johnson (1968) concluded that 90% of APE generation occurred within the 200–700 hPa layer. This means that, like TPE theory, dry APE theory is not suited to investigating boundary layer processes, which are known to have an important effect on TC development.

Including latent energy as part of the energy cycle also leads to some confusion about the energy source for TCs, highlighted recently by Emanuel (2018). Rather than recognising surface enthalpy fluxes as the source of a TC’s energy, authors have stated that latent heat release during moist convection provides the energy source (e.g. Nolan et al., 2007), or suggested that it is some combination of the two (Frank, 1977). TC-like vortices have been simulated in dry atmospheres (Mrowiec et al., 2011; Cronin and Chavas, 2019), which demonstrates that latent heat release is not necessary for their development. The TPE and dry APE energy pathways depicted in Figures 2.2a and 2.2b are clearly not useful for interpreting the energetics of these theoretical dry TC-like vortices, since they regard latent heat release as the key source of diabatic heating. In order to draw a less ambiguous link between surface enthalpy fluxes and APE, the representation of TC energy transfers in moist APE theory is considered next.

2.2.3 Moist Available Potential Energy

This section focuses on the local form of APE theory, since this is more easily applied to the moist atmosphere because it does not require computationally expensive domain rearrangements to obtain a reference state.

The budget (2.28) of moist APE density shows that surface fluxes of entropy in a TC will generate APE via the diabatic production term $G_s \frac{Ds}{Dt}$, with moisture fluxes providing an additional effect through the term $G_{qt} \frac{Dqt}{Dt}$. The moist APE energy transfers are depicted in Figure 2.2c. Since the local form of APE theory is being used, the transfer from APE to kinetic energy occurs via buoyancy fluxes, and it is possible to investigate local kinetic energy conversions. In addition to surface fluxes, internal processes such as mixing and diffusion can also produce or dissipate APE, but their net effect is not

clear, so surface fluxes are treated as the major producer of APE here. Surface fluxes are widely regarded as the fundamental source of energy for TCs (Emanuel, 2018), and Pauluis (2007) showed that surface evaporation is expected to be the dominant source of APE in a moist atmosphere in radiative-convective equilibrium. Previous investigations of moist APE in TCs have focused on APE production by surface fluxes, implicitly assuming its dominance, but not compared it to possible internal APE sources (Tang and Emanuel, 2012; Wong et al., 2016). The relative contributions of various diabatic processes to APE production in TCs will be investigated in Chapters 5 and 6; it is expected that surface fluxes will be the key source of APE.

In the moist APE pathway surface fluxes are producing APE directly, rather than via latent energy (as in the TPE and dry APE pathways), because moist APE theory treats latent heat release as an internal parcel process rather than an external energy source (precipitation remains an external process). This avoids confusion regarding the fundamental energy source for TCs: from the moist APE viewpoint the energy is clearly provided by surface fluxes rather than latent heat release. Additionally, the inclusion of moisture in the definition of APE means that this framework is more suitable for investigating moisture-convection coupling, which is known to be important for the representation of TC intensity in numerical models (Kim et al., 2018). The energetics of dry TCs can also easily be understood through this framework: sensible surface heat fluxes can produce APE, which is converted to kinetic energy via buoyancy fluxes in the same way as in the moist case.

The low energetic efficiency of the TC system, which was previously associated with either the transfer of TPE to kinetic energy or of latent energy to dry APE, now occurs as the surface fluxes enter the system. The proportion of the surface enthalpy flux that is converted into moist APE is determined by the APE production coefficients G_s and G_{qt} of the air parcels at the surface, which may be easily calculated using Equations (2.31) and (2.32). This means that energy is no longer allowed to enter into the energy transfer pathway unless it is expected to ultimately be converted into kinetic energy. However, the energetic efficiency now depends on how the reference state is defined.

Since the generation of APE is now expected to be concentrated in near-surface parcels rather than in the mid-troposphere, moist APE theory is likely to be more useful for investigating the effect of boundary layer processes on the system's energetics than TPE or dry APE theory. For example, mixing of temperature in the boundary layer would directly impact the near-surface parcels' moist APE production and production

efficiencies, whereas in dry APE theory the majority of APE production occurs aloft and would thus not be directly affected.

However, it is challenging to apply moist APE theory to a TC: the need to lift parcels to their reference heights makes moist APE a much more expensive diagnostic than TPE, and the question of which reference state ought to be used remains a significant problem. These reasons may explain why there have been few studies of moist APE in TCs so far.

Tang and Emanuel (2012) used the local form of moist APE theory to explain how the ventilation of colder, drier air into a TC decreases its intensity: entropy mixing above the boundary layer destroys APE that could otherwise have been converted into kinetic energy. This work used an axisymmetric numerical model, and took the sounding used to initialise the model as the reference state. Reference temperatures were calculated by lifting parcels to their LNBs with respect to this reference state, and the diabatic APE production due to surface fluxes was then computed as $(T - T_r)F_s$, where F_s is the surface (moist) entropy flux.

This was an important demonstration of the physical insight that can be obtained by using moist APE theory, and using the initial model state as the reference state seems reasonable and minimises computational expense. The main drawback of the investigation is that it did not compute the conversion of APE into kinetic energy, so it is difficult to tell whether the APE in this framework is converted to kinetic energy or just stored as APE, in which case defining it as “available” is problematic. Tang and Emanuel (2012) commented that their APE production is much larger than the kinetic energy dissipation, which implies that an unexpected inefficiency is occurring at some point along the energy transfer pathway of Figure 2.2c; this could be due to large APE storage. Tang and Emanuel (2012) also used a pseudoadiabatic framework, which did not include the contribution of $G_{qt}F_{qt}$ to the production of APE by surface fluxes; this would alter the expected amount of kinetic energy generation.

In an attempt to address questions surrounding the choice of reference state, Wong et al. (2016) computed the conversion of APE to kinetic energy in an axisymmetric TC model and compared it to the moist APE production by surface fluxes calculated using two sorting-based reference states (rather than taking a local, APE density-based approach). This work concluded that a better match to the kinetic energy conversion was obtained when using the reference state with lower APE, and it was therefore suggested that the reference state should be chosen to minimise the storage of APE, $\frac{d\text{APE}}{dt}$. This can be understood by referring to the Lorenz energy cycle equation (2.3) (which also applies to

the local theory, when integrating over a closed volume): minimising APE storage should yield the best agreement between the production of APE and its conversion into kinetic energy. However, neither of the reference states tested by Wong et al. (2016) gave a close match to the kinetic energy conversion towards the end of their model run. As in Tang and Emanuel (2012), this study also did not include the contribution $G_{q_t} F_{q_t}$ to the production of APE by surface fluxes (despite conserving q_t during the reversible parcel sorting).

Wong (2014) attempted to compute moist APE density in this same axisymmetric simulation, and hence a local moist APE budget. The moist APE density was based on the conservation of liquid potential temperature θ_l and total specific humidity q_t . Figure 2.5 shows the APE density and the efficiencies of APE production with respect to θ_l and q_t obtained by Wong (2014) for the mature TC, using the model's initialisation sounding as a reference state. The efficiencies are obtained by normalising the APE production coefficients (this will be described in more detail in Chapter 5). It is notable that parcels at the surface have high APE density and high positive production efficiencies, implying that they are highly buoyant and that surface fluxes will generate large amounts of APE. The maximum values of moist APE efficiency ($\approx 30\%$) are much higher than the maxima of the TPE or dry APE efficiencies.

The similarity between the θ_l and q_t efficiencies in Figures 2.5b and 2.5c is surprising. It is expected that the θ_l efficiency would be positive at low levels: parcels here are positively buoyant, moving upwards to their reference heights, so that increases in θ_l , which would increase parcel buoyancy, would also increase APE density. However, the positivity of the q_t efficiency is unexpected. Pauluis (2007) described how precipitation out of a buoyant parcel would increase its APE by reducing water loading—this would imply a negative q_t efficiency.

Since Wong (2014) did not compute a closed budget of APE, there is no verification that the APE density or production efficiencies are correct. Errors could arise from the thermodynamic approximations made by the axisymmetric model, which are not accounted for when computing the production efficiencies. There are also issues with the budget terms that are computed: the work concludes that changes in θ_l and q_t make approximately equal contributions to the diabatic production of APE, but fails to include the model's precipitation term in the budget of q_t . Chapter 5 will therefore focus on obtaining a closed budget of moist APE density for the axisymmetric model, to ensure that all terms used are the correct ones.

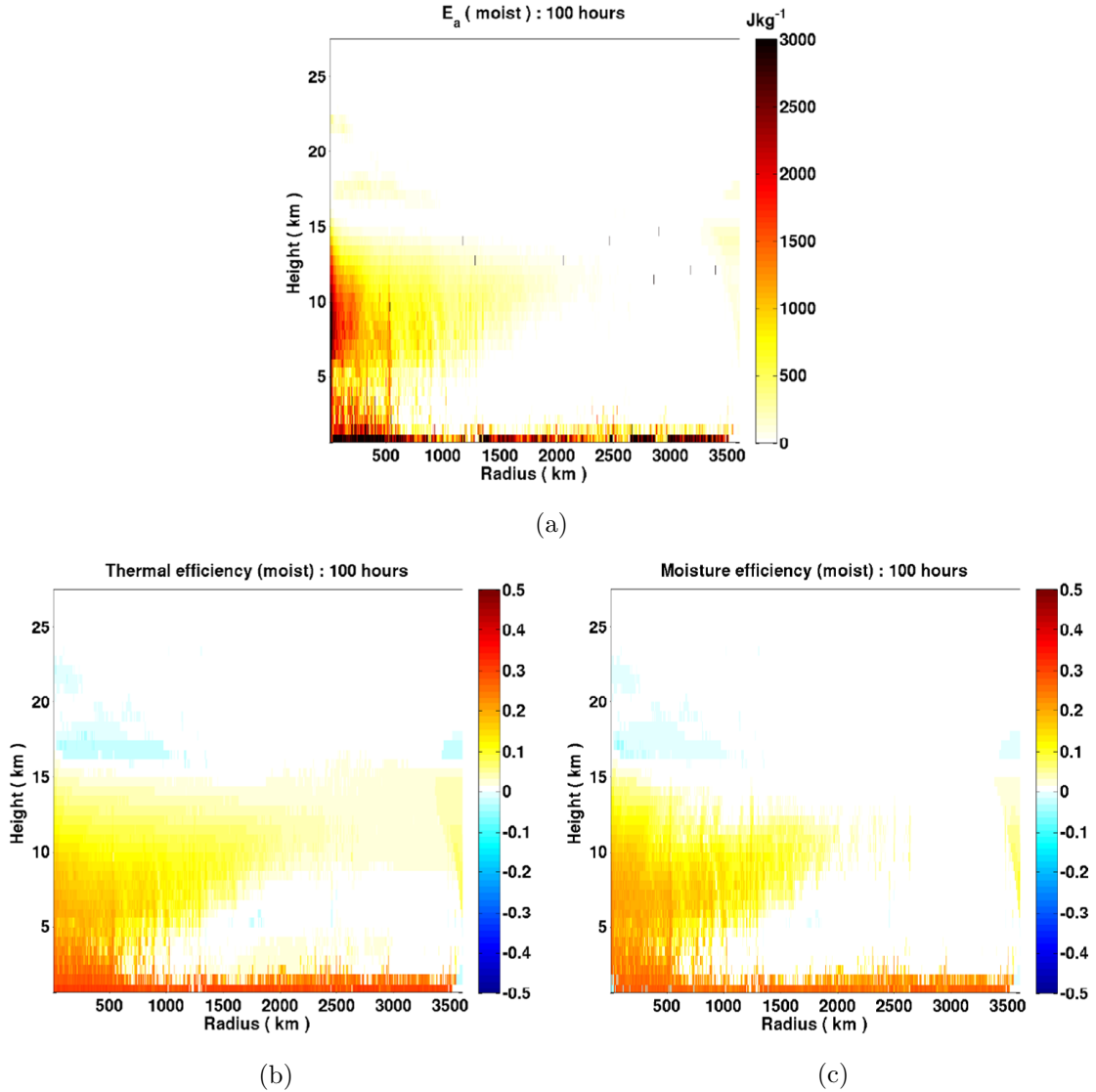


Figure 2.5: (a) Moist APE density (J kg^{-1}) and APE production efficiencies (unitless) with respect to (b) θ_t and (c) q_t in a mature axisymmetric TC, using model’s initial sounding as a reference state. From Wong (2014).

Although it does not use moist APE theory, the work of Tang et al. (2016)—investigating how the spin-up time of an axisymmetric TC is affected by the initial entropy deficit in the troposphere—is sufficiently closely related to merit discussion here, and highlights the lack of agreement on how a reference state should be chosen. Tang et al. (2016) used a budget of *potential available enthalpy*, defined by Marquet (1991, 1993) as

$$a_p = k - k_r - T_r (s - s_r), \quad (2.37)$$

where the subscript r denotes reference state values. The potential available enthalpy measures the work done as parcels reach equilibrium with a reference state through reversible processes (this is based on the concept of exergy, reviewed in Section 2.1.2). The

reference state values of temperature and pressure, T_r and p_r , should be constant, so that the reference state is in thermodynamic equilibrium (Marquet, 1991). Tang et al. (2016) used the properties at the tropopause in the initial state of their model: $T_r = -70^\circ\text{C}$ and $p_r = 135\text{ hPa}$.

The link between potential available enthalpy and APE is clear, since they both address the concept of the energy that may be obtained as a fluid undergoes reversible transformations to reach some notional reference state. The diabatic production of potential available enthalpy is $(T - T_r) \frac{Ds}{Dt}$ (again Tang et al. (2016) neglected contributions from q_t), which is of the same form as the APE production, the only difference being that T_r is constant rather than obtained by lifting to an LNB.

This reference state is certainly easy to obtain, but its usage seems to contradict the advice of Wong et al. (2016) that APE storage should be minimised. Using this choice of isothermal reference state is equivalent to assuming, in local APE theory, that all parcels have their LNB at the tropopause. In reality, not all parcels would move to this level, so a lot of APE would not be converted to kinetic energy, but stored instead. It is therefore perhaps unsurprising that Tang et al. (2016) found that the conversion of potential available enthalpy into kinetic energy is “barely discernible” when viewed as part of the potential available enthalpy budget. The enthalpy is only available in the sense that it could be converted to kinetic energy if equilibrium with the reference state were reached, but the model will never realistically achieve this state. Since only a tiny fraction of the potential available enthalpy is converted to kinetic energy, this framework repeats the issue found with TPE: it is possible to budget the diabatic processes producing potential available enthalpy, but not to directly link them with intensification in terms of increasing kinetic energy.

This review shows that there is much work to be done on the available energetics of TCs. Even though local moist APE theory should be able to remedy some of the problems with TPE and dry APE frameworks (by only considering energy that can be converted to kinetic energy from the beginning, and not focusing solely on energetics above the boundary layer), the approach of Tang et al. (2016) shows that if an unrealistic reference state is used, moist APE theory can simply repeat the old issues. The only concrete guidance on which reference state to use is Wong et al. (2016)’s assertion that it should be chosen to minimise APE storage, but Wong et al. (2016) did not succeed in computing an APE production that matched kinetic energy conversion.

Additionally, neither Tang and Emanuel (2012) nor Wong et al. (2016) performed a

full budget of moist APE density, instead only considering surface fluxes (and dissipative heating) as sources of APE. This means that it is unclear what effect internal processes such as precipitation and turbulent mixing have on the APE density.

There have also been no attempts to use local moist APE theory with a non-resting reference state to study a modelled TC, even though Section 2.1.3 suggests that it may be important to include the constraints of the dynamically stable state provided by an axisymmetric vortex.

The work in Chapters 5 and 6 will therefore attempt to construct a full budget of moist APE density for an axisymmetric TC, develop a method for assessing the suitability of reference states for studying TC available energetics, and investigate whether a non-resting reference state can provide improved physical insight into the energy transfers that lead to the generation of kinetic energy in TCs.

2.3 Efficiency of tropical cyclones

The review of the energetics of tropical cyclones in Section 2.2 featured different concepts of energetic efficiency associated with each view of the energy transfers leading to kinetic energy generation. Existing work investigating the concept of energetic efficiency in TCs has suggested that variations in efficiency may be critical to TC development, but has been focused on TPE rather than APE efficiency. In this section, two specific aspects of TC efficiency are reviewed: firstly, the temporal evolution of the energetic efficiency of the entire TC system, and secondly the theory of potential intensity, which uses the maximum thermodynamic efficiency of a TC to predict the wind speeds it can produce. This will enable the work in Chapter 7 to explore how existing notions of efficiency relate to the moist APE production efficiencies, and whether moist APE efficiencies can improve the understanding of how efficiency impacts TC development. The review of potential intensity also includes a discussion of why a moist APE budget is preferable to an entropy budget for studying the generation of kinetic energy in TCs.

2.3.1 Temporal variation of efficiency

Work on the temporal evolution of energetic efficiency in TCs has been based on analytical models of dry balanced vortices (Schubert and Hack, 1982; Hack and Schubert, 1986; Nolan et al., 2007; Vigh and Schubert, 2009). All these studies have emphasised that when heating occurs in regions of higher inertial stability, more kinetic energy can

be produced in the TC per unit of heating. Inertial stability is defined as

$$I = \left(f + \frac{2v}{r} \right) \left(f + \frac{\partial v}{\partial r} + \frac{v}{r} \right), \quad (2.38)$$

and measures resistance to radial displacements (Schubert and Hack, 1982). Here, f is the Coriolis parameter and v is the azimuthal wind speed. For example, Nolan et al. (2007) used a dry analytical vortex model with asymmetric heat sources to show that kinetic energy efficiency (defined as the ratio of kinetic energy retained in the vortex winds to the heat supplied) increased as the vortex's inertial stability increased. The idea that the generation of kinetic energy depends on the efficiency of a TC, as well as on the supply of energy, has led to hypotheses that changes in efficiency play an important role in the intensification process.

Schubert and Hack (1982) defined efficiency as the ratio of the rate of warming in their idealised vortex, $\frac{\partial \theta}{\partial t}$, to the (constant) rate of diabatic heating. They found that the efficiency of the vortex as a whole increased throughout its intensification, and therefore suggested that rapid intensification (RI) could occur as a result of increasing efficiency in a TC.

There is some observational evidence to support this idea: Rodgers et al. (1994) found that the correlation between diabatic heating in the inner core and the intensity change in the subsequent 12 h period was higher for more intense TCs, implying that intense TCs are more efficient at producing kinetic energy. Satellite observations of Hurricane Opal also suggested that latent heat release led to greater increases in maximum wind as the hurricane intensified (Rodgers et al., 1998). However, Vigh and Schubert (2009) pointed out that it is difficult for an observational study to distinguish the response of a TC's intensification to increases in inner-core diabatic heating from the increases in inner-core diabatic heating that might result from a more intense TC organising the heating nearer to the centre.

A similar theory concerning increases in energetic efficiency was presented by Hack and Schubert (1986), this time using the TPE efficiency introduced in Section 2.2.1. Their experiments used a dry, inviscid vortex, forced by a constant heating function designed to approximate the diabatic effect of latent heat release.

Figure 2.6 shows the time series of the TPE efficiency of the vortex as a whole, for experiments with a varying height of maximum heating. The efficiency increases over the course of the model run for each experiment (note that the vortex continues to intensify throughout the run for each experiment). The results are similar if the radius of maximum

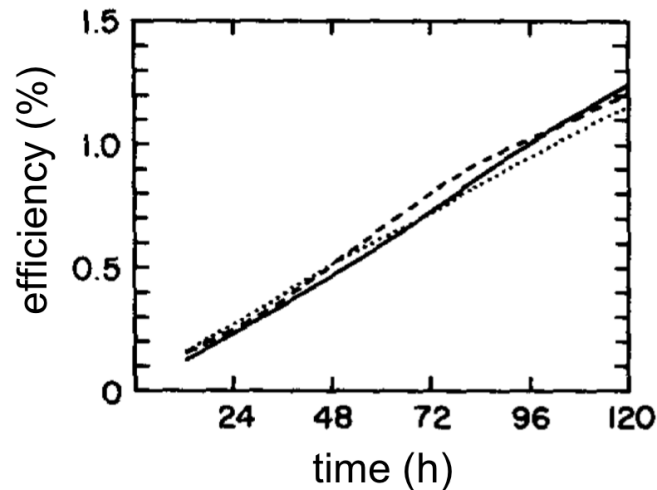


Figure 2.6: Temporal variation in the overall TPE efficiency of a heating-forced balanced vortex system. The different time series lines indicate experiments with maximum heating at varying vertical levels (dotted: 400 hPa, solid: 500 hPa, dashed: 600 hPa). Adapted from Hack and Schubert (1986). © American Meteorological Society. Used with permission.

heating is varied (not shown). Hack and Schubert (1986) attributed the model’s non-linear increase in total kinetic energy to this increase in the bulk system TPE efficiency, again positing that such increases in efficiency could be responsible for periods of RI in TCs.

However, Smith and Montgomery (2016) disputed that these findings prove the importance of efficiency increases for TC development. They argued that the constant heating rates used to force the models of Schubert and Hack (1982) and Hack and Schubert (1986) are not sufficiently representative of the forcing that would occur in a real TC. The increasing efficiency is associated with increasing inertial stability, which means that the TC is more stable to radial displacements. This increased radial stability should reduce the radial inflow to the core of the TC, thus weakening the secondary circulation. A weakened secondary circulation would reduce the rate at which heat is supplied to the TC. Therefore, the increase in kinetic energy generation due to the increased efficiency should be at least somewhat compensated by a decrease in kinetic energy generation due to a decreased energy supply.

As was discussed in Section 2.2, Smith and Montgomery (2016) also pointed out that these concepts of efficiency are focused above the boundary layer, and therefore fail to include any of the boundary layer dynamics or thermodynamics that are known to be integral to TC spin-up. It was highlighted in Section 2.2 that moist APE theory would introduce more of a focus on boundary layer processes than TPE or dry APE theory; it is therefore hopeful that a moist APE definition of efficiency could be more satisfactory

in this regard.

Temporal changes in moist APE efficiency in a TC and their effect on TC development have not previously been well-discussed. Wong et al. (2016) found some increases in APE production efficiency towards the end of their axisymmetric model run, which coincided with the mature stage of the TC rather than its intensification. However, this work only considered the efficiency associated with the production coefficient G_s (neglecting G_{qt}), and did not attempt to draw any conclusions on how the evolution of the efficiency impacted the overall development of the TC.

Chapter 7 will therefore explore the evolution of the moist APE efficiency in an axisymmetric model. The use of an axisymmetric TC model with interactive surface fluxes will mean the issue of using an inappropriate constant forcing is avoided. The aim here will be to investigate whether the conclusion of Schubert and Hack (1982), that RI can be due to increases in energetic efficiency, holds true in the context of local moist APE theory.

2.3.2 Potential intensity

A particularly useful theory, which is linked to the concept of efficiency in a TC, is that of potential intensity (PI). PI theory uses information about the thermodynamic environment of a TC to predict the maximum wind speed it can attain (its PI). One particular form of PI theory, which will turn out to have important links to moist APE, is the gradient PI proposed by Emanuel (1986). The gradient PI provides an upper bound on the azimuthal wind under the assumption that the TC is in gradient wind balance, i.e. that the radial pressure gradient force is balanced by the sum of the centrifugal and Coriolis forces.

Gradient PI is derived by first writing the equations for thermal wind balance (gradient wind balance and hydrostatic balance) in terms of specific volume α and angular momentum $M = rv + \frac{fr^2}{2}$:

$$\frac{1}{r^3} \left(\frac{\partial M^2}{\partial p} \right)_r = - \left(\frac{\partial \alpha}{\partial r} \right)_p. \quad (2.39)$$

Assuming reversible thermodynamics, and saturation in parcels above the boundary layer, this can be rewritten as

$$\frac{1}{r^3} \left(\frac{\partial M^2}{\partial p} \right)_r = - \left(\frac{\partial T}{\partial p} \right)_{s^*} \left(\frac{\partial s^*}{\partial r} \right)_p, \quad (2.40)$$

where s^* is the specific saturation entropy. In addition, moist slantwise neutrality is assumed: s^* does not vary along M surfaces. This yields

$$\frac{1}{r^3} \left(\frac{\partial M^2}{\partial p} \right)_r = - \left(\frac{\partial T}{\partial p} \right)_{s^*} \frac{ds^*}{dM} \left(\frac{\partial M}{\partial r} \right)_p, \quad (2.41)$$

which can be rearranged into

$$\frac{1}{r^3} \left(\frac{\partial r}{\partial p} \right)_M = \frac{1}{2M} \frac{ds^*}{dM} \left(\frac{\partial T}{\partial p} \right)_{s^*}. \quad (2.42)$$

If Equation (2.42) is integrated upwards along an angular momentum surface from the top of the boundary layer to the outflow (defined as the point where $v = 0$), this becomes

$$M = -r_b^2 \frac{ds^*}{dM} (T_b - T_{\text{out}}), \quad (2.43)$$

where the subscript b denotes a value at the top of the boundary layer and the subscript ‘out’ denotes a value in the outflow. Substituting in the form of M at the top of the boundary layer and assuming that $v \gg fr$ near the radius of maximum wind, this is equivalent to

$$\frac{v_b}{r_b} = - \frac{ds^*}{dM} (T_b - T_{\text{out}}), \quad (2.44)$$

where it should be remembered that v_b is the gradient wind, since thermal wind balance was assumed at the start of the derivation.

The form of $\frac{ds^*}{dM}$ is found using a boundary layer closure that assumes turbulent fluxes through the top of the boundary layer are negligible near the eyewall. The derivative $\frac{ds^*}{dM}$ is then equal to the ratio of the surface fluxes of entropy F_s and angular momentum F_M , defined by

$$F_s = \frac{\rho}{T_s} C_k |\mathbf{v}| (k^* - k), \quad (2.45)$$

$$F_M = -\rho r C_D |\mathbf{v}| v, \quad (2.46)$$

where C_k and C_D are the surface exchange coefficients for enthalpy and momentum respectively and \mathbf{v} is the surface horizontal velocity. The density ρ , azimuthal wind speed v and enthalpy $k = c_p T + Lq$ are evaluated at the top of the mixed layer. The saturation enthalpy k^* is evaluated at the sea surface temperature T_s .

Assuming that v and T are approximately constant throughout the depth of the boundary layer, and that M surfaces are vertical in the boundary layer, Equation (2.44)

becomes

$$v_g^2 = \frac{C_k}{C_D} \frac{T_b - T_{\text{out}}}{T_b} (k^* - k), \quad (2.47)$$

with v_g being the gradient wind PI.

Whilst the derivation above sets out the thermodynamic assumptions involved in PI theory, which will help the understanding of connections between PI and APE, the link between PI and efficiency can most clearly be seen by idealising the TC's secondary circulation as a heat engine (Emanuel, 1986, 1988). This idea is illustrated in Figure 2.7. Air spiralling inward towards the eye near the sea surface (from point a to point c in Figure 2.7) is heated by surface enthalpy fluxes. This addition of (mostly latent) heat results in an approximately isothermal expansion of the air. The air then ascends in the eyewall from point c : this can be treated as adiabatic expansion, because the pressure reduces but the total heat content of the air remains constant, simply transferring from latent to sensible heat as condensation occurs. The air reaches point o at the top of the TC at some large radius, where it loses heat via radiation to space, in an isothermal compression, as it moves to point o' . The air subsequently returns to its starting point, with this leg treated as adiabatic compression.

For such a closed heat engine cycle, which receives heat input Q_{in} at a temperature T_{in} and transfers it to a heat output Q_{out} at temperature T_{out} , the first law of thermodynamics

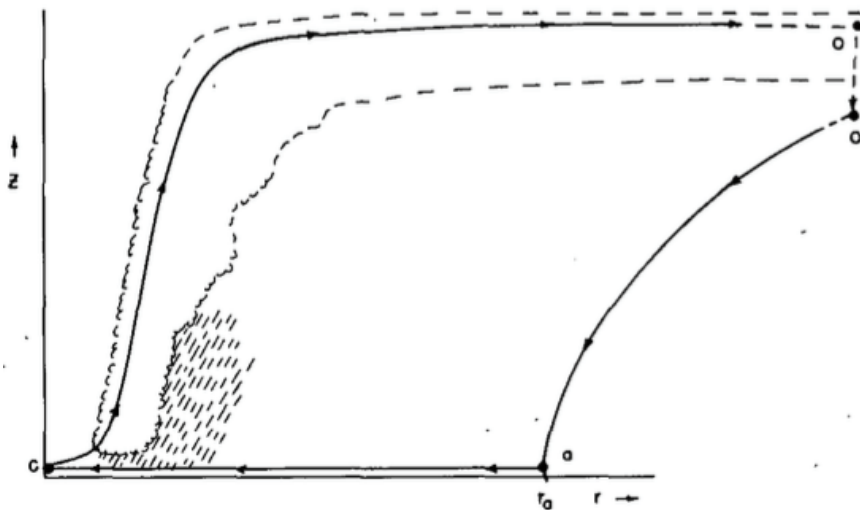


Figure 2.7: The Carnot heat engine cycle representing the secondary circulation of a tropical cyclone. The path $a \rightarrow c \rightarrow o \rightarrow o' \rightarrow a$ marks the trajectory of an air parcel in the TC, idealised as a closed cycle. From Emanuel (1988). © American Meteorological Society. Used with permission.

can be employed to express the total work done by the cycle W as

$$W = Q_{\text{in}} - Q_{\text{out}}. \quad (2.48)$$

The second law of thermodynamics can be used to express the entropy budget of the closed cycle as

$$\frac{Q_{\text{in}}}{T_{\text{in}}} - \frac{Q_{\text{out}}}{T_{\text{out}}} + \Delta s_{\text{irr}} = 0, \quad (2.49)$$

where Δs_{irr} is the production of entropy by irreversible processes over the cycle; the second law states that $\Delta s_{\text{irr}} \geq 0$ for an isolated system.

Equations (2.48) and (2.49) can be combined to give the total work done by the cycle in the form

$$W = \frac{T_{\text{in}} - T_{\text{out}}}{T_{\text{in}}} Q_{\text{in}} - T_{\text{out}} \Delta s_{\text{irr}}. \quad (2.50)$$

The maximum work is achieved in the case that the cycle is reversible, $\Delta s_{\text{irr}} = 0$. This reversible cycle is known as a *Carnot cycle*, and it achieves the maximum possible efficiency for a heat engine working between two heat reservoirs at T_{in} and T_{out} . Expressing the efficiency as the ratio of mechanical work generation to heat input, the Carnot efficiency is

$$\eta = \frac{W}{Q_{\text{in}}} = \frac{T_{\text{in}} - T_{\text{out}}}{T_{\text{in}}}. \quad (2.51)$$

Any irreversible processes act as a source of entropy, reducing the work done by the heat engine cycle and thus its efficiency. The work lost is proportional to the irreversible entropy production; this is known as the *Gouy-Stodola theorem* (Gouy, 1889; Tailleux, 2010; Ambaum, 2010).

In the case of a TC, the heat engine is considered to be reversible, working between the boundary layer temperature T_b and the outflow temperature T_{out} , so its Carnot efficiency is

$$\eta = \frac{T_b - T_{\text{out}}}{T_b}. \quad (2.52)$$

The mechanical work produced by the engine is the TC's kinetic energy; in the steady state, the generation of mechanical work is balanced by frictional dissipation, which mostly occurs at the sea surface. Therefore,

$$\rho C_D v_s^3 = \frac{T_b - T_{\text{out}}}{T_b} \rho C_k v_s (k^* - k), \quad (2.53)$$

from which, if it is assumed that $v_s \approx v_b$, Equation (2.47) for the PI can easily be obtained

(although it should be noted that gradient balance was not assumed in this instance). Recent work by Rousseau-Rizzi and Emanuel (2019) also showed that by considering two infinitesimally separated Carnot cycles, it is possible to derive a PI for the surface winds without requiring the entire secondary circulation to approximate a Carnot heat engine: only the circulation in the eyewall needs to do so.

There are many variations of PI theory, which account for processes not accounted for in Equation (2.53). Bister and Emanuel (1998) showed that including the effect of dissipative heating in the boundary layer was equivalent to increasing the efficiency by a factor of $\frac{T_s}{T_{\text{out}}}$. Modifications have also been proposed to include the effects of ocean coupling (Lin et al., 2013; Balaguru et al., 2015). The lost work due to irreversible frictional dissipation associated with falling rain was studied by Sabuwala et al. (2015), who suggested that this effect could reduce PI by 20% on average.

A common method of computing PI, which will be used in Chapter 7, is the CAPE-based algorithm developed by Bister and Emanuel (2002). Equation (2.47) can be rewritten as

$$v_g^2 = \frac{C_k}{C_D} (\text{CAPE}^* - \text{CAPE}), \quad (2.54)$$

where CAPE^* (the CAPE of saturated air at sea level relative to the environment) and CAPE (the CAPE of boundary layer air) should be evaluated near the radius of maximum wind. Since CAPE^* also depends on the surface pressure at this radius, the algorithm iterates between solving Equation (2.54) for v_g and solving for the central surface pressure by assuming thermal wind balance in the outer regions of the TC, until convergence is achieved. The specific humidity needed to calculate CAPE is found by assuming that the boundary layer relative humidity at the radius of maximum wind is equal to the relative humidity in the far-field environment.

Figure 2.8 shows the annual maximum PI obtained by applying the algorithm of Bister and Emanuel (2002) to ERA-Interim reanalysis data, averaged between 1976 and 2016. The spatial distribution of maximum PI strongly resembles the spatial distribution of maximum SST, since SST is the key parameter for determining T_b and the moist enthalpy difference in Equation (2.47). Maximum intensity has been shown to increase rapidly as SST increases (Emanuel, 1988).

The areas of high PI include the main regions in which TCs are observed to form, but also cover some regions where TCs are rarely observed. This is because the PI theory presented here is thermodynamic in nature, so it fails to account for dynamical aspects of TC development. For example, Figure 2.8 shows high PI near the equator, where TCs

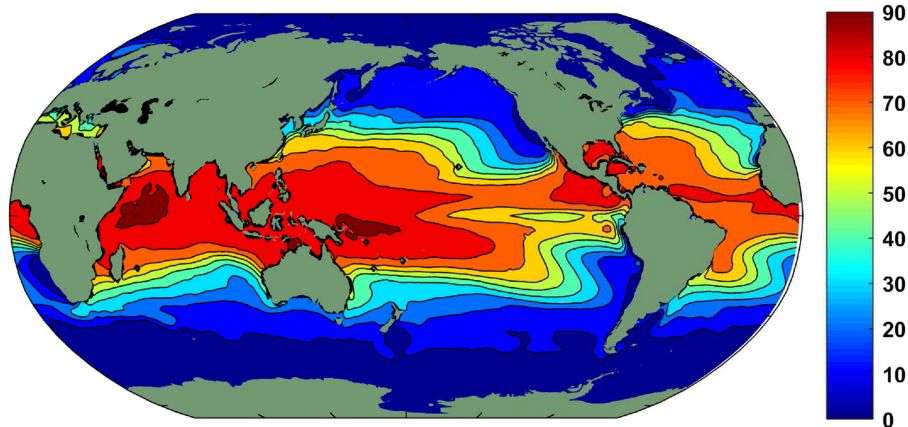


Figure 2.8: Annual maximum potential intensity (PI) in m s^{-1} for averaged ERA-Interim reanalysis data from 1979–2016, computed using the CAPE-based algorithm of Bister and Emanuel (2002). From Emanuel (2018). © American Meteorological Society. Used with permission.

do not occur in reality; Equations (2.47) and (2.54) assume the existence of a vortex in thermal wind balance, but near the equator there is insufficient Coriolis force to spin up such a vortex. In regions such as the South Atlantic and North Indian Oceans, high vertical wind shear prevents TCs from forming or reduces their intensity (Gray, 1968), so that the values of PI displayed in Figure 2.8 are rarely reached in practice.

PI has been found to reasonably estimate the actual maximum intensity achieved in idealised TC models for varying values of SST and outflow temperature (Rotunno and Emanuel, 1987; Rousseau-Rizzi and Emanuel, 2019). For observed TCs, PI provides a realistic upper bound on intensity; Emanuel (2000) found that there is “virtually no possibility” of a TC having a maximum wind speed above its PI, unless it moves along a strong negative PI gradient. However, DeMaria and Kaplan (1994) showed that on average a TC will only reach 55% of its PI. Even after accounting for the fact that some storms have their intensification impeded by landfall or cold areas of ocean, Emanuel (2000) found that the observed maximum intensity of tropical storms is in fact approximately uniformly distributed up to the threshold of hurricane intensity, and then uniformly distributed (with a different probability) up to the PI. Factors that could prevent TCs from attaining their PI include vertical wind shear and cooling of the sea surface due to mixing induced by the TC itself.

Despite PI being intended as an upper bound on wind speed, observations from Hurricane Isabel showed that it may have exceeded its PI by up to 35 m s^{-1} (Montgomery et al., 2006; Bell and Montgomery, 2008). Numerically simulated TCs can also exceed their PI—this is referred to as *superintensity* (Persing and Montgomery, 2003). Wind

speeds can be 50% higher than the PI in numerical models (Bryan and Rotunno, 2009a). Bryan and Rotunno (2009a) showed that this mostly occurred due to the assumption of gradient wind balance being invalid in the boundary layer, and added a term to the PI equation that accounts for a gradient effects, in order to predict the maximum azimuthal wind speed rather than the maximum azimuthal gradient wind speed.

Although PI can be derived from an argument based on the maximum efficiency of a TC, there is not an obvious link between this Carnot efficiency and the TPE or dry Lorenz APE efficiencies discussed in the previous sections. The Carnot efficiency has a typical value of $\frac{1}{3}$, whereas the maximum TPE or dry APE efficiency does not exceed 10%. This may be linked to the fact that TPE and dry APE treatments of efficiency are treating latent heat release as their energy source, whereas in the Carnot engine framework the energy source is clearly surface enthalpy fluxes—as in moist APE theory. The moist APE efficiencies computed by (Wong, 2014) (shown in Figure 2.5) reach a maximum value more similar to the Carnot efficiency.

The similarity between the Carnot efficiency $\eta = \frac{T_b - T_{\text{out}}}{T_b}$ and the moist APE production efficiencies is easily sketched out: a surface flux of entropy $\frac{Ds}{Dt}$ produces local available energy $(T - T_r) \frac{Ds}{Dt} = \frac{T - T_r}{T} \frac{DQ}{Dt}$, where Q is the surface heat flux, making use of the second law (see Section 2.1.2 for details on diabatic APE production in a local framework). The production occurs in a near-surface parcel, so $T \approx T_b$, and if the parcel's reference position is in the outflow then $T_r \approx T_{\text{out}}$ from the Carnot derivation. Therefore, surface entropy fluxes near the radius of maximum wind should produce APE at approximately the Carnot efficiency. Many studies dealing with the Carnot cycle viewpoint of TCs even refer to the mechanical energy output of the heat engine as the “available energy” (Emanuel, 1987, 1997, 2003; Shen, 2004). However, this energy is based on an entropy budget around a closed cycle and is therefore fundamentally different to the moist APE described in the previous sections of this chapter, which concerns the work done by buoyancy forces as air parcels move to a level of neutral buoyancy.

A major difference between the two viewpoints is obvious when considering the effect of irreversible processes on the PI. In the entropy-based framework, any irreversible process is a source of entropy and must reduce the efficiency and work output of the heat engine; it would therefore reduce the PI. In contrast, any irreversible process may be either a source or a sink of APE, dependent upon the sign of the APE production coefficients in the parcel in which it occurs. It does not appear to necessarily be the case that irreversible processes must inhibit the generation of kinetic energy in a TC or lower

the PI when the problem is examined in terms of APE. Therefore, even if the maximum efficiency of moist local APE generation is approximately equal to the Carnot efficiency, the two are derived from quite different underlying physical principles.

Whilst it is possible to study the generation of kinetic energy in TCs—or in convection in general (Pauluis and Held, 2002a,b; Warner, 2005)—by treating parts of the circulation as idealised heat engines and computing their entropy budgets (Pauluis and Zhang, 2017), entropy is not fundamentally linked to the local generation of kinetic energy as APE density is. The existence of closed cycles is also a significant idealisation. Advanced methods are required to approximate heat engine cycles in numerical model output by representing parcel trajectories using isentropic streamfunctions (Pauluis, 2016), whereas APE density can be diagnosed for any air parcel regardless of the existence of a closed circulation. An APE analysis is therefore more flexible for studying parcels throughout a TC and does not require any kind of steady state assumption in order to calculate efficiencies or energy production.

Chapter 7 will explore in more detail the assumptions required to construct an expression for PI based on moist APE theory, and assess which reference states are suitable for computing values of APE-based PI. Whereas previously the overall energetic efficiency of a TC (in terms of TPE, as reviewed in Section 2.3.1) and its maximum efficiency (in terms of the Carnot efficiency) have been presented as discrete concepts, Chapter 7 aims to unify the two under a definition based on moist APE efficiency.

2.3.3 Summary of tropical cyclone energetics and efficiency

The energetics of TC development have previously been analysed using total potential energy (TPE) or dry APE. The main source of both of these types of potential energy is the latent heat release that occurs when water vapour condenses in the eyewall. TPE and dry APE are associated with efficiencies of kinetic energy generation, which are maximal in the upper troposphere. It has been suggested that increases in the overall TPE efficiency of a TC could be responsible for rapid intensification. However, the TPE efficiency is not satisfactory for explaining TC development because it does not directly account for any boundary layer processes, which strongly govern TC intensification. TPE and dry APE efficiencies also have no apparent link with the Carnot efficiency of a TC, which can be used to determine its maximum intensity by predicting the fraction of the surface enthalpy flux that can be converted into kinetic energy.

Using local moist APE theory to investigate TC energetics would be advantageous

because it correctly treats surface enthalpy fluxes, rather than latent heat release, as the main source of potential energy for the TC. This means that boundary layer processes could be influential in the theory, and it makes it possible to link the Carnot efficiency to the concept of energetic efficiency using the APE production efficiencies. However, moist APE is a complex diagnostic, since it requires all parcels to be lifted to their levels of neutral buoyancy. There has been no previous closed budget of moist APE density for the atmosphere, and the best choice of reference state for studying local APE in a TC remains unknown.

Chapters 5–7 will therefore investigate the behaviour of moist APE density in an axisymmetric model of a TC, in order to establish the key sources and sinks of APE density affecting the generation of kinetic energy. Chapter 5 will detail the energetics of the model in terms of kinetic energy, available elastic energy density and moist APE density. This includes complete budgets of APE density and the diabatic processes leading to APE production and dissipation, using the model’s initial environmental sounding as a reference state. Chapter 6 will assess the effects of using various reference states on the budgets and explore which reference state is optimal for studying local available energetics in a TC. Finally, Chapter 7 will examine the importance of the temporal evolution of moist APE efficiency on TC development, and demonstrate how the moist APE efficiency can be used to predict potential intensity.

Chapter 3:

Assessment of algorithms for computing moist available potential energy

This chapter is adapted from a paper published in the Quarterly Journal of the Royal Meteorological Society:

Harris, B. L. and R. Tailleux, (2018). Assessment of algorithms for computing moist available potential energy. *Q. J. R. Meteorol. Soc.*, **144**, 1501–1510, doi:10.1002/qj.3297.

Reproduction of the paper is permitted under the Creative Commons license CC BY 4.0. Some modifications have been made to the original text to preserve the narrative flow of the thesis and keep notation consistent.

BLH designed the study with assistance from RT. BLH carried out all analysis and led the writing of the paper, with contributions from RT. The estimated contribution of BLH to the paper is 90%.

3.1 Introduction

Atmospheric available potential energy (APE) has been traditionally defined as the potential energy of the atmosphere relative to that of the adiabatically sorted reference state defining a global potential energy minimum (Lorenz, 1955), as reviewed in Section 2.1.1.

Obtaining this reference state is a far more complex problem for a moist atmosphere

than a dry one. Considering only the single-column case, knowledge of the potential temperature field θ is sufficient to determine the dry reference state, since the minimum potential energy is achieved simply by a profile of θ that increases monotonically with height. As discussed in Section 2.1.1, the presence of moisture means that the relative density of two parcels depends on the pressure level they occupy (since condensation and associated latent heat release may occur at some levels). This results in the possible existence of local potential energy minima, as well as the global minimum that defines the Lorenzian reference state (Turner and Norbury, 2020). Hence there is no analytical method for constructing the moist reference state from the distribution of entropy and specific humidity.

As a result, previous methods of calculating APE have relied on heuristic approaches, which involve discretising atmospheric domains into parcels of equal mass and sorting them according to density at differing pressure levels to obtain a reference state. From a computational viewpoint, the discretised approach to computing APE is equivalent to finding the permutation of the actual state with the lowest total potential energy. Simpler non-rearrangement-based minimisation methods, such as varying parcel temperatures at each level to test whether the value of TPE would be lowered, are not suitable because entropy (and moisture) must be conserved when constructing the reference state from the actual atmospheric state.

Tailleux and Grandpeix (2004) characterised such a discretised sorting approach as an asymmetric travelling salesman problem, but recently, it was realised by Hieronymus and Nycander (2015) that the computation of the reference state in this way is in fact a linear assignment problem. Unlike travelling salesman problems, a linear assignment problem can be exactly solved, using the Munkres algorithm (Munkres, 1957).

Whilst the Munkres algorithm is exact, it is also computationally expensive, and therefore it is still desirable to use approximate algorithms for speed. The Munkres algorithm can be used when the considered atmospheric domain comprises a small number of parcels n , but the runtime of the algorithm increases as n^3 (Stansifer et al., 2017), so it quickly becomes infeasible for large domains. This has prompted much interest in developing cheaper heuristic methods for computing moist APE in practice.

A review of existing approximate sorting algorithms is given by Stansifer et al. (2017), who discussed their accuracy compared to the exact Munkres algorithm. However, the comparison was made over only three test case soundings. This showed that none of the approximate algorithms was able to compute the exact APE in every case, but clearly the

small number of cases presented means that it is impossible to draw conclusions about the general relative performance of the algorithms, and therefore difficult to know which is most useful to study atmospheric energetics. This chapter provides an assessment of the algorithms' performance across a wide range of atmospheric soundings, in two different locations.

It is also not certain that parcel-sorting algorithms calculate the most physically suitable form of APE. Finding the exact minimum potential energy parcel rearrangement using the Munkres algorithm does not consider whether certain parcel movements may be restricted, for example by the presence of Convective Inhibition (CIN). The bottom-up algorithm introduced by Wong et al. (2016) is designed to prevent the unrealistic release of Convective Available Potential Energy (CAPE) during sorting, but does not directly consider either CAPE or CIN in its computation. For a 2D or 3D atmosphere, it may also be more appropriate to use a non-resting reference state to account for dynamical constraints (see Section 2.1.3), which cannot be achieved using existing sorting algorithms.

Section 3.2 briefly describes all the existing algorithms that have been designed to calculate APE in a moist atmosphere. To investigate the possibility of using a more physically-based approach to compute APE, a novel algorithm is also developed, which is based on the relationship between CAPE and APE found by Emanuel (1994). It does not appear to have been previously investigated whether this relationship can be used to obtain similar results to those of the parcel-sorting approaches.

All the APE algorithms are then applied to 3130 soundings from the Atmospheric Radiation Measurement (ARM) station on Nauru, and to 584 soundings from the ARM sites on the Southern Great Plains. This enables an assessment of which approximate algorithms are likely to compute an APE close to the true value, and an investigation of the variation in their accuracy over a large number of soundings. The data used for the assessment is described in Section 3.3. Section 3.4 presents the results of the approximate algorithms' performance against the Munkres algorithm, and compares their accuracy between the two locations. Section 3.5 discusses how the results relate to what was previously known about the algorithms, and which algorithms are most suitable for practical application. The implications of the results for the development of a satisfactory theory of APE for a moist atmosphere are also discussed.

3.2 Algorithms for Computing APE

This section describes the algorithms that may be used to compute the reference state, and hence the APE, of a moist atmospheric sounding. It is assumed here that the sounding has been discretised into parcels of equal mass. Whereas Lorenz (1955) calculated APE for a three-dimensional dry atmosphere, here the problem is only being considered in one dimension. Sorting algorithms can be applied to 2D or 3D data, but their computational expense means that it would be difficult to analyse their performance over a wide range of data in more than one dimension. Whereas in a 2D or 3D domain there may be a contribution to the APE due to horizontal motion (if the atmosphere is baroclinic), a 1D atmospheric column can only have APE associated with the vertical motion of parcels.

Assuming hydrostatic balance, minimisation of the total potential energy is equivalent to minimisation of the enthalpy, so that

$$\text{APE} = \int (k - k_{\text{ref}}) dm, \quad (3.1)$$

where k is the specific enthalpy, and the integral is over all the mass in the column.

Firstly, the Munkres algorithm is outlined, which finds the reference state corresponding to the exact minimum enthalpy rearrangement of the parcels. The parcel-sorting algorithms that have been designed to find approximations to the reference state are then described. Due to their approximate nature, these methods are less computationally expensive than the Munkres algorithm, but their typical accuracy compared to the Munkres algorithm is unknown; this will be investigated in Section 3.4. Finally, a method for calculating APE is described, which does not rely on a sorting procedure, but instead makes use of the relationship between APE and CAPE suggested by Emanuel (1994).

3.2.1 Munkres algorithm

The Munkres algorithm (Munkres, 1957) may be used to obtain the exact minimum enthalpy rearrangement of a set of air parcels, by treating the computation of the parcels' reference pressures as a linear assignment problem (Hieronymus and Nycander, 2015; Stansifer et al., 2017). This method first calculates a *cost matrix* C , in which the entry c_{ij} is the enthalpy of the i^{th} parcel at the j^{th} pressure level. Using this cost matrix, the algorithm allocates parcels to the pressure levels resulting in a minimised total enthalpy. This is done by using the linear algebra procedure described by Munkres (1957),

which tracks how difficult it is to find a low-enthalpy position for each parcel during the rearrangement process.

3.2.2 Lorenz's algorithm

The first algorithm for approximating the minimised enthalpy reference state of a moist sounding was developed by Lorenz (1979). For a set of n parcels at pressures $p_1 < p_2 < \dots < p_n$, this algorithm begins by calculating the virtual temperature that each parcel would have if it were lifted reversibly and adiabatically to p_1 , denoted T_{v1} , and if it were similarly lifted to p_n , denoted T_{vn} . The algorithm first finds a parcel to assign to pressure level p_1 , and then moves to progressively higher pressures. This assignment is determined as follows: at each level p_j , the unassigned parcels with the highest values of T_{v1} and T_{vn} are identified. If these values are maximised by the same parcel, this parcel is assigned to p_j . If the two identified parcels differ, then their virtual temperatures at $\frac{p_j+p_{j+1}}{2}$ are calculated. The parcel with the higher T_v here is assigned to p_j . After n assignments are made in this way, all parcels will have been assigned a different reference pressure, thus determining the reference state. Equivalently, the specific volume may be maximised at each pressure rather than the virtual temperature, as has been done in the implementations here. The algorithm aims to obtain the lowest possible parcel density at the topmost remaining level, whilst also ensuring (by testing T_{vn}) that the parcels that remain unassigned once the sorting process begins to reach near-surface pressure levels will not have a very low density at these levels.

3.2.3 Randall and Wang's algorithm

Randall and Wang (1992) noted that it was possible for Lorenz's algorithm to return a negative APE, and designed a similar algorithm that eliminated this problem. For pressure levels $p_1 < p_2 < \dots < p_n$ as before, the procedure begins by labelling $p_A = p_1$, $p_B = p_n$. Once again, the virtual temperatures for all parcels are calculated as if they were lifted to p_A and p_B , and those parcels with the highest values of T_{vA} and T_{vB} are identified. At this point, the two methods diverge. Randall and Wang next compute the total atmospheric enthalpy for two situations: if the parcel with the highest T_{vA} were lifted to p_A , with any intermediate parcels shifted down one pressure level; and if the parcel with the highest T_{vB} were lifted to p_A and the intermediate parcels shifted down. Whichever of these configurations results in the lowest total enthalpy is accepted as the new rearrangement, and p_A is redefined as $p_A = p_2$. The method proceeds until $p_A = p_B$.

3.2.4 Top-down algorithm

The top-down algorithm was used to compute reference states in the study of APE in tropical cyclones by Wong et al. (2016). The performance of the top-down algorithm was also analysed by Stansifer et al. (2017), who referred to it as the “greedy algorithm”. The top-down algorithm for n parcels proceeds as follows: all n air parcels are moved reversibly and adiabatically to p_1 , the lowest pressure in the sounding. Their densities at this pressure are calculated, and the parcel with the lowest density is assigned to have p_n as its reference pressure. This parcel is then eliminated from sorting. The remaining $n - 1$ parcels are moved to p_2 , and again their densities are calculated, and the least dense parcel assigned to p_2 . The algorithm continues in this way until all parcels have been assigned to a reference pressure level.

3.2.5 Bottom-up algorithm

Bottom-up sorting works similarly to top-down sorting, but the parcels are first moved to the highest pressure p_n , assigning the parcel with the highest density to this level, and proceeding to lower pressure levels $p_{n-1}, p_{n-2} \dots$. Bottom-up sorting was suggested by Wong et al. (2016) to limit the inclusion of CAPE in the definition of APE. This may be desirable in practice since not all the CAPE present in the atmosphere will be released, for example due to the presence of Convective Inhibition (CIN) or subsidence.

3.2.6 Divide-and-conquer algorithm

The divide-and-conquer algorithm was introduced by Stansifer et al. (2017). It is similar to top-down or bottom-up sorting, but all the parcels are initially moved to the middle pressure level p_m , where $m = \lfloor \frac{n+1}{2} \rfloor$. The m parcels with the lowest density at this pressure are assigned to the sub-domain $[p_1, p_m]$, and the $n - m$ parcels with the highest density are assigned to $[p_{m+1}, p_n]$. The algorithm then acts recursively on the two sub-domains. In the three test cases analysed by Stansifer et al. (2017), the divide-and-conquer algorithm was found to perform well. It computed the exact minimum enthalpy reference state in one test case and close to the minimum in the other two, even when other approximate algorithms failed to capture significant proportions of the APE. However, since the divide-and-conquer algorithm is not an exact enthalpy minimisation procedure, the fact that it was tested only on a small sample of atmospheric soundings means there is not sufficient evidence to exclude the possibility of atmospheric conditions, yet to be

identified, on which it might perform poorly.

3.2.7 Estimation from Convective Available Potential Energy

Rather than using a parcel-sorting algorithm to compute the vertical component of APE, it is natural to consider its relation to Convective Available Potential Energy (CAPE), since both are measures of the energy available to vertical motion in a sounding. This link was noted by Randall and Wang (1992), who referred to the vertical component of APE as GCAPE (Generalised CAPE), but did not explore the link between CAPE and GCAPE. Tailleux and Grandpeix (2004) suggested the existence of a functional relationship between CAPE and APE, which could permit the inexpensive computation of APE. However, it is still not known how CAPE-based measures of atmospheric energetics compare to the Lorenz APE of Equation (3.1). Here, an algorithm for calculating APE using the CAPE-dependent equations of Emanuel (1994) is outlined. The results of this algorithm will be compared (in Section 3.4) to the APE computed by the sorting algorithms described above.

Emanuel (1994) supposes that APE is due solely to the presence of CAPE in a thin boundary layer of depth Δp_b . In this case an approximation to the APE is given by

$$\text{APE} \approx \frac{\Delta p_b}{g} \left(\text{CAPE}_b - \frac{1}{2} \Delta p_b \overline{p^{\kappa-1}} p_0^{-\kappa} R_d \Delta \theta_v \right), \quad (3.2)$$

where CAPE_b is the mean CAPE in the boundary layer, $\kappa = \frac{R_d}{c_{pd}}$, and $\Delta \theta_v$ is the change in the virtual potential temperature between the top of the boundary layer at $p_{b,\text{top}}$ and the boundary layer's level of neutral buoyancy, p_{LNB} . The overbar denotes a θ_v -weighted average from $p_{b,\text{top}}$ to p_{LNB} . The first term of Equation (3.2) corresponds to the release of CAPE when the boundary layer rises upwards to its LNB. The second term accounts for the energy change that occurs as a result of the remaining air parcels descending by Δp_b . The APE calculated using Equation (3.2) will henceforth be referred to as the *Emanuel APE*.

The Emanuel APE is computed by calculating the value of Equation (3.2) for Δp_b depths ranging from 0 hPa to 150 hPa, and selecting the maximum value of APE returned by any of these Δp_b values. Increments of Δp_b are added simply by including the next lowest parcel in the sounding. Theoretically, it would be possible to use smaller increments in Δp_b , and include fractions of parcels in the boundary layer. This has not been done here because the sorting algorithms discussed earlier in this section are only able to rearrange

whole parcels, so allowing this CAPE-based algorithm to only lift whole parcels provides a fairer comparison of the APE.

The boundary layer CAPE, CAPE_b , is computed using a parcel with a value of θ given by the pressure-weighted mean of θ in the boundary layer, and q given by the mean q in the boundary layer. The CAPE is then

$$\text{CAPE}_b = \int_{p_{\text{LNB}}}^{p_i} (\alpha_p - \alpha_e) dp, \quad (3.3)$$

where α_p is the specific volume of the parcel when it is lifted reversibly and adiabatically, and α_e is the environmental specific volume. The parcel is lifted from its initial position p_i , which is taken to be the bottom of the boundary layer (i.e. the surface), to its highest level of neutral buoyancy.

3.3 Data

To calculate the APE of a sounding, the sorting algorithms outlined in Section 3.2 require the input of the temperature, pressure and total specific humidity profiles. The atmospheric profiles used to compare the algorithms are soundings obtained from the Atmospheric Radiation Measurement (ARM) Program (Stokes and Schwartz, 1994). It is assumed that the total specific humidity q_t in the soundings is equal to the specific humidity q , i.e. that no liquid water is present in the atmosphere. This widens the choice of data since liquid water measurements are not required, and is justified by the fact that large quantities of liquid water are not expected to reside in the atmosphere for long periods of time.

Soundings from Nauru dating from 1 April 2001 to 16 August 2006 have been used. These soundings contain data that have been interpolated onto 5 hPa pressure levels and quality controlled as described by Holloway and Neelin (2009). Soundings are included in the assessment data if they have at least 150 valid measurements of temperature and specific humidity, for which the valid measurements span at least the interval from 1000 hPa to 100 hPa. Any missing temperature or humidity measurements are filled in by linear interpolation. This results in 3130 soundings for which the sorting algorithms can be used to compute the APE in the 1000 hPa to 100 hPa layer using 181 parcels of 5 hPa depth.

To verify whether the performance of the algorithms is significantly affected if the soundings are from a different location, soundings from the ARM Southern Great Plains (SGP) sites during the Intensive Observation Period from 4 June 1997 to 7 July 1997 are

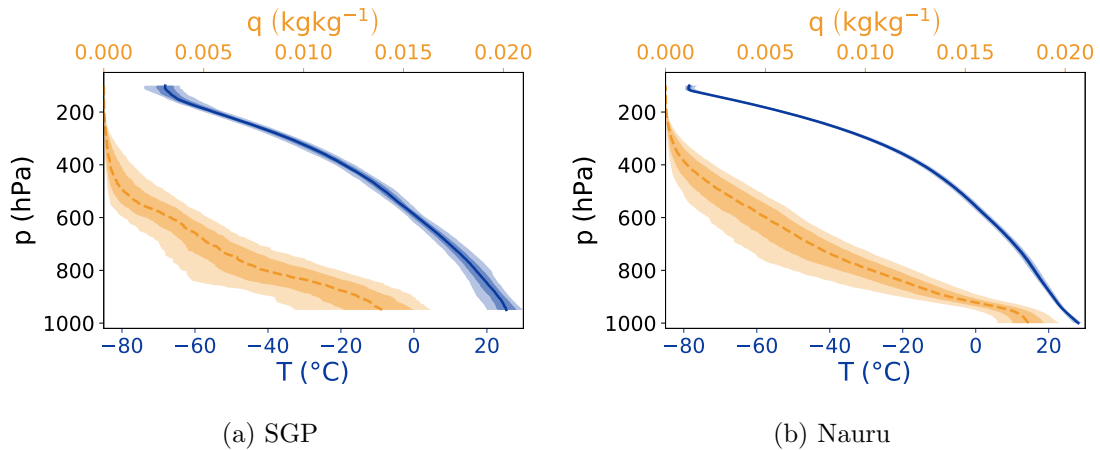


Figure 3.1: Median profiles of temperature T ($^{\circ}\text{C}$, solid line) and specific humidity q (kg kg^{-1} , dashed line) for the ARM soundings used to test the APE sorting algorithms. The dark shading shows the 25th to 75th percentile, and the light shading shows the 10th to 90th percentile.

also used; this dataset is the one used by Tailleux and Grandpeix (2004). The pressure levels measured in the SGP soundings vary, so soundings are included in the assessment if they have at least 2000 valid measurements extending from 950 hPa to 100 hPa, and no more than 50 invalid measurements, resulting in a total of 584 suitable soundings. The temperature and humidity data are interpolated onto 5 hPa-spaced pressure levels between 950 hPa and 100 hPa (resulting in 171 parcels per sounding), to match the parcel mass of the Nauru soundings. The results of Section 3.4 were found to be insensitive to interpolating to a greater number of parcels.

The median profiles of temperature T and specific humidity q are shown for each location in Figure 3.1, along with the 25th to 75th percentiles (dark shading) and 10th to 90th percentiles (light shading). The profiles are similar in the two locations, with Nauru soundings exhibiting higher moisture at lower levels (this is reasonable because Nauru data at higher pressure levels has been kept, where there were insufficient measurements to do so for the SGP data). The Nauru soundings also show colder temperatures at high altitude. It is notable that there is very little variation about the median Nauru temperature profile, and therefore differences in the ability of the algorithms to accurately calculate APE here will be mostly due to the differences in humidity profiles between the soundings.

3.4 Comparison of Algorithms

All the sorting algorithms discussed in Section 3.2 were used to calculate the APE of each of the 3714 ARM soundings described in Section 3.3. To summarise, these algorithms are: Munkres, Lorenz, Randall and Wang, top-down, bottom-up, divide-and-conquer, and Emanuel. Stansifer et al.'s implementation of the Munkres algorithm is used, with a modification to compute the cost matrix using a vectorised iterative method as described in Appendix A. Original implementations are used for the other algorithms, incorporating the iterative method approach. The APE found by the Munkres algorithm is the maximum APE computable by sorting; in the following section this is compared to the APE computed by the approximate algorithms to assess their accuracy.

To quantify the accuracy of each algorithm, the percentage relative difference in APE is defined as

$$D_R = \begin{cases} \frac{|\text{APE}_{\text{munk}} - \text{APE}_{\text{app}}|}{\text{APE}_{\text{munk}} + \text{APE}_{\text{app}}} \times 100, & \text{if } \text{APE}_{\text{app}} \geq 0 \\ 100, & \text{otherwise,} \end{cases} \quad (3.4)$$

where APE_{app} is the APE computed by the approximate algorithm, and APE_{munk} is the APE computed by the Munkres algorithm. This provides a measure of the amount of APE that each approximate algorithm fails to capture. All the approximate algorithms that are based on sorting parcels must compute an APE lower than the value computed by the Munkres algorithm, while the Emanuel APE may exceed this value.

The absolute percentage difference (computed by replacing the denominator of Equation (3.4) with APE_{munk}) was not used because it is extremely high (up to 7000%) in cases where the Munkres APE is very small and the Emanuel APE overestimates it. In these cases both values of APE are small and so the discrepancy between them is of little consequence to the expected atmospheric motion. It is preferred that the largest percentage differences correspond to cases where the atmospheric column contains high APE but the approximate algorithm fails to predict this, as is the case when D_R is used. The definition of D_R is chosen to yield values between 0% and 100%.

The distributions of D_R for each approximate algorithm across all the soundings are displayed in Figure 3.2. It is clear from these results that Randall and Wang's algorithm is the most accurate of the six approximate algorithms, with a median D_R of 0.0077% for the SGP soundings and 0.0015% for the Nauru soundings. However, there remain outlying cases in which even Randall and Wang's algorithm fails to capture a large proportion of the APE. Of the other sorting algorithms, only divide-and-conquer provides a reasonable

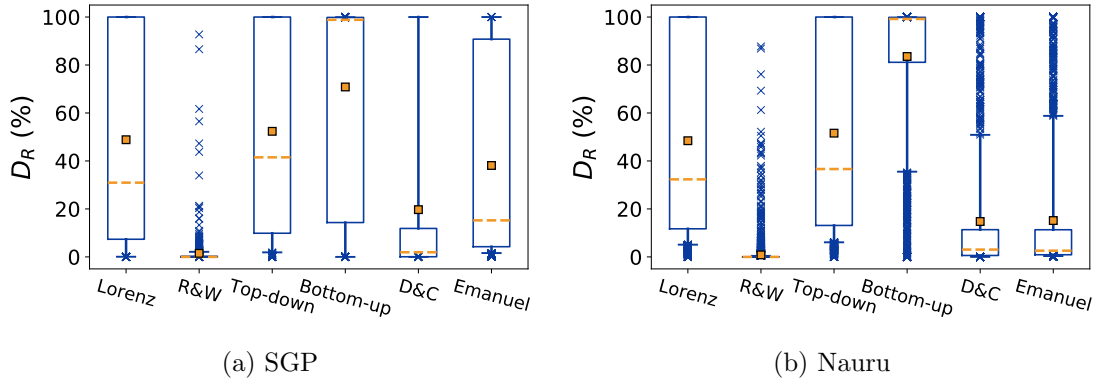


Figure 3.2: Box plots of the percentage relative difference D_R , as defined in Equation (3.4), between each approximate algorithm and the exact Munkres algorithm. The dashed lines denote the median D_R across the soundings, the squares the mean D_R , the boxes the 25th to 75th percentiles, and the whiskers the 10th to 90th percentiles. Crosses represent soundings with outlying D_R values.

approximation to the Munkres algorithm, with a median D_R of 1.9% across the soundings from the SGP, and 3.0% across those from Nauru.

The bottom-up algorithm fails to capture the majority of the APE in most cases; this is expected since the sorting procedure is designed to limit the release of CAPE from buoyant surface parcels, and hence should result in a smaller vertical component of APE. There is still a wide range of D_R across the soundings, particularly in the SGP case.

Lorenz’s algorithm exhibits a very similar D_R distribution to the top-down algorithm, with both medians around 50% for each location. The poor accuracy is largely due to the fact that both the top-down and Lorenz procedures frequently compute a negative APE, which is unphysical by the definition of APE as the difference between the enthalpies of the atmosphere and its rearranged, minimised total enthalpy state. A negative value of APE simply means that the “minimised” enthalpy reference state computed by the approximate algorithm in fact has a higher enthalpy than the real atmospheric state. The top-down and Lorenz algorithms compute a negative APE for between 30 to 40% of the soundings, for both the SGP and Nauru data.

To illustrate why this occurs, Figure 3.3 shows the difference in enthalpy for each parcel between the original sounding and the reference state, for the Nauru sounding measured at 1200 UTC on 24 September 2001. Referring to Equation (3.1), the total APE of the sounding will be equal to the sum of this enthalpy difference $k - k_{\text{ref}}$ over all parcels. The circular markers show the enthalpy difference when using the Munkres algorithm, which computes a APE of 6.87 J kg^{-1} . The crosses show the enthalpy difference using top-down sorting, which results in a APE of -19.9 J kg^{-1} . It is evident that the nega-

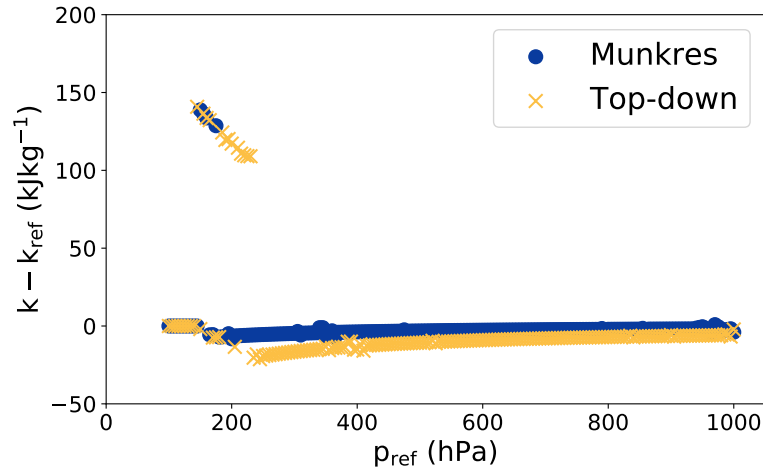


Figure 3.3: Difference between the enthalpy of each parcel from the 24 September 2001 1200 UTC Nauru sounding and its enthalpy in the reference state, plotted against the parcel’s pressure in the reference state. Reference states are calculated both using the Munkres algorithm, which computes the exact APE, and the top-down algorithm, which computes a negative APE.

tive APE is a result of the top-down algorithm lifting parcels to low reference pressures (150–250 hPa), in such a way that these particular parcels experience a large decrease in enthalpy, but the parcels at higher reference pressures exhibit a slight increase in enthalpy. When computing the overall APE, the smaller enthalpy decreases over many parcels at high reference pressures outweigh the large enthalpy decreases of the few parcels at low reference pressures. Parcels at high reference pressures in the Munkres reference state also show a decrease in enthalpy, but, since this decrease is smaller than in the top-down case, the net APE remains positive. The divide-and-conquer algorithm also computes negative APE for some soundings, but this does not occur as frequently as for the Lorenz and top-down algorithms (13% of SGP soundings, 6.5% of Nauru soundings).

In contrast, a non-negative value of APE is systematically returned by the bottom-up, Randall and Wang, and Emanuel algorithms on all soundings tested. This is expected for the latter two algorithms, since these are specifically designed to ensure that the enthalpy of the computed reference state is less than that of the original configuration of the fluid parcels.

Although no such constraint is imposed for the bottom-up algorithm, negative values are highly unlikely, because bringing fluid parcels adiabatically to higher pressures makes it nearly impossible for the fluid parcels to ever become saturated and to release latent heat. It follows that in effect, the bottom-up algorithm constructs its reference state by ordering the fluid parcels according to their virtual potential temperature θ_v , and hence that any positive value returned primarily reflects the presence of an inversion in θ_v in

the original sounding. For the unsaturated atmospheric soundings considered, existing inversions are in general not directly associated with the presence of CAPE. This means that the APE computed by the bottom-up algorithm in those cases is more akin to a “dry” APE than a “moist” one, and not prone to the problem seen in Figure 3.3. In the numerical simulations studied by Wong et al. (2016), on the other hand, the bottom-up algorithm can occasionally pick up the APE of fluid parcels with CAPE where a local sounding has become absolutely unstable as the result of fluid parcels having overcome their convective inhibition and reached their level of free convection. This behaviour supports the idea that in 2D and 3D domains, the bottom-up algorithm will primarily access the horizontal component of APE, and access any “vertical” APE only when readily available to fluid parcels after the fluid has become absolutely unstable. This seems to be the simplest way to avoid including CAPE as part of APE when the presence of convective inhibition or subsidence makes its release unlikely.

In general the D_R distributions of the sorting-based algorithms are similar for the two locations, suggesting that the optimal choice of sorting algorithm is not expected to change depending on the typical local atmospheric conditions. However, the accuracy of the Emanuel APE is very different between the locations. For the Nauru soundings, it has a median D_R of 2.6%, which is comparable to the divide-and-conquer sorting algorithm, showing that the Emanuel algorithm would be a sensible choice for estimating APE. In contrast, its median D_R over the SGP is 15%, which is much less accurate than either the divide-and-conquer or Randall and Wang algorithms, and so the Emanuel method would not be a good practical choice for computing APE in this environment.

To investigate why this difference in accuracy occurs, Figure 3.4 shows scatter plots of the Emanuel APE against the APE computed using the Munkres algorithm, for each location. The dashed lines display the best linear fit to the data; for the Nauru soundings the correlation coefficient is $r = 0.990$, while for the SGP soundings the correlation coefficient is slightly poorer, at $r = 0.977$, as expected from the higher median value of D_R . The high correlation indicates that most of the APE present in the ARM soundings corresponds to the CAPE of near-surface parcels, in line with the assumption of Emanuel (1994).

Figure 3.4 demonstrates that the poorer correlation for the SGP compared to the Nauru soundings is mostly due to a number of SGP soundings that have very low Emanuel APE, but values of Munkres APE up to 60 J kg^{-1} . Further investigation reveals that these discrepancies arise where an unstable layer that is elevated from the surface is present in

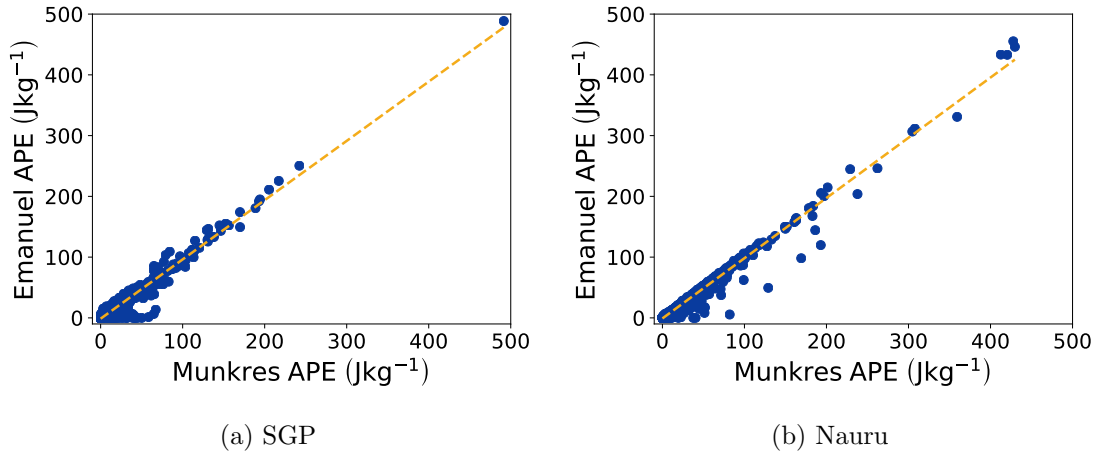


Figure 3.4: Comparison of APE calculated using the Emanuel algorithm against the exact APE calculated using the Munkres algorithm. The dashed line in each case shows the linear best fit to the data.

the sounding. Since the Emanuel algorithm assumes that the CAPE-containing boundary layer begins at the surface, these elevated instabilities are not correctly captured. This issue could be solved by designing an algorithm that varied both Δp_b and the pressure of the boundary layer bottom, although this would increase the computational expense. The main advantage of the Emanuel algorithm is that it provides greater physical insight into how APE can be converted to kinetic energy via convection, rather than relying on the physically unconstrained rearrangements of a sorting algorithm, as will be discussed further in Section 3.5.

3.5 Discussion

The results presented in Section 3.4 permit a more informed assessment of which algorithms are most suitable for the computation of APE, based on an analysis of a wider range of soundings than in previous studies. The key challenge for APE algorithms stems from the fact that APE is ultimately a residual between the positive work due to the release of CAPE minus the negative work due to compensating subsidence. As a result, sorting a vertical sounding according to decreasing density, which is the approach underlying the majority of algorithms, may occasionally result in a reference state with a larger potential energy than the actual state, if the negative work exceeds the positive work. This is in contrast to the case of a dry atmosphere, for which sorting the actual state according to potential temperature always returns the state of minimum potential energy. Without an explicit procedure to forbid it, most heuristics for computing APE are bound to return a negative value in some cases. How frequently this might occur

in practice has not been previously explored, but it is established here to be a common problem for some of the algorithms across the particular soundings analysed.

It was found that the Lorenz and top-down algorithms have nearly identical levels of accuracy, which was not anticipated. However, the results also indicate that both algorithms are so prone to returning a negative APE that they are not suited to practical application. While the accuracy of such algorithms has been questioned previously by Randall and Wang (1992) and Stansifer et al. (2017), this is the first time that their limitation is established for a wide range of real world data. These results therefore confirm that these algorithms are poorly suited to the computation of APE in practice, and hence that their use should be avoided.

The algorithm introduced by Randall and Wang (1992) was found to be a good predictor of the exact APE across the soundings studied. The relative difference between the Randall and Wang and Munkres algorithms exceeded 10% for only 2% of the soundings studied. This algorithm also benefits from the fact it is specifically designed to never return a negative APE. However, it is the most computationally expensive of the approximate algorithms; for a sounding with a small number of parcels it takes even longer to run than the Munkres algorithm (see Appendix A).

As was outlined in Section 3.4, the divide-and-conquer algorithm is the only other approximate sorting method showing reasonable accuracy over the soundings studied here. It is also the fastest of the approximate algorithms (see Appendix A). It is therefore concluded that the divide-and-conquer algorithm is the best option for the approximation of APE, since it offers a balance between accuracy and speed, as was suggested by Stansifer et al. (2017). On the other hand, the relative difference between the divide-and-conquer and Munkres algorithms is greater than 50% for 11% of the total soundings studied, and divide-and-conquer sorting may result in a negative APE. This clearly suggests that the three test cases analysed by Stansifer et al. (2017), for which the algorithm was found to perform well, might be special cases which are not sufficiently representative of the variety of situations that can be encountered in nature.

This work has also demonstrated the feasibility and good performance of an algorithm exploiting Emanuel (1994)'s theoretical expression for APE, which does not involve any form of sorting nor require discretising the vertical sounding into parcels of equal mass, and which by construction always return a positive value of APE.

So far, the implicit assumption of this chapter and many previous studies has been that it is legitimate or most useful to define the APE of a moist atmosphere in terms of

the reference state that defines the absolute minimum in potential energy, but this is not necessarily the case. For a moist atmosphere, it is possible to construct alternative sorted reference states that define only a local minimum in potential energy. Although such reference states would result in a lesser global value of APE, it is unclear why this would necessarily invalidate their use. In tropical cyclones, for instance, numerical simulations reveal that boundary layer parcels away from the eyewall may have CAPE whose release is suppressed by the subsidence in that region, as pointed out by Wong et al. (2016). Since the CAPE of such parcels can rarely if ever be released, it is unclear why it should be included in the definition of a tropical cyclone APE, as will normally be the case if the reference state defining a global potential energy minimum is selected.

From a practical viewpoint, it is important to remark that the choice of reference state affects the overall value of APE as well as its diabatic generation rate $G(\text{APE})$, but neither affects the energy conversion between APE and kinetic energy, nor the general form of the APE evolution equation, given by:

$$\frac{d\text{APE}_i}{dt} = C(\text{KE}, \text{APE}) + G(\text{APE})_i, \quad (3.5)$$

where the index i is used to indicate dependence on the reference state chosen. Equation (3.5) states that the conversion $C(\text{KE}, \text{APE})$ between kinetic energy and APE always appears as a residual between the APE storage term $d\text{APE}_i/dt$ and the APE generation rate $G(\text{APE})_i$ (see Pauluis (2007) for a discussion of how moist processes may affect the latter). From a theoretical viewpoint, Equation (3.5) represents a balance between three terms, of which the storage term is the least interesting or meaningful. For this reason, Wong et al. (2016) argued that the reference state should be chosen so as to minimise the storage term, in order to potentially make it possible to predict the APE/KE conversion from the knowledge of the APE generation rate. In this regard, Wong et al. (2016) found the use of the bottom-up sorted reference state to yield a lower storage term than the top-down sorted reference state, but more research is required to establish whether this can be regarded as a general result.

Given the computational and conceptual difficulties entailing their use, it is important to question whether sorting algorithms are really needed to study the energetics of a moist atmosphere. The idea that simpler alternatives might exist is indeed justified by the fact that some recent APE studies successfully moved away from the use of sorting algorithms by resorting to p.d.f. approaches instead, as in the case of Saenz et al. (2015), itself an extension of Tseng and Ferziger (2001), although it is unclear how such a method could

be applied to a moist atmosphere.

Also, the local theory of APE reviewed in Section 2.1.2, which was recently generalised for multi-component compressible stratified fluids by Tailleux (2018), demonstrates that it is possible to construct a local theory of APE based on an arbitrary reference state defined by a reference pressure $p_0(z, t)$ and specific volume $\alpha_0(z, t)$ in hydrostatic equilibrium. In contrast to what is often assumed, a sorting algorithm is not required to calculate the reference pressure p_r . As shown in Section 2.1.2, p_r can be simply estimated by solving the Level of Neutral Buoyancy (LNB) equation with respect to the arbitrary reference state (see Equation (2.16)). This corresponds to the use of an LNB in the Emanuel APE algorithm, demonstrating the link between the local and global approaches to APE. Approaching APE using the concept of LNBs is physically clearer than relying on heuristic sorting algorithms. The use of an arbitrary reference state in local APE theory also allows the possibility of employing a non-resting reference state, which may be more appropriate for highly symmetric flows, without the need to design a sorting algorithm that incorporates momentum constraints.

Illustrations of how to construct energy budgets in the oceans and dry atmosphere in the case where the reference density profile is defined from a horizontal or isobaric average are discussed by Tailleux (2013b) and Novak and Tailleux (2018) respectively. These recent developments, combined with the physical insights brought about by Emanuel (1994)'s theoretical expression for APE, suggest that a satisfactory theory of available potential energy for a moist atmosphere, which has been lacking so far, might be at hand provided that one moves away from sorting algorithms altogether.

Although local APE permits the use of an arbitrary balanced reference state, with each choice of reference state leading to different values of APE density and APE production efficiencies, it is not the case that these quantities will be equally physically useful for every reference state. As discussed by (Wong et al., 2016) for the case of sorted reference states, some reference states will lead to high APE storage, with the production of APE by diabatic processes being much larger than the conversion of APE to kinetic energy. It is preferable that the reference state should be chosen to minimise available energy storage, so that the production of APE directly leads to the generation of kinetic energy; otherwise, the advantage of using APE over a less complicated framework such as TPE becomes unclear. However, there has so far been no suggested approach for choosing a reference state that fulfils this criterion.

The remaining chapters of this thesis will therefore be concerned with applying local

APE theory to a moist atmosphere, using an idealised tropical cyclone as an example case. As the first complete budget of local APE for any moist atmospheric application, this will provide a concrete example that allows fundamental theoretical issues regarding local APE to be addressed, such as the existence of multiple LNBS and the optimal choice of reference state, in addition to advancing the understanding of tropical cyclone energetics.

Chapter 4:

Model setup

The axisymmetric tropical cyclone model of Rotunno and Emanuel (1987) (hereafter RE87) is a non-hydrostatic model designed for studying the prototypical TC intensification problem, in which an existing vortex intensifies over a warm sea surface with no disturbance by a synoptic environment. This model will be used in the remaining chapters of the thesis to investigate the local available energetics of TCs.

More advanced axisymmetric TC models are available, but the simplicity of the RE87 model is key to enabling the development of a closed APE budget that accounts for the diabatic generation of APE by all modelled processes. The axisymmetric setup of Cloud Model 1 (CM1, detailed by Bryan and Rotunno (2009b)) uses more accurate numerical methods, allows the use of a fully mass- and energy-conserving equation set under reversible saturated conditions, and includes a boundary layer scheme and the effect of dissipative heating. However, its more complicated thermodynamics mean that it would be extremely challenging to construct a budget of a conserved variable such as moist entropy, which would be required for a complete APE budget.

Another axisymmetric TC model, ASPECH (Axisymmetric Simplified Pseudoadiabatic Entropy Conserving Hurricane), was designed by Tang and Emanuel (2012) with the aims of conserving mass, entropy and energy without compromising the convenient simplicity of the RE87 model. In this case, the issue with constructing an APE budget arises from ASPECH's use of pseudoadiabatic entropy as its conserved entropy variable. Local APE theory can be applied to the moist atmosphere using reversible thermodynamics as described in Section 2.1.2 (conserving moist entropy and total specific humidity), but it is not clear how to apply it for pseudoadiabatic thermodynamics. It is not possible to compute a moist parcel's lifted buoyancy profile using only one conserved variable (unless saturation is assumed everywhere), and if liquid water is removed from the parcel during

lifting there is no second conserved variable to take on the role played by the total specific humidity in the reversible case.

The simple model of RE87 is therefore the best starting point for designing and analysing a budget of moist APE density. The version of the model used here has been modified by Craig (1995, 1996) to include ice-phase microphysics and a closed radial boundary. Henceforth, this modified version of the RE87 model will be referred to as “the axisymmetric model”, or simply “the model”. The method used to construct the APE budget for the axisymmetric model will be described in Chapter 5.

In this chapter, the structure and setup of the model are detailed. First, the equation set solved by the model is presented, then the configurations used for the experiments in this thesis are described, including the resolution, domain size and initial conditions. The finite difference scheme used by the model is also outlined, since understanding this is important for the construction of closed energy budgets; this section includes details of a correction made to the advection scheme to improve conservation. Finally, the structure and evolution of a TC produced by the model are examined, to provide context for the energetics analysed in the following chapters.

4.1 Domain and resolution

The model domain is two-dimensional, representing a radial-vertical cross-section through a TC—since the model is axisymmetric, there is no variation in the azimuthal direction. The radial coordinate will be denoted by r , and the vertical coordinate by z .

The axisymmetric model is run at a radial resolution of $\Delta r = 2.5$ km and a vertical resolution of $\Delta z = 625$ m. This resolution is high enough to permit convection, so that the conversion of available potential energy into kinetic energy via convection can be studied without the need to consider a convective parameterisation. A cloud band in a TC has a typical width scale of tens of kilometres (Emanuel, 2003), so these features can be represented by the model. The resolution is easily sufficient to capture TC intensification, although a higher resolution could represent some processes with higher fidelity. For example, Bryan and Rotunno (2009b) note that the boundary layer may be artificially deep in axisymmetric simulations with $\Delta z \geq 500$ m. The resolution is not increased any further due to the high computational expense of APE diagnostics.

The domain is 22.5 km in the vertical direction, with a further 5 km of sponge layer, in which the three components of velocity are damped to absorb gravity waves, so that

these do not reflect from the upper boundary. The domain extends 3150 km in the radial direction, and the no-flux outer boundary condition of (Craig, 1996) is used. However, the original width of the outer sponge layer (450 km) was found to be insufficient to absorb radially-propagating gravity waves in some simulations, leading to cyclonic anomalies at the sponge boundary. The outer sponge layer is therefore extended to 900 km. Using these parameters, the intensification of the TC is not found to be sensitive to the radial extent of the domain.

4.2 Model equations

The axisymmetric model solves the compressible equations for nine prognostic variables: the radial, azimuthal and vertical components of velocity, u , v and w ; the perturbation of the Exner pressure from the initial sounding, $\pi = \Pi - \bar{\Pi}$; the potential temperature, θ ; and the mixing ratios of water vapour r_v , cloud liquid water r_l , liquid precipitation r_p , and ice r_i . The ice variable is intended to represent a range of particle scales, from small crystals to snow (Craig, 1996). The non-dimensionalised Exner pressure is defined by

$$\Pi = \left(\frac{p}{p_{00}} \right)^{\frac{R_d}{c_p}}, \quad (4.1)$$

where p is pressure, $p_{00} = 1000$ hPa is a constant reference pressure level, $R_d = 287$ J kg⁻¹ K⁻¹ is the specific gas constant of dry air, and $c_p = 1004.5$ J kg⁻¹ K⁻¹ is the specific heat capacity at constant pressure of dry air.

The momentum equations of the axisymmetric model are

$$\frac{Du}{Dt} - \left(f + \frac{v}{r} \right) v = -c_p \bar{\theta}_v \frac{\partial \pi}{\partial r} + D_u \quad (4.2)$$

$$\frac{Dv}{Dt} + \left(f + \frac{v}{r} \right) u = D_v \quad (4.3)$$

$$\frac{Dw}{Dt} = -c_p \bar{\theta}_v \frac{\partial \pi}{\partial z} + D_w + b, \quad (4.4)$$

where overbars denote variables in the model's initial undisturbed environment; these variables vary in the vertical direction only. The Lagrangian derivative in axisymmetric cylindrical coordinates is $\frac{D}{Dt} = \frac{\partial}{\partial t} + u \frac{\partial}{\partial r} + w \frac{\partial}{\partial z}$, and $\theta_v = \theta (1 + 0.61 r_v)$ is the virtual potential temperature. The domain is assumed to be an f -plane with Coriolis parameter $f = 6.14 \times 10^{-5}$ rad s⁻¹, corresponding to a latitude of approximately 25°N. The buoyancy

b is defined by

$$b = g \left\{ \frac{\theta - \bar{\theta}}{\bar{\theta}} + 0.61 (r_v - \bar{r}_v) - r_l - r_p - r_i \right\}, \quad (4.5)$$

where $g = 9.81 \text{ m s}^{-2}$ is gravitational acceleration.

The D_i are subgrid terms parameterising turbulent mixing based on an eddy viscosity computed at first order from the Richardson number. The scale of the mixing is set by horizontal and vertical mixing lengths. These are set to the model's default values for the chosen resolution, which are 500 m and 200 m respectively. The subgrid terms also include the effect of surface friction on the momentum; this is dependent on the momentum drag coefficient C_D , which is calculated using Deacon's formula (Roll, 1965, p. 160):

$$C_D = 1.1 \times 10^{-3} + 4 \times 10^{-5} \sqrt{u^2 + v^2} \Big|_{\Delta z/2}. \quad (4.6)$$

Heating due to frictional dissipation is not included in the model, and there is no boundary layer scheme.

The equations for the evolution of the potential temperature and mixing ratios are

$$\frac{D\theta}{Dt} = M_\theta + D_\theta + R, \quad (4.7)$$

$$\frac{Dr_v}{Dt} = M_{r_v} + D_{r_v}, \quad (4.8)$$

$$\frac{Dr_l}{Dt} = M_{r_l} + D_{r_l}, \quad (4.9)$$

$$\frac{Dr_p}{Dt} = M_{r_p} + D_{r_p} + P_{r_p}, \quad (4.10)$$

$$\frac{Dr_i}{Dt} = M_{r_i} + D_{r_i} + P_{r_i}. \quad (4.11)$$

R is a radiative cooling tendency, for which the simple Newtonian cooling of Rotunno and Emanuel (1987) is used, rather than the more complicated parameterised radiation of Craig (1995). The cooling is capped at a rate of 2 K d^{-1} , as suggested by Tang and Emanuel (2012) on the grounds that radiative cooling does not exceed this limit in clear-sky tropical conditions (Hartmann et al., 2001).

As in the momentum equations, the D_i terms are parameterisations of subgrid turbulence. In the cases of θ and r_v , these terms include surface fluxes defined by

$$F_\theta = C_T \sqrt{u^2 + v^2} \Big|_{\Delta z/2} \left(\theta_{\text{surf}} - \theta \Big|_{\Delta z/2} \right), \quad (4.12)$$

$$F_{r_v} = C_E \sqrt{u^2 + v^2} \Big|_{\Delta z/2} \left(r_{v_{\text{surf}}} - r_v \Big|_{\Delta z/2} \right), \quad (4.13)$$

with surface heat flux and evaporation coefficients $C_T = 1 \times 10^{-3}$, $C_E = 1.2 \times 10^{-3}$ as in Craig and Gray (1996). Variables with a subscript ‘surf’ are evaluated at the sea surface, $z = 0$ m, assuming saturation.

The M_i terms in Equations (4.7)–(4.11) represent the effects of changes resulting from the microphysics scheme (other than fluxes due to precipitation). This covers: the condensation and evaporation of cloud liquid water; the nucleation, deposition and riming of cloud liquid water to ice; the capture of rain water by ice species and the melting of ice to rain water; the autoconversion and accretion of cloud liquid water to rain water; the re-evaporation of rain water; the evaporation of melting snow; and sublimation and nucleation of water vapour to ice. P_{r_p} and P_{r_i} are the net sources of mass from falling rain and ice respectively. Further details of the microphysics scheme can be found in Golding (1993); Figure 4.1 provides a schematic of the processes affecting water and ice species.

Finally, the model’s equation for the conservation of mass is

$$\frac{\partial \pi}{\partial t} = -\frac{\bar{c}^2}{c_p \bar{\rho} \bar{\theta}_v^2} \nabla \cdot (\bar{\rho} \bar{\theta}_v \mathbf{v}) + \frac{\bar{c}^2}{c_p \bar{\theta}_v^2} \frac{D\theta_v}{Dt}, \quad (4.14)$$

where $\mathbf{v} = (u, v, w)$ and the divergence operator in axisymmetric cylindrical coordinates is given by $\nabla \cdot \psi = \frac{1}{r} \frac{\partial(r\psi)}{\partial r} + \frac{\partial\psi}{\partial z}$. The speed of sound in the initial model state is defined by

$$\bar{c}^2 = \frac{c_p R_d \bar{\Pi} \bar{\theta}_v}{c_v}, \quad (4.15)$$

where $c_v = 717.5 \text{ J kg}^{-1} \text{ K}^{-1}$ is the specific heat capacity at constant volume of dry air.

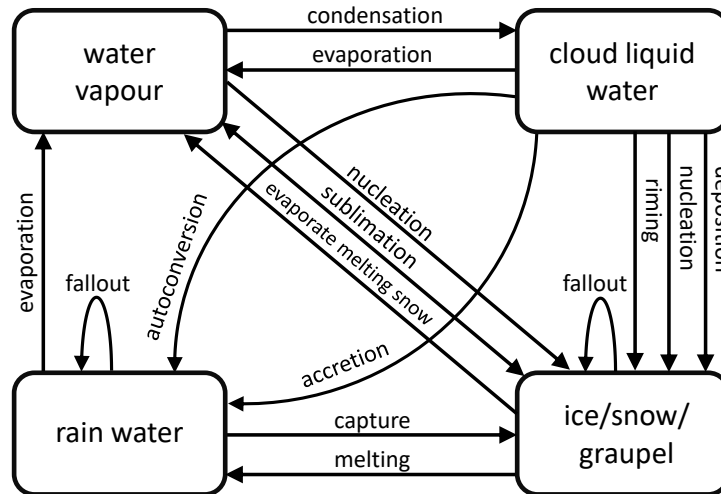


Figure 4.1: Processes affecting water species in the microphysics scheme of the axisymmetric model.

Equation (4.14) does not exactly conserve mass; it is an approximation to the full equation for $\frac{D\Pi}{Dt}$ derived by Klemp and Wilhelmson (1978). The term proportional to $\frac{D\theta_v}{Dt}$ appears in this full derivation, but was neglected in the original RE87 model. It has been re-included here to prevent the strong diabatic heating in the eyewall leading to a large mass sink, as documented by Tang (2010).

4.3 Initial conditions

There are two main initial conditions that can be varied in the axisymmetric model: the sea surface temperature (SST), which is constant throughout a model run, and the initialisation sounding, which defines the quiescent environment to which a vortex is introduced. Model runs with six different sets of initial conditions were performed.

The initialisation sounding used is either the Jordan mean hurricane-season sounding for the West Indies (Jordan, 1958), or the neutral sounding created by Rotunno and Emanuel (1987)¹. The neutral sounding is a modified version of the Jordan sounding, which is designed to be neutral to moist convection in the axisymmetric model for an SST of 26.3°C (whereas the Jordan sounding contains approximately 700 J kg⁻¹ of CAPE). When the neutral sounding is used with an SST of 26.3°C, the TC cannot obtain energy from the release of environmental CAPE; this was used by Rotunno and Emanuel (1987) to demonstrate that environmental CAPE is not necessary for intensification to take place.

The profiles $\bar{\theta}$ and \bar{r}_v are specified by linearly interpolating the soundings to the model's vertical levels, and $\bar{\Pi}$ is determined from these by assuming a surface pressure of 1015.1 hPa and integrating the hydrostatic balance equation upwards.

The two initialisation soundings are shown on the tephigram in Figure 4.2. The neutral sounding is colder and drier than the Jordan sounding at the lowest level ($z = \frac{\Delta z}{2}$), but then slightly warmer and moister through the rest of the lower troposphere. It is also characterised by a drier layer between 300 and 500 hPa.

The SST is set to either 26.3°C, 28.3°C or 30.3°C. Model runs will be referred to throughout the thesis using the notation J26.3 (for example), where the letter denotes the initialisation sounding (J=Jordan, N=neutral) and the number indicates the SST.

The soundings are not adjusted to the SST. This approach is chosen so that the model runs with warmer SST will possess higher values of environmental CAPE, to permit the identification of differences in energetics between simulations with differing environmental

¹http://www2.mmm.ucar.edu/people/bryan/cm1/soundings/input_sounding_rotunno_emanuel

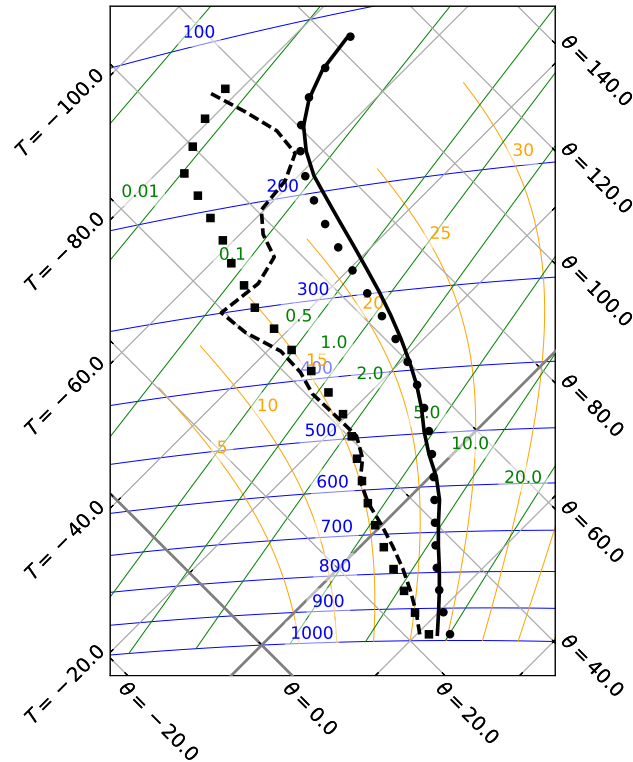


Figure 4.2: Tephigram of soundings used to initialise axisymmetric model. Grey diagonal lines are isotherms (constant temperature T) and dry adiabats (constant dry potential temperature θ) as labelled (both in $^{\circ}\text{C}$). The thicker grey lines mark the isotherm $T = 0^{\circ}\text{C}$ and the dry adiabat $\theta = 0^{\circ}\text{C}$. Blue lines are isobars, labelled in hPa. Green lines are lines of constant saturation mixing ratio, labelled in g kg^{-1} . Orange curves show moist adiabats, labelled by their value of equivalent potential temperature θ_e in $^{\circ}\text{C}$. The black circles show the temperature profile of the Jordan mean hurricane-season sounding and the black squares show the dewpoint temperature of the same sounding. The solid black line shows the temperature profile of the neutral sounding, and the dashed black line shows the neutral dewpoint temperature profile.

CAPE. The Jordan and neutral soundings are commonly used in TC simulations with SSTs above the observed value of surface air temperature of 26.3°C (Hausman, 2001; Persing and Montgomery, 2003, 2005; Montgomery et al., 2009; Rousseau-Rizzi and Emanuel, 2019), since the SST is expected to routinely be $1\text{--}2^{\circ}\text{C}$ warmer than the ambient surface air temperature in TCs (Riehl, 1954). The influence of environmental CAPE on TC development is an area of ongoing research. Rotunno and Emanuel (1987) showed that CAPE is not necessary for intensification to take place, and Persing and Montgomery (2005) found that changing the environmental CAPE had little effect on the maximum intensity obtained by numerical simulations provided the SST and outflow temperature remained similar. However, Lee and Frisius (2018) showed that the intensification rate of TCs increased for higher environmental CAPE. Increasing the SST for a fixed environmental sounding provides a simple method of increasing the environmental CAPE, as

was done by Persing and Montgomery (2005).

For the purposes of illustrating the TC model output, the rest of this chapter focuses on the J30.3 model run. This run is chosen because it will prove particularly useful for the investigation of available energetics in Chapter 5. These initial conditions provide a plentiful supply of energy, since the SST is high and there is environmental CAPE available. This results in a larger and more intense TC than in runs with a lower energy supply, but the basic TC structure and evolution are the same for all runs. In cases where results or conclusions do not apply to all six model runs, this will be specifically noted.

The initial vortex is prescribed using azimuthal winds of the form

$$v(r, z) = F(r) \begin{cases} \left(1 - \frac{z}{z_t}\right) & \text{if } z \leq z_t \\ \frac{z_{\text{sponge}}}{z_t} \left(1 - \frac{z}{z_{\text{sponge}}}\right) \left(\frac{z_t - z}{z_{\text{sponge}} - z_t}\right) & \text{if } z > z_t, \end{cases} \quad (4.16)$$

where

$$F(r) = v_{\text{max}} \frac{2 \frac{r}{r_{\text{max}}}}{1 + \left(\frac{r}{r_{\text{max}}}\right)^2}, \quad (4.17)$$

following (Emanuel and Rotunno, 1989). The maximum prescribed wind is $v_{\text{max}} = 12 \text{ m s}^{-1}$, occurring at radius $r_{\text{max}} = 75 \text{ km}$. The wind decreases linearly with height until it reaches zero at the tropopause, $z_t = 15 \text{ km}$, and then becomes weakly anticyclonic before increasing back to zero at the edge of the vertical sponge layer, $z_{\text{sponge}} = 22.5 \text{ km}$.

The initial thermodynamic fields are adjusted to the vortex by integrating the Exner pressure inwards to gradient wind balance, and then integrating the potential temperature upwards to hydrostatic balance. Figure 4.3 shows the perturbations of v, Π, θ and temperature T in the initial vortex from the quiescent environment. The adjustment results in a warm-core cyclone with a minimum near-surface pressure perturbation of -7.7 hPa compared to the environmental sounding, and a weak, cold anticyclone aloft.

4.4 Model numerics

The axisymmetric model uses a split-explicit finite difference method to advance its equation set, based on the non-hydrostatic cloud model of Klemp and Wilhelmson (1978). The equations outlined in Section 4.2 permit fast-propagating sound waves, which necessitate the use of a very small time step to ensure stability. To maintain efficiency, the equations for u, w and π are integrated using a shorter time step than the equations for v, θ and r_j , for which the sound waves are not of physical interest. The long time step

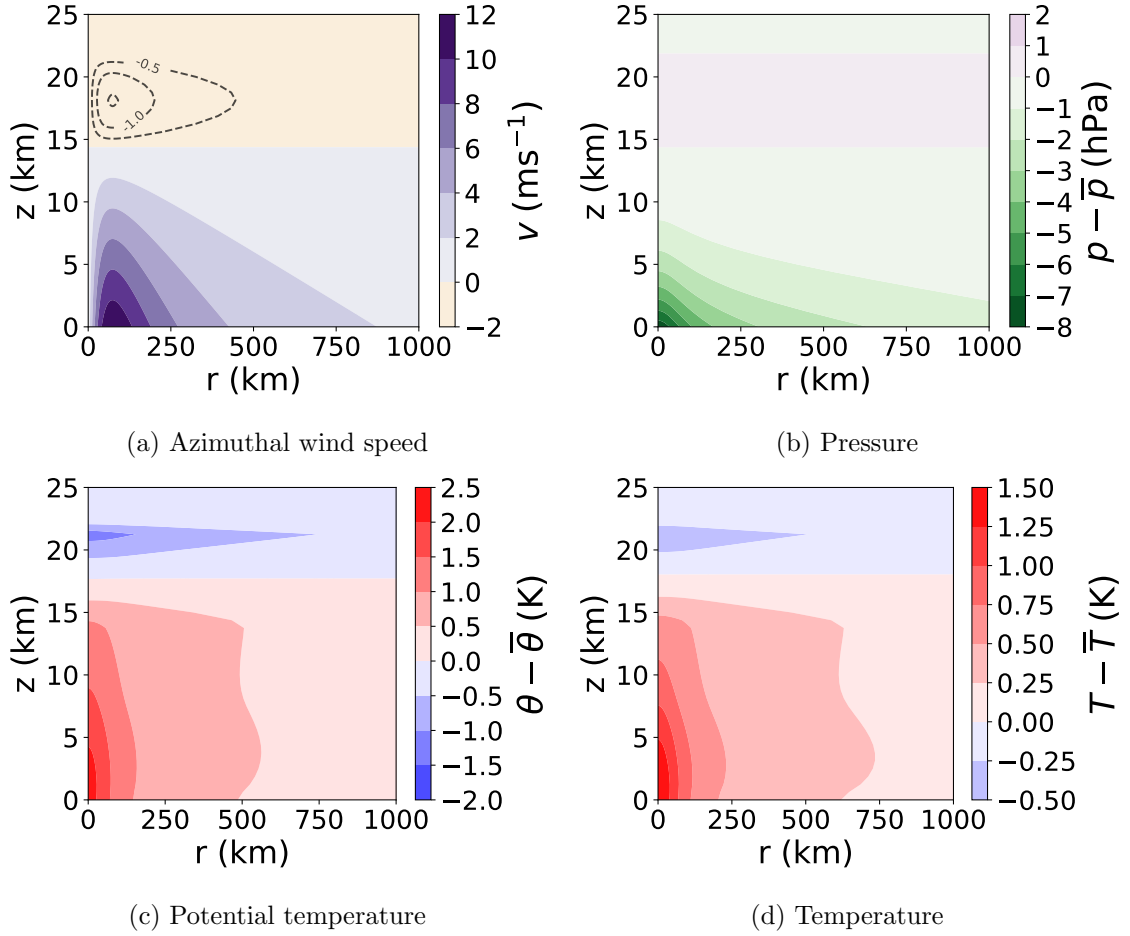


Figure 4.3: Perturbations of initial vortex from quiescent Jordan hurricane-season mean environment. Dashed contours in (a) indicate 0.5 m s^{-1} intervals in the weak upper-level anticyclonic flow, which are not captured by the colour scheme.

is $\Delta t = 6 \text{ s}$, while the short time step is $\Delta t_s = 0.6 \text{ s}$. The small time steps are integrated forward using a semi-implicit scheme, while a second-order leapfrog scheme is used for the long time step. For the purposes of the energy budgets in subsequent chapters, it is found to be sufficient to consider only the long time step, and therefore this section will focus on the discretisations of the leapfrog scheme and advection terms, which are computed on the longer timescale.

The leapfrog scheme discretises an equation of the form

$$\frac{\partial \psi}{\partial t} = f_\psi \quad (4.18)$$

as

$$\delta_t(\bar{\psi}^t) = \frac{\psi(t + \Delta t) - \psi(t - \Delta t)}{2\Delta t} = f_\psi, \quad (4.19)$$

where the overbar and delta operators are defined by

$$\overline{\psi}^x = \frac{\psi\left(x + \frac{\Delta x}{2}\right) + \psi\left(x - \frac{\Delta x}{2}\right)}{2}, \quad (4.20)$$

$$\delta_x \psi = \frac{\psi\left(x + \frac{\Delta x}{2}\right) - \psi\left(x - \frac{\Delta x}{2}\right)}{\Delta x} \quad (4.21)$$

for a variable ψ and dimension x . The discrete averaging operator denoted here by an overbar should not be confused with the overbar used to denote variables in the model's initial sounding; the averaging operator will always be paired with a superscript denoting the dimension along which the average is being taken.

Whilst the leapfrog scheme is advantageous because it does not require multiple computations at each time step, it can lead to spurious oscillations between odd and even time steps (Lilly, 1965). To suppress this behaviour, a Robert filter is used to smooth the solution in time (Robert, 1966). More details on the filter are given by Klemp and Wilhelmson (1978), but its contribution to the model's energy budgets is found to be negligible, so its effects are not considered any further here.

The model is structured on a staggered grid, with all three components of velocity computed at different grid points. The grid is illustrated in Figure 4.4. All other prognostic variables are computed at v -points. At the inner and outer radial boundaries it is assumed that $u = 0$, and at the top and bottom boundaries that $w = 0$.

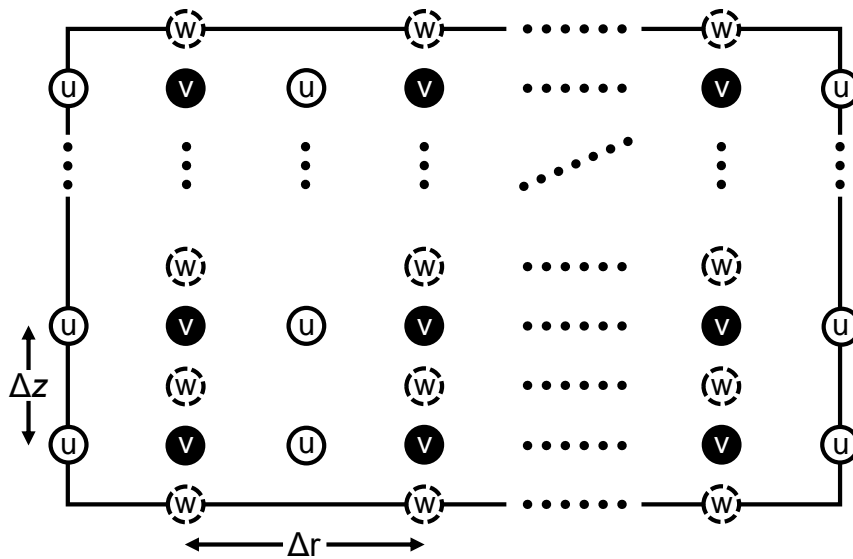


Figure 4.4: Axisymmetric model grid structure. The solid black rectangle marks the boundaries of the domain. The components u , v and w of the velocity are computed at the labelled grid points. All thermodynamic variables (e.g. θ , r_v , Π) are computed at the same locations as v . Dots show where the grid pattern repeats.

The second-order advection scheme is designed following Lilly (1964). In axisymmetric cylindrical coordinates, the advection operator is

$$\mathbf{v} \cdot \nabla = u \frac{\partial}{\partial r} + w \frac{\partial}{\partial z}. \quad (4.22)$$

Using the discrete grid operators defined in Equations (4.20) and (4.21), the advection of variables at each of the three different grid points is discretised as

$$\mathbf{v} \cdot \nabla \psi \longrightarrow \begin{cases} \frac{1}{r} \overline{r u}^r \delta_r \psi^r + \frac{1}{\overline{\rho r}} \overline{\rho r w}^z \delta_z \psi^z & \text{if } \psi \text{ at } u\text{-points} \\ \frac{1}{r} \overline{r u} \delta_r \psi^r + \frac{1}{\overline{\rho}} \overline{\rho w} \delta_z \psi^z & \text{if } \psi \text{ at } v\text{-points} \\ \frac{1}{\overline{\rho}} \overline{\rho u}^z \delta_r \psi^r + \frac{1}{\overline{\rho}} \overline{\rho w}^z \delta_z \psi^z & \text{if } \psi \text{ at } w\text{-points.} \end{cases} \quad (4.23)$$

This advection scheme is claimed by RE87 to be conservative. It can be verified that the advection scheme is conservative for u - and v -points (conserving $\overline{\rho\psi}$) for an anelastic system with continuity equation

$$\nabla \cdot (\overline{\rho\mathbf{v}}) = 0 \quad (4.24)$$

assumed (this condition is approximately satisfied in the axisymmetric model). However, $\overline{\rho\psi}$ is not conserved if ψ is a w -grid variable, even for the anelastic case. The following explains why advection on the u - and v -grids is conservative and demonstrates why advection on the w -grid is not. A new form for the w -grid advection is then developed, which is conservative for the anelastic case. This new advection operator will be implemented in all runs of the model used in the thesis; this was necessary in order to provide a finite difference representation that could be manipulated to obtain the correct energy budgets required for the work in Chapter 5.

Denoting by ψ^v some variable defined on the model's v -grid, and assuming that ψ^v is affected only by advection (i.e. it is a passive tracer), the evolution equation of ψ^v is

$$\frac{\partial \psi^v}{\partial t} = \mathbf{v} \cdot \nabla \psi^v. \quad (4.25)$$

The conservation of $\overline{\rho\psi^v}$ by advection requires that

$$\frac{\partial (\overline{\rho\psi^v})}{\partial t} = \overline{\rho\mathbf{v}} \cdot \nabla \psi^v = \nabla \cdot \mathbf{F}_{\psi^v}, \quad (4.26)$$

where $\mathbf{F}_{\psi^v} = \overline{\rho\psi^v}\mathbf{v}$ is the flux of ψ^v , and the fact that $\overline{\rho}$ is independent of time has been used. Hence when integrated over a volume of the model domain V , the divergence

theorem shows that the only change to the total $\bar{\rho}\psi^v$ is due to fluxes through the volume's surface $S(V)$:

$$\iiint_V (\nabla \cdot \mathbf{F}_{\psi^v}) dV = \oiint_{S(V)} (\mathbf{F}_{\psi^v} \cdot \hat{\mathbf{n}}) dS, \quad (4.27)$$

where $\hat{\mathbf{n}}$ is the outward unit normal vector to S .

The finite-difference form of the advection of ψ^v , according to Equation (4.23), is

$$\frac{\partial (\bar{\rho}\psi^v)}{\partial t} = \bar{\rho}\mathbf{v} \cdot \nabla\psi^v \longrightarrow \frac{\bar{\rho}}{r} \overline{ru\psi^{vr}} + \overline{\rho w \delta_z \psi^{vz}}. \quad (4.28)$$

Employing the identity

$$\varphi \delta_x \psi = \delta_x (\overline{\varphi^x} \psi) - \overline{\psi \delta_x \varphi^x}, \quad (4.29)$$

adapted from Lilly (1964), and noting that $\bar{\rho}$ does not vary in the radial direction, Equation (4.28) can be rewritten in the form

$$\frac{\partial (\bar{\rho}\psi^v)}{\partial t} \longrightarrow \frac{1}{r} \delta_r (\overline{\rho r u \psi^{vr}}) + \delta_z (\overline{\rho w \psi^{vz}}) - v \left[\frac{1}{r} \delta_r (\overline{\rho r u}) + \delta_z (\overline{\rho w}) \right]. \quad (4.30)$$

The first two terms on the RHS of Equation (4.30) are of the form $\nabla \cdot \mathbf{F}_{\psi^v}$; it can be verified that their volume integral reduces to a boundary flux by multiplying by $2\pi r \Delta r \Delta z$ (the volume of a grid box in axisymmetric cylindrical coordinates) and taking the sum over indices in the r - and z - directions. The final two terms on the RHS of (4.30) correspond to the continuity equation (4.24) and so

$$\frac{1}{r} \delta_r (\overline{\rho r u}) + \delta_z (\overline{\rho w}) = 0. \quad (4.31)$$

Therefore the only changes in the volume integral of $\bar{\rho}\psi^v$ are due to fluxes through the volume boundary. It should be noted that the continuity condition is not actually enforced in the model (since the model is compressible rather than anelastic), and therefore in practice the advection will not be strictly conservative, but the continuity equation does approximately hold.

Similarly, the advection of a variable ψ^u defined on the model's u -grid may be shown to be conservative using a form of the continuity equation obtained by multiplying Equation (4.31) by r and averaging in the r direction:

$$\delta_r (\overline{\rho r u^r}) + \delta_z (\overline{\rho r w^r}) = 0. \quad (4.32)$$

In the case of a variable ψ^w defined on the w -grid, the equivalent expression to Equation (4.30) is

$$\frac{\partial (\bar{\rho}\psi^w)}{\partial t} \longrightarrow \delta_r \left(\overline{\bar{\rho}u^z\psi^r} \right) + \delta_z \left(\overline{\bar{\rho}w^z\psi^z} \right) - \psi^w \left[\delta_r \left(\overline{\bar{\rho}u^z} \right) + \delta_z \left(\overline{\bar{\rho}w^z} \right) \right]. \quad (4.33)$$

This shows that the advection of ψ^w is not conservative: the first term on the RHS will not reduce to a boundary flux when the volume integral is taken, since the factor r in the integral will prevent interior terms from cancelling. Additionally, the terms inside the square brackets, which should correspond to a discretisation of the continuity equation, cannot be derived from Equation (4.31).

These problems can be resolved by introducing a weighted radial average into the first term in the expression for w -grid advection, so that the finite-difference advection operator becomes

$$\mathbf{v} \cdot \nabla \psi \longrightarrow \begin{cases} \frac{1}{r} \overline{\bar{r}u^r} \delta_r \psi^r + \frac{1}{\bar{\rho}r} \overline{\bar{\rho}rw^r} \delta_z \psi^z & \text{if } \psi \text{ at } u\text{-points} \\ \frac{1}{r} ru \delta_r \psi^r + \frac{1}{\bar{\rho}} \bar{\rho} w \delta_z \psi^z & \text{if } \psi \text{ at } v\text{-points} \\ \frac{1}{\bar{\rho}r} \overline{\bar{\rho}ru^z} \delta_r \psi^r + \frac{1}{\bar{\rho}} \overline{\bar{\rho}w^z} \delta_z \psi^z & \text{if } \psi \text{ at } w\text{-points.} \end{cases} \quad (4.34)$$

With the new expression, w -grid advection is conservative for an anelastic system, following

$$\frac{\partial (\bar{\rho}\psi^w)}{\partial t} \longrightarrow \frac{1}{r} \delta_r \left(\overline{\bar{\rho}ru^z\psi^r} \right) + \delta_z \left(\overline{\bar{\rho}w^z\psi^z} \right) - \psi^w \left[\frac{1}{r} \delta_r \left(\overline{\bar{\rho}ru^z} \right) + \delta_z \left(\overline{\bar{\rho}w^z} \right) \right]. \quad (4.35)$$

The continuity equation required for the terms in the square brackets here to be zero can be easily derived by averaging Equation (4.31) in the vertical direction to obtain

$$\frac{1}{r} \delta_r \left(\overline{\bar{\rho}ru^z} \right) + \delta_z \left(\overline{\bar{\rho}w^z} \right) = 0. \quad (4.36)$$

Figure 4.5 compares the intensity of the TC simulated by the original, non-conservative advection scheme with the intensity when the advection scheme is corrected. With the corrected advection scheme, the onset of the fastest intensification is delayed, but the general characteristics of the intensity evolution (a period of rapid intensification followed by a roughly steady maximum wind speed, with a decline in v_{\max} after 150 h) remain unchanged. The maximum azimuthal wind speed at any time is 73.3 m s^{-1} with the original advection scheme, compared to 76.4 m s^{-1} using the corrected scheme, an increase of 4.2%. The minimum surface pressure is also sensitive to the change in advection scheme,

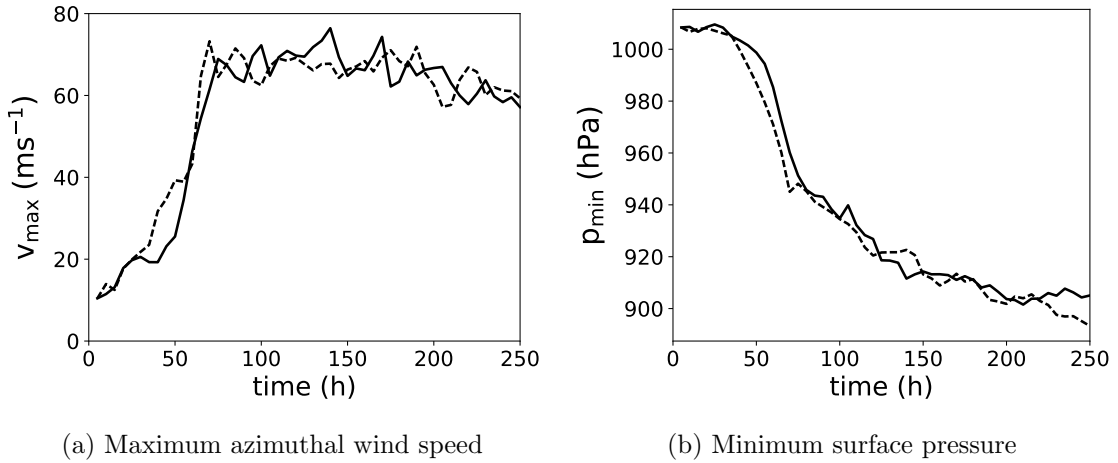


Figure 4.5: Intensity of tropical cyclone in axisymmetric model using the original and corrected advection schemes for the w -grid. Dashed lines show intensity using original advection scheme from Equation (4.23). Solid lines show intensity using corrected advection scheme given in Equation (4.34).

increasing from 893.3 hPa to 901.5 hPa. The conservative version of the advection scheme allows the model to reach a steady state in terms of p_{\min} in this case. Further study would be required to ascertain whether correcting the advection scheme has a significant effect on the intensity of the TCs produced by the axisymmetric model—this result suggests it might exacerbate the model’s known positive v_{\max} bias (Bryan and Rotunno, 2009b)—but for the purposes of this thesis, the importance of the correction is that it permits the computation of energy budgets without spurious terms arising from errors in momentum conservation.

4.5 Tropical cyclone characteristics

An overview of the tropical cyclone produced by the J30.3 axisymmetric model run described in the preceding sections is now provided, to describe its basic characteristics and verify that its TPE-based energetics conform to the expectations described in Chapter 2.

Firstly, the intensity of the TC in terms of both maximum azimuthal wind speed v_{\max} and minimum surface pressure p_{\min} is shown in Figure 4.6. The maximum wind speed typically occurs in the second vertical level of the model, since surface friction acts to reduce the speed in the lowest level. The values of intensity are identical to those presented in Figure 4.5 when comparing the advection schemes, but are reproduced here for clarity.

The initial stages of intensification are relatively slow, with v_{\max} increasing from

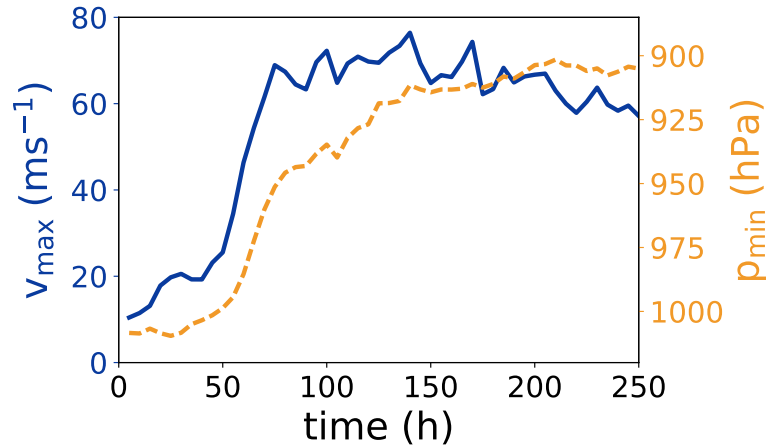


Figure 4.6: Intensity of the TC produced by the axisymmetric model, in terms of maximum azimuthal wind speed (blue solid line) and minimum surface pressure (orange dashed line).

10.4 m s^{-1} to 19.3 m s^{-1} over the period from 5 to 40 h; the pressure only decreases by 5.0 hPa during this time, reaching a minimum of 1003.4 hPa. This slow development is followed by a period of rapid intensification (RI) from 40 to 75 h; v_{max} increases by 49.7 m s^{-1} over this 35 h, easily exceeding the 15 m s^{-1} increase in 24 h by which RI is usually defined (Kaplan et al., 2010; Lee et al., 2016). This RI period is also marked by a fast deepening of the central pressure.

After 75 h, v_{max} increases slowly to its maximum value of 76.4 m s^{-1} (equivalent to a Category 5 hurricane on the Saffir-Simpson scale) at 140 h, then declines for the rest of the simulation. The central pressure decreases until it becomes approximately steady, with an average value of 904.6 hPa over the final 50 h of the simulation.

The character of the intensification is clarified by inspecting a Hovmöller plot of the maximum azimuthal wind speed v_{max} . In Figure 4.7, the maximum of v is taken over all vertical levels for each grid radius at each time step (only the inner 500 km are shown). The rapid intensification of the TC is associated with the contraction of the radius of maximum wind (RMW); as a surface of fixed angular momentum $M = rv + \frac{fr^2}{2}$ contracts, r decreases and so v correspondingly increases. Once this initial contraction is complete (at around 70 h), the rapid intensification ceases. After 100 h, the TC begins to undergo eyewall replacement cycles (ERCs): high winds associated with a region of convection occur at a larger radius than the existing eyewall, and this outer M surface contracts until it replaces the old, inner eyewall. These replacements are associated with an additional increase in intensity between 100 and 140 h. After 150 h, the RMW grows with each eyewall replacement, and this is associated with a larger but weaker TC.

The other model runs all exhibit the same contraction of the RMW at the time of

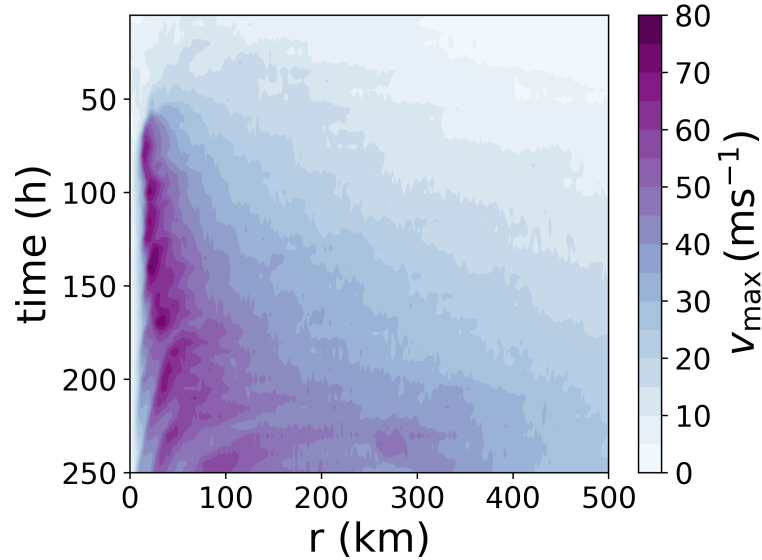


Figure 4.7: Hovmöller plot of the maximum azimuthal wind speed v_{\max} at each grid radius over time, for radii within 500 km of the TC centre. Coloured contour levels are spaced every 5 m s^{-1} .

intensification onset, but the runs with $\text{SST} = 26.3^\circ\text{C}$ remain approximately constant in size after reaching maturity and do not undergo any identifiable ERCs. This may be because less energy is supplied to these TCs, or because they are smaller and therefore there are not sufficient grid points near the inner core to resolve ERCs.

To explore the structure of the TC further, Figure 4.8 shows the azimuthal wind field v at 100 h, when the RI phase of the TC’s development is complete. Figure 4.8a covers the inner 2000 km of the domain, showing that as well as intensifying the cyclonic circulation near the centre, the model develops a strong upper-level anticyclonic circulation, which moves outwards and downwards from its position in the initial vortex (Figure 4.3a).

Figure 4.8b focuses on the central 250 km of the domain to show the structure of the cyclone more clearly. The cyclonic wind speeds increase as r decreases until reaching a maximum at the eyewall, at approximately 25 km. The model maintains a quiescent eye inwards of the eyewall.

The modelled TC’s radial wind u at 100 h is plotted in Figure 4.9. There is a clear structure of low-level inflow and upper-level outflow. The upper-level branch of the radial flow extends over a greater depth than the low-level inflow; since the density of the upper-level air is lower, a more extensive outflow is required for the upper-level mass export to match the mass import at low levels, given that the magnitudes of the radial wind speeds in the two branches are similar. The model’s circulation is as expected from observations of the axisymmetric structure of TCs (e.g. Hawkins and Rubsam, 1968).

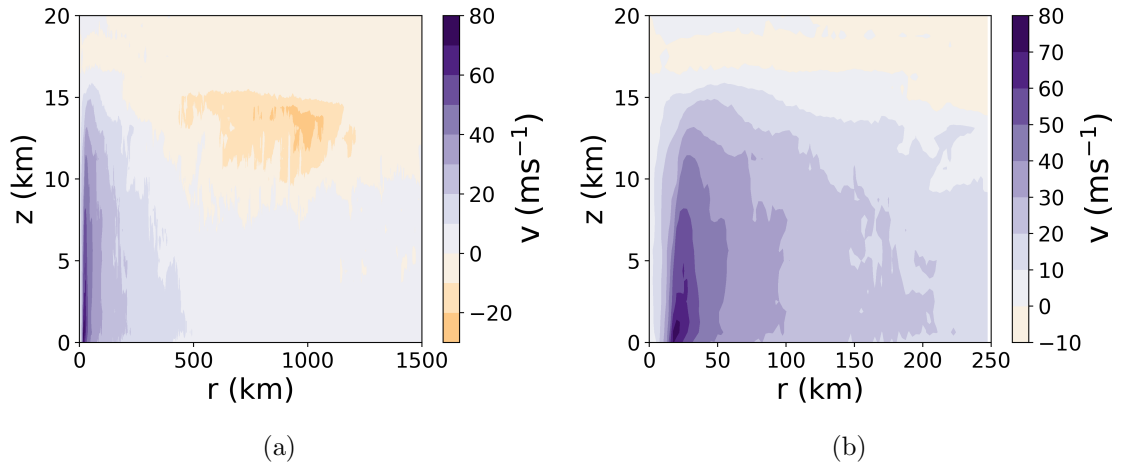


Figure 4.8: Azimuthal wind v of the axisymmetric TC at 100 h, in the inner (a) 2000 km and (b) 250 km of the domain. Coloured contour levels are spaced every 10 m s^{-1} . Purple shading corresponds to positive v (cyclonic flow), while orange shading corresponds to negative v (anticyclonic flow).

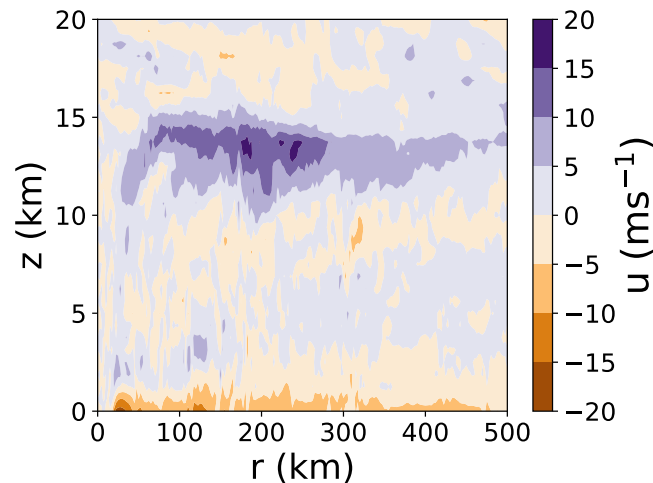


Figure 4.9: Radial wind u in the axisymmetric model at 100 h. Coloured contour levels are spaced every 5 m s^{-1} . Purple shading corresponds to positive u (outflow), while orange shading corresponds to negative u (inflow).

Since subsequent chapters will seek to compare the available energetics of TCs with the energetics as defined by TPE, the final part of this chapter verifies that the modelled TC exhibits the TPE-related features expected from Section 2.2.1. The TC should be a net exporter of TPE, and should have an overall TPE efficiency on the order of 2%.

Figure 4.10 shows the flux of TPE across the cylindrical surface $r = 300 \text{ km}$ for all vertical v -levels at 200 h, computing TPE as $\bar{\rho}(c_p T + gz) = \bar{\rho}(c_p \theta \Pi + gz)$. TPE is imported into the $r < 300 \text{ km}$ region in the low-level inflow, and exported in the middle to upper troposphere. Overall, TPE is exported from the TC by its secondary circulation, as expected. The runs with the six sets of initial conditions all exhibit a net export of

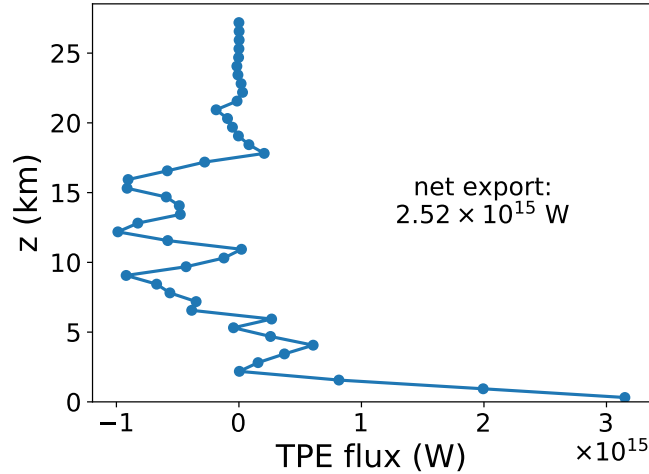


Figure 4.10: Flux of TPE across the $r = 300$ km surface at 200 h. Blue circles indicate the v -grid vertical levels, at which the flux is calculated. Positive values correspond to an influx of TPE to the inner region at that vertical level, while negative values correspond to an outward flux.

TPE from the TC in the mature stage, with an import in the low-level inflow and an export in the outflow. The J26.3 and N26.3 runs also have an additional layer of TPE import just below the outflow.

The diagnosed TPE efficiency of the inner 300 km of the TC is shown in Figure 4.11; the result is not particularly sensitive to the region chosen. This is computed following the method of Hogsett and Zhang (2009): the kinetic energy generation $-u \frac{\partial p}{\partial r}$ is integrated over the region, then divided by the integral of the change in latent energy due to latent heat release by condensation. The resulting efficiency is of a similar magnitude to the

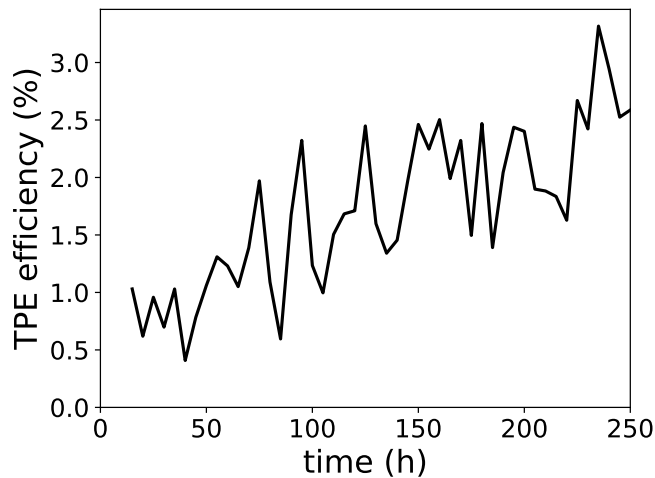


Figure 4.11: TPE efficiency of the axisymmetric model TC. Only the inner 300 km are included in the computation. Time series starts at 15 h to omit very large values of efficiency during spin-up.

TPE efficiencies computed by previous numerical and observational studies (reviewed in Section 2.2.1). There is also an increase in the TPE efficiency over time, the potential importance of which was discussed in Section 2.3.1. The TPE efficiency of each of the six runs shows a similar temporal increase, with steady state values ranging from 1% to 3% depending on the initial conditions and the region of integration.

The axisymmetric model simulates the prototypical TC intensification problem satisfactorily for the purpose of investigating the local available energetics of TC development. The results presented for the J30.3 run show that the model produces the expected primary and secondary circulations, developing a TC that intensifies rapidly to reach Category 5 hurricane wind speeds, before becoming approximately steady in terms of minimum central pressure and slowly declining in terms of maximum wind speed. The modelled TC exports TPE as expected and has a TPE efficiency in line with previously calculated values. The following chapters therefore proceed to analyse the available energetics of this TC.

Chapter 5:

Available energetics of an axisymmetric tropical cyclone

This chapter investigates the energetics of the axisymmetric TCs described in Chapter 4, using budgets of kinetic energy, available elastic energy and available potential energy. Previous energy budgets of TCs have used budgets of total potential energy or dry APE to link diabatic processes to the ultimate production of kinetic energy in the storm, but as discussed in Section 2.2, using a moist APE framework should provide a more relevant account of the energy available to the TC. All budgets in this section are computed using output from the axisymmetric model at intervals of 5 h.

Section 5.1 presents kinetic and available elastic energy budgets for the axisymmetric model. Closed budgets for these are obtained by manipulating the model's finite difference equations. Computing a budget based on local APE theory for the moist atmosphere is much more challenging, and has not previously been done. Therefore, much of Section 5.2 is dedicated to developing the methods needed to compute the moist APE budget for the axisymmetric model. This includes the investigation of a key novel result for local APE theory: APE density may be discontinuous in time and space. Once a budgeting method has been established, budgets of APE and diabatic APE production in the TC are analysed. The links between the moist APE budget and previous TC energy budgets are discussed in Section 5.3. The budgets presented are those for the J30.3 model run (see Chapter 4 for details; recall that the letter denotes either the Jordan or neutral sounding and the number is the fixed SST), since this run permits an investigation of the APE budget in the absence of discontinuity, but the results obtained for different sets of initial conditions will also be discussed.

5.1 Kinetic and available elastic energies

In this section, budgets for the azimuthal kinetic energy, the radial kinetic energy, the vertical kinetic energy, and the available elastic energy in the axisymmetric model will be derived and computed. Kinetic energy budgets have previously been computed for the axisymmetric model by Wong (2014), but the work here will improve upon these by demonstrating budget closure and including available elastic energy, which allows the conversion of APE to kinetic energy to be fully linked with the ultimate power dissipation by the TC. In this section the conversion between APE and kinetic energy will be examined, but no other sources or sinks of APE; these will be investigated in Section 5.2.

The sources and sinks of each form of energy are the same for each TC across the six sets of initial conditions described in Chapter 4. In cases where multiple sink terms exist, the relative contributions of each sink may vary with the initial conditions. Any differences will be noted.

First, the budget of the azimuthal kinetic energy density $\bar{\rho}e_k^v$ is examined, where $e_k^v = v^2/2$ is the specific azimuthal kinetic energy. All density-weighted quantities in the energy budgets will use the initial state density $\bar{\rho}(z)$, since the actual density ρ is not explicitly computed by the axisymmetric model, and the quantity $\bar{\rho}\psi$ is the one conserved by the advection scheme (for some velocity or scalar ψ). Multiplying Equation (4.3) by $\bar{\rho}v$ yields the equation

$$\bar{\rho}\frac{De_k^v}{Dt} = -\bar{\rho}\left(f + \frac{v}{r}\right)uv + \bar{\rho}vD_v, \quad (5.1)$$

which can be converted to flux form using the relation

$$\frac{De}{Dt} = \frac{\partial(\bar{\rho}e)}{\partial t} + \nabla \cdot (\bar{\rho}e\mathbf{v}) - e\nabla \cdot (\bar{\rho}\mathbf{v}), \quad (5.2)$$

since $\bar{\rho}$ is independent of time. This relation is valid for any scalar e . Assuming that e is a specific energy, the terms on the right hand side of Equation (5.2) are: the local time tendency of the energy; the energy flux divergence, which when integrated over a volume will give the net flow of energy into or out of the volume; and a mass divergence term. This mass divergence term is zero in an anelastic system, since the anelastic continuity equation states that $\nabla \cdot (\bar{\rho}\mathbf{v}) = 0$ (Dudhia, 1993); it will therefore be referred to as the *elastic mass divergence* term, similar to the terminology used by Xue and Lin (2001). The elastic mass divergence term is very small in all the energy budgets presented in this chapter.

The flux-form budget for e_k^v is

$$\frac{\partial (\bar{\rho} e_k^v)}{\partial t} = -\nabla \cdot (\bar{\rho} e_k^v \mathbf{v}) - \bar{\rho} \left(f + \frac{v}{r} \right) uv + \bar{\rho} v D_v + e_k^v \nabla \cdot (\bar{\rho} \mathbf{v}). \quad (5.3)$$

Changes in e_k^v are due to (in order of RHS terms): fluxes of e_k^v , the exchange of kinetic energy between the primary circulation and the secondary circulation, subgrid turbulent and frictional processes, and elastic mass divergence.

Figure 5.1 shows the azimuthal kinetic energy budget integrated over the model domain (excluding sponge layers—sponge layers will always be excluded from budgets unless otherwise specified). A value of 1×10^{14} W is equivalent to an average of 3.2 W m^{-2} across the domain. The discretised form used to implement the budget, as well as plots showing budget closure, can be found in Appendix B for this and all further budgets.

The source of azimuthal kinetic energy in the axisymmetric model is the conversion from radial kinetic energy to azimuthal kinetic energy via the Coriolis and centrifugal forces. The chief sink of azimuthal kinetic energy is the subgrid frictional dissipation; this largely occurs at the surface. The elastic mass divergence term is very small, as is the flux of azimuthal kinetic energy out of the domain. It is notable that the total tendency of $\bar{\rho} e_k^v$ is positive throughout the simulation, indicating that kinetic energy is consistently increasing in the primary circulation until the end of the run. This contrasts with the fact that the TC does not intensify after 140 h (in terms of v_{\max} —see Figure 4.6). To understand how this arises, the domain is split into three different regions: the *cyclone* region, defined as all grid points in the domain where $v > 10 \text{ m s}^{-1}$, the *anticyclone* region, defined as all grid points where $v < -10 \text{ m s}^{-1}$, and the *other* region containing all the

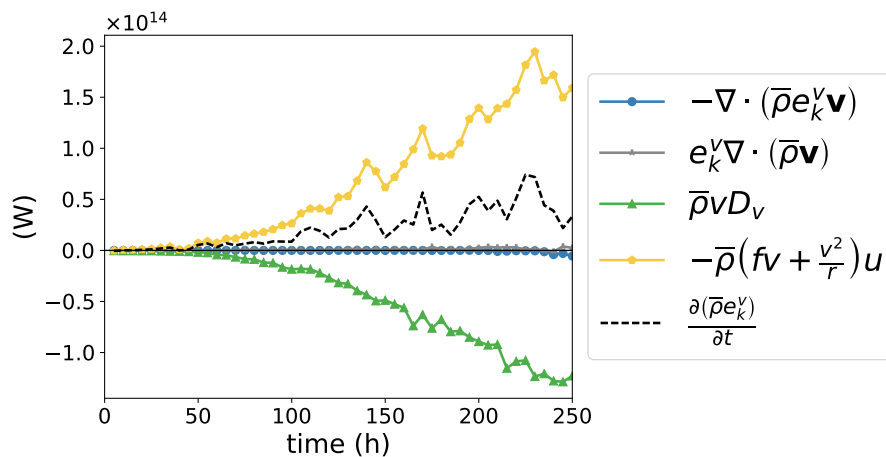
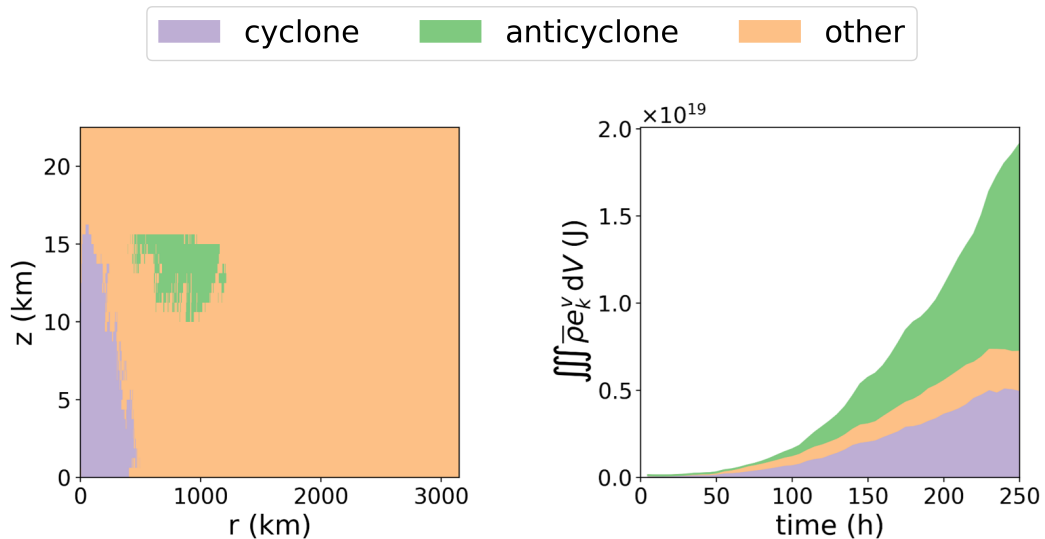


Figure 5.1: Budget of azimuthal kinetic energy according to Equation (5.3), integrated over model domain. The horizontal black line marks 0 W.

non-sponge grid points that are not in either the cyclone or the anticyclone region. Figure 5.2a illustrates these regions at 100 h into the model run, and Figure 5.2b shows a stacked plot of the total azimuthal kinetic energy in each region over time.

Figure 5.2b reveals two explanations for the continued growth in azimuthal kinetic energy throughout the run. Firstly, the kinetic energy in the cyclone region does not stabilise when intensification, in terms of the metric of maximum wind speed, stops (at 140 h). Indeed, it is obvious that this need not be the case; Figure 4.7 established that the TC continues to grow after maximum intensity is reached, which will increase the integrated kinetic energy. It is therefore important going forwards not to assume that a steady state in intensity corresponds to a steady state energetically.

The kinetic energy in the cyclone region does reach a maximum and stabilise towards the end of the run, but this does not happen until well after the occurrence of maximum intensity. This eventual stabilisation may be due to the warming and moistening of the middle and upper levels of the environment throughout the domain, which reduce the CAPE available to parcels in the outer regions of the TC, and thus inhibit the generation of additional kinetic energy there. In the model run with a moist neutral environment and an SST of 26.3°C (N26.3), where there is no environmental CAPE, the maxima in intensity and integrated kinetic energy occur at approximately the same time. These results suggest that whilst environmental CAPE has been found to have little effect on the



(a) Domain regions at 100 h.

(b) Total azimuthal kinetic energy (J) in each region.

Figure 5.2: Regional distribution of azimuthal kinetic energy between *cyclone* region ($v > 10 \text{ m s}^{-1}$), *anticyclone* region ($v < -10 \text{ m s}^{-1}$), and *other* region (any other non-sponge parcels).

maximum intensity achieved by a TC (Persing and Montgomery, 2005), it has a stronger influence on the maximum integrated kinetic energy.

The second issue made obvious by Figure 5.2b is that once the TC reaches maturity, the majority of the increase in kinetic energy is found in the anticyclone region. A similar indefinite growth of the upper-level anticyclone was seen by Schmidt and Smith (2016) using a minimal three-layer axisymmetric model, in which the anticyclonic circulation continued to intensify for 20 days of integration.

To explore why such a dramatic increase in the kinetic energy of the anticyclone region occurs, the e_k^v budget integrated over the anticyclone region is compared with the budget integrated over the cyclone region. These budgets are displayed in Figure 5.3. Whilst the cyclone region has more energy supplied to it by the secondary circulation, the majority of the kinetic energy storage occurs in the anticyclone region, because there is much less frictional dissipation of kinetic energy here.

In the cyclone region, the energy supply is approximately balanced by the subgrid terms representing frictional dissipation (as was seen in the integral over the whole domain), whereas in the anticyclone region the subgrid terms are a relatively smaller sink of energy, leading to a large storage of kinetic energy. This result applies to all initial conditions tested other than N26.3. In this run the anticyclone does not develop sufficiently to dominate the storage term, remaining much weaker and smaller than in J30.3, and so the storage term is a much smaller part of the e_k^v budget. If the definition of the anticyclone region is changed to $v < -5 \text{ m s}^{-1}$, the imbalance between the anticyclone's energy supply and subgrid dissipation can also be seen in the N26.3 run.

The difference between the subgrid terms in the two regions seems reasonable, since

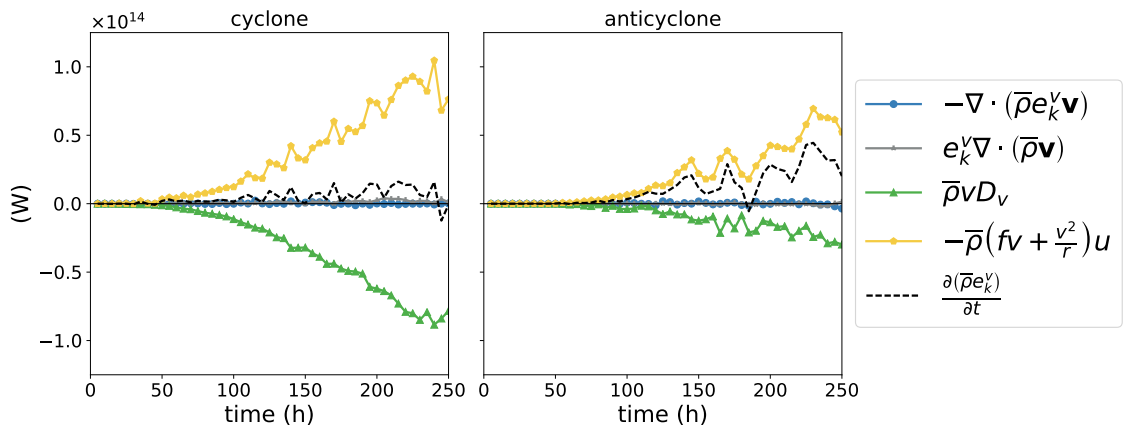


Figure 5.3: Azimuthal kinetic energy budgets for regions of domain illustrated in Figure 5.2a. The horizontal black lines mark 0 W.

turbulent and frictional processes in the boundary layer would differ from those aloft, but it does not seem realistic for the anticyclonic circulation to continue growing in such a fashion. However, the investigation of intensification in this thesis will be mostly concerned with the evolution of the cyclonic part of the circulation, which becomes approximately energetically steady, although it may still be impacted by the sink of angular momentum provided by the anticyclonic circulation. In real-world TCs, the anticyclonic circulation would be disrupted by interactions with upper-level synoptic features not represented in this model.

The budgets of radial kinetic energy and vertical kinetic energy are investigated next. The flux-form budget for the radial kinetic energy density is obtained by multiplying the model's radial momentum equation (4.2) by $\bar{\rho}u$ and rearranging using the identity (5.2), to give

$$\frac{\partial(\bar{\rho}e_k^u)}{\partial t} = -\nabla \cdot (\bar{\rho}e_k^u \mathbf{v}) + \bar{\rho} \left(f + \frac{v}{r} \right) uv - c_p \bar{\rho} \bar{\theta}_v u \frac{\partial \pi}{\partial r} + \bar{\rho} u D_u + e_k^u \nabla \cdot (\bar{\rho} \mathbf{v}). \quad (5.4)$$

The budget terms on the RHS, in order, are: fluxes of radial kinetic energy, the exchange of kinetic energy between the primary circulation and the secondary circulation, the work done on parcels moving along the radial pressure gradient, subgrid turbulent and frictional processes, and the elastic mass divergence. Note that the term representing the exchange of kinetic energy between the primary and secondary circulations appears with opposite sign in the azimuthal kinetic energy budget (5.3) and the radial kinetic energy budget (5.4); since the secondary circulation supports the primary circulation, the term is a sink of e_k^u and a source of e_k^v .

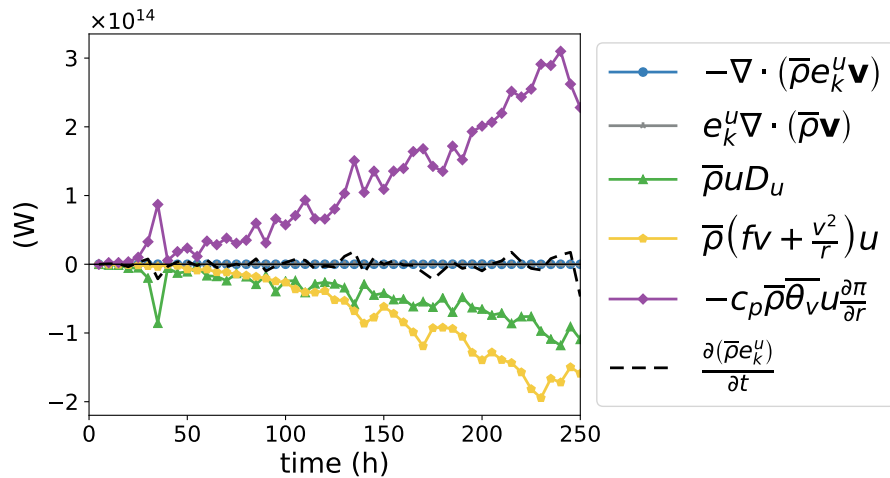


Figure 5.4: Budget of radial kinetic energy according to Equation (5.4), integrated over model domain. The horizontal black line marks 0 W.

The budget of radial kinetic energy for the whole domain is shown in Figure 5.4. The chief source of radial kinetic energy is the acceleration of air parcels along the radial pressure gradient; this energy is then either converted to e_k^v or dissipated. Unlike in the case of the azimuthal kinetic energy, there is no systematic storage of radial kinetic energy. This is likely because the anticyclone is able to convert its radial kinetic energy into azimuthal kinetic energy in the same way the cyclone does (via adjustment to gradient wind balance), whereas the behaviour of dissipation differed between the two.

The relative magnitude of the sinks of e_k^u varies with SST; for the two runs at SST = 30.3°C, the exchange with the primary circulation is a larger sink than the subgrid term, for the two runs at SST = 28.3°C they are approximately equal, and for the runs at SST = 26.3°C the subgrid term becomes the larger sink. This means that the TCs modelled over higher SSTs are more efficient at feeding the energy obtained from the radial pressure gradient through to the primary circulation. This is a consequence of these TCs having higher wind speeds: as v and u increase, the exchange $(fv + \frac{v^2}{r})u$ with the primary circulation (in particular the second term, with its quadratic dependence on v) increases more quickly than the subgrid term does.

It is also instructive to look at the budget of horizontal kinetic energy density, $e_k^h = e_k^u + e_k^v$. In this budget, the exchange between e_k^u and e_k^v cancels, leaving

$$\frac{\partial (\bar{\rho} e_k^h)}{\partial t} = -\nabla \cdot (\bar{\rho} e_k^h \mathbf{v}) - c_p \bar{\rho} \bar{\theta}_v u \frac{\partial \pi}{\partial r} + \bar{\rho} (uD_u + vD_v) + e_k^h \nabla \cdot (\bar{\rho} \mathbf{v}). \quad (5.5)$$

Figure 5.5 shows the integrated horizontal kinetic energy budget, which makes it clear that the main source of horizontal kinetic energy is the acceleration of air parcels along the

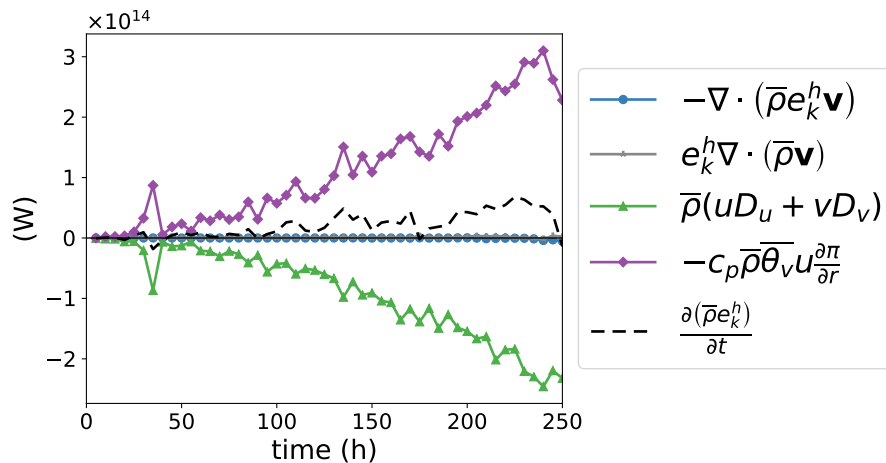


Figure 5.5: Budget of horizontal kinetic energy according to Equation (5.5), integrated over model domain. The horizontal black line marks 0 W.

radial pressure gradient, and that this is approximately balanced by frictional dissipation (except in the anticyclone region, where the deficit of dissipation leads to some storage of horizontal kinetic energy). These results are in accordance with the traditional view of kinetic energy generation in TCs, namely that the main generator of kinetic energy is the acceleration of near-surface inflowing parcels as they move along the radial pressure gradient towards the centre of the TC (Anthes, 1974).

Although the vertical kinetic energy density e_k^w is very small compared to e_k^h , and has therefore traditionally been neglected from energy budget analyses, the physical interpretation of kinetic energy generation changes significantly if the vertical component of kinetic energy is included in the budget. Smith et al. (2018) highlighted that the contribution to the total kinetic energy tendency from the vertical kinetic energy was not negligible in a global kinetic energy budget for the axisymmetric CM1 model (Bryan and Rotunno, 2009b), because the total work of the radial pressure gradient largely cancels between positive contributions in inflow regions and negative contributions in outflow regions. For the purposes of this thesis, it is crucial to consider the processes affecting vertical kinetic energy since they provide the link between APE and the development and maintenance of a TC.

The vertical momentum equation (4.4) includes a buoyancy term and a vertical pressure gradient term; the sum of these is unique, but the individual terms depend on the choice of reference state. Rather than considering only the effect of their total on the energetics, as was done by Smith et al. (2018), here the two terms are considered separately, using the initial sounding reference state that is employed in the model equations. This allows analysis of the conversion of APE to kinetic energy, which only involves the buoyancy term. Since the model equations use the initial sounding reference state in practice, quantities with respect to this reference state are of specific interest. However, the dependence of both the vertical momentum equation terms and the APE on the choice of reference state is important to address, and this will be investigated in Chapter 6.

The budget of vertical kinetic energy density is obtained by multiplying the vertical momentum equation (4.4) by $\bar{\rho}w$ and converting to flux form, to give

$$\frac{\partial(\bar{\rho}e_k^w)}{\partial t} = -\nabla \cdot (\bar{\rho}e_k^w \mathbf{v}) + \bar{\rho}bw - c_p \bar{\rho} \bar{\theta}_v w \frac{\partial \pi}{\partial z} + \bar{\rho}w D_w + e_k^w \nabla \cdot (\bar{\rho} \mathbf{v}). \quad (5.6)$$

The budget terms are: fluxes of vertical kinetic energy; the exchange between APE and vertical kinetic energy via vertical buoyancy fluxes, as seen in Equation (2.28); the work done on parcels moving along the vertical perturbation pressure gradient; subgrid turbu-

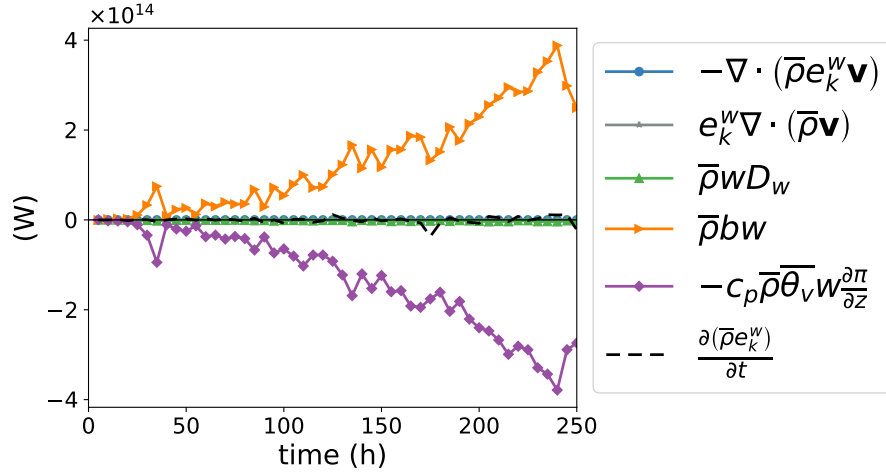


Figure 5.6: Budget of vertical kinetic energy according to Equation (5.6), integrated over model domain. The horizontal black line marks 0 W.

lent and frictional processes; and the elastic mass divergence.

The integral of the vertical kinetic energy budget over the domain is displayed in Figure 5.6. The conversion of APE to vertical kinetic energy acts as the source of vertical kinetic energy, which is approximately balanced by the work done by the vertical pressure gradient, to maintain something close to hydrostatic balance, as expected.

It is also evident that the sink of vertical kinetic energy associated with the vertical pressure perturbation gradient is approximately equal and opposite to the source of horizontal kinetic energy arising from the radial pressure gradient (seen in Figure 5.5). This is because the sink of e_k^w is due to upward motion in the eyewall, where $\frac{\partial \pi}{\partial z} > 0$, whilst the source of e_k^h arises when air flows inwards to the base of the eyewall at low levels. The strength of the low-level inflow is linked to the vertical motion in the eyewall by continuity, leading the two pressure gradient terms to act in opposition.

The budget of total kinetic energy density can now be studied; the sum of Equations (5.5) and (5.6) is

$$\frac{\partial(\bar{\rho}e_k)}{\partial t} = -\nabla \cdot (\bar{\rho}e_k \mathbf{v}) + \bar{\rho}bw - c_p \bar{\rho} \bar{\theta}_v \mathbf{v} \cdot \nabla \pi + \bar{\rho} \mathbf{v} \cdot \mathbf{D} + e_k \nabla \cdot (\bar{\rho} \mathbf{v}), \quad (5.7)$$

where $\mathbf{D} = (D_u, D_v, D_w)$. Figure 5.7 shows the integral of this budget over the domain. The closure of this budget is verified in Appendix B (Figure B.1d). In contrast to the horizontal kinetic energy budget in Figure 5.5, in which the source of kinetic energy was the acceleration of parcels by the radial pressure gradient, when the vertical kinetic energy is included, the source of kinetic energy is the conversion of APE into vertical kinetic energy through buoyancy fluxes. Most of this energy is dissipated either internally

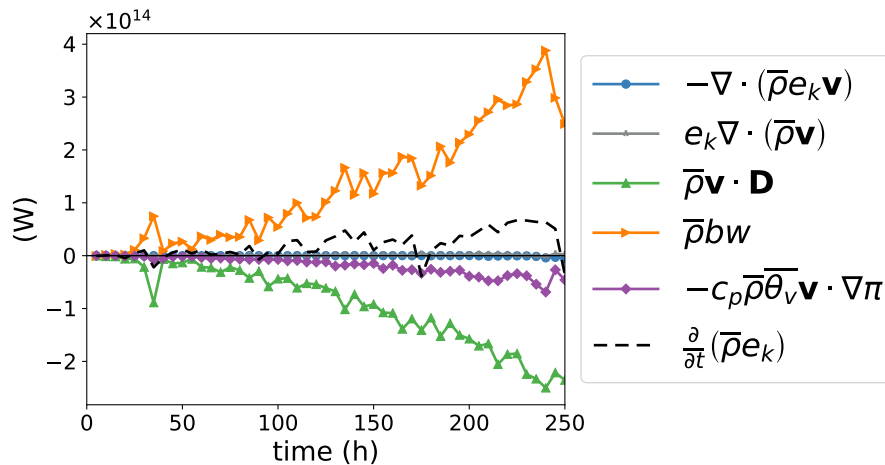


Figure 5.7: Budget of kinetic energy according to Equation (5.7), integrated over model domain. The horizontal black line marks 0 W.

through turbulence or by surface friction, with a small amount working to maintain or strengthen pressure gradients, and some being stored as kinetic energy (as discussed for the azimuthal kinetic energy budget). Viewing the conversion of APE to kinetic energy as the source of kinetic energy is advantageous because it will allow links to be drawn between diabatic processes, which produce or dissipate APE, and the intensification of the TC, which results from the generation of kinetic energy.

Figure 5.8 shows the spatial distributions of the buoyancy b , vertical wind speed w and the conversion of APE to kinetic energy $\bar{\rho}bw$ at 150 h into the model run. It is evident from Figure 5.8a that the majority of parcels near the centre of the TC are positively buoyant, due to the warm-cored nature of the TC. Strong updrafts in the eyewall and rainbands occur in this central region of high positive buoyancy, leading to large conversion of APE to kinetic energy (the location of the eyewall may be observed in Figure 5.8d as the innermost column of strong buoyancy flux). In contrast, parcels with negative buoyancy mostly occur above the tropopause, where there is little vertical motion, or in the outer regions of the domain, where the magnitude of buoyancy is weaker. The production of kinetic energy is therefore chiefly due to the upward motion of positively buoyant parcels.

This is somewhat different to the Lorenzian view of kinetic energy generation occurring due to the rising of warm air and the sinking of cold air, which can be used to explain kinetic energy generation in extratropical cyclones, for example (Lorenz, 1955; Kenney and Smith, 1983). Here, the sinking of colder air in the environment makes little contribution. This is a result of the time-independent basic state chosen for the model and used here as the reference state: since almost all parcels in the domain become warmer than the initial environment, positive buoyancy is widespread and so there are no regions of

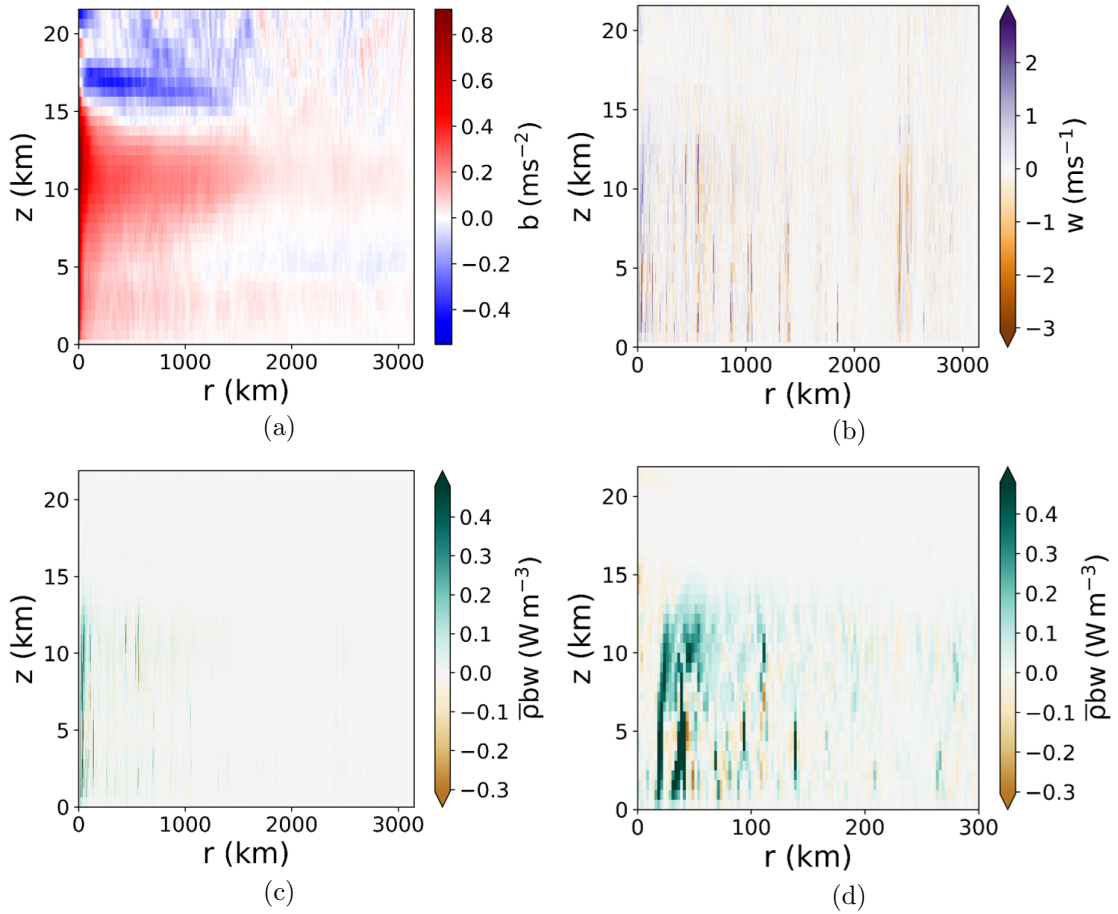


Figure 5.8: Vertical buoyancy flux and its components at 150 h. The first three panels show (a) buoyancy b (ms^{-1}), (b) vertical wind speed w (ms^{-2}), and (c) vertical buoyancy flux $\bar{\rho}bw$ (W m^{-3}), i.e. rate of conversion of APE to kinetic energy, throughout the domain. Panel (d) shows the same vertical buoyancy flux as (c), but in the inner 300 km of the domain only.

subsidence associated with strongly negatively buoyant parcels. If, for example, a time-evolving horizontal mean profile were used as a reference state, then the outer regions of the domain would exhibit more negative buoyancy, and the sinking of cold air outside the TC might contribute more to the overall conversion of APE to kinetic energy. Chapter 6 will more thoroughly investigate how the reference state should be defined in order to obtain an APE that is most useful for interpreting kinetic energy generation.

The sink of kinetic energy that is associated with the work done against pressure gradients acts as a source of available elastic energy in the model. The next budget to investigate is therefore the budget of available elastic energy. The specific available elastic energy is defined as

$$e_e = \frac{c_p^2 \bar{\theta}_v^{-2}}{\bar{c}^2} \frac{\pi^2}{2}, \quad (5.8)$$

where \bar{c} is the speed of sound defined in Equation (4.15)—this form of the available

elastic energy is equivalent to the one derived in Equation (2.22) in terms of the pressure p . The budget for available elastic energy density is obtained by multiplying the model's conservation of mass equation (4.14) by $\frac{\bar{\rho}c_p\bar{\theta}_v^2}{\epsilon^2}\pi$ to give

$$\begin{aligned}\frac{\partial(\bar{\rho}e_e)}{\partial t} &= -c_p\pi\nabla\cdot(\bar{\rho}\bar{\theta}_v\mathbf{v}) + \bar{\rho}c_p\pi\frac{D\theta_v}{Dt} \\ &= -\nabla\cdot(\bar{\rho}c_p\bar{\theta}_v\pi\mathbf{v}) + \bar{\rho}c_p\bar{\theta}_v\mathbf{v}\cdot\nabla\pi + \bar{\rho}c_p\pi\frac{D\theta_v}{Dt},\end{aligned}\quad (5.9)$$

where the divergence term has been rearranged to establish the link between the available elastic and kinetic energies via the reappearance of the term $\bar{\rho}c_p\bar{\theta}_v\mathbf{v}\cdot\nabla\pi$. The three terms of the budget on the RHS are respectively: the pressure work performed on the domain boundaries, the conversion between kinetic energy and available elastic energy, and the change in available elastic energy due to the mass correction associated with changes in θ_v .

The integrated available elastic energy budget over the domain is shown in Figure 5.9: the conversion of kinetic energy into elastic energy provides the major source of available elastic energy. The sinks of available elastic energy are the pressure work on the boundaries of the domain and the correction to the pressure due to changes in θ_v . The total tendency of the available elastic energy is positive overall, indicating that available elastic energy is stored in the domain as the pressure increasingly deviates from the pressure profile of the initial sounding. This should be expected since the TC structure is characterised by negative pressure perturbations in the cyclonic circulation and positive pressure perturbations in the anticyclone, so a stronger TC should be associated with greater available elastic energy.

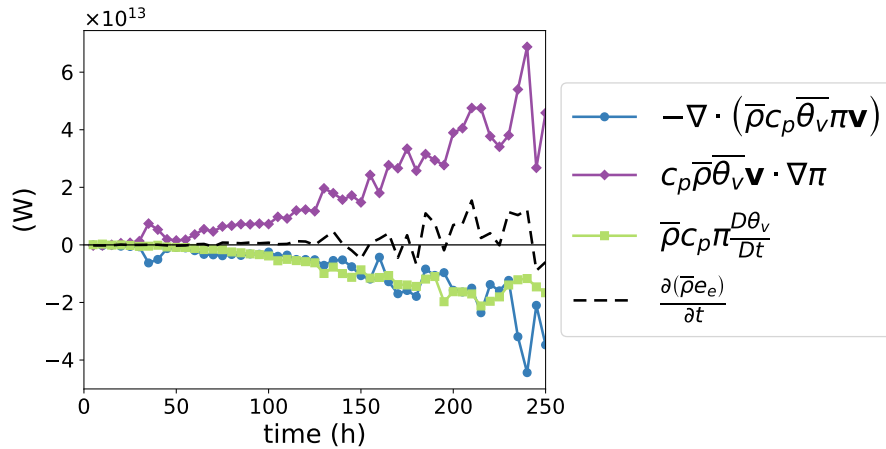


Figure 5.9: Budget of available elastic energy according to Equation (5.9), integrated over model domain. The horizontal black line marks 0 W.

The two sink terms are approximately equal in this case (at least until the final 20 h, when pressure work dominates), and this also applies to the other two runs using the Jordan sounding. For the runs that use the neutral sounding, the sink due to the $\frac{D\theta_v}{Dt}$ pressure correction term is stronger than the sink due to boundary pressure work. Using the Jordan sounding increases the magnitude of all the terms, as does increasing the SST, since more energy is supplied to the TC in both cases, but it is not clear why changing the initialisation sounding should have this impact on the relative effects of the available elastic energy sinks.

To obtain the budget that draws the clearest link between the conversion of APE into kinetic energy and the power dissipation of the TC, the sum of the kinetic and available elastic energy budgets (5.7) and (5.9) is studied, in order to eliminate the conversion between these two forms of energy. The budget for the sum of the kinetic and available elastic energies is

$$\frac{\partial}{\partial t} [\bar{\rho}(e_k + e_e)] = -\nabla \cdot [\bar{\rho}(e_k + c_p \bar{\theta}_v \pi) \mathbf{v}] + \bar{\rho} \mathbf{v} \cdot \mathbf{D} + \bar{\rho} b w + e_k \nabla \cdot (\bar{\rho} \mathbf{v}) + \bar{\rho} c_p \pi \frac{D\theta_v}{Dt}. \quad (5.10)$$

Here, the RHS budget terms are: the flux of mechanical energy density (Gill, 1982), comprising the flux of kinetic energy and the boundary pressure work; the frictional dissipation of kinetic energy; the conversion between APE and vertical kinetic energy; the elastic mass divergence; and changes in available elastic energy due to changes in θ_v .

The domain-integrated budget of kinetic plus available elastic energy in Figure 5.10 shows a clear balance between the conversion of APE into kinetic energy and the frictional dissipation of kinetic energy, which occurs mostly at the sea surface. There is some export of mechanical energy, which occurs due to pressure work rather than the export of kinetic

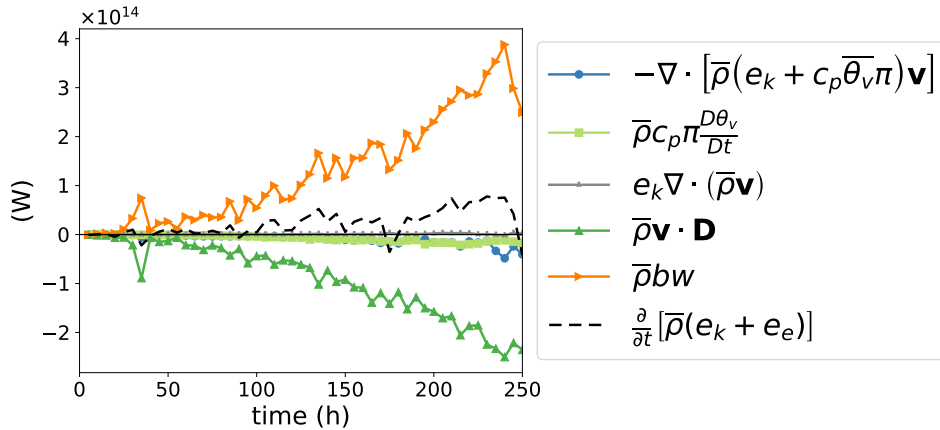


Figure 5.10: Budget of kinetic plus available elastic energy according to Equation (5.10), integrated over model domain. The horizontal black line marks 0 W.

energy, while the other terms are small. The previously established storages of azimuthal kinetic energy and available elastic energy result in a positive total tendency.

This budget does not provide any information about the contributions of diabatic processes to the development of the TC, since the source of energy is simply taken to be the conversion of APE to kinetic energy, with no investigation of the diabatic sources or sinks of APE. However, constructing this closed budget (see Figure B.1f for closure verification) shows that the kinetic energy that is ultimately frictionally dissipated by the TC is sourced from APE, and so the power dissipation of the TC should be strongly controlled by the production of APE. Once APE is converted to kinetic energy via buoyancy fluxes, most of this energy is frictionally dissipated, with only a small portion stored as kinetic or available elastic energy.

In the following sections, an APE budget is constructed in order to link the generation of APE by diabatic processes to the conversion of APE into kinetic energy. The demonstration of Figure 5.10 that the conversion of APE into kinetic energy is opposed by the dissipation of kinetic energy in the model will allow this conversion to be linked to the intensity of the TC; an increase in the conversion of APE to kinetic energy results in a more intense TC. It is important to note that the relevant intensity to be discussed is the integrated kinetic energy dissipation of the TC, rather than the maximum wind speed or minimum surface pressure. These latter two metrics are of course important measures of intensity, but they are not as directly linked to the total production of APE by diabatic processes. The maximum wind speed will be analysed from the viewpoint of local moist APE theory in Chapter 7.

5.2 Available potential energy

In Section 5.1, it was shown that when the model's initialisation sounding is used as a reference state, the conversion of APE into vertical kinetic energy is approximately balanced by the power dissipation of the modelled TC. Understanding how the power dissipation is linked to diabatic processes requires the construction a complete budget of APE, which includes the generation of APE by diabatic processes.

A full moist budget of APE based on local APE theory has not previously been computed for the atmosphere. Previous studies of atmospheric APE have either used a dry APE framework based on the conservation of θ , or incorporated moisture through the use of sorting algorithms. This section develops a method for computing a moist APE budget

for the axisymmetric model based on constructing a discretised APE density that is appropriate for the model's grid structure and conserved variables. Section 5.2.5 describes an important finding arising from the computation of this budget, namely that APE density may behave discontinuously, and discusses why this occurs and its physical relevance. Finally, Section 5.2.6 presents a full budget of APE for the axisymmetric model, including budgets of the generation and dissipation of APE by diabatic processes. Throughout this section, as in Section 5.1, the model's initialisation environmental sounding will be used as the reference state. Alternative reference states are discussed and analysed in Chapter 6.

5.2.1 Conserved variables

As discussed in Section 2.1.2, the APE density of a moist air parcel is calculated by taking the integral of the parcel's buoyancy as it moves reversibly and adiabatically to its nearest Level of Neutral Buoyancy (LNB) in the direction of its *in situ* buoyancy. The first step in constructing an APE budget for the axisymmetric model is therefore to choose the variables to be conserved during the lifting process.

The original axisymmetric model was noted by Rotunno and Emanuel (1987) to approximately conserve equivalent potential temperature

$$\theta_e = \theta \exp\left(\frac{L_v r_v}{c_p T}\right) \approx \theta + \frac{L_v}{c_p \Pi} r_v \quad (5.11)$$

in near-saturation conditions, where the approximation uses the relationship $T = \Pi\theta$. The microphysical terms M_θ and M_{r_v} are defined such that $M_\theta = -\frac{L_v}{c_p \Pi} M_{r_v}$, where $L_v = 2.5 \times 10^6 \text{ J kg}^{-1}$ is the latent heat of vaporisation for water, so that the approximate material derivative of θ_e is

$$\frac{D\theta_e}{Dt} \approx \frac{D\theta}{Dt} + \frac{L_v}{c_p \Pi} \frac{Dr_v}{Dt} = D\theta + \frac{L_v}{c_p \Pi} D_{r_v} + R, \quad (5.12)$$

where all notation has been defined in Chapter 4. Equation (5.12) states that θ_e is conserved by all processes other than radiative cooling and the subgrid contributions to θ and r_v , when variation in Π is neglected.

Since the modifications by Craig (1995) add mixing ratios for rain water and ice to the model, θ_e will no longer be conserved (for example, the freezing of liquid water to ice will increase θ due to latent heat release, without any compensating change in r_v). An

extended version of θ_e is therefore used to suit the new microphysical scheme:

$$\theta_{ei} = \theta \exp\left(\frac{L_s r_v}{c_p T}\right) \exp\left[\frac{L_f (r_l + r_p)}{c_p T}\right] \approx \theta + \frac{L_s}{c_p \Pi} r_v + \frac{L_f}{c_p \Pi} (r_l + r_p), \quad (5.13)$$

where $L_s = 2.834 \times 10^6 \text{ J kg}^{-1}$ is the latent heat of sublimation and $L_f = 0.334 \times 10^6 \text{ J kg}^{-1}$ is the latent heat of fusion. This choice of potential temperature is based on the definition of Pauluis (2016), but neglects variations in c_p and T since these are not accounted for in the model. Again neglecting variations in Π , the material derivative of θ_{ei} is

$$\begin{aligned} \frac{D\theta_{ei}}{Dt} &\approx \frac{D\theta}{Dt} + \frac{L_s}{c_p \Pi} \frac{Dr_v}{Dt} + \frac{L_f}{c_p \Pi} \frac{D(r_l + r_p)}{Dt} \\ &= D\theta + \frac{L_s}{c_p \Pi} D r_v + \frac{L_f}{c_p \Pi} (D r_l + D r_p + P_{r_p}) + R. \end{aligned} \quad (5.14)$$

Whilst θ_e is approximately conserved by condensation and evaporation of cloud liquid water, θ_{ei} is also approximately conserved by the freezing, melting and sublimation processes included as part of the modified microphysics. The relationship (5.14) is verified in Appendix B.

The neglect of variation in Π in Equation (5.14) poses an obstacle for the APE budget. If the APE density e_a is computed for moist air parcels based on the definition of θ_{ei} in Equation (5.13), then changes in e_a will result from changes in θ_{ei} according to the material derivative

$$\frac{D\theta_{ei}}{Dt} = \frac{D\theta}{Dt} + \frac{L_s}{c_p \Pi} \frac{Dr_v}{Dt} + \frac{L_f}{c_p \Pi} \frac{D(r_l + r_p)}{Dt} - \frac{L_s r_v + L_f (r_l + r_p)}{c_p \Pi^2} \frac{D\Pi}{Dt}. \quad (5.15)$$

The term proportional to $\frac{D\Pi}{Dt}$ will change θ_{ei} and therefore appear to contribute to the diabatic production/dissipation of e_a , but it is not associated with the production of APE due to any diabatic process in Equation (5.14). To solve this problem, the density-weighted average of Π throughout the domain (over all time steps) is computed; this will be denoted by $\tilde{\Pi}$. When computing θ_{ei} for use in the APE budget, it is approximated to

$$\theta_{ei} = \theta + \frac{L_s r_v}{c_p \tilde{\Pi}} + \frac{L_f (r_l + r_p)}{c_p \tilde{\Pi}}, \quad (5.16)$$

and wherever Π appears in the definitions of the APE production coefficients it is replaced with $\tilde{\Pi}$. This results in a production of APE by changes in θ_{ei} that is approximately equal to the production computed directly from the surface fluxes, subgrid mixing and precipitation fallout, when integrated regionally (demonstrated in Appendix B).

A second approximately conserved variable is given by the total mixing ratio

$$r_t = r_v + r_l + r_p + r_i, \quad (5.17)$$

which has material derivative

$$\frac{Dr_t}{Dt} = P_{r_p} + P_{r_i} + \sum_j D_j, \quad (5.18)$$

with $j = v, l, p, i$. The variables (θ_{ei}, r_t) are approximately conserved by all modelled processes other than radiative cooling, the fallout of precipitation (both liquid and ice), surface fluxes, and subgrid turbulence and frictional dissipation.

5.2.2 Reference height

Using the conserved variables (θ_{ei}, r_t) described in Section 5.2.1, the reference height z_r of a moist air parcel is defined through the LNB equation

$$b[\theta_{ei}, r_t, \bar{\Pi}(z_r)] = 0, \quad (5.19)$$

where b is calculated using the model's definition of buoyancy (4.5). Each point on the model's v -grid is taken to represent a parcel, since this is where all thermodynamic properties are computed. For each parcel in the model, z_r is computed as follows. The initial profiles $\bar{\theta}, \bar{r}_v$ and $\bar{\Pi}$, which are defined at all model v -levels and at the top and bottom of the domain, are linearly interpolated to the model w -levels, to give reference state profiles with a vertical resolution of $\frac{\Delta z}{2} = 312.5$ m. Henceforth, "all vertical levels" will refer to the combination of v - and w -levels. First, θ_{ei} and r_t are calculated for the parcel, and these are used to compute the parcel's buoyancy at all vertical levels with a bisection algorithm as follows.

When a parcel is lifted to a vertical level z_{lift} , the parcel's new Exner pressure is $\bar{\Pi}(z_{\text{lift}})$, and θ_{ei} and r_t are conserved. The bisection algorithm computes the parcel's new temperature T_{lift} by successively narrowing the possible interval of final temperatures that would make this conservation possible. Starting from an interval $[T_{\text{bottom}}, T_{\text{top}}] = [-273.15^\circ\text{C}, 500^\circ\text{C}]$, the algorithm takes the midpoint of the temperature interval, T_{mid} , and computes $\widehat{\theta}_{ei} = \theta_{ei}(T_{\text{mid}}, r_t, \bar{\Pi}(z_{\text{lift}}))$. In order to compute $\widehat{\theta}_{ei}$ with r_t as the only information about the parcel's water content, it is assumed that whenever $T < 0^\circ\text{C}$, all liquid water freezes; this will overestimate the occurrence of freezing, since in reality

some liquid water would continue to exist down to about -40°C . Additionally, some water would precipitate out of the parcel before reaching the freezing level, which is not accounted for by the reversible thermodynamics used.

The condition $\widehat{\theta}_{ei} = \theta_{ei}$ is required in order for the lifting to be reversible adiabatic. If $\widehat{\theta}_{ei} > \theta_{ei}$, then the temperature interval is narrowed to $[T_{\text{bottom}}, T_{\text{mid}}]$. If $\widehat{\theta}_{ei} < \theta_{ei}$, the interval is narrowed to $[T_{\text{mid}}, T_{\text{top}}]$. This procedure is repeated, taking a new T_{mid} at each step, until the lifted temperature of the parcel is determined to an accuracy of 10^{-6} K, which requires 30 iterations.

The major advantage of using a bisection algorithm is that it can be easily vectorised, which means that the parcel's buoyancy can be quickly computed at all vertical levels at once. Once T_{lift} is determined, it is used to compute the lifted values of θ, r_v, r_l and r_i , and hence the lifted buoyancy. Any two adjacent vertical levels between which the buoyancy changes sign are identified, and the associated LNB is calculated by assuming a linear profile of buoyancy between the levels. In some cases many LNBs are identified at this stage. It is important to note that z_r can occur at any height, rather than being restricted to discrete model levels.

The reference height z_r is then assigned depending on the parcel's *in situ* buoyancy, computed using the reference pressure at the parcel's actual height, $b_0 = b[\theta_{ei}, r_t, \bar{\Pi}(z)]$, following the method of Tailleux (2013b). If $b_0 = 0$, then $z_r = z$. If $b_0 > 0$, then z_r is chosen to be the first LNB above z . If no such LNB exists, z_r is chosen to be the top of the domain, $z_r = 27.5$ km. If $b_0 < 0$, then z_r is chosen to be the first LNB below z , or the bottom of the domain $z_r = 0$ km if no such LNB exists.

Figure 5.11a shows the reference height z_r of each parcel in the axisymmetric TC

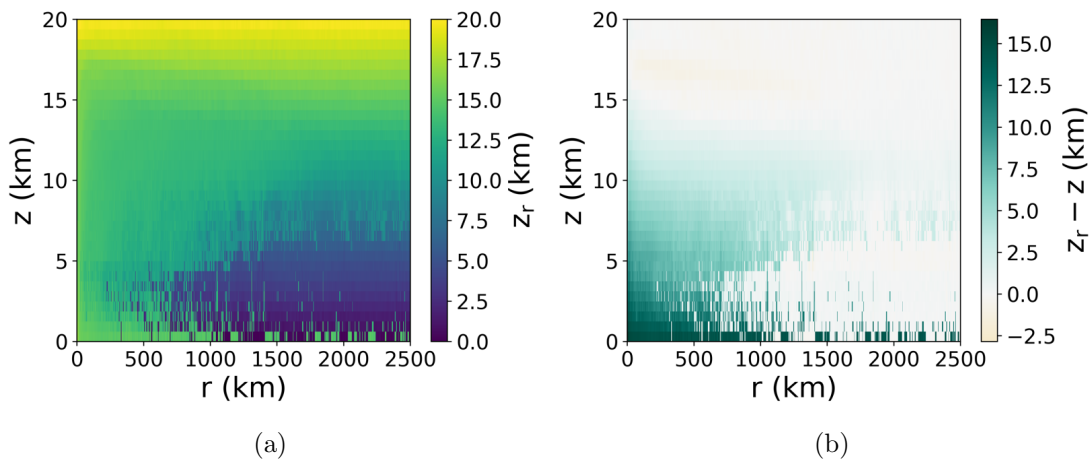


Figure 5.11: (a) Reference height of each moist air parcel at 150 h. (b) Difference between reference height and actual height of parcels.

at 150 h, and Figure 5.11b shows the difference between each parcel's reference height and its actual height, $z_r - z$. Below the tropopause at $z \approx 15$ km, parcels generally have $z_r > z$, indicating that they are positively buoyant with respect to the initial sounding reference state. Parcels above $z = 15$ km have $z_r < z$, meaning that they are negatively buoyant with respect to the reference state. This suggests that the model atmosphere is generally warming and/or moistening at most levels, with cooling above the tropopause.

The highest differences between z and z_r are found near the centre of the TC and in parcels near the sea surface. This suggests that these parcels will have the highest APE densities, since their buoyancy will be integrated over a greater distance to reach their reference heights. This result will be returned to once the APE density has been computed.

5.2.3 APE density

Using the conserved variables from the model, the analytic expression for the APE density e_a of a moist air parcel is

$$e_a = \int_z^{z_r} b(\theta_{ei}, r_t, z') dz', \quad (5.20)$$

where b is evaluated at the reference pressure $\bar{\Pi}(z')$ (Tailleux, 2018)—see Section 2.1.2 for a derivation.

In order to construct the appropriate discretised form of e_a for the axisymmetric model, it is stipulated that the property

$$\left(\frac{\partial e_a}{\partial z} \right)_{\theta_{ei}, r_t} = -b \quad (5.21)$$

of the APE density must be retained in its discretised form. This property is necessary to derive the known form $\bar{\rho}bw$ for the conversion between APE and kinetic energy, since

$$\begin{aligned} \bar{\rho} \frac{De_a}{Dt} &= \bar{\rho} \frac{\partial e_a}{\partial z} \frac{Dz}{Dt} + \dots \\ &= \bar{\rho} \frac{\partial e_a}{\partial z} w + \dots, \end{aligned} \quad (5.22)$$

and so enforcing this property ensures that the APE budget can be linked to the kinetic and available elastic energy budgets of Section 5.1. The discretised version of Equation (5.21) is

$$\frac{e_a(\theta_{ei}, r_t, z + \Delta z) - e_a(\theta_{ei}, r_t, z)}{\Delta z} = -b \left(\theta_{ei}, r_t, z + \frac{\Delta z}{2} \right), \quad (5.23)$$

where e_a is computed on the model's v -grid (where the thermodynamic variables are located), whereas b is computed on the model's w -grid (as is done in practice when computing the term bw for the vertical momentum equation).

A discretised APE density that obeys Equation (5.23) is constructed as follows. The conserved variables θ_{ei} and r_t are fixed and the notation ψ_j is used for the value of the variable ψ on the j^{th} vertical level of the v -grid (i.e. at $z = (2j - 1) \frac{\Delta z}{2}$). It is assumed here that the parcel under consideration has $z_r > z$ (an analogous construction applies for $z_r < z$). Once z_r has been computed, the integer n is identified such that z_r lies between z_n and z_{n+1} . The APE density is then defined as

$$e_{a_j} = \sum_{k=j}^n b_{k+\frac{1}{2}} \Delta z + b_{n+\frac{1}{2}} (z_r - z_n). \quad (5.24)$$

Figure 5.12 provides a schematic of the computation of APE density. It is easy to show that $e_{a_{j+1}} - e_{a_j} = -b_{j+\frac{1}{2}} \Delta z$, and hence that Equation (5.23) is satisfied, since fixing θ_{ei} and r_t means that the two parcels have identical z_r .

Whereas the APE density defined in the continuous theory is positive definite, Equation (5.24) can yield $e_a < 0$ in the case where $|z_r - z| < \frac{\Delta z}{2}$. However, where the reference height is so close to the actual height e_a is expected to be small, and therefore this pos-

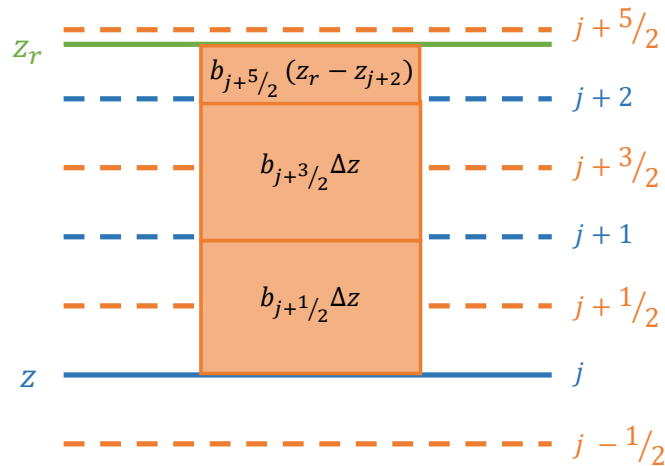


Figure 5.12: Schematic of method for computing APE density for a parcel at vertical v -level j with $z_r > z$. Blue lines indicate vertical v -grid levels, which are spaced Δz apart. The solid blue line labelled z shows the parcel's initial position. Orange dashed lines mark vertical levels on the w -grid, which occur midway between v -levels. The green line labelled z_r is the parcel's reference height (chosen arbitrarily for the purposes of the demonstration). The shaded orange boxes show each term contributing to the sum (5.24), and are labelled with the term's value (box widths are not proportional to value).

sibility is not found to be important for the APE budget over a region. It is preferable to sacrifice the positive definite nature of e_a in order to enforce the vertical derivative property (5.23) and ensure the link between the APE and kinetic energy budgets.

An issue can arise with the property (5.23) if $b_j < 0$ and $b_{j+1} > 0$. In this case, the computation of $e_{a_{j+1}}$ will proceed by taking a sum upwards from z_{j+1} , whilst the computation of e_{a_j} will take a sum downwards from z_j , resulting in $b_{j+\frac{1}{2}}$ failing to enter the computation at all. This appears to be an unavoidable consequence of using vertically-discretised parcels; the situation would not be remedied even if exact continuous integrals were used for the two parcels, as long as they remained separated by Δz . The computed partial vertical derivative of e_a may therefore not reflect b as well in regions where neighbouring parcels have buoyancies of opposite signs. However, this does not appear to have a large impact on the overall budget since the magnitude of buoyancy is generally small in these locations.

The APE density e_a in the axisymmetric model at 150 h is shown in Figure 5.13. As expected from the results for z_r , parcels near the sea surface exhibit high values of e_a , and e_a increases towards the centre of the TC. The high APE density in the centre reflects the baroclinicity of the system; APE is stored in the warm core of the cyclone relative to the outer environment. This APE could be released if the vortex were to dissipate. The high APE at the surface seems likely to be a result of the production of APE by air-sea fluxes, which will be verified by further budget analysis later in this section.

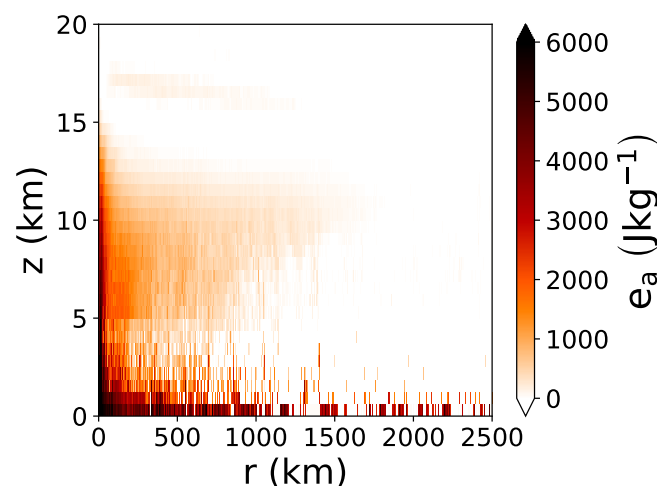


Figure 5.13: APE density e_a in the axisymmetric TC 150 h into the simulation, computed using Equation (5.24).

5.2.4 APE production coefficients

Constructing the full budget of APE for the model also requires computing the efficiency with which diabatic processes produce or destroy APE density. The material derivative of e_a , analogously to Equation (2.28), is

$$\frac{De_a}{Dt} = G_{\theta_{ei}} \frac{D\theta_{ei}}{Dt} + G_{r_t} \frac{Dr_t}{Dt} - b(z)w + b(z_r) \frac{Dz_r}{Dt}, \quad (5.25)$$

where the APE production coefficients are defined by

$$G_{\theta_{ei}} = \frac{\partial e_a}{\partial \theta_{ei}}, \quad (5.26)$$

$$G_{r_t} = \frac{\partial e_a}{\partial r_t}, \quad (5.27)$$

which govern the amount of e_a produced by a given change in θ_{ei} and r_t respectively. It was noted in Chapter 2 that these derivatives are sometimes referred to as APE production *efficiencies*, but for the purposes of this thesis, this term is reserved for the scaled forms of the coefficients defined later in this section, which take values between -1 and 1 .

Section 5.2.4.1 first derives the analytic forms of $G_{\theta_{ei}}$ and G_{r_t} , since these will assist the physical interpretation of the distributions of production coefficients computed for the model. Section 5.2.4.2 then derives the discretised forms of the production coefficients, which are appropriate for computing the APE production in the axisymmetric model.

5.2.4.1 Continuous form of production coefficients

The starting point for deriving the APE production coefficients with respect to θ_{ei} and r_t is the general theory of local APE for compressible binary fluids (Tailleux, 2018), which is based on the conservation of specific entropy (denoted here by s) and a composition variable (here total specific humidity q_t ; note that total mixing ratio r_t is not used because a measure of composition per unit moist air rather than dry air is required).

The APE production coefficients are most easily derived from the expression for APE density e_a in pressure coordinates, which is

$$e_a = \int_{p_0(z_r)}^{p_0(z)} [\alpha(s, q_t, p') - \hat{\alpha}_0(p')] dp', \quad (5.28)$$

where α is specific volume and the subscript 0 denotes a variable in an arbitrary vertically-varying, hydrostatically-balanced reference state (see Equation (2.23) and surrounding

text for more details on the derivation of this expression). The function $\hat{\alpha}_0(p)$ returns the value of α_0 at the height where the reference pressure is p ; defining $Z_0(p)$ as the inverse of $p_0(z)$, it can be expressed as $\hat{\alpha}_0(p) = \alpha_0(Z_0(p))$.

Deriving the APE production coefficients from this requires using the differential of moist specific enthalpy k ,

$$dk = Tds + \mu dq_t + \alpha dp, \quad (5.29)$$

where μ is chemical potential (e.g. Landau and Lifshitz, 1980, p. 71). Equation (5.29) provides the relations

$$T = \left(\frac{\partial k}{\partial s} \right)_{q_t, p}, \quad (5.30)$$

$$\mu = \left(\frac{\partial k}{\partial q_t} \right)_{s, p}, \quad (5.31)$$

$$\alpha = \left(\frac{\partial k}{\partial p} \right)_{s, q_t}, \quad (5.32)$$

$$(5.33)$$

which can be used in combination with (5.28) to write

$$\begin{aligned} G_s &= \frac{\partial e_a}{\partial s} \\ &= \frac{\partial}{\partial s} \int_{p_0(z_r)}^{p_0(z)} [\alpha(s, q_t, p') - \hat{\alpha}_0(p')] dp' \\ &= \frac{\partial}{\partial p} \int_{p_0(z_r)}^{p_0(z)} \frac{\partial k}{\partial s}(s, q_t, p') dp' \\ &= \frac{\partial k}{\partial s}(s, q_t, p_0(z)) - \frac{\partial k}{\partial s}(s, q_t, p_0(z_r)) \\ &= T(s, q_t, p_0(z)) - T(s, q_t, p_0(z_r)). \end{aligned} \quad (5.34)$$

Defining the subscripts h and r by $f_h = f(s, q_t, p_0(z))$, $f_r = f(s, q_t, p_0(z_r))$ for any thermodynamic variable f , and performing a similar procedure for G_{q_t} , the production coefficients are

$$G_s = T_h - T_r, \quad (5.35)$$

$$G_{q_t} = \mu_h - \mu_r, \quad (5.36)$$

as seen in Equation (3.4b) of Tailleux (2018).

To obtain the production coefficients with respect to θ_{ei} and r_t , Equation (5.29) must

therefore be written in terms of θ_{ei} and r_t . The relationship between equivalent potential temperature and moist specific entropy is

$$s = c_p(q_t) \ln \theta_{ei} - (1 - q_t) R_d \ln p_{00} \quad (5.37)$$

where p_{00} is a fixed reference pressure, usually 1000 hPa (Emanuel, 1994, Equation (4.5.10), adapted to quantify specific entropy per unit of moist rather than dry air). This can be used to write the differential of moist specific entropy ds as a function of θ_{ei} and q_t :

$$ds = \frac{\partial s}{\partial \theta_{ei}} d\theta_{ei} + \frac{\partial s}{\partial q_t} dq_t = \frac{c_p}{\theta_{ei}} d\theta_{ei} + \left(\frac{\partial c_p}{\partial q_t} \ln \theta_{ei} + R_d \ln p_{00} \right) dq_t. \quad (5.38)$$

Substituting Equation (5.38) into (5.29) and using $dq_t = \frac{dr_t}{(1+r_t)^2}$ gives an enthalpy differential in terms of the chosen conserved variables:

$$dk = \frac{c_p T}{\theta_{ei}} d\theta_{ei} + \frac{1}{(1+r_t)^2} \left(\mu + \frac{\partial c_p}{\partial q_t} T \ln \theta_{ei} + R_d T \ln p_{00} \right) dr_t + \alpha dp. \quad (5.39)$$

In practice the axisymmetric model uses a constant parameter $c_p = c_{pd}$ for heat capacity, so that $\frac{\partial c_p}{\partial q_t} = 0$. Following the method used to derive G_s in Equation (5.35), the desired APE production coefficients are then

$$G_{\theta_{ei}} = c_p \frac{T_h - T_r}{\theta_{ei}} \quad (5.40)$$

$$G_{r_t} = \frac{1}{(1+r_t)^2} [\mu_h - \mu_r + (T_h - T_r) R_d \ln p_{00}]. \quad (5.41)$$

The amount of APE produced in a moist air parcel by a change in θ_{ei} is determined by the difference between the parcel's temperature at its actual height z (evaluated at the reference pressure $p_0(z)$), and its temperature when lifted to its reference height z_r . Therefore, APE production is expected to be higher in parcels that have high buoyancy and hence move a greater distance to reach their reference height.

The production coefficient G_{r_t} similarly depends on the difference between the parcel's properties at z and z_r , in this case being a combination of the differences in chemical potential and temperature.

5.2.4.2 Discretised production coefficients

To construct the forms of $G_{\theta_{ei}}$ and G_{r_t} that are appropriate for the model's thermodynamic approximations and grid structure, the method used to discretise e_a is re-employed.

To do this, Equation (5.20) is used to write the production coefficients as

$$G_{\theta_{ei}} = \int_z^{z_r} \frac{\partial b}{\partial \theta_{ei}} (\theta_{ei}, r_t, z') dz', \quad (5.42)$$

$$G_{r_t} = \int_z^{z_r} \frac{\partial b}{\partial r_t} (\theta_{ei}, r_t, z') dz', \quad (5.43)$$

and the integrals from z to z_r are taken using the method of (5.24):

$$G_{\theta_{eij}} = \sum_{k=j}^n \frac{\partial b}{\partial \theta_{ei}} \Big|_{k+\frac{1}{2}} \Delta z + \frac{\partial b}{\partial \theta_{ei}} \Big|_{n+\frac{1}{2}} (z_r - z_n), \quad (5.44)$$

$$G_{r_{tj}} = \sum_{k=j}^n \frac{\partial b}{\partial r_t} \Big|_{k+\frac{1}{2}} \Delta z + \frac{\partial b}{\partial r_t} \Big|_{n+\frac{1}{2}} (z_r - z_n). \quad (5.45)$$

All that remains to be done to obtain the production coefficients is to find expressions for the partial derivatives $\frac{\partial b}{\partial \theta_{ei}}$ and $\frac{\partial b}{\partial r_t}$. This requires the differentials

$$db = \frac{\partial b}{\partial \theta} d\theta + \frac{\partial b}{\partial r_v} dr_v + \frac{\partial b}{\partial r_l} dr_l + \frac{\partial b}{\partial r_i} dr_i + \frac{\partial b}{\partial z} dz, \quad (5.46)$$

$$d\theta_{ei} = d\theta + \frac{L_s}{c_p \Pi} dr_v + \frac{L_f}{c_p \Pi} dr_l, \quad (5.47)$$

$$dr_t = dr_v + dr_l + dr_i, \quad (5.48)$$

derived from Equations (4.5), (5.14) and (5.17) respectively. Here liquid precipitation is incorporated into r_l for brevity.

Denoting the saturated mixing ratio of a parcel by r_{vs} , the problem may be split into three cases: where the parcel is unsaturated ($r_l = r_i = 0$, $dr_t = dr_v$), where the parcel is saturated but no freezing has occurred ($r_i = 0$, $dr_t = dr_l + dr_{vs}$), and where the parcel has undergone freezing ($dr_t = dr_i + dr_{vs}$).

The change in saturated mixing ratio can be linked to the change in potential temperature using the Clausius-Clapeyron equation

$$\frac{de_s}{dT} = \frac{Le_s}{R_v T^2}, \quad (5.49)$$

where e_s is the saturated vapour pressure, $R_v = 461.5 \text{ J kg}^{-1} \text{ K}^{-1}$ is the specific gas constant for water vapour, and L is the appropriate latent heat coefficient (L_v if the water vapour is saturated over liquid water, L_s if it is saturated over ice). Since $r_{vs} \approx \frac{R_d e_s}{R_v p}$, the

derivative of r_{vs} with respect to θ is

$$\begin{aligned}\frac{dr_{vs}}{d\theta} &= \frac{dr_{vs}}{dT} \cdot \frac{dT}{d\theta} \\ &= \frac{Lr_{vs}}{R_v T^2} \cdot \frac{T}{\theta} \\ &= \frac{Lr_{vs}}{R_v T \theta}.\end{aligned}\tag{5.50}$$

Equations (5.46), (5.47) and (5.48) can be rearranged for each of the three cases, making use of Equation (5.50). Defining the factors

$$F_s = \frac{1 + \frac{L_v r_{vs}}{R_d T}}{1 + \frac{\epsilon L_v^2 r_{vs}}{c_p R_d T \theta \Pi}},\tag{5.51}$$

$$F_f = \frac{1 + \frac{L_s r_{vs}}{R_d T}}{1 + \frac{\epsilon L_s^2 r_{vs}}{c_p R_d T \theta \Pi}},\tag{5.52}$$

where $\epsilon = \frac{R_d}{R_v}$, the required partial derivatives are

$$\frac{\partial b}{\partial \theta_{ei}} = \begin{cases} \frac{g}{\theta} & \text{if unsaturated} \\ \frac{g}{\theta} F_s & \text{if saturated, } T > 0^\circ\text{C} \\ \frac{g}{\theta} F_f & \text{if saturated, } T < 0^\circ\text{C}, \end{cases}\tag{5.53}$$

$$\frac{\partial b}{\partial r_t} = \begin{cases} g \left(0.61 - \frac{L_s}{c_p \Pi \theta} \right) & \text{if unsaturated} \\ -g \left(1 + \frac{L_f}{c_p \Pi \theta} F_s \right) & \text{if saturated, } T > 0^\circ\text{C} \\ -g & \text{if saturated, } T < 0^\circ\text{C}. \end{cases}\tag{5.54}$$

The use of these expressions in Equations (5.44) and (5.45) respectively allows the required discretised APE production coefficients to be computed. Although the forms found in this section look very different to the exact theoretical forms of the coefficients, when used in practice the results are similar.

The *APE production efficiencies* are defined by scaling the APE production coefficients so that they specify the APE produced for a given change in enthalpy. If the effect of the latent heat of fusion is included in the definition of enthalpy, a change $d\theta_{ei} = d\theta + \frac{L_s}{c_p \Pi} dr_v$ corresponds to an enthalpy change $dk = c_p dT + L_s dr_v \approx c_p \Pi d\theta + L_s dr_v = c_p \Pi d\theta_{ei}$. Assuming no changes in r_l and r_i for simplicity, the change in r_t is $dr_t = dr_v$, which is equivalent to an enthalpy change $dk = L_s dr_v$. The APE production efficiencies with

respect to θ_{ei} and r_t are therefore defined as

$$\varepsilon_{\theta_{ei}} = \frac{G_{\theta_{ei}}}{c_p \Pi}, \quad (5.55)$$

$$\varepsilon_{r_t} = \frac{G_{r_t}}{L_s}, \quad (5.56)$$

which provide efficiency values between -1 and 1 . The material derivative of APE (Equation (5.25)) can be rewritten in terms of the production efficiencies as

$$\frac{De_a}{Dt} = \varepsilon_{\theta_{ei}} c_p \Pi \frac{D\theta_{ei}}{Dt} + \varepsilon_{r_t} L_s \frac{Dr_t}{Dt} - b(z) w + b(z_r) \frac{Dz_r}{Dt}. \quad (5.57)$$

Figure 5.14 shows the APE production efficiencies at 150 h into the model run. The two efficiencies are broadly similar in pattern and generally of opposite sign. The similar pattern results from the dependence of both efficiencies on the reference height z_r . Where $|z - z_r|$ is large, the air parcel will have very different properties at its reference height versus its actual height, so $|T_h - T_r|$ and $|\mu_h - \mu_r|$ are both large. Hence the magnitudes of the efficiencies tend to covary.

Regions in which $\varepsilon_{\theta_{ei}}$ is positive are the regions in which air is positively buoyant and therefore $z_r > z$. An increase in θ_{ei} will further increase the buoyancy, leading to an increase in APE density. Since $\varepsilon_{\theta_{ei}}$ is mostly positive near the surface, surface fluxes of θ_{ei} will generally produce APE, as expected. The maximum value of $\varepsilon_{\theta_{ei}}$ at 150 h is 30.4%. This is a similar efficiency to the maximum Carnot efficiency calculated by treating a TC as a heat engine (Emanuel, 1986), as was hypothesised in Section 2.3.2; the relationship

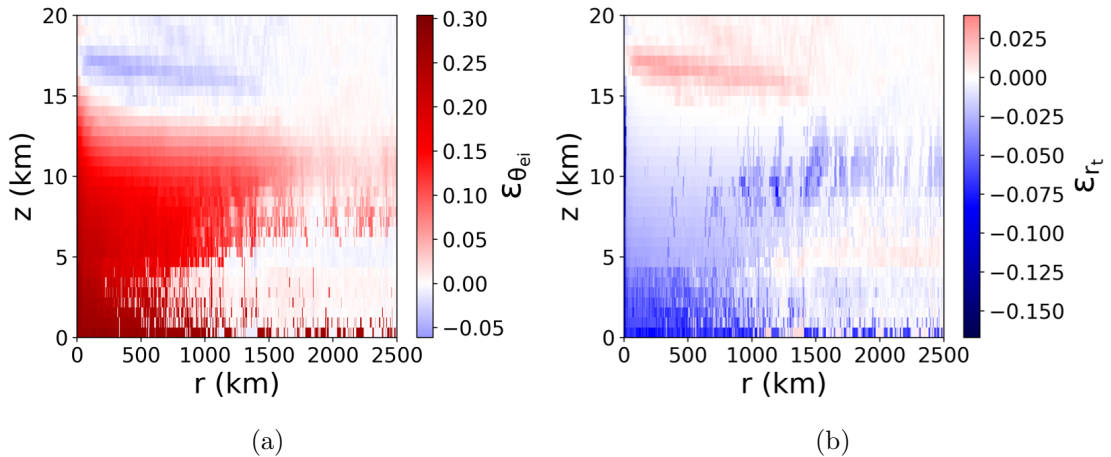


Figure 5.14: APE production efficiencies at 150 h. Red parcels have positive efficiency, meaning that an increase in the relevant quantity (θ_{ei} for (a), r_t for (b)) will increase e_a . Blue parcels have negative efficiency, meaning that an increase in the quantity will decrease e_a .

between these efficiencies will be explored further in Chapter 7. This is a high efficiency for an atmospheric circulation, because the TC core contains very deep convection, which is associated with high values of $T_h - T_r$ for near-surface core parcels. Regions of negative $\varepsilon_{\theta_{ei}}$ are found where $z_r < z$, which occurs mostly at upper levels but also in a few surface parcels, which are negatively buoyant with respect to the environmental sounding. For these parcels, an increase in θ_{ei} results in a decrease in APE density.

The efficiency ε_{r_t} is generally negative below $z = 15$ km for two reasons. Firstly, the moist air buoyancy (4.5) contains negative contributions from liquid water and ice. This means that for saturated parcels, an increase in r_t will act to increase the water loading, decrease the buoyancy and decrease the APE density (since $z_r > z$). The second reason stems from the addition of water vapour to unsaturated air near the surface, which will become saturated when lifted to its reference height. As documented by Pauluis (2011), lifting unsaturated air to saturation reduces the efficiency of an atmospheric heat engine, because energy must be used to increase the Gibbs free energy of the water vapour (Pauluis terms this the *Gibbs penalty*). Such a reduction in efficiency was demonstrated for approximate heat engine cycles in a numerically simulated TC by Pauluis and Zhang (2017). Similarly, this effect acts to decrease APE density.

The values of ε_{r_t} computed here are very different to the ones found by Wong (2014) using the same axisymmetric model. Wong (2014) found that ε_{r_t} was generally positive below 15 km (see Figure 2.5c), with very similar values to $\varepsilon_{\theta_{ei}}$. However, Wong (2014) did not account for any of the model's thermodynamic approximations and did not present a closed APE budget. The efficiencies presented in this section will be used to produce a closed APE budget in Section 5.2.6, which provides confidence that these efficiencies are the correct ones. The negative values of ε_{r_t} are also easier to explain physically, as was done above.

It is important to note that some physical processes act to influence the APE density through changes in both θ_{ei} and r_t , and their effects should not be assessed without considering the sum of the two production terms (since the partitioning depends on the choice of conserved variables). For example, precipitation of liquid water out of parcels in the lower atmosphere acts to increase APE through the r_t term, by reducing the water loading, but decreases APE through the θ_{ei} term because the latent heat of fusion that could have been released if the parcel were lifted to its freezing level is now lost (the increase in APE due to water loading reduction is found to be the dominant effect here, so that precipitation generally provides a source of APE). The surface flux of water

vapour increases APE by adding latent heat through the θ_{ei} term, but decreases APE due to the Gibbs penalty. The relative magnitudes of the efficiencies indicate the relative contributions of the two terms. For example, the maximum value of $\varepsilon_{\theta_{ei}}$, which occurs in near-surface parcels, is approximately twice the maximum absolute value of ε_{r_t} ; this means that the net effect of the water vapour surface flux is to increase APE via the θ_{ei} term.

The final issue that must be addressed in order to complete the APE budget is the contribution from the last term of Equation (5.57), $b(z_r) \frac{Dz_r}{Dt}$. In previous studies using local APE theory, this has been taken to be zero, since $b(z_r) = 0$ by the definition of reference height (Tailleux, 2013b). However, this is only valid if z_r is a continuous function in time and space; it will be shown in the next section that this is not necessarily the case.

5.2.5 Discontinuous behaviour of APE density

APE density and reference height have previously always been treated as continuous variables in both space and time. However, recognising that discontinuous transitions in z_r and hence e_a can occur is crucial to closing the local APE budget in some scenarios. This section provides an example to illustrate how these transitions may occur, discusses the implications of the discontinuous property for the energetic conversions involved in local APE theory, and describes the methods used to account for the discontinuous behaviour of APE density when constructing the budget for the axisymmetric model.

For this illustration, freezing has not been included, and all quantities have been computed using exact thermodynamics, following Emanuel (1994), to ensure that discontinuities are not a product of model features such as the linear approximation to the buoyancy.

An example parcel is taken at $z = 200$ m with $\theta_e = 340$ K, $r_t = 0.014$ kg kg⁻¹. The parcel is positively buoyant with respect to the reference profile and so $z_r > z$. Figure 5.15a shows the parcel's temperature and liquid water mixing ratio as it is lifted reversibly and adiabatically along the reference pressure profile $\bar{p}(z)$. This demonstrates that the parcel becomes saturated just below a height of 2 km.

The parcel's reference height z_r is then the lowest height z at which $b(z) = 0$. The lifted buoyancy profile is shown by the solid line in Figure 5.15b, with the dashed black line indicating where $b = 0$. The parcel reaches neutral buoyancy shortly before it saturates. In this case $z_r = 1.25$ km (indicated by the lower green star). If the parcel were heated

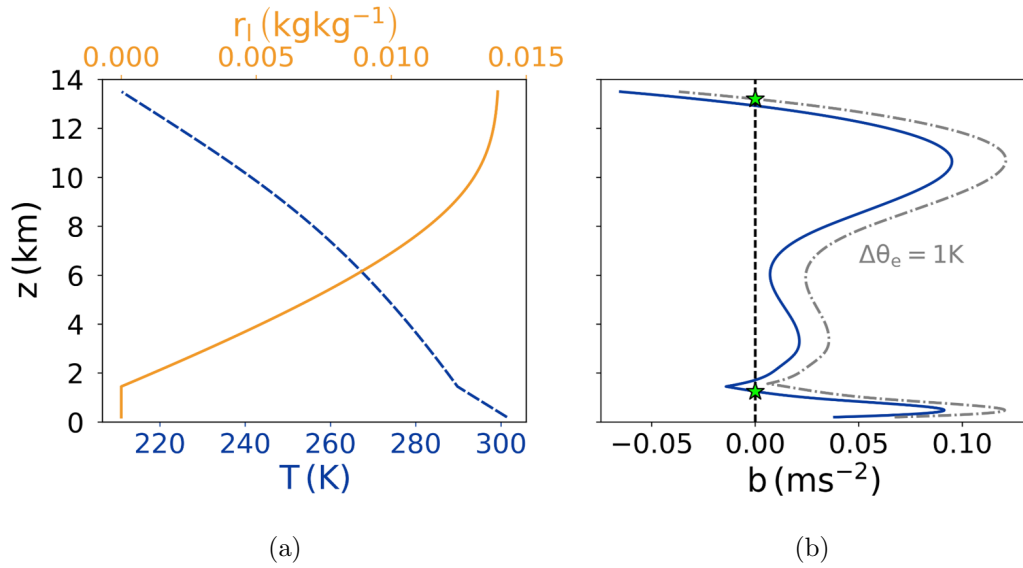


Figure 5.15: Thermodynamic properties of a parcel with $\theta_e = 340$ K, $r_t = 0.014$ kg kg^{-1} when lifted reversibly and adiabatically upwards from 200 m through the Jordan hurricane-season mean sounding (freezing not included). (a) Temperature (dashed blue line) and liquid water mixing ratio (solid orange line) as parcel is lifted. (b) Buoyancy relative to Jordan sounding during lifting (blue solid line). The grey dashed-dotted line shows the buoyancy profile when θ_e is perturbed by 1 K. The black dashed line indicates where $b = 0$ ms^{-2} . Green stars mark reference heights for the two parcels.

so that $\theta_e = 341$ K, while maintaining constant r_t , its new buoyancy profile would be the one shown by the dashed-dotted line. The parcel now remains positively buoyant around its saturation level, and attains a much higher LNB, $z_r = 13.2$ km (indicated by the upper green star). At some temperature 340 K $< \theta_e < 341$ K, z_r discontinuously transitions from approximately 1.25 km to approximately 13.2 km without taking on any value in between.

Figure 5.16 explores this example in more detail. The parcel's height and total mixing ratio are kept constant, while θ_e is increased continuously from 340 K to 341 K, to represent a sensible heating of the parcel.

As the parcel is heated, Figure 5.16a shows that its APE density increases continuously until a threshold is reached at $\theta_e \approx 340.7$ K, at which point the APE density jumps to a much higher value. At this θ_e , the production efficiency ε_{θ_e} also discontinuously becomes much higher (Figure 5.16b), so that further heating increases the APE density at a greater rate.

These plots are an important demonstration that the discontinuous nature of APE density is not related to numerical model discretisation or thermodynamic approximations, but is a previously unrecognised fundamental feature of local APE theory. Even if

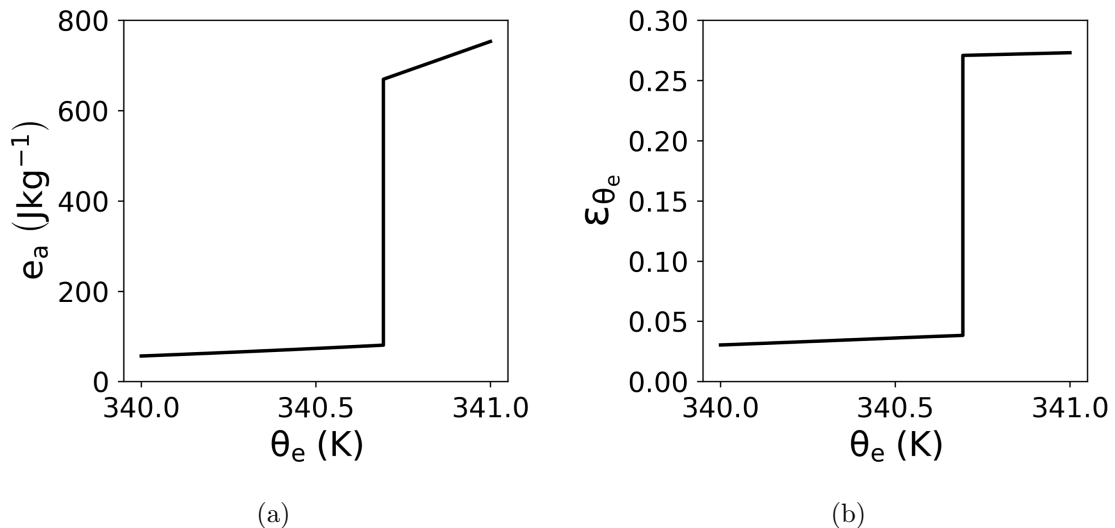


Figure 5.16: APE density e_a (a) and production efficiency ε_{θ_e} (b) of a moist air parcel with increasing θ_e . The parcel’s height is fixed at $z = 200$ m and the total mixing ratio is fixed at $r_t = 0.014 \text{ kg kg}^{-1}$, so at $\theta_e = 340$ K the parcel is identical to the example case illustrated in Figure 5.15. APE is calculated relative to the Jordan hurricane-season mean sounding.

θ_e varies continuously in time and space, temporal discontinuities in z_r and hence e_a can occur.

Spatial discontinuities in e_a are then also expected, as a result of the fact that one parcel may have accessed a higher LNB in this manner whilst a neighbouring parcel, despite having similar thermodynamic properties, has not. The increase of θ_e in Figure 5.16 can either be thought of as representing a single parcel being heated, or as representing horizontal or vertical variation in θ_e at a fixed time, with the jump in e_a then representing a spatial discontinuity. However, if a Lagrangian budget of APE density were performed, then only temporal discontinuities could appear in the budget of the parcel being followed, so spatial discontinuities are an artefact of an Eulerian budget rather than a physically important process impacting the development of a moist air parcel.

In Figure 5.16b, the efficiency $\varepsilon_{\theta_e} = \frac{G_{\theta_e}}{c_p \Pi}$ has been computed using $G_{\theta_e} = c_p \frac{T_h - T_r}{\theta_e}$ and assuming an Exner pressure $\Pi = 1$. (see Equations (5.40) and (5.55)). This is well-defined for all values of θ_e , since the parcel’s reference height always exists. However, the fundamental definition of the APE production coefficient, $G_{\theta_e} = \frac{\partial e_a}{\partial \theta_e}$, is not well-defined everywhere; at the point of discontinuity, the derivative of APE density with respect to θ_e is infinite. There is an increase in APE density that cannot be attributed to its generation by diabatic processes using the traditional definition of production, which will lead to discrepancies in APE budgets.

The example presented above is analogous to the release of Convective Available Po-

tential Energy (CAPE), the main difference being that buoyancy is defined relative to the reference state rather than necessarily the local environment. At $\theta_e = 340$ K, z_r lies below the parcel's level of free convection (LFC); some energy can be considered unavailable to the parcel due to the presence of convective inhibition (CIN). The perturbation of θ_e by 1 K is sufficient to allow the parcel to attain its LFC and its higher LNB at 13.2 km, increasing the APE suddenly in the same way that a reservoir of CAPE can suddenly become available for release via vertical motion.

The discontinuous behaviour of z_r is a signal that a reservoir of Background Potential Energy (BPE) has become APE (recall that BPE is the part of the total potential energy not available for reversible conversion to kinetic energy; $TPE = APE + BPE$). Similar behaviour can be seen in cases where the parcel's *in situ* buoyancy is close to zero, so that a small amount of heating or moistening may switch a parcel with marginally negative buoyancy and $z_r = 0$ m to a positively buoyant parcel with z_r high in the troposphere (or vice versa).

However, since APE is defined relative to a non-local sounding in this case, the appearance of large amounts of APE has less physical significance than the release of CAPE. When CAPE is released, deep convection occurs as parcels move to their LNB. However, in the case of APE, a parcel could have z_r high in the troposphere when calculated relative to some far-field environmental sounding, but not actually move upwards because it is not buoyant relative to its local environment. It is therefore important to bear in mind that a discontinuous increase in local APE need not be associated with any rapid change in vertical motion.

The discontinuous behaviour of z_r is not unique to the atmospheric context; the possibility of the existence of multiple LNBs has also been identified in the ocean (Saenz et al., 2015), which would enable discontinuous transitions of z_r in seawater parcels.

The discontinuity of z_r in time can be thought of as an instantaneous transfer of potential energy into APE from BPE. As z_r transitions, the partition between APE and BPE is suddenly altered. This view contrasts with previous interpretations of local APE budgets, in which transfer between APE and BPE occurs only through diabatic processes. Here, the transfer may occur adiabatically via changes in z_r (although the transition could be triggered by diabatic processes).

Some part of the BPE can be considered to be *latent APE*, meaning that it is not available for reversible conversion to kinetic energy, but it can become so without the need for diabatic processes. In contrast, the rest of the BPE is inert, i.e. it will not become

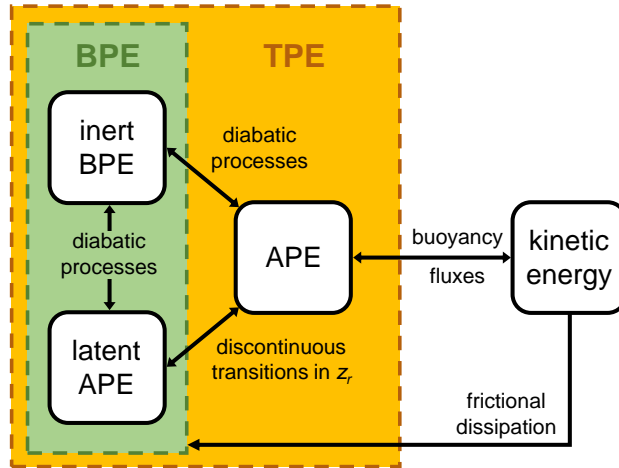


Figure 5.17: Possible transfers between forms of potential energy and kinetic energy when z_r can exhibit discontinuity. External energy sources (e.g. surface fluxes) are not included.

APE without diabatic processes altering the partition between BPE and APE. These forms of potential energy and the transfers between them are depicted in Figure 5.17. Discontinuous transitions may either convert latent APE to APE, as described above, or vice versa, if the transition moves the reference height closer to the parcel’s actual position (for example, if the parcel illustrated in Figure 5.15 were cooled from 341 K to 340 K). Latent APE can be generated from inert BPE by diabatic processes in much the same way that APE is generated, but latent APE must undergo a transition to APE before it can be converted to kinetic energy.

Temporal discontinuities in reference pressure p_{ref} were recognised by Pauluis (2007) to occur in the Lorenz APE theory, in which the reference state is obtained by adiabatic rearrangement of the domain. However, in that case, the term arising from changes in p_{ref} was shown to vanish when integrated over the whole atmospheric domain, due to the fact that the Lorenz reference state minimises total static energy. In the case of local APE theory, since APE density is calculated independently for each moist air parcel, there is no such guarantee of cancellation over a domain. Therefore, whilst local APE theory brings the advantages that a cheaper reference state can be used and the local energy conversions can be investigated, its main disadvantage may be the need to consider discontinuities in reference height and therefore in APE density.

To account for discontinuous behaviour of z_r , Eq. (5.57) should be reformulated as

$$\frac{De_a}{Dt} = \varepsilon_{\theta_{ei}} c_p \Pi \frac{D\theta_{ei}}{Dt} + \varepsilon_{r_t} L_s \frac{Dr_t}{Dt} - bw + \sum_{t_n \in \tau} c_n(r, z) \delta(t - t_n). \quad (5.58)$$

Here, δ is the Dirac delta function. It has been assumed that discontinuous re-partitioning from BPE to APE occurs at a countable set of times τ (which in particular must be true for a numerical model with a finite number of time steps). The coefficient c_n represents the jump in parcels' APE due to discontinuities at time t_n , and is defined by

$$c_n(r, z) = \lim_{\varepsilon \downarrow 0} \int_{z_r(t_n - \varepsilon)}^{z_r(t_n + \varepsilon)} b[\theta_{ei}(r, z, t_n), r_t(r, z, t_n), z'] dz'. \quad (5.59)$$

Note that $c_n(r, z) = 0$ for any parcel that does not exhibit discontinuous behaviour at time t_n .

It is difficult to work with delta functions on a discretised grid, because the discontinuous transitions will generally occur at some location between grid points. For this reason, in the APE budget the final term on the RHS of Equation (5.58) is diagnosed as a budget residual, computed only for grid points that show variations in z_r consistent with discontinuous behaviour. The residual is computed for parcels that exhibit a change in z_r of greater than the vertical grid spacing Δz in a single time step. Since the model time step is short, $\Delta t = 6$ s, this magnitude of change in z_r cannot be due to changes in θ_{ei} and r_t over the time step. It is also computed if a grid point has either radially or vertically neighbouring points with a difference in z_r greater than $10\Delta z$ (a higher threshold is used than for the temporal discontinuity because there may be large variations in θ_{ei} and r_t between grid points, so some larger changes in z_r are to be expected).

When presenting results from the axisymmetric model, the contribution to the time derivative of APE density from temporally discontinuous parcels is masked out, because otherwise these introduce high-magnitude noise to the budget and prevent analysis of the continuous evolution of APE due to diabatic processes. The conversion of APE to kinetic energy depends on the reference state, but does not exhibit any apparent temporal discontinuities. Therefore, the continuous evolution appears to be more physically relevant to intensification. It is not possible to assess the overall effect that the temporal discontinuities have on the evolution of the total APE, because the model data is only output every 5 h, whereas discontinuities happen on a single 6 s time step, and may contribute very differently from one time step to the next. Such sparse sampling is not adequate to capture the overall effect of the discontinuities, but it would not be feasible to perform the APE budget on the large amount of data required to capture processes occurring on the scale of single time steps.

With the issue of discontinuity addressed, it is now possible to compute the complete APE budget for the axisymmetric model. To ensure that no physically important effects

are being hidden by the temporal discontinuity masking, the final budget presented will be one in which temporal discontinuities vanish.

5.2.6 Available Potential Energy budget

This section presents the full budget for the APE of the axisymmetric model, using the initial sounding as the reference state. The budget is computed using the flux form of Equation (5.58),

$$\frac{\partial(\bar{\rho}e_a)}{\partial t} = -\nabla \cdot (\bar{\rho}e_a \mathbf{v}) + e_a \nabla \cdot (\bar{\rho} \mathbf{v}) + \varepsilon_{\theta_{ei}} c_p \Pi \frac{D\theta_{ei}}{Dt} + \varepsilon_{r_t} L_s \frac{Dr_t}{Dt} - \bar{\rho}bw + \text{discontinuities.} \quad (5.60)$$

The terms contributing to the time tendency of APE in a fixed volume are: the flux of APE through the volume boundaries; a source/sink of APE due to elastic mass divergence; the diabatic production/dissipation of APE, dependent on the APE production efficiencies $\varepsilon_{\theta_{ei}}$ and ε_{r_t} ; the conversion between APE and vertical kinetic energy; and spatial discontinuities in APE (temporal discontinuities are masked, as described in Section 5.2.5). The details of the finite-difference forms of the derivatives are included in Appendix B, along with verification of the budget accuracy.

The integral of the APE budget over the whole model domain is displayed in Figure 5.18. The chief budget contributor is the effect of spatial discontinuities in e_a . This makes the budget difficult to interpret physically, because it was discussed in Section 5.2.5 that the physical relevance of spatial discontinuities in e_a is unclear. The spatial discontinuities would vanish in a Lagrangian budget of APE density, and discontinuities in e_a are not likely to result in discontinuities in velocity.

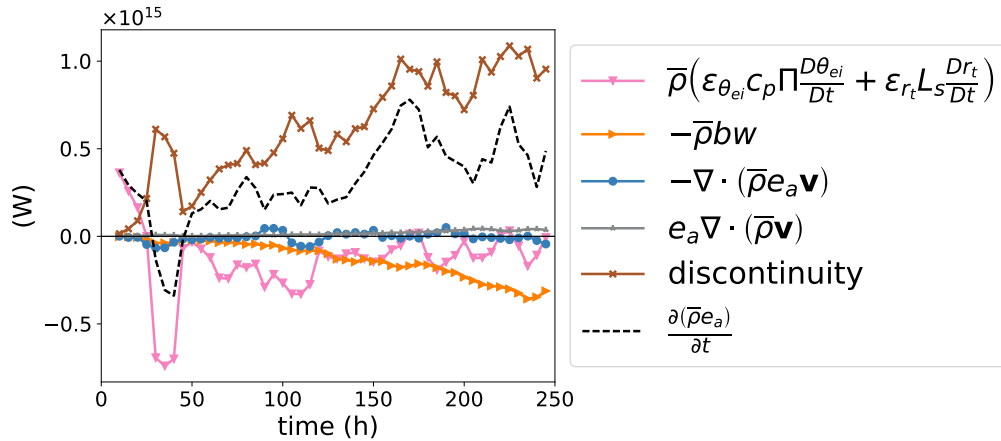


Figure 5.18: APE budget (5.60) integrated over the model domain. Time series have been smoothed using a 15 h running mean. The horizontal black line marks 0 W.

Figure 5.18 also shows that, during the intensification of the TC, the production of APE by spatial discontinuities is somewhat compensated for by the dissipation of APE due to diabatic processes. However, there is no clear physical reason why the two should be linked, and closer investigation of the data did not uncover any plausible mechanism for the relationship. During the mature stage of the TC, there is less compensation due to diabatic processes, and the majority of the APE generated via the spatial discontinuities is stored (i.e. contributes to $\frac{\partial(\bar{\rho}e_a)}{\partial t}$), rather than being converted to vertical kinetic energy. The storage of APE is associated with warming throughout the domain. This suggests that it is unhelpful to label the energy as *available*, since it does not generate kinetic energy in practice. A more desirable definition of APE would be one that resulted in a small storage term, so that APE production and kinetic energy generation would be directly connected.

Instead of considering the whole domain, the focus of the APE budget is therefore narrowed to the inner radial regions, where the majority of the generation of kinetic energy is expected to occur. In Figure 5.19, the APE budget is integrated over only the inner 300 km of the domain. This radial threshold is chosen such that all surface hurricane-force winds ($v > 33 \text{ m s}^{-1}$) are included within the region considered. This subset of the domain will henceforth be referred to as the *inner region*. From 170 h, there are no temporal discontinuities in APE density in the inner region, so it is assured that the temporal discontinuities are not having any effect on the TC's development in its mature stage.

In the inner region of the TC, spatial discontinuities still dominate during the early

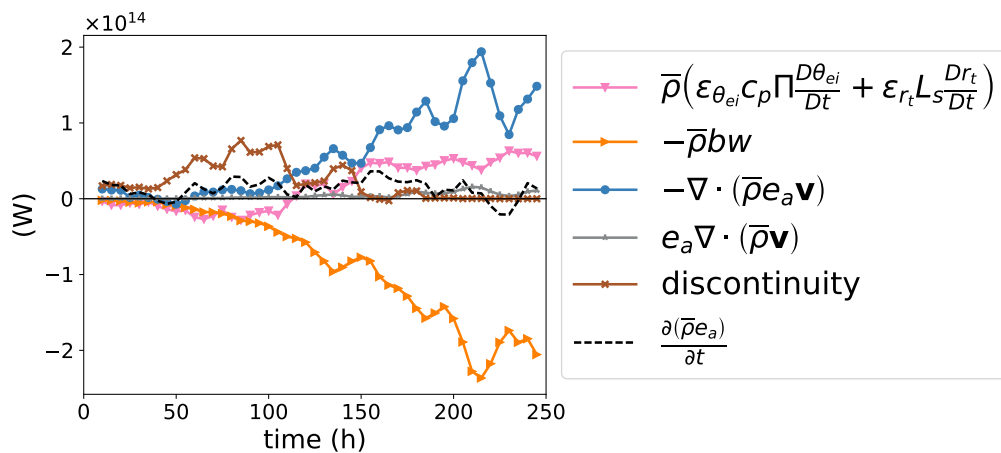


Figure 5.19: APE budget (5.60) integrated over all grid points in the inner region (within $r = 300 \text{ km}$ of the TC centre). Time series have been smoothed using a 15 h running mean. The horizontal black line marks 0 W.

stages of development, so it is difficult to use the APE budget to draw any conclusions about the intensification process. This points to a significant limitation of the local APE budget using the initial sounding reference state, which is that its physical meaning only becomes clear once the TC is generally warmer than the initialisation sounding. It can be seen from Figure 5.19 that after 150 h, once the TC has reached maturity, the contribution of spatial discontinuities to the budget disappears in the inner region, since all lower-level parcels have become positively buoyant relative to the initial sounding.

After 150 h, the predominant source of APE in the inner region is the flux of APE into the region. The vertical profile of the flux of APE across the $r = 300$ km surface at 200 hours (Figure 5.20) shows that this flux enters through the low-level radial inflow, with very little exported at upper levels. This can be contrasted with the vertical profile of the TPE flux in Figure 4.10, which also exhibited a potential energy influx at low levels, but in that case the export at upper levels was much higher, leading to a net TPE export.

The sum of the influx of APE into the region and the local diabatic production is approximately balanced by the conversion of APE to kinetic energy, demonstrating that the definition of the APE as “available” for conversion to kinetic energy is reasonable in this region—the definition does not significantly overestimate the portion of the potential energy that is actually available to be converted into kinetic energy.

It is therefore concluded that in the simulated mature tropical cyclone, the diabatic production of APE in the inner region is less important to the budget than the transport of APE into the region by the secondary circulation. To confirm where and how this

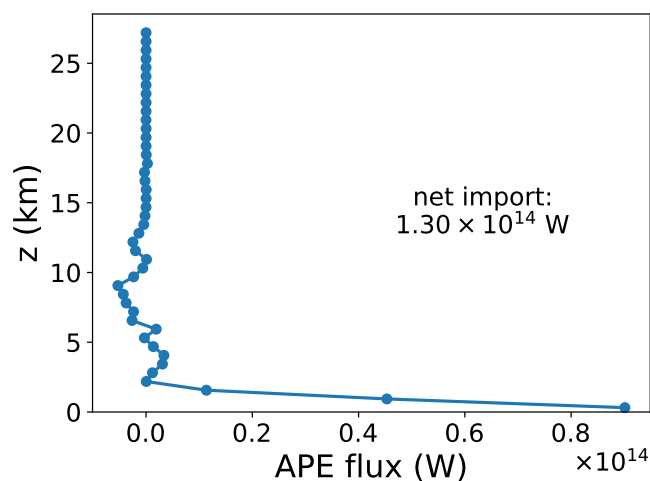


Figure 5.20: Flux of APE across the $r = 300$ km surface at 200 h. Blue circles indicate the v -grid vertical levels, at which the flux is calculated. Positive values correspond to an influx of APE to the inner region at that vertical level, while negative values correspond to an outward flux.

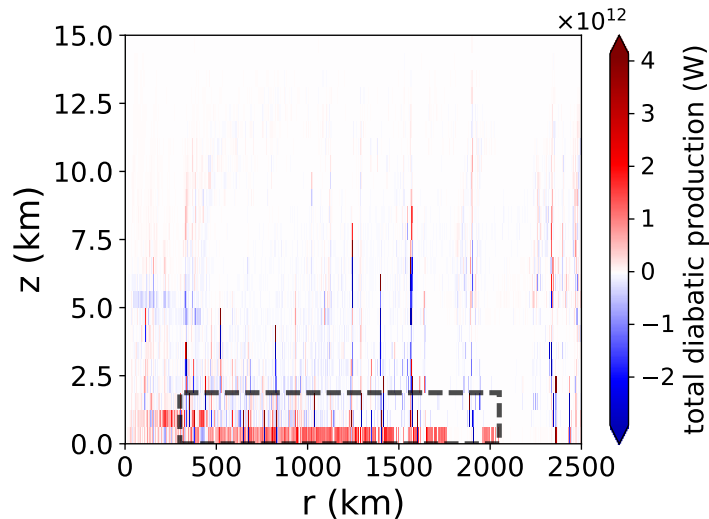


Figure 5.21: Total diabatic production of APE at 200 h. Dashed box marks region of inflow integration.

transported APE is originally produced, the total diabatic APE production at all grid points in the domain at 200 hours is plotted in Figure 5.21. The majority of APE production occurs in the lowest model level. The APE production is largest in parcels at 1000–1500 km, partly because parcels at larger radii represent a larger volume over which APE can be produced.

To determine the processes that produce the APE that is ultimately transported to the inner region, the total diabatic production is integrated over the inflow region shown by the dashed box in Figure 5.21, to produce the budget in Figure 5.22. The APE production by subgrid processes is split into the contribution from surface fluxes and the contribution from internal mixing (the latter being computed by subtracting the surface flux APE production from the total subgrid APE production). This budget confirms that surface fluxes are the primary source of APE, as was hypothesised in Chapter 2. In the inflow region, mixing acts as a sink of APE, with the imposed Newtonian radiative cooling also reducing APE slightly. This demonstrates that the choice of subgrid turbulence parameterisation affects the APE generated in the key production region, and therefore an APE budget could be used to link such parameterisation choices to the energy available for a TC.

The production of APE by surface fluxes in the inflow region is broken down further in Figure 5.23 to investigate the relative contributions of the sensible and latent heat fluxes. The contribution of the sensible heat flux is small compared to the latent heat flux. The production of APE driven by the surface moisture flux's contribution to latent

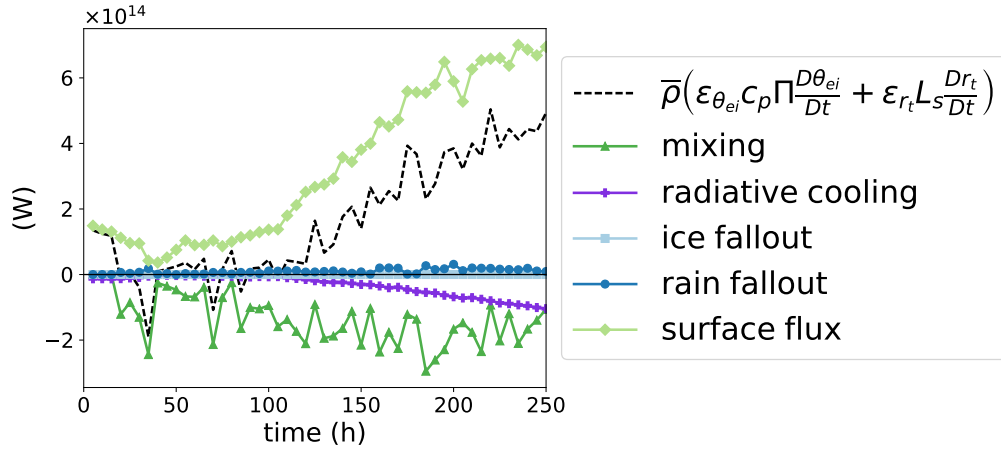


Figure 5.22: Components of total diabatic production of APE in inflow region. The horizontal black line marks 0 W.

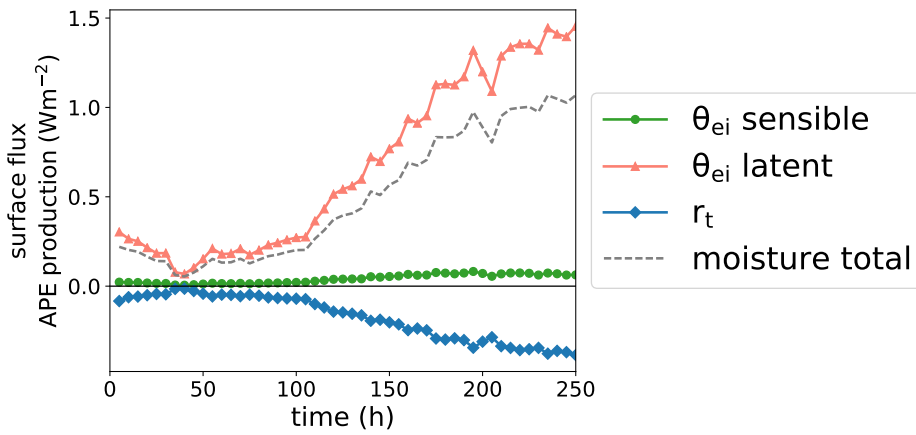


Figure 5.23: Contributions to APE production by components of surface flux, integrated over inflow region. The green circles show the production of APE via the θ_{ei} term due to surface fluxes of θ , while the pink triangles show the production via the θ_{ei} term due to surface fluxes of r_v . The blue diamonds show the production via the r_t term due to surface fluxes of r_v . The grey dashed line shows the total APE production by surface fluxes of r_v , combining their effects through the θ_{ei} and r_t production terms. The horizontal black line marks 0 W m⁻².

heat (via the θ_{ei} term) is reduced by about 25% due to the decrease in APE arising from the Gibbs penalty.

Finally, the APE budget for the inner region can be linked to its kinetic + available elastic energy budget, as defined in Equation 5.10. Figure 5.24 shows the integral of the kinetic + available elastic energy budget over the inner 300 km of the domain. Note that since the $\bar{\rho}bw$ term is the conversion of APE to kinetic energy, it appears with identical magnitude but opposite sign in Figures 5.19 and 5.24.

Once APE is converted to kinetic energy in the inner region, it is mostly exported as mechanical energy. Almost all the export of mechanical energy occurs through the $c_p \bar{\theta}_v \pi$

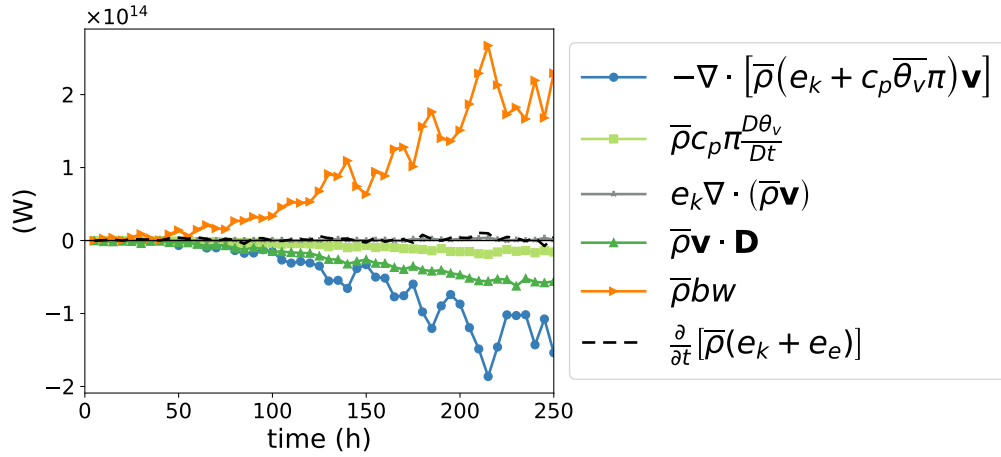


Figure 5.24: Kinetic plus available elastic energy budget for inner region. Time series have been smoothed using a 15 h running mean. The horizontal black line marks 0 W.

term, so it is due to pressure work on the volume boundary rather than the transport of kinetic energy out of the region. This pressure work, which results from the radial force exerted on the $r = 300$ km surface by the pressure perturbation π being moved with radial speed u , is an export term in both the inflow and the outflow because π and u are of matching sign in each case. Some kinetic energy is also dissipated by friction within the inner region. At an SST of 26.3°C , the subgrid dissipation becomes a stronger sink than the export of mechanical energy.

The overall picture of the energetics in the inner region of the axisymmetric model's mature TC is now complete: APE is produced by surface fluxes of latent heat outside the inner region and transported into the core by the low-level radial inflow; it is then converted into kinetic energy by vertical buoyancy fluxes, some is dissipated by friction, and the remainder is exported as mechanical energy via pressure work on the region boundary.

5.3 Discussion and Conclusions

5.3.1 Kinetic and available elastic energy budgets

Section 5.1 presented budgets for the three components of kinetic energy and the available elastic energy in the axisymmetric model. Over the whole domain, the source of kinetic + available elastic energy is the conversion from APE to kinetic energy via vertical buoyancy fluxes; this energy is mostly dissipated internally by friction in turbulent eddies or by friction at the sea surface. Some energy is stored: the integrated kinetic energy of the TC increases due to intensification and expanding wind fields, and the available

elastic energy increases as the pressure perturbation of the TC relative to the environment becomes larger. When the budget is taken over a smaller cylinder around the TC centre, the conversion of APE to kinetic energy is still the source of kinetic + available elastic energy, but the export of mechanical energy from the region, via pressure work on the region boundary, becomes an important sink of energy.

Whilst APE has previously been recognised as the source of energy for a TC (Anthes and Johnson, 1968; Tang and Emanuel, 2012; Wong et al., 2016), the traditional view of energetics states that kinetic energy is generated by the acceleration of inflowing parcels by the radial pressure gradient (e.g. Anthes, 1974). It is important to recognise that the results of Section 5.1 are not at odds with this view—this conversion to radial kinetic energy is implicit within the total kinetic + available elastic energy budget. The vertical kinetic energy generated by conversion from APE is very quickly converted to available elastic energy via the vertical pressure gradient, resulting in the total vertical kinetic energy in the model being much smaller than the horizontal kinetic energy. The work done by the radial pressure gradient therefore still generates most of the kinetic energy in the modelled TC. However, considering the total kinetic energy budget rather than just the horizontal kinetic energy budget is crucial to linking the generation of APE to the generation of kinetic energy, and hence linking diabatic processes to the ultimate intensification of the TC.

Recent work has highlighted the non-uniqueness of the formulation of the kinetic energy budget for a TC (Smith et al., 2018), a problem originally addressed by Smith (1970) for open atmospheric systems in general, as reviewed in Section 2.2. The available elastic energy budget equation (5.9) could equivalently have been written as

$$\frac{\partial(\bar{\rho}e_e)}{\partial t} = -c_p\pi\nabla \cdot (\bar{\rho}\bar{\theta}_v\mathbf{v}) + \bar{\rho}c_p\pi\frac{D\theta_v}{Dt}, \quad (5.61)$$

and the conversion with kinetic energy maintained by reformulating the kinetic energy budget (5.7) as

$$\frac{\partial(\bar{\rho}e_k)}{\partial t} = -\nabla \cdot [\bar{\rho}(e_k + c_p\bar{\theta}_v\pi)\mathbf{v}] + c_p\pi\nabla \cdot (\bar{\rho}\bar{\theta}_v\mathbf{v}) + \dots \quad (5.62)$$

Smith et al. (2018) refer to the version of the kinetic energy budget used in Section 5.1, which features a radial kinetic energy source term of the form $-\mathbf{v}_h \cdot \nabla_h p'$, as the *Anthes* formulation of the kinetic energy budget (p' is the pressure perturbation, and the subscript h denotes the horizontal component of a vector). The version in Equation

(5.62), which instead features the work by the perturbation pressure, $p'\nabla_h \cdot \mathbf{v}_h$, is referred to as the *Gill* formulation, since it is the one used by Gill (1982).

Smith et al. (2018) concluded that the Anthes formulation was preferable to the Gill formulation, in part because it gave a smaller boundary flux of kinetic energy. However, if the total kinetic + available elastic energy budget is considered, then the sum of the Gill formulation equations (5.61) and (5.62) gives precisely the same boundary flux of mechanical energy, $-\nabla \cdot [\bar{\rho} (e_k + c_p \bar{\theta}_v \pi) \mathbf{v}]$, as was seen when using the Anthes formulation in Equation (5.10). It is therefore concluded that the budget of kinetic + available elastic energy is more useful than the budget of kinetic energy only, because it eliminates the ambiguity in the boundary flux of energy based on an arbitrary choice of budget formulation. Whereas the two kinetic energy budgets of Smith et al. (2018) have different sources of kinetic energy and different boundary fluxes of kinetic energy out of the budget region, using a total kinetic + available elastic energy budget means that the conversion from APE is treated as the source of energy, and the boundary flux of mechanical energy does not change when the budgets are rearranged.

The definitions of the pressure perturbations and APE have to this point been based on the use of the model's initialisation sounding as a reference state. This reference state is particularly relevant to the energetics of the axisymmetric model because the model equations are defined relative to the initial state. This is why, for example, the frictional dissipation of kinetic energy, which is independent of reference state, approximately balances the conversion from APE to kinetic energy defined using the initial reference state. However, in the real world, the equations of motion are not defined relative to a reference state in this way, and since the reference state in local APE theory is arbitrary, it is not obvious how to choose the most appropriate measure of APE to study the energetics. This issue will be investigated in Chapter 6.

5.3.2 APE budget

Section 5.2 demonstrated that it is possible to construct a budget of moist Available Potential Energy for a TC, based on the local formulation of APE theory. This allows a complete budget of the available energetics, down to the diabatic processes responsible for generating APE. In the mature TC simulated by the axisymmetric model, the main source of APE production is latent surface heat flux. The production of APE occurs mostly in the outer part of the TC, and the APE is then advected into the inner region of the storm where it is converted to kinetic energy.

One of the main findings in terms of the practical implementation of local APE theory is that APE density is not necessarily a continuous function of space and time; discontinuities in e_a can contribute significantly to the budget. This provides an obstacle to interpreting TC intensification in terms of APE theory, but it is a major fundamental result for local APE theory itself. The energy transfers that occur in the presence of discontinuities can be understood by introducing the concept of latent APE. This is the portion of the BPE that could become APE via a discontinuous transition in reference height, rather than only via continuous evolution through diabatic processes.

The APE budget was presented for the J30.3 run in Section 5.2.6, but budgets with small discontinuity terms have also been successfully constructed for the N26.3, N28.3 and N30.3 runs, which yield the same conclusions (the J30.3 budget was preferred for presentation because the temporal and spatial discontinuity terms become exactly zero in the inner region of the domain— $r < 300$ km—once the TC reaches maturity, so there are no questions regarding their impacts on budget closure). Implementing budgets for these other runs required adapting the size of the inner region to account for differences in TC size, and altering $\tilde{\Pi}$ to better represent the effective pressure at which APE production occurs in the runs.

Attempted APE budgets for the J26.3 and J28.3 runs exhibited large contributions from spatial discontinuities throughout the run, even when integrating over very small inner regions. This poses an obstacle to the interpretation of the APE budget because the physical consequences of the discontinuities are not clear. This suggests that it is preferable to use a reference state that is neutral to convection if discontinuities are to be minimised. The J30.3 run still eliminates discontinuities despite its use of the Jordan sounding because the SST is sufficiently high to heat/moisten all inner parcels enough that they become buoyant relative to the initial sounding.

It may be possible to produce a completely discontinuity-free budget of APE density if an exact thermodynamic framework were employed and a conditionally neutral sounding were used as reference state. The discontinuity illustrated in Figure 5.15 arises because the reference state exhibits conditional instability for a lifted parcel, which allows parcels to have one level of neutral buoyancy much higher than another. If there were no conditional instability present, discontinuous transitions in z_r might not be possible. However, practically speaking, the neutral environment of the N26.3 run does not eliminate discontinuities from the budget—this may be due to the model’s thermodynamic approximations.

The difficulty of navigating discontinuities in APE density means that it is unlikely that the full APE budget could be flexibly applied to output from climate models, which would produce TCs over a range of SSTs and in different environments, and would not necessarily use exact thermodynamics. Although an APE framework may provide physical insight even if it cannot easily be applied to all models or cases, it would be preferable to have diagnostics that could be widely implemented, for example to facilitate model intercomparison. Chapters 6 and 7 will focus on developing some local APE-based metrics that provide information about the model's treatment of diabatic processes and intensification, but are not as sensitive to discontinuities.

The results of Section 5.2.6 are robust to changes in initial conditions, provided that the initial conditions do not lead to widespread discontinuous behaviour of e_a . Most of the APE production in the domain is due to latent heating by surface moisture fluxes. The influx of APE to the inner region of the TC was shown to be a larger contributor to the APE budget than local diabatic production. This makes sense in the context of the results of previous TC budgets; the latent energy budgets performed on numerical simulations by Kurihara (1975) and Tuleya and Kurihara (1975) showed that in the inner area of the simulated TCs, evaporation was negligible compared to moisture flux convergence. Since the majority of APE is being generated by surface fluxes of moisture, this is the equivalent to the dominance of APE flux convergence in the results presented here. The dominance of moisture convergence over local evaporation can also be seen in budgets of more realistic, three-dimensional TC simulations, such as the moisture budgets of Hurricanes Ivan and Katrina by Trenberth et al. (2007), which used the Weather Research and Forecasting (WRF) model at a convection-permitting horizontal resolution of 4 km.

The energetics of the TC from the moist APE viewpoint can now be compared to TC energetics in terms of total potential energy (TPE) and dry APE. From the TPE viewpoint, the source of the TC's energy is latent energy, which is produced by surface fluxes of moisture. This is then converted into TPE when latent heat is released by condensation. The TPE is converted to kinetic energy with a very low efficiency, typically on the order of 5% (Kurihara, 1975; Tuleya and Kurihara, 1975; Hogsett and Zhang, 2009). The APE budget for the inner region in Figure 5.19 shows that, at least in the core region of high winds, almost all the APE transported into or produced locally within the region is converted into kinetic energy. This demonstrates that the low efficiency of conversion from TPE to kinetic energy is a result of a suboptimally-defined reservoir of potential energy; most of the TPE is never available to be converted into kinetic energy, but what

is available is indeed converted. Chapter 6 will further assess how much of the APE is converted to kinetic energy, in order to determine the optimal reference state for defining the APE of the TC.

The source of APE in a TC differs between the full moist APE and theories based on the dry potential temperature θ . The budgets in Section 5.2.6 confirmed that the latent surface heat flux is the key generator of moist APE, whereas in a dry framework the source of APE is the latent heat released during condensation (Anthes and Johnson, 1968; Nolan et al., 2007). Whilst the release of this latent heat is undoubtedly a key influence on the dynamics of the TC (and is implicitly accounted for in the moist APE theory, being released when moist parcels are lifted reversibly and adiabatically to their reference heights), treating it as the source of APE disguises the role of the surface moisture fluxes. An extra step is required in the energy cycle compared to the moist APE theory: the surface fluxes produce latent energy, which is converted to dry APE via the latent heat release, whereas in the moist theory the surface fluxes generate APE directly.

One consequence of this is that moist APE theory may be more easily linked to boundary layer processes. The properties of boundary layer air will affect the efficiency at which moist APE is generated, and mixing will change the moist APE of parcels in the boundary layer. Since the spin-up of the maximum winds occurs in the boundary layer (Smith et al., 2009), an APE theory that incorporates boundary layer processes would appear to be preferable.

The efficiency of a TC has previously been defined in terms of the percentage of TPE generated by latent heat release that is converted to kinetic energy (Schubert and Hack, 1982). Efficiency theories such as this, which do not account for boundary layer dynamics or thermodynamics, were criticised by Smith and Montgomery (2016) as having little relevance to real-world intensification processes, since the boundary layer plays such a key role. In light of the APE budget results from this chapter, it is suggested that a more relevant energetic efficiency metric can be constructed based on moist APE production efficiencies. This would prevent the appearance of low efficiencies arising from the fact that TPE is never all available for conversion to kinetic energy, and allow processes affecting APE in the boundary layer to be accounted for. A definition for moist APE-based efficiency is developed and explored in Chapter 7. This chapter will also use the efficiency of moist APE generation to link available energetics to the widely established theory of potential intensity, demonstrating a further advantage of the moist APE approach.

Previous energy budgets based on both TC observations and numerical simulations

noted large exports of TPE at upper levels (Palmén and Riehl, 1957; Kurihara, 1975; Tuleya and Kurihara, 1975), and Anthes (1974) suggested that the export of heat at high levels could result in a large APE boundary flux. In contrast, when using the local moist APE framework there is relatively little export of APE at higher levels compared to the import at lower levels, since parcels in the outflow are much closer to their reference heights and therefore have less APE density.

Considering only the available energetics rather than the total energetics leads to the conclusion that the export of energy from inner regions of the TC is due to pressure work at the region boundary rather than simply the transport of TPE away from the centre. The small APE export demonstrates that the vast majority of the imported APE is either converted to kinetic energy or stored in the warm core vortex; both of these options are related to a strengthening of the TC (in the case of the warm core storage, this is not an instantaneous strengthening of wind speed, but would be associated with a drop in central pressure and an increase in the reservoir of APE that may be converted to kinetic energy at a later time). Therefore the APE supplied to the inner region contributes directly to intensification, whereas much of the latent energy supplied to the inner region does not directly contribute to the increase of kinetic energy, since it is simply converted to TPE and then exported back out of the region at upper levels.

The work in this chapter has provided a basic picture of how moist local APE theory can be applied to a TC in the axisymmetric model. The diabatic APE production (which is mostly due to surface fluxes of moisture), the influx of APE to the core region of high winds, and the conversion of APE to kinetic energy have all been computed. However, the results so far have all been based on the definition of APE with respect to a time-independent reference state, taken to be the initial environmental sounding of the model. In local APE theory, any stable balanced reference state may be used, and it is not clear which reference state provides the “best” definition of APE. The next chapter compares the suitability of different reference states for defining APE in an axisymmetric TC, based on their predictions of kinetic energy generation.

Chapter 6:

Optimal choice of reference state for studying available energetics in tropical cyclones

Chapter 5 developed budgets of kinetic energy, available elastic energy and available potential energy for the axisymmetric tropical cyclone model designed by Rotunno and Emanuel (1987). Since the axisymmetric model equations are formulated relative to a base state defined by an initial sounding, it was particularly relevant to calculate the available energies using this initial sounding as a reference state. However, other reference states could be used, which would affect the APE density, the APE production efficiencies and the conversion of APE into kinetic energy. It is therefore of interest to investigate the physical implications of using different reference states, in order to ascertain whether there are objective physical criteria that can justify the use of one reference state over another for studying available energetics in tropical cyclones.

It has been suggested that, when using local APE theory, suitable reference states could be constructed by taking the horizontal mean properties of a domain (Tailleux, 2013b), or using sorting algorithms (Wong et al., 2016). There has not been a study comparing the physical understanding that can be obtained using different reference states for a practical example in a numerical model. Therefore, it is difficult to know which reference state should be preferred when calculating APE density.

In this chapter, the simulated TCs from the axisymmetric model described in Chapter 4 are used as concrete examples that permit a comparison of the usefulness of various reference states. Section 6.1 describes the reference states that have been tested, and the reasons for choosing each of these. Section 6.2 then introduces an objective criterion

for assessing reference state suitability, which is used to compare these reference states, and explores the impact that a change of reference state has on the APE and associated properties.

6.1 Possible reference states

The reference states that have been tested for the axisymmetric model fall into three categories. The first category is Lorenzian reference states, which represent a rearrangement of atmospheric mass, conserving entropy and total water content, into a configuration that minimises total potential energy. Therefore, these reference states aim to compute the maximum kinetic energy that could be released through reversible adiabatic motion. As was reviewed in Section 2.1.1, there is no analytic solution for Lorenz's reference state in a moist atmosphere, so heuristic sorting algorithms must be employed. These algorithms seek to approximate a minimised TPE state, which may be a local rather than a global maximum. Two sorting algorithms are tested here: the *top-down* and *bottom-up* methods designed by Wong et al. (2016). These are the only sorting algorithms that have been designed for use with a two-dimensional moist atmosphere.

The second category encompasses reference states that are defined by a vertical atmospheric profile, which is not based on an adiabatic rearrangement of mass, but merely acts as a representation of a hydrostatic environment relative to which APE density may be computed. The reference state profile may evolve in time but has no radial dependence. Reference states falling into this category will be referred to as *environmental* reference states. For example, an environmental reference state could be specified by an atmospheric sounding, such as the model initialisation sounding used in Chapter 5, or a horizontal domain average of thermodynamic state variables. When using either a Lorenzian or an environmental reference state, APE is being measured relative to a quiescent, barotropic atmosphere.

The final reference state is a vortex in thermal wind balance. Based on the work of Andrews (2006) and Codoban and Shepherd (2003, 2006), as reviewed in Section 2.1.3 and revisited by Tailleux and Harris (2020, Appendix C), the APE of a TC is expected to be constrained by its balanced dynamics. This reference state can be used to measure the APE relative to the balanced part of the flow.

This section describes the construction of the different reference states and, where necessary, the modifications made to the computation of APE density and production

coefficients. Henceforth, the subscript 0 will be used to denote reference state variables, rather than an overbar, since the overbar specifically denoted the initial sounding in the model equations.

6.1.1 Lorenzian reference states

Top-down sorting

The *top-down* sorting method for constructing the reference state of a two-dimensional moist atmospheric domain was designed by Wong et al. (2016); it is similar to the one-dimensional version described in Section 3.2.4. A two-dimensional domain of parcels is rearranged into a single column covering the entire surface area of the domain (i.e. radial variation is removed).

For each model time step, the reference pressure level nearest the surface, p_n , is taken to be the average pressure in the lowest model level at that time step. The reference pressure at the top of the domain, p_1 , is then determined based on the value of p_n and the total mass and surface area of the domain, such that the final reference column can exist in hydrostatic balance. All n parcels in the domain at the time step are lifted reversibly and adiabatically to p_1 . The new density of each lifted parcel is calculated and the least dense parcel is assigned to the reference pressure p_1 . The next pressure level p_2 is computed based on the mass of the assigned parcel and the assumption of hydrostatic balance—effectively, the assigned parcel is stretched horizontally to cover the whole area of the domain to determine what thickness Δp it should occupy (see Figure 3 of Wong et al. (2016) for a schematic illustration). Then all the parcels are lifted to p_2 , and so on until all parcels have been assigned a reference pressure. This creates the *top-down* reference state profile, which varies with height and time. The APE computed using the top-down reference state is intended to be an approximation of the Lorenz APE, representing the maximum amount of kinetic energy that could be generated under reversible adiabatic transformations.

Bottom-up sorting

The *bottom-up* reference state is computed similarly to the top-down reference state, but the sorting algorithm first moves all parcels to the highest pressure (lowest height) p_n , which is taken to be the average pressure in the lowest model level, and works upwards. The bottom-up sorting method was intended by Wong et al. (2016) to minimise the release of CAPE that could not be realised in practice. The reference state obtained by

bottom-up sorting can be considered as a local minimum in potential energy.

The reference profiles θ_0 and r_{v_0} obtained using top-down and bottom-up sorting can exhibit rapid variation with height. Therefore, it is not practical to use the local APE theory approach of lifting parcels along the reference profiles. Instead, since the sorting algorithms determine the reference pressure of each parcel, the APE production coefficients can be computed using the exact forms of Equation (5.40) and (5.41). The APE density itself is not computed relative to the Lorenzian reference states here.

6.1.2 Environmental reference states

Initial sounding

The *initial* reference state is the model's initialisation sounding as described in Chapter 4. This is the reference state used to obtain the energy budgets in Chapter 5. The APE computed using the initial reference state is the APE relative to the model's initial quiescent environment, before the vortex is introduced, or equivalently to the far-field environment.

Mean profile

The *mean* reference state uses time-varying radial averages of θ and r_v (weighted by the volume represented by each grid point), and the Exner pressure Π that is in hydrostatic balance with these. When using this reference state, APE is computed relative to the quiescent environment with the mean properties of the model domain. This may be preferable to using the initial reference state because it will be able to account for general heating and moistening across the domain, which alters the environment in which the TC is situated.

Cold profile

The *cold* reference state is computed by taking the initial sounding and subtracting 5 K from θ . The r_v profile is then determined such that the relative humidity profile is the same as in the initial state. Finally, Π is adjusted to hydrostatic balance. APE is therefore computed relative to a much colder environment than the one inhabited by the model TC. The motivation behind this choice was to eliminate discontinuities in reference height; when measured relative to this cold sounding, all parcels in the domain are buoyant at the start of the model run, and therefore jumps in reference height do not occur.

Each of the environmental reference states is displayed on the tephigram in Figure 6.1, at 150 h into the J30.3 model run (recall that the model initial conditions are denoted

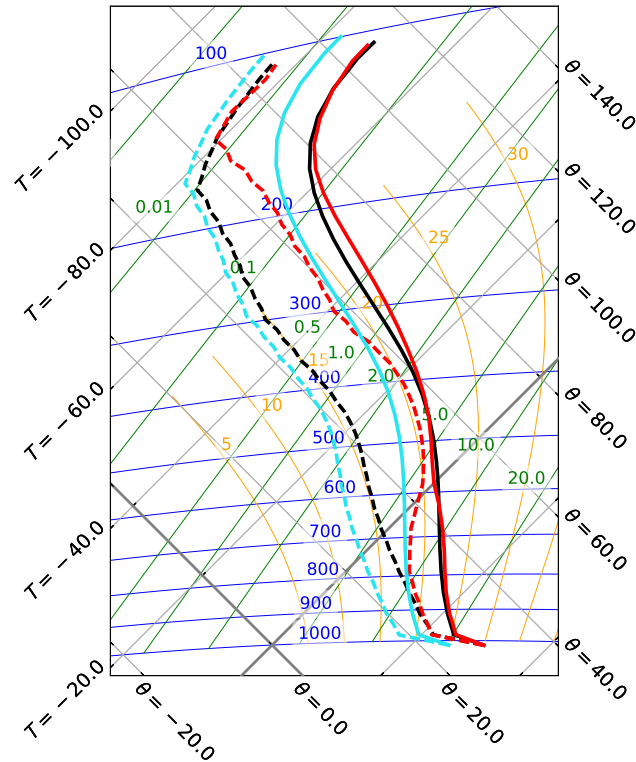


Figure 6.1: Tephigram showing environmental reference states for the J30.3 model run. Grey diagonal lines are isotherms (constant temperature T) and dry adiabats (constant dry potential temperature θ) as labelled (both in $^{\circ}\text{C}$). The thicker grey lines show the isotherm $T = 0^{\circ}\text{C}$ and the dry adiabat $\theta = 0^{\circ}\text{C}$. Blue lines are isobars, labelled in hPa. Green lines are lines of constant saturation mixing ratio, labelled in g kg^{-1} . Orange curves show moist adiabats, labelled by their value of equivalent potential temperature θ_e in $^{\circ}\text{C}$. The black lines show the initial reference state, with the solid black line being the temperature profile and the dashed black line the dewpoint temperature profile. Similarly, the red lines show the profiles defining the mean reference state at 150 h, and the light blue lines show the cold reference state.

using a letter to represent either the Jordan (J) or neutral (N) initialisation sounding, followed by the SST). The mean reference state is warmer than the initial reference state throughout most of the troposphere, with a particularly notable warming in the 200–400 hPa layer due to latent heat release. The mean state is also moister than the initial state throughout the mid-troposphere. This indicates that the model domain is generally warming and moistening over time. As expected, the cold reference state has a lower temperature and dewpoint temperature than the initial state at all levels, since it is constructed to be colder and contain less water vapour.

For each of the environmental reference states, the APE density and production coefficients are calculated using the method described in Chapter 5, replacing $\bar{\theta}$ with θ_0 and so on.

6.1.3 Balanced vortex reference state

To investigate the possibility of using a non-resting (radially-varying) reference state, this section introduces a method for computing APE density relative to a vortex in thermal wind balance. At each time t , the azimuthal wind speed of the reference vortex is set as the azimuthal wind field from the model, $v_0(r, z, t) = v(r, z, t)$. The thermodynamic fields that hold this vortex in hydrostatic balance,

$$\frac{\partial \Pi_0}{\partial z} = -\frac{g}{c_p \theta_{v_0}}, \quad (6.1)$$

and gradient wind balance,

$$\frac{\partial \Pi_0}{\partial r} = \frac{1}{c_p \theta_{v_0}} \left(f v_0 + \frac{v_0^2}{r} \right), \quad (6.2)$$

are then found using the method of Nolan and Montgomery (2002): iterating between integrating inwards to gradient wind balance and adjusting vertically to hydrostatic balance, the thermodynamic fields converge to a reference state determined by v_0 , θ_{v_0} and Π_0 .

Whilst this method determines a reference virtual potential temperature θ_{v_0} , a decomposition into θ_0 and r_{v_0} is required in order to continue using the model's approximation for buoyancy, Equation (4.5). It is assumed that $r_{v_0} = r_v$ and then θ_0 is calculated from this. This decomposition is non-unique, but the overall results of the APE calculations were found to be insensitive to choosing a different reference mixing ratio, for example using $r_{v_0} = \bar{r}_v$.

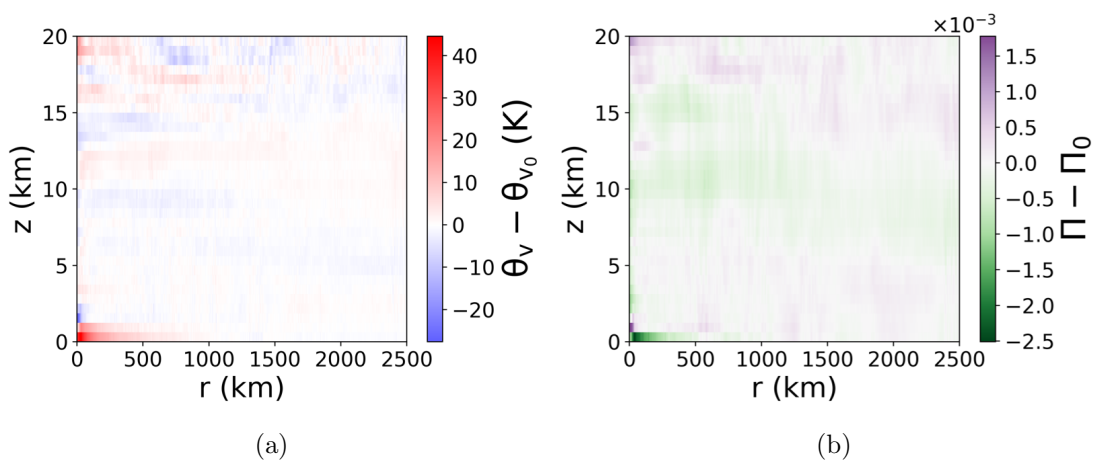


Figure 6.2: Difference in (a) virtual potential temperature θ_v and (b) Exner pressure Π between TC and balanced vortex reference state at 150 h.

The differences between the actual modelled TC and the balanced reference vortex are shown in Figure 6.2. The largest differences are found in the lowest vertical levels, where the balanced vortex has much lower θ_v (Figure 6.2a) and higher pressure (Figure 6.2b) near the centre. These differences at low levels can be explained by the effects of friction in the boundary layer. In the balanced vortex, gradient wind balance is assumed between the radial pressure gradient and the sum of the Coriolis and centrifugal forces. However, in the actual modelled TC, surface friction will act to reduce these forces, leading to an inward backing of the flow. Hence parcels that experience this surface friction will not be in balance, leading to large differences between their actual properties and their properties in the balanced reference state.

The lack of gradient wind balance in the lowest model level has been confirmed by comparing the modelled radial profile of Π to the profile obtained by integrating Π inwards from the environment under the assumption of gradient wind balance (i.e. completing the first step in the procedure to obtain the reference vortex). These two profiles (not shown) show much more disparity in the lowest level than in any other vertical level, indicating that gradient wind balance approximately holds except in parcels affected by surface friction.

The properties of the balanced vortex are in accordance with the conclusions of Bui et al. (2009), who found that a balanced vortex solution in a three-dimensional TC model could capture most of the dynamics of the azimuthally-averaged circulation, except in the

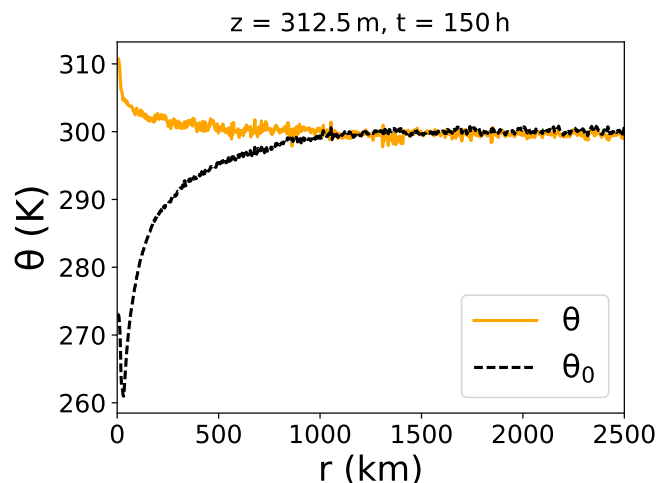


Figure 6.3: Radial profiles of potential temperature θ demonstrating the cold-core nature of the balanced vortex reference state at low levels. The orange solid line shows θ in the lowest atmospheric vertical level of the axisymmetric model at 150 h for the J30.3 TC. The black dashed line shows the equivalent profile for the corresponding balanced vortex reference state.

boundary layer, where surface friction resulted in significant imbalance. The departure from gradient wind balance in the boundary layer means that the computed balanced vortex is cold-cored at the lowest levels (both here and in Bui et al. (2009)), as plotted in Figure 6.3. Low-level air parcels are therefore likely to be buoyant relative to this cold core, and thus may be expected to possess more APE than other parcels.

Using a radially-varying reference state necessitates a slightly different approach to computing APE density compared to the one used in Chapter 5. When using a reference state that varied only in the vertical, it was acceptable to simply lift parcels vertically to their LNB, since a parcel's radial location was irrelevant to the calculations once θ_{ei} and r_t were known. With the introduction of the non-resting state, the path along which a parcel is lifted to its LNB must be more carefully defined.

In addition to θ_{ei} and r_t , the specific angular momentum

$$M = rv + \frac{fr^2}{2} \quad (6.3)$$

is now also used as a conserved variable, as was done by Andrews (2006) and Codoban and Shepherd (2006) when using an axisymmetric vortex as a reference state. The conservation of M in the axisymmetric TC in the absence of turbulent and frictional effects can be derived from the model's azimuthal wind equation (4.3):

$$\frac{DM}{Dt} = rD_v, \quad (6.4)$$

where D_v is the parameterised effect of subgrid turbulent and frictional processes on the azimuthal wind speed.

The APE density of a moist air parcel with respect to the vortex reference state is therefore computed by lifting it reversibly and adiabatically along a surface of constant angular momentum (interpolating the state variables onto this surface) until it reaches an LNB. Unlike the method used with the profiles that vary in the vertical only, this approach uses information about the trajectory the parcel is expected to follow in the TC.

Since the reference state now varies radially, the vertical buoyancy force is replaced with a generalised buoyancy force based on the one defined by Smith et al. (2005) for tropical cyclones and other rotating vortices, which includes the effect of radial forces.

When using the vertical buoyancy force,

$$b(\theta_{ei}, r_t, z) = g \frac{\alpha(\theta_{ei}, r_t, \Pi_0(z)) - \alpha_0(z)}{\alpha_0(z)} \quad (6.5)$$

the APE density was defined in Equation (5.20) as

$$e_a = \int_z^{z_r} b(\theta_{ei}, r_t, z') dz'. \quad (6.6)$$

In terms of the two-dimensional coordinate $\mathbf{x} = (r, z)$, the generalised buoyancy force is defined as

$$\mathbf{b}(\theta_{ei}, r_t, M_0, \mathbf{x}, t) = \mathbf{g} \frac{\alpha(\theta_{ei}, r_t, \Pi_0(\mathbf{x}, t)) - \alpha_0(\mathbf{x}, t)}{\alpha_0(\mathbf{x}, t)}, \quad (6.7)$$

where \mathbf{g} is the effective gravity

$$\mathbf{g} = (C_0, g), \quad (6.8)$$

which accounts for the radial force $C_0 = -\left(fv_0 + \frac{v_0^2}{2}\right)$ experienced by the parcel in the reference vortex. C_0 is the sum of the centrifugal and Coriolis forces. Henceforth, whenever *buoyancy* is referred to in the context of the balanced vortex, this refers to the generalised buoyancy (6.7).

Note that since here the reference vortex has been defined by $v_0 = v$, the effective gravity \mathbf{g} is identical to the one defined by Smith et al. (2005), but for any other choice of balanced vortex reference state this would not be true. In the general case, an additional term would be required in the APE budget to account for forces arising from the difference between v and v_0 . This is investigated further for the case of dry vortices in Appendix C. The particular definition of the vortex here also means that $M_0 = M$, so that conserving a parcel's angular momentum is equivalent to conserving its reference angular momentum.

The APE density using the generalised buoyancy force is, analogously to Equation (6.6) for the vertical case,

$$e_a = \int_{\mathbf{x}}^{\mathbf{x}_r} \mathbf{b}(\theta_{ei}, r_t, M_0, \mathbf{x}', t) \cdot d\mathbf{x}'. \quad (6.9)$$

This equation defines APE density as the work done by the generalised buoyancy force when a parcel is lifted reversibly and adiabatically along a surface of constant angular momentum, from its actual position $\mathbf{x} = (r, z)$ to its reference position $\mathbf{x}_r = (r_r, z_r)$. In addition to a reference height, the parcel now also possesses a *reference radius*.

The reference position is defined as an LNB similarly to the reference height of

Chapter 5, but now with respect to the generalised buoyancy:

$$\mathbf{b}(\theta_{ei}, r_t, M_0, \mathbf{x}_r, t) = 0. \quad (6.10)$$

Both components of the generalised buoyancy must be zero, which is satisfied if and only if

$$\alpha(\theta_{ei}, r_t, \Pi_0(\mathbf{x}_r, t)) = \alpha_0(\mathbf{x}_r, t). \quad (6.11)$$

The conservation of angular momentum provides the second constraint necessary to calculate the reference position, namely that

$$M_0(\mathbf{x}_r, t) = M_0(\mathbf{x}, t). \quad (6.12)$$

Analogously to the procedure used in Chapter 5 to find the reference height, the reference position is defined as the first point satisfying Equation (6.11) that is encountered when a parcel moves reversibly and adiabatically along a surface of constant angular momentum in the direction of its *in situ* generalised buoyancy.

The APE production coefficients $G_{\theta_{ei}}$ and G_{r_t} have the same form as in the case of the resting reference state. This can be shown by using the thermal wind balance relation for the reference state,

$$\mathbf{g} = -\left(fv_0 + \frac{v_0^2}{r}, -g\right) = -\alpha_0 \nabla p_0, \quad (6.13)$$

to rewrite the line integral

$$\begin{aligned} G_{\theta_{ei}} &= \frac{\partial e_a}{\partial \theta_{ei}} \\ &= \frac{\partial}{\partial \theta_{ei}} \int_{\mathbf{x}}^{\mathbf{x}_r} \frac{\alpha(\theta_{ei}, r_t, p_0(\mathbf{x}, t))}{\alpha_0(\mathbf{x}, t)} \mathbf{g} \cdot d\mathbf{x}' \end{aligned} \quad (6.14)$$

as

$$G_{\theta_{ei}} = \frac{\partial}{\partial \theta_{ei}} \int_{p_0(\mathbf{x}_r)}^{p_0(\mathbf{x})} \alpha(\theta_{ei}, r_t, p') dp', \quad (6.15)$$

where $p' = p_0(\mathbf{x}', t)$. From this point the logic of Equation (5.34) can simply be repeated to obtain the production coefficient in the form

$$G_{\theta_{ei}} = c_p \frac{T_h - T_r}{\theta_{ei}}, \quad (6.16)$$

where now $T_h = T(\theta_{ei}, r_t, p_0(\mathbf{x}, t))$ and $T_r = T(\theta_{ei}, r_t, p_0(\mathbf{x}_r, t))$. Similarly,

$$G_{ri} = \frac{1}{(1 + r_t)^2} [\mu_h - \mu_r + (T_h - T_r) R_d \ln p_{00}], \quad (6.17)$$

with $\mu_h = \mu(\theta_{ei}, r_t, p_0(\mathbf{x}, t))$ and $\mu_r = \mu(\theta_{ei}, r_t, p_0(\mathbf{x}_r, t))$. Using a reference state in thermal wind balance, the production coefficients are identical in form to Equations (5.40) and (5.41) for the hydrostatically balanced reference state, with thermodynamic variables evaluated at the parcel's original and reference positions in the r - z plane, rather than just at its original and reference heights.

Computing the APE density (6.9) in the axisymmetric model first requires the construction of the angular momentum surface, along which the generalised buoyancy will be integrated. For a parcel with specific angular momentum M_p , the difference $\Delta M(r, z, t) = M_0(r, z, t) - M_p$ is computed at all v -points. For each vertical v -level (denoted by its index k), linear interpolation is then used to find the radius $r_{M_k}(r, z, t)$ at which $\Delta M = 0$. If multiple such roots exist, the one closest to the parcel's actual radius r is selected. The profile r_{M_k} is linearly interpolated in the vertical to include w -levels, and computed at $z = 0$ by assuming that $v_0|_{\text{sfc}} = 0.8 v_0|_{\Delta z/2}$.

The discretisation of the parcel's angular momentum surface at time t therefore comprises the points

$$P_M = \left\{ \mathbf{x}_{M_k} = (r_{M_k}, z_k) : k = \frac{1}{2}, 1, \frac{3}{2}, 2, \dots, \frac{z_{\text{top}}}{\Delta z} + \frac{1}{2} \right\}, \quad (6.18)$$

where an integer value k denotes the k^{th} vertical v -level and a half-integer value indicates a w -level. At each point $\mathbf{x}_{M_k} \in P_M$, the values of θ_0 , C_0 , r_{v_0} and Π_0 are computed, using linear vertical and radial interpolation where necessary. This produces reference profiles along the parcel's angular momentum surface.

Figure 6.4 illustrates the structure of the reference angular momentum field: in general, M_0 increases with radius, and M_0 surfaces flare outwards at upper levels. To demonstrate a typical result of the procedure used to obtain the points P_M , the white line in Figure 6.4 shows the path of constant M_0 followed by the parcel originating at $r = 150$ km, $z = 312.5$ m, $t = 150$ h when it is lifted to its reference position. There is some non-monotonic behaviour in the path, but this does not appear to have any important effects on the APE density or diabatic production efficiencies, which remain very similar if slight changes in r_{M_k} are made (for example by choosing a different root of $\Delta M = 0$).

The computation of the reference position and the APE density requires the val-

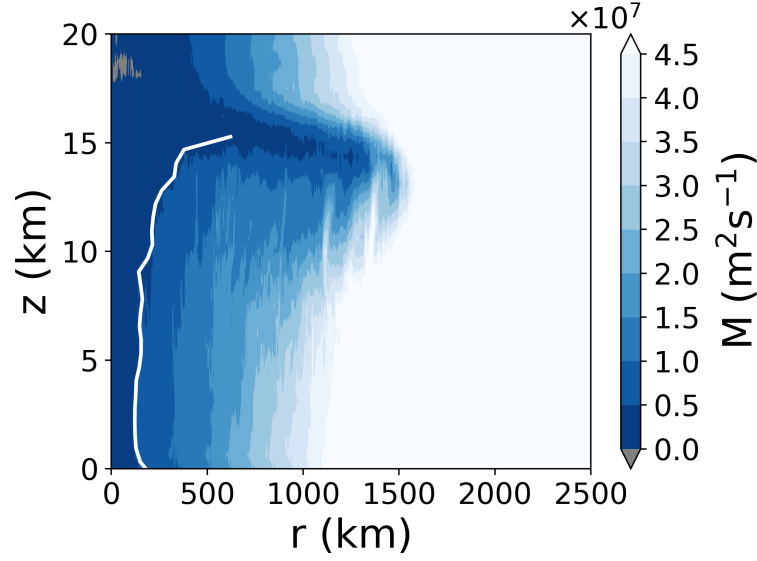


Figure 6.4: Reference specific angular momentum M_0 in the J30.3 axisymmetric TC at 150 h. The white line shows the path of constant angular momentum followed when lifting the parcel from $r = 150$ km, $z = 312.5$ m to its reference position.

ues of both the radial and vertical components of the generalised buoyancy, b_r and b_z , along the angular momentum surface. The parcel is lifted reversibly and adiabatically to $\Pi_0(\mathbf{x}_{M_k}, t)$ for each \mathbf{x}_{M_k} , and θ, r_v, r_l, r_p and r_i are calculated using the same lifting procedure as in Section 5.2.2. For brevity, the notation $\hat{\theta}(\mathbf{x}, t) = \theta(\theta_{ei}, r_t, \Pi_0(\mathbf{x}, t))$ is used in the following. The components of buoyancy are computed using the model's buoyancy approximation:

$$b_{r_k} = -C_0(\mathbf{x}_{M_k}, t) \left\{ \frac{\hat{\theta}(\mathbf{x}_{M_k}, t) - \theta_0(\mathbf{x}_{M_k}, t)}{\theta_0(\mathbf{x}_{M_k}, t)} + 0.61 [\hat{r}_v(\mathbf{x}_{M_k}, t) - r_{v_0}(\mathbf{x}_{M_k}, t)] - \hat{r}_l(\mathbf{x}_{M_k}, t) - \hat{r}_p(\mathbf{x}_{M_k}, t) - \hat{r}_i(\mathbf{x}_{M_k}, t) \right\}, \quad (6.19)$$

$$b_{z_k} = g \left\{ \frac{\hat{\theta}(\mathbf{x}_{M_k}, t) - \theta_0(\mathbf{x}_{M_k}, t)}{\theta_0(\mathbf{x}_{M_k}, t)} + 0.61 [\hat{r}_v(\mathbf{x}_{M_k}, t) - r_{v_0}(\mathbf{x}_{M_k}, t)] - \hat{r}_l(\mathbf{x}_{M_k}, t) - \hat{r}_p(\mathbf{x}_{M_k}, t) - \hat{r}_i(\mathbf{x}_{M_k}, t) \right\}. \quad (6.20)$$

Once the profile of b_z has been computed, the reference height z_r is found using the same method as in Section 5.2.2 (since $\mathbf{b} = 0$ if and only if $b_z = 0$), and $r_r = r_M(z_r)$ is obtained by linearly interpolating between r_{M_k} points.

The parcel's APE density is then computed by taking a discretised line integral along

the path of conserved angular momentum. For illustrative purposes it is assumed, as in Chapter 5, that $z_r > z$. If the parcel resides at vertical level j ($z = z_j$), and n is the integer such that $z_n < z_r < z_{n+1}$, then

$$e_a = \sum_{k=j}^n \left[b_{z_{k+\frac{1}{2}}} \Delta z + b_{r_{k+\frac{1}{2}}} (r_{M_{k+1}} - r_{M_k}) \right] + b_{z_{n+\frac{1}{2}}} (z_r - z_n) + b_{r_{n+\frac{1}{2}}} (r_r - r_{M_n}). \quad (6.21)$$

This method of integration is illustrated in Figure 6.5. For each line segment from (r_{M_k}, z_k) to $(r_{M_{k+1}}, z_{k+1})$, the generalised buoyancy is evaluated at the midpoint of the line segment, $(b_{r_{k+\frac{1}{2}}}, b_{z_{k+\frac{1}{2}}})$. This value of the generalised buoyancy is assumed to be constant along the whole line segment and is then integrated over the line segment. An equivalent method is applied in the case $z_r < z$.

As was done for the resting reference states, the method of integration is reused to define the discretised production coefficients as

$$G_{\theta_{ei}} = \frac{\partial e_a}{\partial \theta_{ei}} = \sum_{k=j}^n \left[\frac{\partial b_z}{\partial \theta_{ei}} \Big|_{k+\frac{1}{2}} \Delta z + \frac{\partial b_r}{\partial \theta_{ei}} \Big|_{k+\frac{1}{2}} (r_{M_{k+1}} - r_{M_k}) \right] + \frac{\partial b_z}{\partial \theta_{ei}} \Big|_{n+\frac{1}{2}} (z_r - z_n) + \frac{\partial b_r}{\partial \theta_{ei}} \Big|_{n+\frac{1}{2}} (r_r - r_{M_n}), \quad (6.22)$$

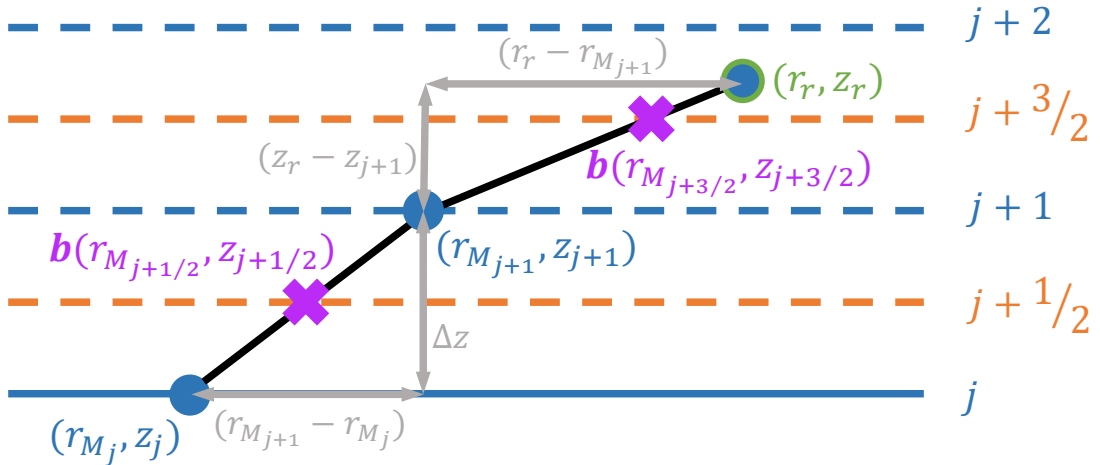


Figure 6.5: Illustration of the path integration used to compute the APE density of a parcel with respect to the vortex reference state in Equation (6.21). Blue lines mark the model's vertical v -levels, with the solid line indicating the parcel's actual height, and orange lines mark the vertical w -levels. The black line segments constitute the path of integration (i.e. the surface of constant M): they join the parcel's M -conserving positions at each v -level (blue circles) and at the reference level (blue circle with green border). The purple crosses indicate the points at which the generalised buoyancy \mathbf{b} is evaluated. The grey arrows and labels show the dimensions of each leg of the integration.

$$G_{r_t} = \frac{\partial e_a}{\partial r_t} = \sum_{k=j}^n \left[\frac{\partial b_z}{\partial r_t} \Big|_{k+\frac{1}{2}} \Delta z + \frac{\partial b_r}{\partial r_t} \Big|_{k+\frac{1}{2}} (r_{M_{k+1}} - r_{M_k}) \right] + \frac{\partial b_z}{\partial r_t} \Big|_{n+\frac{1}{2}} (z_r - z_n) + \frac{\partial b_r}{\partial r_t} \Big|_{n+\frac{1}{2}} (r_r - r_{M_n}). \quad (6.23)$$

The partial derivatives of b_z are identical to the derivatives of the vertical buoyancy given in Equations (5.53) and (5.54), while the partial derivatives of b_r are easily found by observing that

$$\frac{\partial b_r}{\partial \theta_{ei}}(\mathbf{x}, t) = -\frac{C_0(\mathbf{x}, t)}{g} \frac{\partial b_z}{\partial \theta_{ei}}(\mathbf{x}, t), \quad (6.24)$$

and similarly with respect to r_t .

6.2 Comparison of reference states

In order to determine which of the reference states described in Section 6.1 is most suitable for describing the available energetics of the modelled axisymmetric TCs, some objective criterion for what makes a reference state “suitable” is required.

The key property of APE, which originally motivated the use of the theory in this thesis, is that the diabatic production of APE should be directly linked to the generation of kinetic energy, and thus to the intensification of the TC. The metric for the suitability of a reference state will therefore be how closely the rate of APE production with respect to that reference state matches the rate of kinetic energy production in the model.

The production of kinetic energy is not dependent on a reference state. Directly from the Navier-Stokes equations, the material derivative of specific kinetic energy can be written as

$$\frac{De_k}{Dt} = -gw - c_p \theta_\rho \mathbf{v} \cdot \nabla \Pi + \mathbf{v} \cdot \mathbf{D}, \quad (6.25)$$

which contains no reference state quantities. The density potential temperature is defined by

$$\theta_\rho = \theta \left(\frac{1 + \frac{r_v}{\epsilon}}{1 + r_t} \right), \quad (6.26)$$

and so $\theta_{\rho_0} = \theta_{v_0}$, since none of the reference states studied here contain liquid water or ice.

The equations for hydrostatic and gradient wind balance can be used to rewrite (6.25) in terms of an arbitrary balanced reference state:

$$\frac{De_k}{Dt} = \mathbf{b} \cdot \mathbf{v} - c_p \theta_{v_0} \mathbf{v} \cdot \nabla (\Pi - \Pi_0) - \left(f v_0 + \frac{v_0^2}{r} \right) u + \mathbf{v} \cdot \mathbf{D}, \quad (6.27)$$

where $\mathbf{b} = -\mathbf{g} \left(1 - \frac{\theta_\rho}{\theta_{v_0}}\right) \approx \mathbf{g} \left[\frac{\theta - \theta_0}{\theta_0} + 0.61(r_v - r_{v_0}) - r_l - r_p - r_i\right]$. The approximation $\theta_\rho \approx \theta_{\rho_0} = \theta_{v_0}$ has also been used, in the pressure gradient term only. Note that for any resting reference state (i.e. all reference states previously described, other than the vortex reference state), $v_0 = 0$ and the buoyancy flux $\mathbf{b} \cdot \mathbf{v}$ reduces to bw .

Equation (6.27) proves that under these approximations, the non-reference-state-dependent definition of kinetic energy production in Equation (6.25) is identical to the expression for the production of kinetic energy in the axisymmetric model equations, where the initial reference state is used.

Only the positive parts of the APE production and the kinetic energy production rates are compared, rather than their net production rates. This is done at the parcel level: the APE production rate $\bar{\rho} \left(G_{\theta_{ei}} \frac{D\theta_{ei}}{Dt} + G_{r_i} \frac{Dr_i}{Dt}\right)$ is integrated over all (non-sponge-layer) parcels for which the APE production is positive. Different diabatic processes could be having competing effects on the APE production within the parcel, but its overall APE production must be positive. Similarly, the kinetic energy production rate $\bar{\rho} \left[\mathbf{b} \cdot \mathbf{v} - c_p \theta_{v_0} \mathbf{v} \cdot \nabla (\Pi - \Pi_0) - \left(fv_0 + \frac{v_0^2}{r}\right) u\right]$ is integrated over those parcels for which the kinetic energy production is positive. The final term of Equation (6.27) is not included in the kinetic energy production rate since it represents the sink of kinetic energy due to frictional dissipation rather than a reversible conversion between available energy and kinetic energy. For brevity, these integrals will be referred to as simply the rates of ‘‘APE production’’ and ‘‘kinetic energy production’’, but it should be understood that they only include the positive contributions to the production.

The positive production rates are studied because there is a direct causal link between the (positive) APE production and (positive) kinetic energy production, which does not hold for the dissipation rates. The production of APE should result in the production of kinetic energy, otherwise the definition of the potential energy as ‘‘available’’ is problematic. Additionally, kinetic energy must be produced (i.e. converted from APE) before it can be dissipated. In contrast, the dissipation of APE is only linked to a reduction in kinetic energy in the case that the APE in question was produced by the reversible conversion of kinetic energy into APE, which is not necessarily the case. APE can be dissipated without there being any direct effect on the kinetic energy. This will be confirmed once the reference states have been compared using the positive rates.

The positive production of APE is also of interest because it results from more predictable large-scale surface enthalpy fluxes, whereas the dissipation of APE is due to small-scale mixing in internal turbulent eddies. This was seen in the APE production

budget for the inflow region in Figure 5.22 and is also true for the budget over the whole domain (not shown).

A similar argument was presented by Tailleux (2010) when seeking to define the the power input to the ocean by surface buoyancy fluxes. Tailleux (2010) suggested that the relevant power input is the positive part of the rate of exchange between internal and mechanical energy, rather than the net rate. The net rate includes the negative contribution of small-scale, non-viscous dissipation of mechanical energy, which does not assist the understanding of buoyancy-driven motion. The consideration of only the positive APE production is somewhat analogous to the consideration of only the positive heat input when defining the Carnot efficiency of a heat engine, rather than the net heat input.

There is no need to mask or otherwise account for discontinuities when assessing these rates of production, since the APE production rate only concerns continuous APE production by diabatic processes. The inclusion of spatial discontinuities in e_a in the APE budget in Chapter 5 was necessary to explain their effect on the APE flux, which is not being considered here. The APE production coefficients may be discontinuous, but this does not pose an obstacle to computing the instantaneous rates of local production.

Figure 6.6 compares the rate of kinetic energy production, which is independent of reference state, to the rate of APE production computed using each of the reference states, for the J30.3 run of the axisymmetric model. The poorest estimation of the kinetic

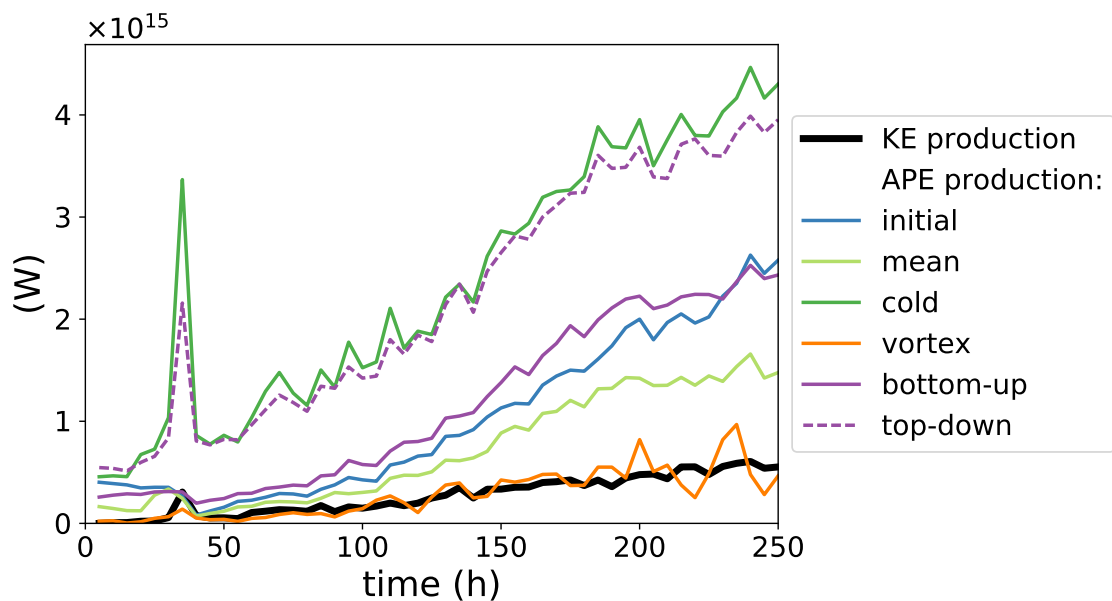


Figure 6.6: Comparison between the positive part of the kinetic energy production rate in the axisymmetric model (thick black line) and the positive production rates of APE with respect to each reference state described in Section 6.1 (coloured lines).

energy production is given by the APE production relative to the cold reference state. This is because when the potential temperature of the reference state is decreased, it no longer resembles the environment that the cyclone actually inhabits, and so the APE production loses physical meaning for the intensification. Measured relative to the cold reference state, all parcels below $z = 15.5$ km are positively buoyant during the mature stage (at 200 h), and 99.6% of the parcels below 2.5 km have $z_r > 10$ km. However, this large-scale positive “buoyancy” is not associated with upward vertical motion of all parcels, and so these notional reference heights are mostly not achieved. Most of the APE produced by diabatic processes therefore does not contribute to the generation of kinetic energy, and so even though the cold reference state can produce a budget without discontinuities, it is not the most physically relevant budget.

The mean profile yields a much closer match than the initial sounding to the kinetic energy production towards the end of the model run. Taking radial means of θ and r_v accounts for general heating and moistening in the domain, which alter the environment experienced by the cyclone. Therefore, using the mean state appears to be preferable to using the initial state if considering overall kinetic energy production.

The Lorenzian reference states perform worse than the initial or mean environmental reference states. These results indicate that the sorting procedures are releasing too much APE, even in the case of bottom-up sorting, which was specifically intended to limit the APE release to realistic levels. The sorted states are also far more computationally expensive to obtain (taking longer than the model run itself). Therefore, it is preferable to use an environmental reference state to study TC APE rather than the sorting methods of Wong et al. (2016), although it is possible that other sorting methods could be designed that would perform better.

The best predictor of the kinetic energy production in this case is the vortex reference state. This is likely because using a reference state that is as close as possible to the actual model state minimises the stored available elastic energy and APE density, and therefore yields the most direct correspondence between the production of APE and the production of kinetic energy. If a direct link between APE production and kinetic energy production is to be drawn, these results show that accounting for the balanced dynamical structure of the TC is essential. The kinetic energy generation can be entirely explained in this case by the unbalanced part of the flow. The expected results for a TC that intensifies slowly and close to balance will be discussed shortly.

It was asserted earlier in this section that the link between the dissipation of APE

by diabatic processes and the negative kinetic energy production is not as strong as the link between the two positive productions. This can now be confirmed by comparing the rate of negative kinetic energy production to the rate of negative APE production with respect to the vortex reference state. Whereas the positive production rates (Figure 6.6) match closely, the magnitude of the negative APE production rate is approximately 2.5 times larger than the negative kinetic energy production rate. This indicates that much of the APE dissipation by diabatic processes is not linked to changes in kinetic energy, supporting the choice to focus on the positive production rates.

In order to establish whether the APE production relative to the balanced vortex reference state is the best predictor of kinetic energy production for TCs in a range of environmental conditions, the reference state comparison is now conducted for the model runs with all six sets of initial conditions described in Chapter 4.

Since the sorted reference states are very expensive to compute, and the results for the J30.3 run showed that the environmental and vortex reference states yield better agreement between the production rates of APE and kinetic energy, the sorted reference states are not computed for the additional model runs. The cold reference state is also not computed, since it gives a very poor prediction of kinetic energy production for the J30.3 run. Therefore, the APE production rates are only computed with respect to the initial, mean and vortex reference states across the six runs. Figure 6.7 compares these production rates to the rate of kinetic energy production for each run.

The conclusions drawn from the J30.3 model run—that the APE production rate with respect to the vortex reference state gives the closest match to the kinetic energy production rate, and that the mean reference state performs better than the initial—hold true for all the runs except J26.3. Using APE theory with the vortex reference state enables the approximate prediction of the kinetic energy generation across model runs with a range of initialisation parameters. The prediction is closer for runs with higher SST. Chapter 7 will explore how the APE production rate can also be used to predict the maximum intensity of a TC.

In the case of J26.3, the vortex reference state still provides the best match to the kinetic energy production rate in the early stages of the TC's evolution (up to 70 h). However, in the mature stage, the APE production rates with respect to the initial and vortex reference states are similar but too low, while the mean reference state matches the kinetic energy production more closely. This is also the only run in which the mean reference state's APE production rate in the mature stage is higher than the initial ref-

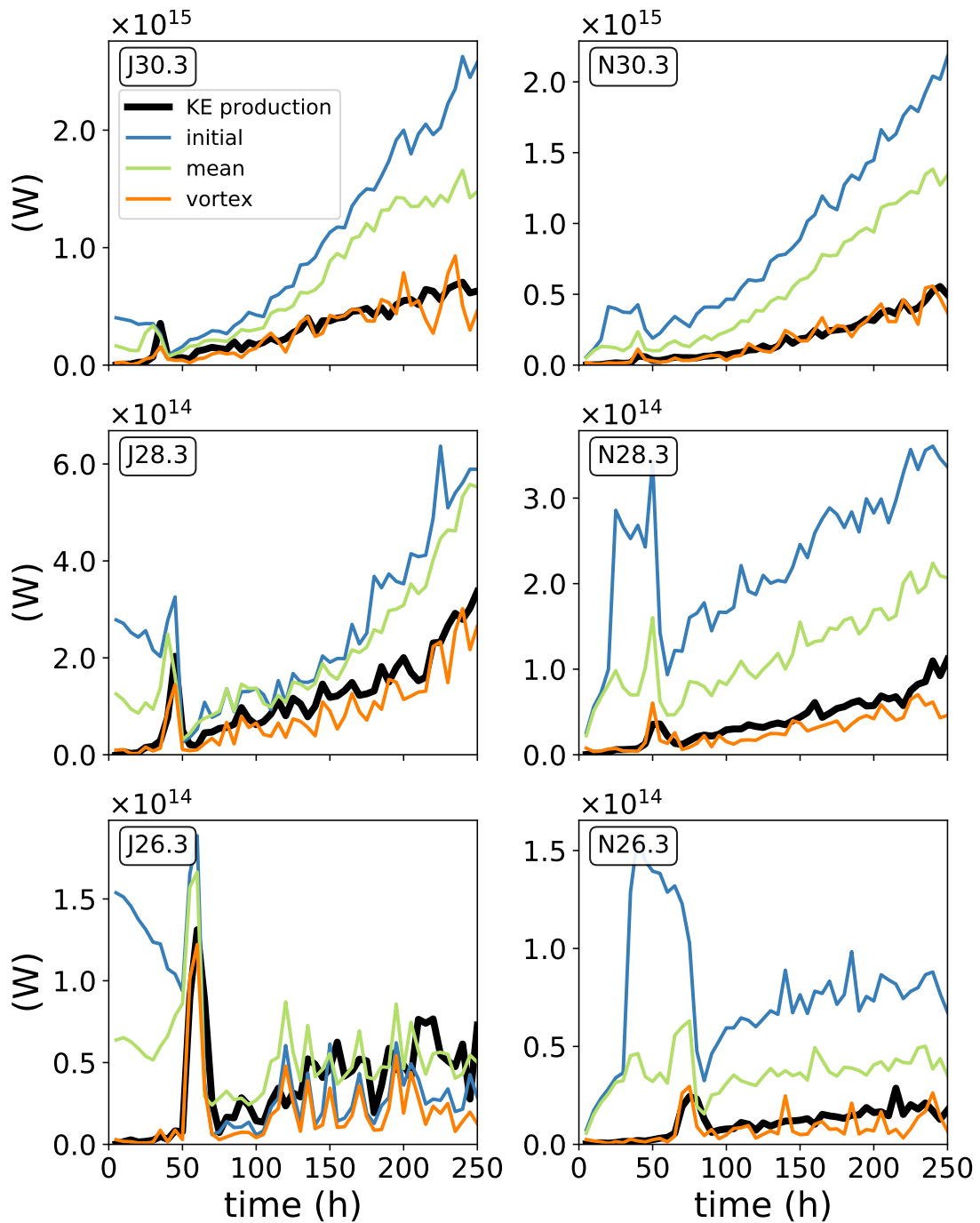


Figure 6.7: Comparison between the positive part of the kinetic energy production rate (thick black line) and the positive production rates of APE with respect to different reference states (coloured lines) for model runs with varying initial conditions. The labels in the upper left of each plot indicate the model run used, with the letter signifying the initialisation sounding (Jordan or neutral) and the number being the SST.

reference state's. This occurs because, in the lowest model level ($z = \frac{\Delta z}{2}$), the radial mean θ becomes lower than the initial sounding value $\bar{\theta}$, and similarly the lowest level becomes on average less moist than its initial state. Therefore, parcels in the lowest level will be more buoyant relative to the moist reference profile than the initial one, leading to higher values of APE density and higher rates of diabatic APE production.

There is not as much difference between the three reference states in J26.3 compared to the other runs because the model environment remains more similar to the initial conditions. However, it is not clear why the vortex reference state is performing worse than the environmental reference states in this case. It is possible that the APE production rate is more sensitive to the exact numerical method used to construct the balanced vortex in J26.3 than in the other runs, because the combination of the sounding and the low SST means that many of the lowest-level parcels have buoyancy very close to zero. However, varying the method of vortex construction was not found to give better estimates of the APE production rate.

Another possibility, which could explain why the prediction of kinetic energy generation improves as SST increases, is that intensification occurs closer to balance in the J26.3 run. The APE production relative to the vortex reference state focuses on processes occurring in the unbalanced part of the flow; the balanced part is contained within the reference vortex. For a slowly intensifying vortex, which remains close to balance at all times, the unbalanced part of the flow may be less relevant, with the evolution of the balanced vortex itself increasing in importance; this evolution is not predicted by the APE theory presented here. In this case the buoyancy relative to the large-scale environment could be more relevant to the generation of kinetic energy, rather than the buoyancy relative to the local vortex structure. As the SST increases, the rate of intensification increases and the intensification may be more due to processes linked to the unbalanced flow and thus better captured by the vortex-relative APE production.

6.3 APE properties with respect to balanced vortex reference state

Since Section 6.2 showed that the vortex reference state is the most suitable for predicting the production rate of kinetic energy in the model, it is of interest to explore the APE-related properties of the air parcels with respect to this reference state. This section therefore investigates the APE density, reference position and APE production

efficiencies relative to the vortex reference state. The APE relative to the vortex reference state will also be placed in the context of general theories for available energetics using non-resting, dynamically stable reference states (Codoban and Shepherd, 2003; Andrews, 2006; Codoban and Shepherd, 2006; Tailleux and Harris, 2020), and changes in APE due to the non-conservation of angular momentum will be investigated. Results from the J30.3 run are presented here, so that they can be compared to those for the initial reference state presented in Section 5.2. Any major differences in results that occur when other initial conditions are used will be noted.

As in Section 5.2, the APE properties are investigated in the TC's mature stage, at 150 h. Figure 6.8 shows the APE density with respect to the vortex reference state at this time. Whereas most parcels near the surface or the centre of the TC had high APE density when computed using the initial reference state (see Figure 5.13), high APE density with respect to the vortex reference state is mostly limited to parcels in the lowest model level.

This result demonstrates that most parcels in the domain are not buoyant (either positively or negatively) relative to the balanced vortex, i.e. they exist close to thermal wind balance. The exception of the lowest model level can be explained by the effects of surface friction, as discussed in Section 6.1.3. Surface friction results in gradient wind imbalance in the boundary layer, leading to a cold-core reference vortex (at low levels). The near-surface parcels are warm and therefore buoyant relative to this cold core, and so $z_r > z$. Heating and moistening of near-surface parcels through surface fluxes will

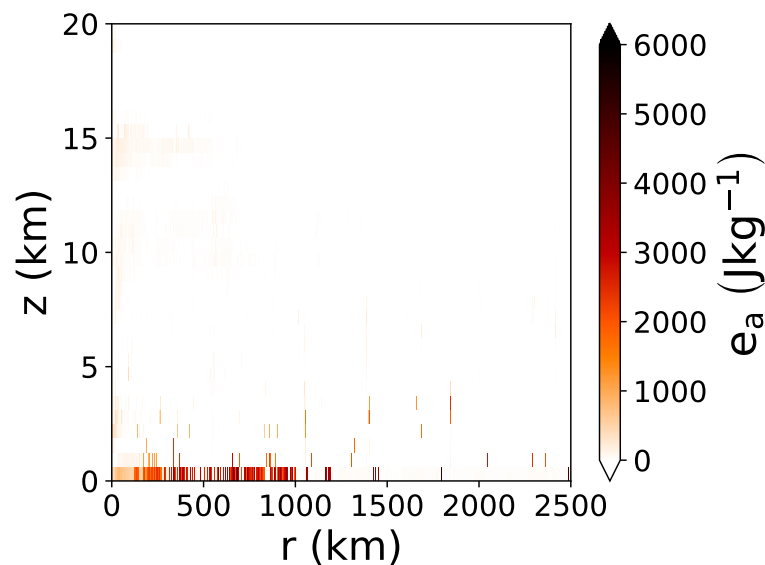


Figure 6.8: APE density e_a in the axisymmetric TC 150 h into the simulation, computed using the vortex reference state.

also enhance their APE density, allowing them to attain reference heights higher in the troposphere.

It can therefore be concluded that the reservoir of APE diagnosed using the initial reference state in Section 5.2, which extended throughout most of the troposphere and out to $r \approx 1000$ km, was APE stored in the TC’s warm core structure that mostly did not contribute to the intensification or maintenance of the TC in terms of the generation of kinetic energy. The APE that is relevant to intensification and maintenance is the APE of near-surface parcels, which are out of balance with the vortex structure.

Given the distribution of APE density, near-surface parcels are expected to have $z_r \gg z$, since they must be lifted a great distance along surfaces of constant M in order to compute a high APE density. Indeed, Figure 6.9a shows this to be the case. Whereas for the initial reference state, most parcels in the lower troposphere within 1000 km of the TC centre had $z_r > z$, now the main differences $|z_r - z|$ are found in the near-surface unbalanced parcels, which possessed the bulk of the vortex-relative APE.

Figure 6.9b shows that these same parcels also possess the largest differences between their actual radii and their reference radii. This is a consequence of the parcels being lifted along surfaces of constant M , which move outwards with height. Therefore, parcels with higher positive buoyancy, which can be lifted further upwards before reaching an LNB, will also reach a larger radius. For parcels in the lowest 5 km of the model, the correlation coefficient between $z_r - z$ and $r_r - r$ is 0.84.

As was found for the initial reference state, the highest magnitudes of APE production efficiencies occur in near-surface parcels (Figure 6.10). Once again, these parcels have

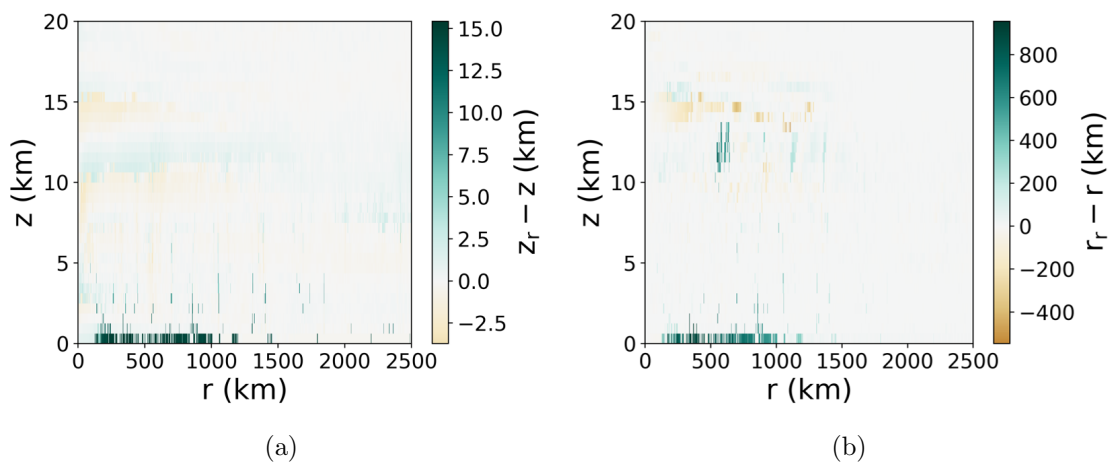


Figure 6.9: (a) Difference between the reference height—relative to the vortex reference state—and actual height of each moist air parcel at 150 h. (b) Difference between reference radius and actual radius of parcels.

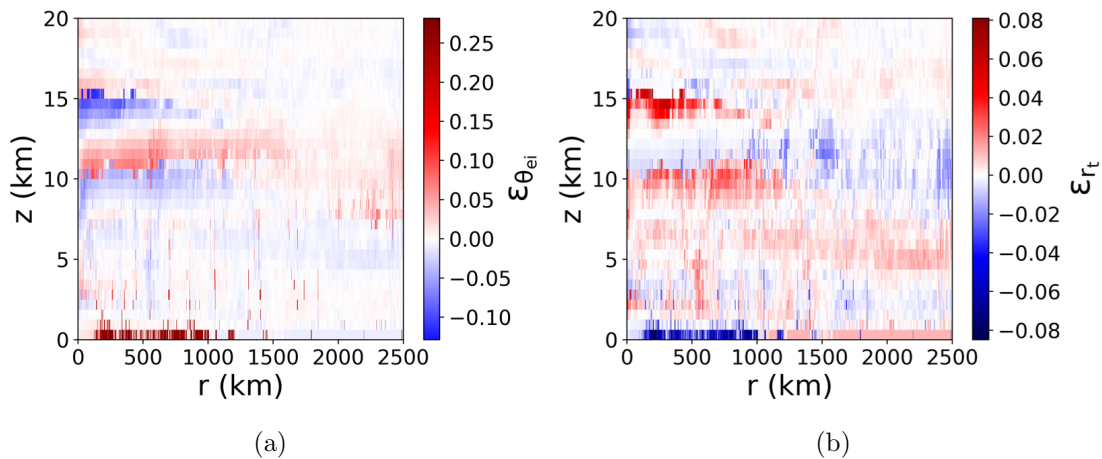


Figure 6.10: APE production efficiencies at 150 h, computed using the vortex reference state. Red parcels have positive efficiency, meaning that an increase in the relevant quantity (θ_{ei} for (a), r_t for (b)) will increase e_a . Blue parcels have negative efficiency, meaning that an increase in the quantity will decrease e_a .

positive efficiency with respect to θ_{ei} and negative efficiency with respect to r_t . Surface fluxes are therefore expected to have a broadly similar effect on APE production (i.e. to be a key source of APE) when using the vortex reference state as when using the initial reference state. It is noticeable that near-surface parcels in the inner 100 km do not exhibit these high efficiencies, indicating as before that surface fluxes near the radius of maximum wind (which occurs at $r = 21.25$ km at this time) are less important to the APE budget than surface fluxes in the inflow region.

For all the sets of initial conditions tested, high values of e_a , z_r , r_r , $|\varepsilon_{\theta_{ei}}|$ and $|\varepsilon_{r_t}|$ were similarly restricted to parcels in the lowest model levels. The main difference seen when using different initial conditions was a reduction in the number of parcels exhibiting high e_a (and high efficiencies) at lower SSTs. This is expected, since if less energy is supplied to the TC by surface fluxes, the TC is generally smaller and less APE will be produced.

Away from the surface, Figure 6.10 shows coherent horizontal bands of efficiency; these are related to horizontal bands of $\theta_0 - \bar{\theta}$ generated by the process of adjustment to the balanced vortex. The magnitude of these efficiencies is generally lower than in the near-surface parcels. It is also more difficult to predict what impact these efficiencies will have on the overall APE production, because whilst surface fluxes must affect the lowest-level parcels, it is not known, without diagnosis, exactly where other diabatic processes such as rain fallout will occur, and therefore whether they will occur in parcels with positive or negative efficiency. For the production efficiencies with respect to the initial reference state, the sign of efficiency was predictable because it was the same over the entire troposphere. However, it did not correctly predict whether diabatic processes would

lead to the generation of kinetic energy.

For the initial reference state, Figure 5.22 presented a budget of the total diabatic production of APE in the inflow region. The main source of APE was found to be surface fluxes, the main sink was subgrid mixing, and in the mature stage the source was much larger than the sink, so that the rate of APE production became positive and increasing. Figure 6.11 displays this budget for the vortex reference state.

In this case, the surface fluxes remain the key source of diabatic APE production, but in the mature stage they are approximately in balance with the sink provided by the subgrid mixing, resulting in an APE production rate that is only slightly positive. When using the vortex reference state, the surface fluxes do not produce large amounts of APE that is simply stored in the inflow region.

The magnitude of the APE sink provided here by mixing is dependent on the model's formulation of the subgrid mixing parameterisation. The relationship between APE production and dissipation in the inflow could hence differ between models, depending on how they represent boundary layer mixing processes.

It is also possible to break down the diabatic processes that contribute to the positive production of APE with respect to the vortex reference state, which was seen in Figure 6.6 to match the positive production of kinetic energy. Figure 6.12 shows the budget of positive APE production over the model domain.

In the mature stage, surface fluxes are the largest contributor to positive APE production, but there are also non-negligible contributions from rain fallout (22% of the contribution from surface fluxes, when averaged from 150–250 h), ice fallout (43%) and

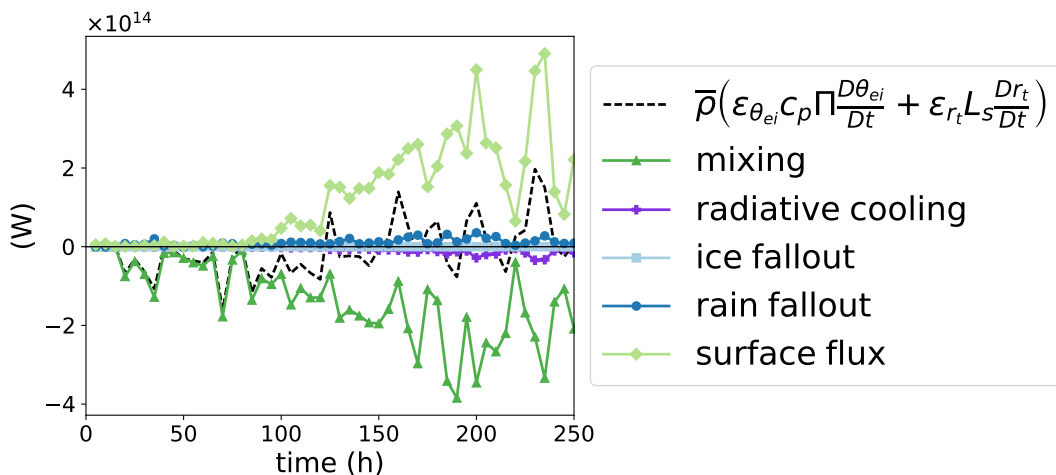


Figure 6.11: Budget of total diabatic production of APE in inflow region, using vortex reference state. The horizontal black line marks 0 W.

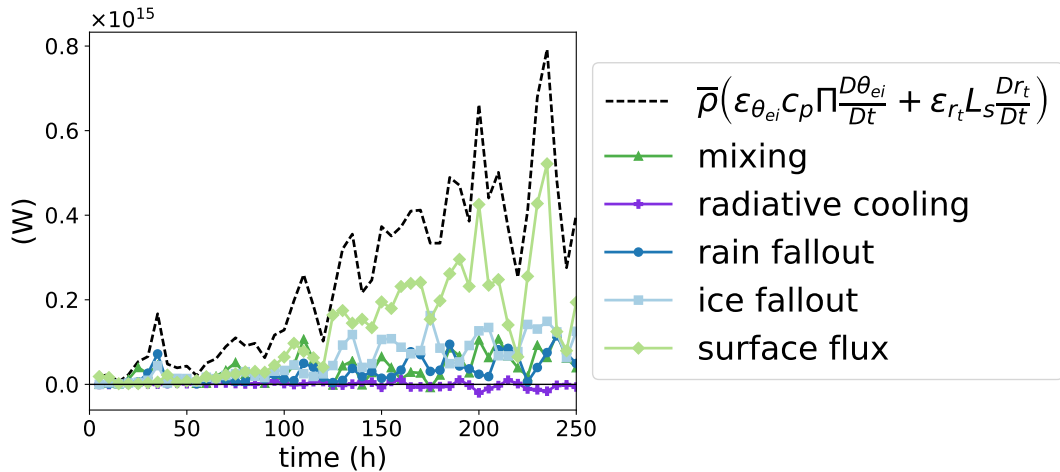


Figure 6.12: Budget of diabatic processes leading to positive production of APE with respect to the vortex reference state, integrated over whole domain.

subgrid mixing (23%).

The spike in APE/kinetic energy production that occurs at 35 h is caused by increases in diabatic production by subgrid mixing, rain and ice fallout. This shows that processes other than surface fluxes can be dominant during the early stages of the TC's development, while it is still spinning up to the steady state configuration that enables it to most efficiently transfer energy from surface enthalpy fluxes into kinetic energy.

In the runs with varied initialisation soundings and SSTs, the relative contribution of the surface fluxes to the total positive diabatic APE production decreases as the SST decreases, since the surface fluxes are weaker. For example, in the N28.3 run, the surface fluxes and subgrid mixing make approximately equal contributions to the total positive production. This suggests that the choice of subgrid parameterisation may be more crucial to the total kinetic energy production in cases with lower SST.

Whereas the APE relative to resting reference states (e.g. the initial environmental profile) was computed assuming conservation of θ_{ei} and r_t , the computation of APE relative to the balanced vortex reference state also required the angular momentum M to be conserved. Consequently, it is possible to produce or dissipate APE through changes in M , i.e. through frictional processes as well as through diabatic processes (Codoban and Shepherd, 2003; Andrews, 2006; Codoban and Shepherd, 2006). To assess the contribution of frictional processes to the APE budget, the form of this frictional APE production/dissipation term is required. This is obtained from the theory of available energetics for an axisymmetric vortex in a single-component compressible stratified fluid developed by Tailleux and Harris (2020), which was motivated by the formulation of APE density in terms of a generalised buoyancy in Section 6.1.3. The paper describing the theory is

included in full in Appendix C, but the relevant points of the theory are summarised here.

The available energy relative to a balanced axisymmetric vortex can be split into two components: a thermodynamic part and a mechanical part. The mechanical part depends on the difference between a parcel's actual angular momentum and the angular momentum of the reference state, $M - M_0$. Since the balanced vortex used in this chapter has been derived from the actual wind field, this difference is zero and the mechanical part of the available energy is zero. The thermodynamic part of the available energy is then the APE density already derived in Equation (6.9) (for the moist atmospheric case).

The key changes to the budget of APE density relative to a resting reference state (Equation (5.25)) are the conversion between APE and kinetic energy becoming $\mathbf{b} \cdot \mathbf{v}$ rather than bw , and the introduction of the term representing frictional APE production. The production/dissipation of APE by changes in M is

$$\bar{\rho} \frac{De_a}{Dt} = \dots + \bar{\rho} \left(\frac{1}{2r^2} - \frac{1}{2r_r^2} \right) \frac{DM^2}{Dt} = \dots + \bar{\rho} \left(\frac{1}{r^2} - \frac{1}{r_r^2} \right) MrD_v, \quad (6.28)$$

making use of Equation (6.4) for $\frac{DM}{Dt}$. Figure 6.13 compares the production of APE by diabatic processes (6.13a) to the production by frictional processes (6.13b). The diabatic production occurs, as expected, chiefly in the near-surface parcels that have high APE production efficiencies. These parcels also exhibit frictional dissipation of APE, with frictional (positive) production occurring nearer the TC centre. The parcels in which frictional production occurs have smaller values of $|r - r_r|$ than the outer parcels, but much larger MD_v because they are near the radius of maximum wind.

There are also various parcels in the middle and upper troposphere exhibiting fric-

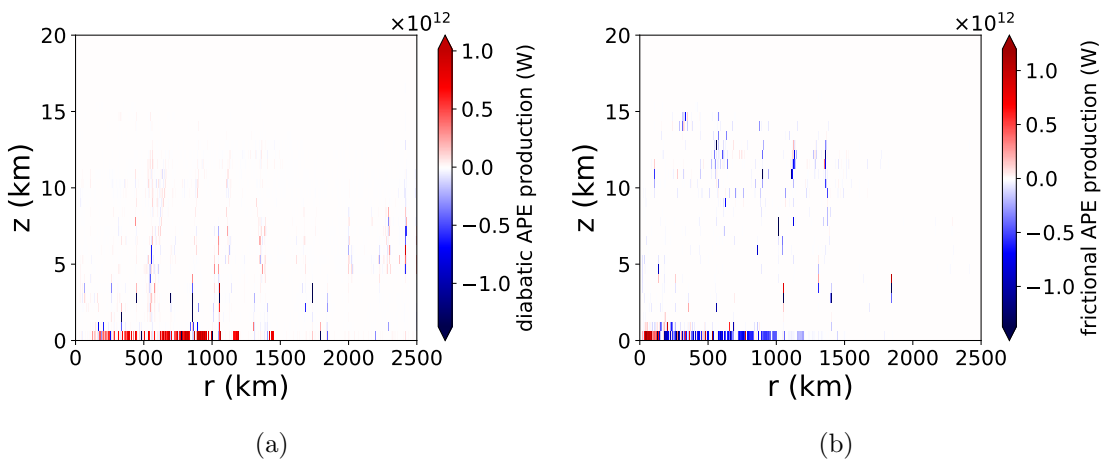


Figure 6.13: Production of APE by (a) diabatic and (b) frictional processes relative to balanced vortex reference state at 150 h.

tional APE dissipation. However, many of these parcels lie in regions where M -surfaces are almost horizontal, which means that their reference radius and hence their frictional APE production is very sensitive to small changes in the method used to integrate along M -surfaces. The frictional APE production is less sensitive for parcels in the low-level inflow, which travel a longer distance before reaching potential candidates for r_r . The integrated positive APE production rate used for the reference state comparisons in Section 6.2 remains very similar if frictional production is included in the definition of APE production.

6.4 Discussion and Conclusions

Previous studies using local APE theory have been limited by the fact that any conclusions drawn about the energetics may depend on the particular choice of reference state, and there has been no established physical basis for preferring one reference state over another. This chapter introduced a method for objectively assessing the suitability of a reference state for studying the available energetics of a system. The production of APE by diabatic processes should correspond as closely as possible to the production of kinetic energy—which does not depend on the choice of reference state—otherwise the potential energy being produced is not truly “available”.

For the TCs simulated by the axisymmetric model, the reference state that gives the best match between APE production and kinetic energy production (out of the states tested) is a vortex in thermal wind balance, constructed from the model’s instantaneous azimuthal wind field. The results given by this reference state highlight the utility of local APE theory: it can be used to estimate the kinetic energy production in the model for a range of model runs (although the production tends to be underestimated at lower SSTs), and hence to budget the contributions of individual diabatic processes to the kinetic energy production.

Physically, the better correspondence between APE and kinetic energy production can be understood by the fact that the vortex reference state is closer to the actual state of the model, and therefore there is less storage of APE and available elastic energy. This means that a greater proportion of the diabatic production of APE will feed through to conversion into kinetic energy, instead of being stored in the warm core of the TC. The boundary pressure work term $-\nabla \cdot [\bar{\rho} c_p \theta_{v_0} (\Pi - \Pi_0)]$ is also minimised, which means that it makes little difference to write the kinetic energy budget in either of the two possible forms discussed in Chapter 5 (see Equations (5.7) and (5.62)).

However, the model's actual state must still differ from the vortex reference state in order to predict intensification. Relative to the vortex reference state, the TC can only possess APE or non-zero APE production efficiencies if it is out of thermal wind balance. For a TC in exact thermal wind balance, the reference vortex would be identical to the TC itself, so that there would be no difference between a parcel's actual position and its reference position, leading to $e_a = \varepsilon_{\theta_{ei}} = \varepsilon_{r_t} = 0$ everywhere. This might appear to imply that it would be impossible to generate APE and thus intensify a balanced, frictionless vortex through heating, which is clearly untrue (Eliassen, 1951; Schubert and Hack, 1982). This apparent contradiction is resolved by noting that the reference vortex is computed using instantaneous fields at each time step. In a model assuming thermal wind balance, the heating would evolve the reference state rather than generating APE in the unbalanced part of the flow. The intensification would be considered as an evolution of the balanced reference state—it is not clear how to use APE theory to predict the balanced intensification in this case. If the reference state were fixed at some point in time rather than being allowed to evolve, then the efficiency of zero would only apply to the first infinitesimal subsequent heating. The vortex would then depart from the reference state due to the heating, the efficiency would increase, and APE production would ensue.

The superior performance of the vortex reference state is compatible with the long-recognised idea that not all the APE contained in a dynamically-constrained flow will be released as kinetic energy (Lorenz, 1955; Andrews, 2006; Codoban and Shepherd, 2003, 2006). The vortex reference state was the only one tested that accounts for the constraint of thermal wind balance on the modelled flow. By accounting for the balanced component of the flow in the reference state, the production of APE is restricted to occur only in parcels which are out of balance, and therefore this APE can be converted to kinetic energy even when accounting for the large-scale constraints imposed by the TC's structure.

The application of APE sorting algorithms to the axisymmetric model by Wong et al. (2016) focused on whether the production of APE using a reference state based on top-down or bottom-up sorting gave a better match to the conversion of APE into kinetic energy. Wong et al. (2016) found that the bottom-up reference state gave a better match to kinetic energy production because it did not include all CAPE present in the model, demonstrating that it is not always optimal to use a reference state that is a global potential energy minimum. The results here agree with the conclusion that the bottom-up reference state is a better predictor of kinetic energy generation, but neither

algorithm accounts for angular momentum constraints. It seems likely that better results could be obtained by a sorting procedure that conserves M in addition to θ_{ei} and r_t , to find a stable balanced vortex, which would be a minimum potential energy configuration among reversible adiabatic rearrangements of mass conserving θ_{ei}, r_t and M (Cullen et al., 2015). However, it is not obvious how to design such an algorithm and it could prove to be prohibitively computationally expensive.

Since the balanced vortex reference state provided the best prediction of kinetic energy generation out of the reference states tested in this chapter, future developments in the study of APE in TCs should focus on accounting for angular momentum constraints to maximise predictive capability. Whilst the importance of dynamical constraints on the APE has been discussed in the theoretical APE literature, it has previously not been considered when applying APE theory to TCs. Tang and Emanuel (2012) used the model initial sounding as a reference state, while Tang et al. (2016) used an isothermal reference state at $T = -70^\circ\text{C}$; the results of this chapter show that both of these options would lead to a large portion of diabatic APE production resulting in APE storage rather than kinetic energy production. If a direct link to the production of kinetic energy is to be drawn, a vortex reference state would make a more suitable basis for similar future studies.

When the APE density and associated properties were computed using the initial reference state in Chapter 5, parcels within $r = 1000\text{ km}$ of the TC throughout the troposphere had high APE density, reference heights well above their actual heights, positive efficiency $\varepsilon_{\theta_{ei}}$ and negative efficiency ε_{r_t} . Using the vortex reference state, these properties are restricted to a much smaller number of near-surface parcels, which are buoyant relative to the balanced vortex.

Although the vortex reference state is the best choice for analysing the generation of kinetic energy in the TC, this does not necessarily mean that the other reference states should be disregarded. The balanced vortex itself contains APE relative to the undisturbed environment, so the mean or initial reference state is needed to capture the total APE of the TC that could be released if its vortex structure were to dissipate entirely. The mean or initial reference states may be more useful if considering the complete life cycle of the TC, rather than just the intensification and steady-state maintenance.

It is important to recognise that the interpretation of a particular diabatic process as a source or sink of APE depends on the choice of reference state. For example, ε_{r_t} is always negative for $z < 10\text{ km}$, $r < 1000\text{ km}$ when computed using the initial reference state (see Figure 5.14b), which leads to the conclusion that the fallout of precipitation

from a parcel increases its APE (since r_t decreases). However, if the efficiency is computed using the vortex reference state, there are many parcels in this region with positive ε_{rt} (Figure 6.10b), resulting in the conclusion that the fallout of precipitation from a parcel decreases its APE. Neither conclusion is necessarily erroneous: if the quantity of interest for a particular study is the change in APE of the total TC system relative to its initial environment, then the initial reference state efficiencies are the relevant ones. For a study investigating the change in APE relative to the balanced state, which drives the production of kinetic energy during the intensification and maintenance stages, the vortex reference state efficiencies are the correct ones to use.

Any statement about whether a diabatic process is a source or sink of APE must be clarified by specifying the reference state. This degree of choice, which is not a part of other energetic theories, is valuable provided that the choice made is a physically informed one. For example, so far in this thesis, the study of production relative to the initial and vortex reference states has permitted investigation of the available energetics of both the total flow and its unbalanced component, a distinction that could not be easily made with a theory based on TPE.

The sensitivity of APE-related quantities to small perturbations in the reference state has not been tested in this work, but it does not appear that slight changes in the reference state will lead to marked qualitative differences in APE budget behaviour. The APE budgets and efficiencies with respect to the mean reference state have not been shown here, but they are similar to those presented in Chapter 5 for the initial reference state (typically the production efficiencies and APE density are slightly lower for the mean reference state, because it is warmer and moister). The positive kinetic energy production rates shown in Figure 6.7 are also reasonably similar for these two reference states. Additionally, the positive kinetic energy production rate with respect to the balanced vortex reference state was found to be insensitive to whether the reference water vapour mixing ratio field was taken to be the initial profile \bar{r}_v or the *in situ* moisture field r_v . This suggests that, even though the discontinuous nature of local APE theory means that a slight change in reference state could cause large changes in APE density for some parcels, the overall APE budgets for the TC are not strongly affected by minor reference state alterations.

Surface fluxes provide a source of APE with respect to all the reference states tested. Although it would be possible to construct a reference state for which surface fluxes are a sink of APE, for example by using a sounding much warmer than the model's initial

state, this shows that the view of surface fluxes as a source of APE is robust for most reasonable choices of reference state. Surface fluxes increase APE relative to both the initial quiescent environment and the balanced part of the flow.

Tailleux (2018) suggested that the APE relative to a non-resting reference state could be treated as an eddy APE, with a mean APE arising from the APE of the non-resting reference state relative to a resting one. From this viewpoint, the APE computed using the vortex reference state can be considered as an eddy APE that arises due to departures from thermal wind balance, in conjunction with the mean APE possessed by the balanced vortex relative to the initial quiescent environment. This is aligned with the concepts of *local* and *system* buoyancy described for an axisymmetric vortex by Smith et al. (2005). The system buoyancy is defined as the buoyancy relative to the far-field environment, and gives rise to the mean APE, while the local buoyancy is calculated relative to the balanced density and pressure fields of the vortex, thus characterising local unbalanced motions, which give rise to the eddy APE.

However, the framework used in this chapter does not permit any analysis of the interaction between the mean and eddy APE, since the balanced vortex is simply diagnosed at each time step based on the instantaneous wind field, i.e. setting $v_0 = v$. This means there is no prediction of the evolution of the vortex reference state, which would form a useful metric of intensification. It should be possible to use a balanced vortex with $v_0 \neq v$ as a reference state, with additional inertial terms arising due to the difference between the actual angular momentum and reference angular momentum of parcels. A local APE theory using an arbitrary axisymmetric balanced vortex reference state for a dry atmosphere has been developed (Tailleux and Harris, 2020), but it remains unclear how to link the diabatic production of APE with respect to the non-resting reference state to the evolution of the reference state itself.

This chapter has also only discussed the positive production of kinetic energy in the TC, since this is the part most closely linked to this thesis' focus of APE. In order to understand the net changes in kinetic energy, the negative part of the kinetic energy production would also have to be included. However, this is less easily explained in terms of changes in APE, since the diabatic dissipation of APE is not always associated with the destruction of kinetic energy.

When constructing APE budgets in Chapter 5, discontinuities in APE density proved to be a significant obstacle for physically interpreting the budgets, and limited the useful application of the budget to the inner regions of mature TCs. The work presented in

this chapter shows that for a suitable choice of diagnostic, the discontinuous behaviour of APE density need not pose a problem. No masking or consideration of discontinuities was required in order to successfully link the diabatic production of APE to the generation of kinetic energy in several different runs of the model.

The close link found in this chapter between APE production and kinetic energy production demonstrates how local APE theory can provide new insight into the link between diabatic processes and the intensification and maintenance of TCs, and puts the choice of reference state on a firmer physical footing. The next chapter further develops these findings to explore how local APE theory can be used to enhance the understanding of TC efficiency and the influence of efficiency on TC development.

Chapter 7:

APE efficiency in tropical cyclones

The review of tropical cyclone energetics in Chapter 2 introduced the concept of the energetic efficiency of a TC in terms of total potential energy (TPE) and dry APE. It highlighted that increases in TPE efficiency have been suggested as a possible cause of TC rapid intensification, since a TC with a higher TPE efficiency can produce more kinetic energy from the same potential energy source. Chapter 2 also described the usefulness of the Carnot efficiency—the theoretical maximum efficiency of a TC—for predicting potential intensity (PI, the maximum azimuthal wind speed of the TC). There was no clear link between the TPE or dry APE definitions of energetic efficiency and the Carnot efficiency: the Carnot efficiency is typically $\frac{1}{3}$, whereas the maximum TPE or dry APE efficiency at any location is approximately 5%. However, it was highlighted that the maximum moist APE efficiency is likely to be similar to the Carnot efficiency, and so it is possible that local moist APE theory could be used to understand PI.

The work in Chapters 5 and 6 included the computation of the local moist APE production efficiencies $\varepsilon_{\theta_{ei}}$ and ε_{r_t} . Here, the links between these APE production efficiencies and the previously existing concepts of TC efficiency are explored. In particular, this chapter investigates whether the temporal variation in APE efficiency is important to TC development, as has been hypothesised for TPE efficiency, and whether APE theory can be used to predict the PI of a TC.

7.1 Definitions of APE efficiency

Chapters 5 and 6 identified that surface enthalpy fluxes provide the main source of APE in a TC. Therefore, in order to obtain a simple definition of APE efficiency, which combines $\varepsilon_{\theta_{ei}}$ and ε_{r_t} , only the efficiency with which surface fluxes produce APE is considered here. Another motivation for focusing on the surface fluxes is that a diagnostic

based on near-surface data only is more likely to be a feasible diagnostic for a realistic TC model, since it would require far less model output than a diagnostic relying on integrals over all vertical levels.

For each parcel in the lowest level of the axisymmetric model atmosphere, the overall APE production efficiency ε is defined as the ratio of the total diabatic APE production by surface fluxes to the surface enthalpy flux:

$$\varepsilon = \frac{\varepsilon_{\theta_{ei}} c_p \Pi F_{\theta} + (\varepsilon_{\theta_{ei}} + \varepsilon_{r_t}) L_s F_{r_v}}{c_p \Pi F_{\theta} + L_s F_{r_v}}. \quad (7.1)$$

All symbols are as defined in previous chapters: $\varepsilon_{\theta_{ei}}$ and ε_{r_t} are the moist APE production efficiencies defined in 5.2.4, $c_p \Pi F_{\theta}$ is the surface sensible heat flux, and $L_s F_{r_v}$ is the surface latent heat flux. The surface enthalpy flux differs slightly from its usual form (e.g. Emanuel, 1995), by replacing the latent heat flux term $L_v F_{r_v}$ with $L_s F_{r_v}$. This reflects that the local APE theory developed in Chapter 5 allows the APE density of a surface parcel to account for the release of latent heat of fusion occurring when the parcel rises past its freezing level. The changes in Π caused by surface fluxes of θ and r_v are neglected in the expression for the enthalpy flux for simplicity; the efficiency values were found to be similar if it was included.

The efficiency ε is essentially an average of $\varepsilon_{\theta_{ei}}$ and ε_{r_t} , weighted based on the partitioning of the surface enthalpy flux between sensible and latent heat fluxes. Defining the evaporative fraction EF as the ratio of the latent heat flux to the sum of the sensible and latent heat fluxes,

$$EF = \frac{L_s F_{r_v}}{c_p \Pi F_{\theta} + L_s F_{r_v}} \quad (7.2)$$

(e.g. Nichols and Cuenca, 1993; Ambaum, 2010, p.59), the efficiency ε becomes

$$\varepsilon = \varepsilon_{\theta_{ei}} + EF \varepsilon_{r_t}. \quad (7.3)$$

Henceforth, ε will be referred to simply as the *surface APE efficiency*. The *maximum surface APE efficiency*, ε_{\max} , is defined as the maximum value of ε for any parcel in the lowest model level.

To provide a measure of the efficiency of the TC system as a whole, the *bulk surface APE efficiency* is defined by integrating both the numerator and denominator of Equation

(7.1) over the surface area of the TC:

$$\varepsilon_{\text{bulk}} = \frac{\iint_S [\varepsilon_{\theta_{ei}} c_p \Pi F_\theta + (\varepsilon_{\theta_{ei}} + \varepsilon_{r_t}) L_s F_{r_v}] dS}{\iint_S [c_p \Pi F_\theta + L_s F_{r_v}] dS}, \quad (7.4)$$

to obtain the ratio of the total APE production by surface fluxes in the area to the total surface enthalpy flux provided to the area. The surface area S may include the surface of the entire model domain or may be restricted to a smaller region around the TC (e.g. the surface within 500 km of the TC's central axis). The surface area included will be specified for each application of the bulk surface APE efficiency in subsequent sections.

Quantities computed over the entire TC model domain, such as the integrated kinetic energy or the total power dissipation, are expected to be strongly affected by the bulk surface APE efficiency, $\varepsilon_{\text{bulk}}$, since this controls the available energy input to the TC as a whole. The potential intensity is expected to be more closely related to the maximum surface APE efficiency, ε_{max} , because PI is concerned with the maximum kinetic energy at a single point.

It should be noted that the definitions of efficiency provided above are dependent on reference state, through the definitions of $\varepsilon_{\theta_{ei}}$ and ε_{r_t} . A typical value of ε_{max} is 20%. Testing the initial, mean and vortex reference states defined in Chapter 6 and taking the maximum value of ε_{max} over the run, the highest value achieved by any of the model runs described in Chapter 4 at any time is 22.34% (N30.3, vortex reference state), while the lowest is 20.36% (N26.3, vortex reference state). The maximum surface APE efficiency therefore does not vary strongly with reference state or initial model conditions, although a slight increase is seen as SST increases.

On the other hand, the bulk surface APE efficiency is very dependent on the choice of reference state. For the J30.3 run, using the initial reference state yields a bulk efficiency that continues to increase until the end of the run at 250 h, by which time it reaches 13%. In contrast, the bulk efficiency with respect to the vortex reference state becomes steady by 150 h, with a 150–250 h average of 4.3%. This difference occurs because many parcels at large radii have large positive APE production efficiencies with respect to the initial reference state, since they are buoyant relative to the initialisation sounding, but low efficiencies relative to the vortex reference state, since they are close to thermal wind balance. This issue was discussed in Chapter 6, where it was shown that the vortex reference state is better able to predict the generation of kinetic energy in the model, and therefore bears more physical relevance to the development of the TC. The outer parcels

may produce more APE and hence appear more efficient relative to the initial reference state, but this APE is largely not converted into kinetic energy. The rest of this chapter will therefore focus on the bulk efficiency with respect to the vortex reference state.

The bulk surface APE efficiency is also sensitive to the region of the domain included. Using the vortex reference state and the J30.3 model run, the maximum value of $\varepsilon_{\text{bulk}}$ that can be obtained is 9%, by integrating over a surface area with a radius of approximately 1000 km. The bulk efficiency then decreases to 4.3% as the size of the region is increased to include the whole domain. This means that care should be taken when interpreting absolute values of bulk efficiency. However, the pattern of temporal variation in $\varepsilon_{\text{bulk}}$, which will be investigated in the next section, is not sensitive to changes in region size.

For the model runs with each of the six sets of initial conditions outlined in Chapter 4, $\varepsilon_{\text{bulk}}$ was calculated for the region $r < r_5$, where r_5 is the radius at which the azimuthal wind speed in the lowest model level declines to 5 m s^{-1} . This permits comparison between the efficiencies, since the region of integration is adjusted to the size of the TC in each model run. The efficiencies ranged from 2.68% to 8.47%, but no trends with SST or systematic differences between the initialisation soundings were observed. It is possible that using a larger sample of initial conditions would uncover relationships with bulk efficiency.

The surface APE efficiency ε plays a role in moist APE theory equivalent to the one played by the TPE efficiency in TPE theory, or by the dry APE efficiency in dry APE theory. TPE theory views latent heat release as the source of potential energy for a TC; the TPE efficiency is defined as the generation of kinetic energy divided by this potential energy source. Dry APE theory similarly views latent heat release as the source of potential energy, but instead defines efficiency as the generation of APE divided by the latent heat release. These two efficiencies should be similar, assuming that the generation of APE implies the generation of kinetic energy. Moist APE theory instead views surface enthalpy fluxes as the source of potential energy, and therefore the equivalent efficiency is the generation of APE divided by the surface enthalpy flux.

The values of $\varepsilon_{\text{bulk}}$ computed here are comparable to the values of whole-TC TPE efficiency ($\approx 3\%$) reviewed in Chapter 2, since both efficiencies quantify the fraction of energy input that can be converted to kinetic energy. However, the maximum value of ε is much higher than the maximum value of TPE efficiency (20% vs 6%). This suggests that the surface APE efficiency may be more useful for linking the concept of bulk energetic efficiency with the theory of potential intensity, since the latter can be derived using the

Carnot efficiency, which has a typical value of 33%. A theory of potential intensity based on APE will be constructed in Section 7.3. First, since increases in TPE efficiency have been linked to the rapid intensification of TCs, the next section investigates the extent to which increases in $\varepsilon_{\text{bulk}}$ contribute to TC intensification.

7.2 Temporal variation of surface APE efficiency

Section 2.3.1 outlined the theory of Schubert and Hack (1982) that the increasing TPE efficiency of a TC could cause periods of rapid intensification (RI). However, the shortcomings of this theory, raised by Smith and Montgomery (2016), were also discussed: regions of high TPE efficiency occur above the boundary layer, so the theory cannot account for boundary layer dynamics or thermodynamics; and the idealised vortices used to investigate efficiency increases by Schubert and Hack (1982) and Hack and Schubert (1986) were forced by fixed heating rates, not allowing any feedback with the secondary circulation.

This section therefore re-frames the concept of increasing energetic efficiency in terms of the bulk surface APE efficiency $\varepsilon_{\text{bulk}}$, as defined in Equation (7.4). This provides a measure of the TC's overall energetic efficiency, similarly to TPE efficiency, but it focuses on the effect of surface fluxes on near-surface parcels. This means that boundary layer processes can directly affect $\varepsilon_{\text{bulk}}$, whereas they cannot directly affect the TPE efficiency. The axisymmetric model used in this thesis does not contain a boundary layer scheme, so a more complex model would be required to properly investigate how boundary layer spin-up mechanisms interact with APE efficiency. However, the work presented here is able to explore whether $\varepsilon_{\text{bulk}}$ increases during TC development in a similar way to TPE efficiency. Using the axisymmetric model also removes the need to use a fixed heating rate, since the surface fluxes are determined interactively in the model.

Figure 7.1 shows time series of ε_{max} (7.1a) and $\varepsilon_{\text{bulk}}$ (7.1b) in the J30.3 run of the axisymmetric model. There are clear increases in both the bulk and maximum efficiencies as the TC develops. The increase in the maximum efficiency from 20.5% to 22.1% is small. The maximum APE production at the surface is the maximum value of the product of the surface APE efficiency ε , as defined in Equation (7.1), and the surface enthalpy flux. The maximum surface enthalpy flux approximately doubles from 5–100 h, so the increase in the maximum APE production during the TC's development is mostly due to this increase in flux rather than the small change in efficiency. The increase in bulk efficiency, from nearly 0 to 5%, is a much larger relative change.

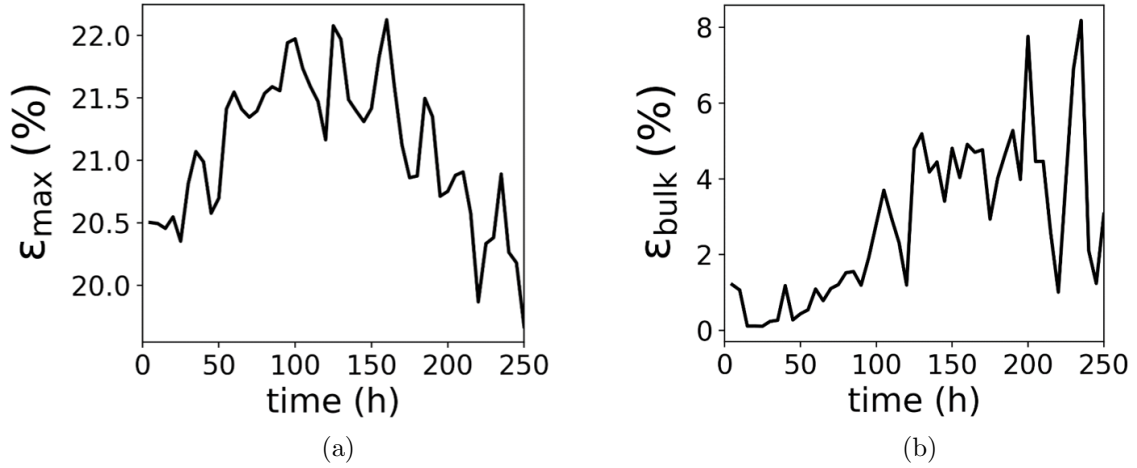


Figure 7.1: (a) Maximum and (b) bulk surface APE production efficiency in the J30.3 axisymmetric model run. Note that the y -axis in (a) does not begin at zero.

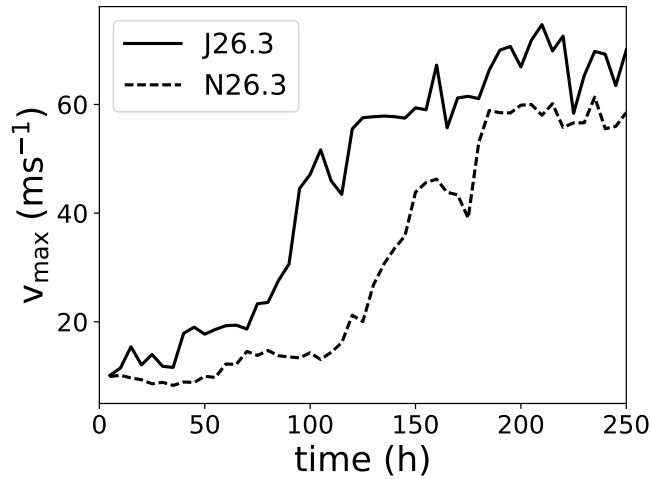


Figure 7.2: Maximum azimuthal wind speed of the TCs in the J26.3 (solid line) and N26.3 (dashed line) model runs.

To investigate how increases in $\varepsilon_{\text{bulk}}$ are timed relative to the intensification of the TC, the evolution of bulk efficiency is compared between the J26.3 and N26.3 model runs. These two runs are chosen because they undergo similar increases in v_{max} , but the intensification of N26.3 occurs around 50 h later, as shown in Figure 7.2, so differences in the timing of efficiency changes can be analysed. The relative delay in intensification in the N26.3 case is most likely because the development of the N26.3 TC cannot be aided by the release of environmental CAPE, since its environment is neutral to convection.

The rate of power dissipation is used as a metric of intensity, rather than v_{max} . The power dissipation rate is computed by integrating the rate of frictional dissipation of kinetic energy over the domain (this includes dissipation at the surface, and internally in turbulent eddies). Since $\varepsilon_{\text{bulk}}$ quantifies the efficiency of the TC as a whole, it should be

more closely linked to the total power dissipation in the system than to the maximum wind speed.

Figure 7.3 compares the power dissipation rate to $\varepsilon_{\text{bulk}}$ for the J26.3 and N26.3 runs, computed over the inner 500 km of the domain, since this includes the main TC circulation and regions of APE production. The results are not sensitive to the region chosen. Both runs exhibit an increase in $\varepsilon_{\text{bulk}}$, and in both cases this coincides temporally with an increase in power dissipation. The intensification and increase in efficiency of J26.3 occurs mostly during the period 50–100 h, whereas the neutral environment of N26.3 results in a delay of both intensification and efficiency increase until 100–150 h. In both cases the product of $\varepsilon_{\text{bulk}}$ and the surface enthalpy flux is of the same order of magnitude as the power dissipation rate; a closer match is not expected due to the storage of kinetic energy, the export of mechanical energy from the 500 km region (leading to power dissipation in the wider domain), and contributions to the APE production from internal processes such as mixing.

It is therefore concluded that, at least in the axisymmetric model, the intensification of a TC is associated with an increase in bulk surface APE efficiency. Higher efficiency means a greater rate of APE production for a given surface enthalpy flux, and so is expected to lead to greater rates of production and subsequent dissipation of kinetic energy. This provides a plausible physical pathway through which increasing efficiency could lead to intensification. However, the results presented so far do not isolate the effect of efficiency changes on the power dissipation, because the surface enthalpy flux is also

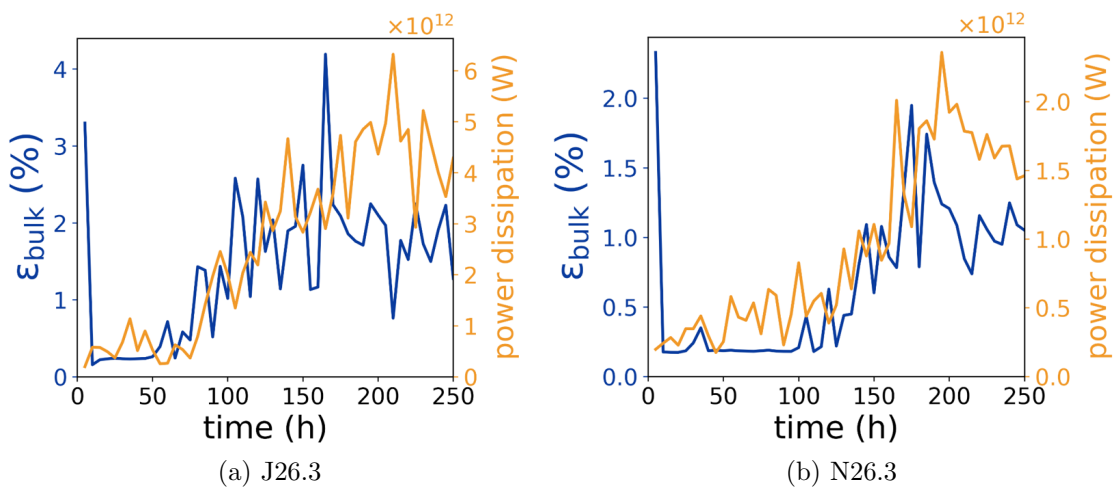


Figure 7.3: Bulk APE efficiency with respect to the vortex reference state (blue lines) and integrated power dissipation (orange lines) in the (a) J26.3 and (b) N26.3 model runs. Quantities are computed over the inner 500 km of the model domain. Note that the y -axes in (a) and (b) have different ranges.

increasing during the periods of intensification. It is possible that the power dissipation is increasing simply because surface fluxes are increasing, without the efficiency playing a necessary role.

The next section asks the question: is it possible for the bulk efficiency to increase in the absence of an increasing surface enthalpy flux? A surface flux capping experiment is performed with the aim of disentangling intensification due to efficiency increases from intensification arising from increasing surface enthalpy fluxes due to the WISHE feedback.

7.2.1 Dependence on WISHE feedback

The Wind-Induced Surface Heat Exchange (WISHE) theory describes the intensification of a TC due to feedback between surface wind speed and surface enthalpy flux (Emanuel, 1986; Rotunno and Emanuel, 1987). Surface heat fluxes increase θ_e in the boundary layer, leading to convection, which warms the troposphere and results in a decrease in central pressure. This increases the horizontal pressure gradient at the surface, increasing the surface wind speed. This in turn causes the surface fluxes to increase (Equations (4.12) and (4.13) demonstrate the dependence of surface fluxes on wind speed), completing the feedback loop. The term *WISHE feedback* is used in this chapter to refer to the general existence of a positive feedback between surface enthalpy flux and surface wind speed, rather than specifically the feedback as it occurs at the radius of maximum winds, which acts to increase intensity in terms of v_{\max} and is therefore the focus of many studies of intensification (e.g. Montgomery et al., 2015; Zhang and Emanuel, 2016).

Figure 7.3b showed that the intensification is associated with an increase in bulk surface APE efficiency. However, it was not possible to discern whether this increase is essentially tied to the wind speed–surface flux feedback of the WISHE mechanism (for example, increasing surface fluxes could raise θ_e in boundary layer parcels, increasing their APE efficiency), or whether it can function as an independent mechanism of intensification. A surface flux capping experiment is therefore performed to cut off the WISHE feedback, so that the surface enthalpy flux no longer increases after a certain time. Since TPE efficiency can increase even under constant forcing (Hack and Schubert, 1986), it is hypothesised that $\varepsilon_{\text{bulk}}$ will be able to increase after the surface flux is capped, and that this will result in an increase in the power dissipation rate, since more APE will be produced by the surface fluxes.

The capped experiment is performed as follows. At 90 h into the N26.3 run, the radial profile of azimuthal wind speed in the lowest model level is defined as v_{cap} . The time of

90 h is chosen because it occurs just before the main period of intensification begins in the uncapped run. At all time steps after 90 h, the surface wind speed in the equations for the surface fluxes of θ and r_v is limited to a maximum of v_{cap} :

$$F_{\theta} = C_T \min \left(v_{\text{cap}}, \sqrt{u^2 + v^2} \Big|_{\Delta z/2} \right) \left(\theta_{\text{surf}} - \theta \Big|_{\Delta z/2} \right), \quad (7.5)$$

$$F_{r_v} = C_E \min \left(v_{\text{cap}}, \sqrt{u^2 + v^2} \Big|_{\Delta z/2} \right) \left(r_{v_{\text{surf}}} - r_v \Big|_{\Delta z/2} \right). \quad (7.6)$$

This cuts off the WISHE feedback between surface wind speed and surface flux after 90 h. The procedure is similar to the ones used by Montgomery et al. (2009), Montgomery et al. (2015) and Zhang and Emanuel (2016) to investigate whether WISHE is essential for intensification, but here a radially-varying v_{cap} is used where those studies used a constant value. Since $\varepsilon_{\text{bulk}}$ and the power dissipation are defined over the region $r < 500$ km, the WISHE feedback should not act in any parcels in this region after the capping time. If a constant value for the cap were applied, parcels at outer radii with $v < v_{\text{cap}}$ could continue to experience the feedback after 90 h.

Figure 7.4a shows the surface enthalpy flux integrated over the inner 500 km for the uncapped (solid line) and capped (dashed line) experiments. The vertical grey line marks 90 h, at which time the cap is applied. Whereas without the cap the enthalpy flux increases from 90–200 h, the flux in the capped experiment remains approximately constant after 90 h. This means that any increases in efficiency or power dissipation after this point will not be related to an overall increasing supply of enthalpy via surface fluxes.

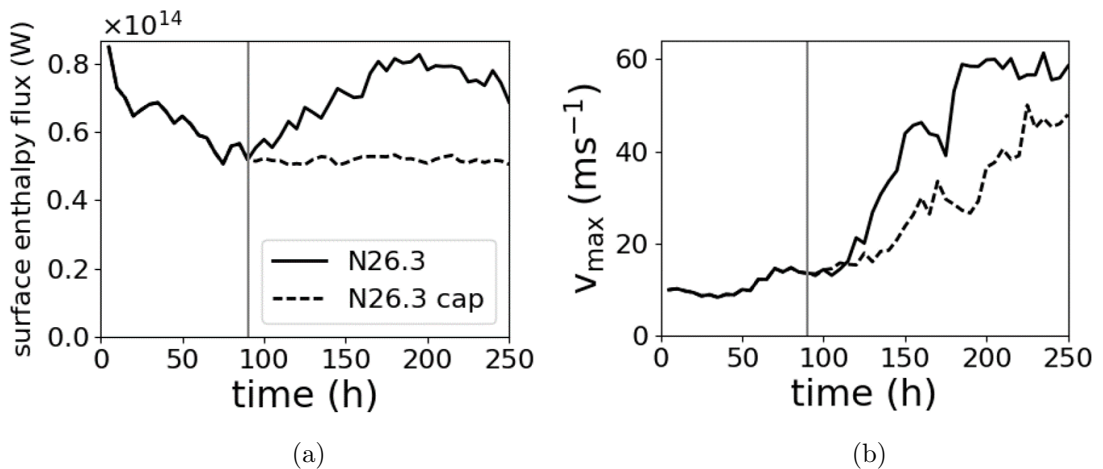


Figure 7.4: (a) Integrated surface enthalpy flux over $r < 500$ km and (b) maximum azimuthal wind speed v_{max} in the N26.3 model runs with uncapped (solid line) and capped (dashed line) surface fluxes. The grey vertical line marks the time after which the surface flux is capped.

The TC in the capped experiment continues to intensify after the cap is applied, but does so more slowly than the TC in the uncapped experiment (Figure 7.4b). It also reaches a lower final intensity. This was also found by previous studies using a constant v_{cap} (Montgomery et al., 2009, 2015; Zhang and Emanuel, 2016).

The bulk efficiency $\varepsilon_{\text{bulk}}$ and power dissipation for the capped experiment are shown in Figure 7.5. The time series are shown starting at 10 h to avoid using an unnecessarily large axis range to include the high value of $\varepsilon_{\text{bulk}}$ during spin-up at 5 h. The time of capping is again marked by the grey vertical line. In this case, $\varepsilon_{\text{bulk}}$ does not increase until after 150 h, but then approximately triples from 0.2% to 0.6% between 150 and 250 h. As hypothesised, the power dissipation also increases. During this period, WISHE is not active and surface fluxes are not increasing. The capped experiment therefore demonstrates that efficiency increases may occur independently of the WISHE feedback.

Figure 7.6 compares the bulk APE efficiency between the capped and uncapped N26.3 model runs. Although the efficiency does increase in the absence of the WISHE feedback, the increase is less than is seen in the uncapped case and occurs later in the simulation. This is similar to the behaviour of v_{max} seen in Figure 7.4b. The WISHE feedback accelerates the efficiency increase and leads to an approximately doubled bulk APE efficiency at the end of the model run in this case.

Although the physics of why an increase in efficiency should result in a higher power

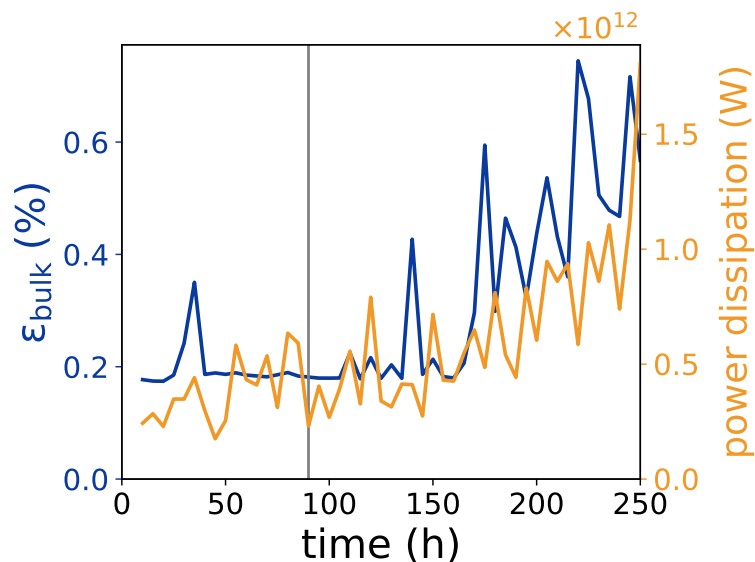


Figure 7.5: Bulk APE efficiency with respect to the vortex reference state (blue line) and integrated power dissipation (orange line) in the capped N26.3 model run. The grey vertical line marks the time after which the surface flux is capped. Quantities are computed over the inner 500 km of the model domain. Time series start at 10 h.

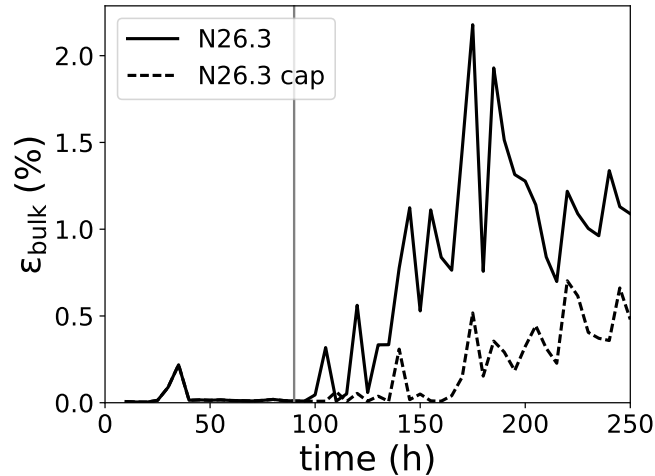


Figure 7.6: Bulk APE efficiency with respect to the vortex reference state for the N26.3 uncapped and capped runs, over the inner 500 km of the model domain. The grey vertical line marks the time after which the surface flux is capped. Time series start at 10 h.

dissipation have been described previously in this chapter, this experiment cannot clearly establish the direction of causality between the two; power dissipation could also be affecting efficiency. Chapter 6 demonstrated that frictional dissipation at the sea surface plays a significant role in determining the balanced vortex reference state, relative to which the APE production efficiencies entering $\varepsilon_{\text{bulk}}$ are calculated. It is therefore possible that the power dissipation itself could increase the bulk efficiency via its effects on the reference state. This would result in a feedback between efficiency and surface wind speed, which does not directly involve increases in the surface enthalpy flux, although θ_e anomalies would still be required in the boundary layer for parcels to attain reference heights in the upper-tropospheric outflow.

Whether or not such a feedback between surface wind speed and APE efficiency exists, it is clear that increases in efficiency lead to increased APE production and therefore increased kinetic energy generation and dissipation. This effect can act simultaneously to WISHE, which could promote rapid intensification in cases where both the enthalpy flux and the efficiency are increasing, but does not rely on WISHE's existence. A TC with increasing efficiency would be expected to intensify more quickly than a TC with identical surface fluxes but a fixed efficiency. Unfortunately, it is not possible to conduct an experiment comparing these two hypothetical cases, since fixing the efficiency would require constraining the vortex to such an extent that v could no longer be independently studied. This means it is not possible to ascertain here whether efficiency increases are strictly necessary for intensification.

The results of this section support the claims of Schubert and Hack (1982) and Hack

and Schubert (1986) that temporal increases in efficiency can enhance TC development. Rather than approaching the topic using TPE theory, the results here have shown that the bulk surface APE efficiency increases during TC intensification, and may do so even in the absence of the WISHE feedback. An increasing efficiency allows the TC to generate more kinetic energy for a fixed surface flux, leading to more rapid intensification. An increasing APE efficiency could augment the WISHE feedback, with increases in surface wind speed leading to both increased surface flux and increased efficiency.

7.3 Potential intensity using APE theory

The prominence of similar concepts of efficiency in the theories of APE and PI suggests a link between the two. PI theory features the Carnot efficiency ($\approx 33\%$), while the maximum surface APE efficiency was found in Section 7.1 to be $\approx 20\%$. This section derives an equation for PI based on local moist APE theory and compares it to existing theories of PI. The term *PI* is used here to refer to both theoretical upper bounds on wind speed that are computed *a priori* (from knowledge of the TC's environment only) and those computed using diagnosed variables from the model, which vary throughout the TC's evolution. The relative merits of these two approaches will be discussed.

The role of the Carnot efficiency in PI theory was elucidated in Section 2.3.2, but is summarised here for clarity. As seen from Equation (2.53), the square of the maximum surface azimuthal wind speed v_{\max} is

$$v_{\max}^2 = \frac{C_k}{C_D} \eta (k^* - k), \quad (7.7)$$

where the Carnot efficiency $\eta = \frac{T_s - T_{\text{out}}}{T_s}$ is the maximum possible efficiency of a heat engine working between the surface temperature T_s and the outflow temperature T_{out} . As before, C_k and C_D are the exchange coefficients for enthalpy and momentum respectively, k is the moist enthalpy of boundary layer air and k^* is the moist enthalpy assuming saturation at the surface temperature and pressure. The axisymmetric model does not include dissipative heating, and so its effects are not considered when discussing PI in this section; dissipative heating would introduce a factor $\frac{T_s}{T_{\text{out}}}$ on the RHS of (7.7).

In order to make the relationship between APE and existing PI theories clear, the assumptions of the axisymmetric model are disregarded for the moment and the exact local available energetics presented by Tailleux (2018) are used (as summarised in Section 2.1.2). The starting point for deriving a PI equation from APE theory is to assume that,

in a steady state, the rate of production of available energy (APE + AEE) by surface fluxes is balanced by the rate of frictional dissipation of kinetic energy at the surface:

$$\rho C_k |\mathbf{v}| [(T - T_r)(s^* - s) + (\mu - \mu_r)(q_t^* - q_t)] = \rho C_D |\mathbf{v}|^3, \quad (7.8)$$

where s is moist entropy, q_t is total specific humidity and μ is chemical potential. All variables are evaluated at the surface, with starred variables calculated at saturation. This approach is used because Chapters 5 and 6 showed surface fluxes to be the main source of moist APE in the TC inflow and therefore the key driver of the ultimate frictional dissipation at the surface. Rearranging this equation, under the assumption that $|\mathbf{v}| \approx v$, gives the form

$$v_{\max}^2 = \frac{C_k}{C_D} [(T - T_r)(s^* - s) + (\mu - \mu_r)(q_t^* - q_t)] \quad (7.9)$$

for the maximum azimuthal surface wind.

Established PI equations can be recovered by neglecting the production term due to the surface flux of q_t . Using the enthalpy differential $dk = Tds + \mu dq_t + \alpha dp$, the approximation $(s^* - s) \approx \frac{1}{T}(k^* - k)$ can also be made, since $p^* - p = 0$ (because the APE production is occurring in air directly at the surface) and terms involving μ are being neglected. This yields

$$v_{\max}^2 = \frac{C_k}{C_D} \frac{T - T_r}{T} (k^* - k), \quad (7.10)$$

which is identical to Equation (7.7), but with the reference temperature T_r in place of the outflow temperature T_{out} . Alternatively, by neglecting the q_t production term in (7.9) and writing $s = c_p \ln \theta_e$, the PI can be expressed as

$$v_{\max}^2 = c_p (T - T_r) \frac{C_k}{C_D} (\ln \theta_e^* - \ln \theta_e), \quad (7.11)$$

which is the form of PI given by Bister and Emanuel (2002), again replacing T_{out} with T_r (and excluding the dissipative heating factor).

This demonstrates that the PI derived using APE theory is similar to traditional definitions of PI, with two key alterations. Firstly, it includes the contribution from surface fluxes proportional to $(q_t^* - q_t)$. This term accounts for the reduction of APE by both water loading and the Gibbs penalty (Pauluis, 2011) when the energy of water vapour must be increased to lift it to saturation (see Section 5.2.4 for a full discussion of why the APE production efficiency ε_{q_t} is negative). Therefore, including the q_t term is

expected to reduce the predicted PI, since less APE and consequently less kinetic energy will be produced by a fixed latent surface heat flux.

Secondly, rather than using an “outflow temperature”, which can be tricky to diagnose in practice¹, the colder temperature featured in the PI equation is the reference temperature T_r , which is calculated using an LNB equation (see Equation (2.16)) and is unambiguously defined once a reference state is chosen. The impact of the choice of reference state on the predicted PI will be addressed later in this section.

A version of Equation (7.9) suitable for use with the axisymmetric model can be obtained by rewriting the APE production in Equation (7.8) in terms of the model’s conserved variables (θ_{ei} and r_t) and their associated APE production efficiencies ($\varepsilon_{\theta_{ei}}$ and ε_{r_t} , as defined in Chapters 5 and 6). The PI equation (7.9) then becomes

$$v_{\max}^2 = \frac{C_k}{C_D} [\varepsilon_{\theta_{ei}} c_p \Pi (\theta^* - \theta) + (\varepsilon_{\theta_{ei}} + \varepsilon_{r_t}) L_s (r_v^* - r_v)]. \quad (7.12)$$

This also requires the approximation that the model’s surface exchange coefficients for potential temperature and water vapour, C_T and C_E , are equal (with value C_k). In terms of the APE surface efficiency ε defined in Equation (7.1), the PI can be written as

$$v_{\max}^2 = \frac{C_k}{C_D} \varepsilon [c_p \Pi (\theta^* - \theta) + L_s (r_v^* - r_v)]. \quad (7.13)$$

The maximum wind speed depends on the surface APE efficiency, the surface enthalpy flux, and the ratio of the enthalpy and momentum exchange coefficients. The similarity to the Carnot form of PI in Equation (7.7) is clear, with the surface APE efficiency ε replacing the Carnot efficiency.

To practically apply Equation (7.12) to output data from the axisymmetric model, all quantities are diagnosed for each parcel in the lowest model level, $z = \frac{\Delta z}{2}$, since these parcels are the ones to which the surface fluxes are applied. The exceptions are the starred variables, which are evaluated at the surface, and the exchange coefficients, for which a constant ratio $\frac{C_k}{C_D} = 0.4$ is assumed—this is representative of the high wind region in the model (as suggested by Bister and Emanuel (1998), to avoid further implicit dependence on v). The results of the PI calculation will be compared to the maximum v occurring in the lowest model level, to match the level of the APE production.

The efficiencies $\varepsilon_{\theta_{ei}}$ and ε_{r_t} have already been diagnosed in Chapters 5 and 6 for the

¹Emanuel (1986) suggested using an average outflow temperature weighted by s^* on M surfaces, while Bister and Emanuel (2002) simply defines it as the “mean outflow temperature”; the region constituting the outflow is ambiguous.

initial, mean and vortex reference states and can be directly substituted into Equation (7.12). The equation is evaluated for each lowest-level parcel and the maximum v_{\max} obtained is assigned to be the predicted PI. The PI computed from these diagnosed efficiencies will be referred to as the *initial, mean or vortex APE-PI*.

It is also possible to use Equation (7.12) to calculate PI using only the initial conditions: a parcel with saturated surface properties θ_{ei}^* and r_t^* (based on the initial SST and sea-level pressure) is placed at $z = \frac{\Delta z}{2}$, and $\varepsilon_{\theta_{ei}}$ and ε_{r_t} are computed by lifting the parcel to its LNB with the usual procedure, using the initialisation sounding as a reference state. PI calculated in this manner will be referred to as the *initial conditions APE-PI*. It should not be confused with the initial APE-PI, which uses the initialisation sounding as a reference state but diagnoses θ_{ei} , r_t and their saturated values at each model time step. The initial conditions APE-PI reflects the knowledge of PI that can be obtained from APE theory without having to run the model itself. It gives the maximum wind that could be achieved if surface fluxes were able to equilibrate the lowest model level with the surface ($\theta^* = \theta$, $r_v^* = r_v$), at which point surface fluxes would cease.

To provide a comparison to the results of APE-PI, the PI is also computed using two established methods. The first, which will be referred to as the Carnot PI, computes v_{\max} using Equation (7.7), again with constant $\frac{C_k}{C_D} = 0.4$. For simplicity, a constant outflow temperature T_{out} is used, equal to the approximate temperature diagnosed in the outflow in the TC's steady state. The surface temperature T_s is replaced with $T_{\frac{\Delta z}{2}}$, the temperature in the lowest model level, since this is the level at which the azimuthal wind speed will be diagnosed. The second method is the widely-adopted CAPE-PI of Bister and Emanuel (2002)² (see Equation (2.54) and surrounding text for details of the method). The CAPE-PI algorithm computes v_{\max} from the SST, sea-level pressure, and initial soundings of T , p and r_v . The algorithm's settings are adjusted to provide as fair a comparison to APE-PI as possible: dissipative heating is turned off, reversible thermodynamics are used, $\frac{C_k}{C_D}$ is set to 0.4, the lifted parcel is taken from $z = \frac{\Delta z}{2}$, and v_{\max} is taken at this same level rather than being adjusted to a surface value.

The CAPE-PI and initial conditions APE-PI are computed using only information about the TC's initial environment, whereas the Carnot PI and other APE-PIs make use of diagnosed variables throughout the TC's evolution (e.g. $\varepsilon_{\theta_{ei}}$ or k^*), as was done by Rousseau-Rizzi and Emanuel (2019) when assessing PI theories. A theory that predicts PI *a priori* is more useful for forecasting purposes, where the maximum possible intensity

²Code obtained from <ftp://texmex.mit.edu/pub/emanuel/TCMAX/>

must be estimated using only the data that is available ahead of time. Such theories are also suited to seasonal prediction, since the PI can be calculated using a seasonal mean environment. The diagnostic theories require more information input and therefore lose predictive power; in the extreme case, computing the vortex APE-PI requires knowledge of the complete azimuthal wind field in order to construct the reference state, meaning that v_{\max} must in fact already be known before the PI can be calculated. However, it is still useful to assess these diagnostic PI theories, as it will provide information on the scientific basis behind them—for example, comparing the initial and mean APE-PIs will indicate whether changes in the TC’s mean environment provide additional constraints on v_{\max} above those already imposed by the initial conditions.

Figure 7.7 compares the various predictions of PI to the diagnosed maximum lowest-level azimuthal wind speed in the model, using the N28.3 run as an example (similar results are found for the other runs, with superintensity above the Carnot PI demonstrated for SST= 26.3 °C). The Carnot PI provides a good estimate of the TC’s steady state v_{\max} , as expected from previous successes of the theory (e.g. Rousseau-Rizzi and Emanuel, 2019). The PIs computed using the diagnosed APE efficiencies are not particularly sensitive to

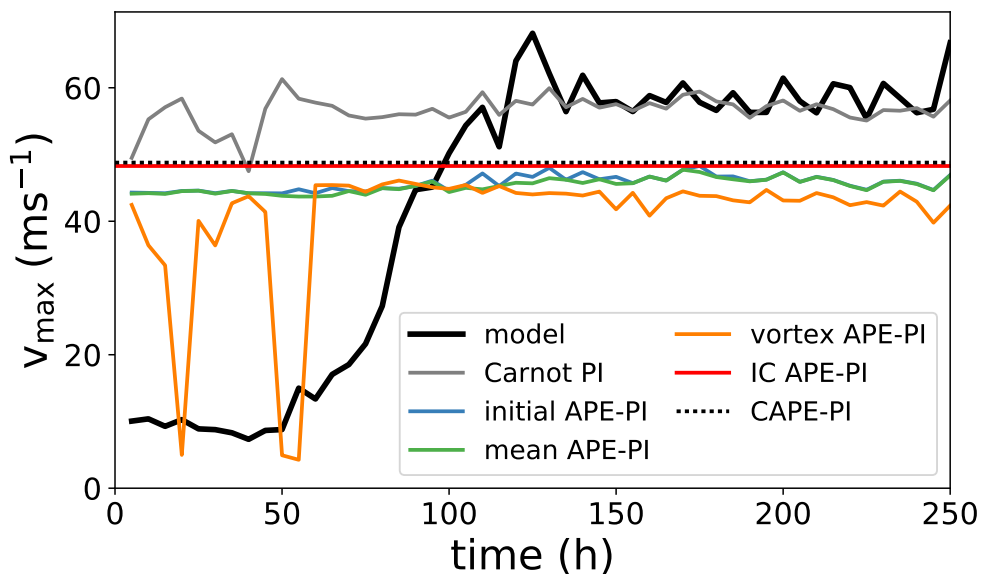


Figure 7.7: Potential intensity (PI) predicted by APE theory, compared to traditional measures of PI, for the N28.3 axisymmetric model run. The solid black line is the actual maximum lowest-model-level azimuthal wind speed diagnosed from the model output. The grey line shows the PI calculated using the Carnot efficiency. The blue, green and orange lines show the PI calculated using the diagnosed APE efficiencies with respect to the initial, mean and vortex reference states respectively. The red line marks the PI calculated by applying APE theory to the initial sounding. The dotted black line shows the PI predicted from the initial sounding by the CAPE-PI method of Bister and Emanuel (2002).

the choice of reference state, but underestimate v_{\max} by approximately 20%.

A key difference between the Carnot PI and the APE-PIs is that the APE-PIs include the water loading/Gibbs penalty term (the q_t term in Equation (7.9)), whereas the Carnot PI does not. APE is computed by assuming reversible adiabatic lifting of parcels, with no water precipitating out. It is therefore perhaps not surprising that APE-PI underestimates v_{\max} , because it includes the highest possible negative contribution of water loading to APE production, when in practice the liquid water in the model *does* precipitate out of parcels, reducing this negative contribution. The effect of the Gibbs penalty on reducing PI is likely to be much smaller than the effect of water loading, because the Gibbs penalty becomes zero for a saturated heat engine cycle (Pauluis, 2011), and the air in the core of the TC is close to saturation. Kamieniecki et al. (2018) highlighted that the correction due to the Gibbs penalty can be neglected when scaling the Carnot efficiency of tropical circulations. The APE-PIs and the CAPE-PI also account for changes in air density due to water content, whilst the Carnot PI does not (Garner, 2015), which is likely why the CAPE-PI is smaller and more similar to the APE-PIs than the Carnot PI.

Another reason that the APE-PI will be an underestimate is that APE efficiencies are calculated based on $\tilde{\Pi}$, a domain-averaged value of Π . This was appropriate when considering APE production over the whole domain, but the PI calculation is focusing on processes at the surface, where the pressure is consistently higher than $\tilde{\Pi}$. If the APE production term by changes in r_t is neglected (by replacing ε with $\varepsilon_{\theta_{ei}}$ in Equation (7.13)), and $\tilde{\Pi}$ is substituted for Π when computing surface APE production, then all of the initial, mean and vortex APE-PIs are within 3% of the Carnot PI on average in the steady state.

The initial conditions APE-PI and the CAPE-PI are almost identical for the case presented in Figure 7.7, but this is not generally true, since the algorithms are significantly different. CAPE-PI iterates between computing v_{\max} and p_{\min} in order to account for changes in the central surface pressure, whereas the initial conditions APE-PI does not consider the evolution of the surface pressure—although it would be possible to create an algorithm based on the initial conditions APE-PI that did so.

This example confirms the presented theory that the maximum local moist APE efficiency is linked to the maximum wind speed of the TC, and can be used to obtain a reasonable estimate of PI. This is in contrast to the maximum TPE or dry APE efficiencies, which have no apparent link to PI, highlighting the usefulness of the moist APE viewpoint.

7.4 Discussion and Conclusions

Previously, the energetic efficiency of a TC as a whole and its maximum efficiency leading to PI theory were considered as discrete concepts. The overall energetic efficiency was typically considered in terms of TPE efficiency (Schubert and Hack, 1982; Hack and Schubert, 1986), which has a maximum value of approximately 5% at any point; this is much smaller than the typical Carnot efficiency of 33%, which appears as the maximum efficiency in PI theory. This chapter has demonstrated that local APE theory can unify the two concepts by considering the efficiency of moist APE production by surface fluxes. The surface APE production efficiency ε can be used either to calculate PI or to define the bulk efficiency of the TC as a whole. The bulk efficiency defined using ε is on the order of a few percent, similar to TPE efficiency, while the maximum ε is approximately 20%. This is similar to the Carnot efficiency, with differences arising from the inclusion of the Gibbs penalty and water loading.

Section 7.2 found an increase in bulk APE efficiency (measured relative to the vortex reference state) during TC development in the axisymmetric model, with the increase in efficiency occurring at the same time as intensification. A surface flux capping experiment showed that increases in efficiency can occur when the surface enthalpy flux is constant. These results support the theory of Schubert and Hack (1982) that increases in TC efficiency could lead to rapid intensification; an increasing bulk APE efficiency increases the rate of APE production (for a fixed surface enthalpy flux), which increases the rates of generation and frictional dissipation of kinetic energy.

Whereas the link between efficiency and intensification has previously been studied using highly idealised dry frictionless vortices with fixed heating rates (Schubert and Hack, 1982; Hack and Schubert, 1986), the work in this chapter confirms that the theory still shows promise in a more realistic setting; the axisymmetric model accounts for frictional dissipation, and includes a full treatment of moisture and convection rather than parameterising latent heat release using a constant heating. Using an APE-based efficiency rather than TPE efficiency also addresses one of the main objections of Smith and Montgomery (2016) to the efficiency-intensification link—that efficiency is focused on latent heat release above the boundary layer and therefore cannot consider key boundary layer processes. The bulk APE efficiency $\varepsilon_{\text{bulk}}$ used in Section 7.2 is defined using surface fluxes and their effect on near-surface parcels, thus accounting for some properties of the boundary layer. The use of the vortex reference state means that the efficiency is dependent on the buoyancy of unbalanced parcels in the boundary layer.

Based on the results of Section 7.2, a two-part WISHE-efficiency feedback is proposed. The first part, which is simply an energetic interpretation of the WISHE feedback, is that increasing surface fluxes increase APE production, which leads to faster surface winds and hence a further increase in surface fluxes and APE production. The second part of the feedback is an enhancement of WISHE by increases in the efficiency of APE production by surface fluxes. One reason this could arise is because increases in θ_e in boundary layer parcels, driven by the increasing surface fluxes, will increase the surface APE efficiency, which even further increases the APE production.

Increases in both surface fluxes and efficiency can contribute to intensification. The efficiency increase can also occur in the absence of the WISHE feedback, meaning that processes other than increasing surface fluxes also act to increase efficiency. One candidate for such a processes is the alteration of the balanced vortex state by frictional dissipation. It is not feasible to run an experiment in which the efficiency is fixed, so it is not known whether the surface fluxes could increase in this case. Increases in efficiency can aid intensification but may not be essential to the intensification process.

The intensification considered here is the increase in the total power dissipation of the TC, rather than the maximum wind speed, since $\varepsilon_{\text{bulk}}$ quantifies the efficiency of the TC as a whole and not at some maximum point. It seems unlikely that the increasing efficiency argument could explain the results of Zhang and Emanuel (2016), who found that a TC can continue to intensify in terms of v_{max} after the WISHE feedback is cut off by a surface flux cap. In this case the relevant efficiency would be the Carnot efficiency or ε_{max} , since these govern the efficiency of energy production at the location of v_{max} . Changes in ε_{max} are found to be very small (less than 1%) in the experiments presented in this chapter, and therefore only make a small contribution to the increases in v_{max} .

Section 7.3 showed that is possible to use APE theory to estimate the potential intensity of a TC by assuming that the maximum rate of APE production by surface fluxes is balanced by the rate of frictional dissipation of kinetic energy. The aim of this work was not necessarily to improve upon existing expressions for PI, but to understand how they can be linked to energetic theory and how the assumptions required to compute PI differ when the problem is approached from the energetic viewpoint.

The link between PI and APE is clear when using the exact local available energetics of Tailleux (2018): the traditional PI equation (7.7) is the same as the APE-PI equation (7.10), using the reference temperature T_r (which is calculated as the LNB—relative to the reference state—of a surface parcel) instead of the outflow temperature T_{out} in

the efficiency. Using an LNB with respect to the initial environmental sounding has been suggested in the past as a method of calculating T_{out} (Emanuel, 1986; Rotunno and Emanuel, 1987), although the link to APE was not made. Rotunno and Emanuel (1987) suggested that using the LNB method could result in a colder value than the actual outflow temperature, because in practice a rising parcel would undergo mixing with the environment, resulting in it reaching neutrality sooner. However, Rotunno and Emanuel (1987) ultimately found that the LNB method gave a good approximation to T_{out} for most cases, and it is much easier to calculate this LNB than it is to employ the alternative method used in that study, which involves tracking properties along parcel trajectories and computing an entropy-weighted temperature average.

The APE-PIs calculated in this chapter were based only on APE production by surface fluxes, since this was shown to be a key driver of intensification in Chapters 5 and 6. It is possible that a more complete PI theory could be developed by including the contributions of other diabatic processes to the APE production/dissipation. For example, the environmental mixing noted by Rotunno and Emanuel (1987) to affect the outflow temperature could be addressed by accounting for the APE dissipation from the subgrid mixing term somehow. However, it is not obvious what the best approach to doing so would be, and including small-scale diabatic processes could result in a PI theory containing terms that are difficult to predict *a priori*. The frictional production/dissipation of APE was also not considered here when using the vortex reference state; attempts to derive a PI theory based on the frictional APE production were unsuccessful.

The derivation of PI using APE theory makes it clear why the original definition of PI (Emanuel, 1986) is equivalent to the simpler derivation in terms of a Carnot heat engine. Both Emanuel's PI theory and APE assume reversible thermodynamics. Emanuel assumes moist slantwise neutrality and thermal wind balance above the boundary layer in the steady state, which is equivalent to parcels above the boundary layer having zero APE relative to the vortex reference state; it was seen in Chapter 6 that APE density was small other than in the lowest model level. The exact theory of local available energetics for multi-component compressible stratified fluids then yields the required efficiency. There is no need to assume any closed heat engine cycle to obtain the efficiency, or to consider infinitesimally perturbed cycles as was done by Rousseau-Rizzi and Emanuel (2019). The fact that the initial conditions APE-PI provides an approximate estimate of PI suggests that the most important assumptions for deriving v_{max} are reversible thermodynamics and hydrostatic balance; whereas accounting for gradient balance was essential in order

to estimate the positive kinetic energy production in Chapter 6, it has little impact here.

A key difference between traditional PI theory and the APE derivation presented here is the treatment of water loading. Garner (2015) highlighted that traditional PI methods (Emanuel, 1986, 1988, 1995) neglect the effect of water content on the density of air, whilst the CAPE-PI algorithm does not. This leads to discrepancies between the methods; including the water loading effect reduces the predicted v_{\max} by around 13% when reversible thermodynamics are used (Garner, 2015). This largely accounts for the difference between the Carnot PI and CAPE-PI seen in Figure 7.7 (14.5% for the steady state average). The APE-PI estimates are closer to the CAPE-PI than the Carnot PI because the effect of water loading is included in the r_t APE production term. Carnot PI also neglects the Gibbs penalty, but this should be small if the eyewall is saturated (Pauluis, 2011). Pauluis and Zhang (2017) showed that, once water loading and the Gibbs penalty are accounted for, the eyewall circulation is able to achieve an efficiency of about 70% of the equivalent dry Carnot cycle.

It is not the purpose of this chapter to assess which of the methods of calculating PI is best, since their performance is dependent on the assumptions made in the model thermodynamics. For example, the APE methods perform better if r_t production is neglected, but there is no sound basis for assuming that water loading and the Gibbs penalty ought to be completely neglected in general in PI theory. It is possible that precipitation in the model, which reduces water loading compared to the predictions of reversible thermodynamics, leads CAPE-PI and the APE-PIs to under-predict v_{\max} , but neglecting water loading altogether should not be the answer, since it causes discrepancies in v_{\max} of around 5% even in the pseudoadiabatic limit, where precipitation is accounted for (Garner, 2015). The model thermodynamics also lacks other factors that can influence PI, such as changes in heat capacity due to water content, and the model's inexact conservation of θ_e meant that the APE budget required the use of an averaged Exner pressure $\tilde{\Pi}$, which is not best suited to investigating surface properties. An assessment of PI theories would be more suited to a study using a model with fewer thermodynamic approximations, or observational data.

It is interesting to note that PI is not nearly as sensitive to the choice of reference state as the bulk surface APE efficiency or the integrated APE production rate studied in Chapter 6. This suggests that PI is strongly constrained by the initial environmental sounding; the APE-PI computed using only the initial sounding is very similar to the APE-PI computed using the vortex reference state, despite the fact that the latter incorporates

information about the complete vortex structure.

The PI estimate provides an additional criterion for what can be considered a “good” reference state; a reference state that predicts a value of v_{\max} close to the actual diagnosed value is useful in that sense. This constraint is much less strict than the one based on the integrated rate of APE production from Chapter 6. Whereas in that case only the vortex reference state was found to reasonably predict the total kinetic energy generation rate, here the initial, mean and vortex reference states could all be considered suitable for predicting PI.

It is also easy to see that a potential enthalpy framework could fit this criterion, for example the one used by Tang et al. (2016), in which every parcel is assigned an identical reference temperature and pressure, which are representative of values at the tropopause. Assuming that the outflow occurs near the tropopause, the maximum efficiency $\frac{T-T_r}{T}$ in this framework would give a reasonable estimate of the Carnot efficiency required to calculate PI. However, the total generation rate of kinetic energy would be vastly overestimated since many parcels would not rise to the tropopause in practice. The conclusion of this work is therefore that the vortex reference state is still most appropriate for studying APE in a TC, but that other reference states may be equally or similarly useful if the maximum efficiency or maximum APE production rate are the quantities of interest for a particular study.

Chapter 8:

Conclusions

This thesis has described the construction of a local moist APE budget for an axisymmetric tropical cyclone model and used this budget to study the behaviour of a TC in terms of APE. The appropriateness and consequences of using various APE reference states were assessed, and the role of APE efficiency on TC development was explored in depth.

This final chapter summarises the key novel findings of the thesis and their implications for future studies of TC development and energetics. The findings are grouped according to the thesis aims stated in Chapter 1. The work from Chapters 3–7 is interpreted in the context of Aims (1) and (2), while the third aim, to suggest diagnostics for less idealised models, is addressed for the first time. Finally, the limitations of the current study are discussed and promising avenues for future work are suggested.

8.1 Key findings and recommendations

Aim (1): To produce a full budget of moist APE for a model of the atmosphere.

A budget of moist APE was successfully implemented for the case of the axisymmetric TC model, using a local APE framework of the kind suggested by Andrews (1981), Holliday and McIntyre (1981) and Tailleux (2018). Previous computations of APE in the moist atmosphere have commonly employed sorting algorithms to construct a reference state; Chapter 3 motivated a transition away from these by demonstrating (for the single-column case) that similar results could be achieved using a simple algorithm based on the relationship between APE and CAPE, which was suggested by Emanuel (1994). Whereas sorting algorithms produce reference states via procedures that do not reflect the

physical processes that will occur in the atmosphere, the CAPE algorithm is physically transparent, calculating APE in single-column soundings by assuming that APE is due to a buoyant mixed layer at the surface. Chapter 3 also showed that some approximate algorithms are prone to finding a reference state—intended to minimise total potential energy—that contains even more total potential energy than the actual atmospheric state. The APE budget for the axisymmetric model was therefore constructed using a local APE framework, which avoids these pitfalls of sorting algorithms. The recommendation of this work is to avoid the use of sorting algorithms for APE studies, since they inhibit physical understanding and are too computationally expensive to apply to large 2D or 3D datasets.

A key discovery made during the construction of the local APE budget, which had not been realised before, is that APE density is not necessarily a continuous quantity. In a binary fluid such as the moist atmosphere, a fluid parcel may have multiple levels of neutral buoyancy with respect to the reference state. Since the reference height of the parcel is defined as its nearest LNB in the direction of its *in situ* buoyancy, this poses a problem when these multiple LNBs are separated by a large height. If this is the case, then it is possible for an incremental heating of the parcel to result in a large change in reference height as it jumps from one LNB to another. This causes a large change in the APE density, which is not associated with a large change in diabatic heating. The discontinuities are not caused by model discretisations or approximations.

Chapter 5 therefore introduced the concept of *latent APE*: the part of the background potential energy that may become APE through this kind of LNB switching rather than through the continuous effect of diabatic processes. Latent APE is analogous to CAPE, in that it may be stored up and then suddenly “released” (transformed from latent APE into APE) by the change in LNB, as CAPE is released when the atmosphere is able to overcome CIN. However, the release of latent APE is of questionable physical relevance depending on the choice of reference state. If the reference state is not close to the local sounding, then it would be possible for a parcel to release a reservoir of latent APE without much change to its local buoyancy or motion. The Eulerian APE budget constructed in Chapter 5 also contains spatial discontinuities, where neighbouring parcels with similar thermodynamic properties have very different LNBs. These spatial discontinuities posed significant difficulties to interpreting the budget but cannot be an important physical feature, since they would disappear in a Lagrangian version of the budget. Careful thought will therefore need to be given to the possible existence of discontinuities when discussing Aim (3)—suggesting practical APE-based model diagnostics—later in this chapter, since

diagnostics that are strongly affected by discontinuities are likely to be difficult to interpret physically.

The successful implementation of the local APE budget in Chapter 5, for a case where discontinuities become zero, demonstrates that it is feasible to obtain an approximately closed budget of APE in the moist atmosphere using this kind of local framework. Achieving this closure enables confidence in the conclusions of the budget. For example, the attempted calculation of moist atmospheric budget terms by Wong (2014) found that the APE production efficiency G_{rt} was generally positive for positively buoyant parcels, meaning that adding total water content increases APE. The new budget shows that G_{rt} is negative, which is more easily explained, because both the Gibbs penalty and the gravitational effect of water loading should result in the addition of water decreasing APE. Since Wong (2014) did not compute a closed budget, there was no way of verifying whether the APE efficiencies and production terms were correct, whereas the budget computed in this thesis can provide this assurance. A local APE budget therefore provides a realistic alternative to one based on rearrangements by a sorting algorithm. The discontinuity of APE density poses an issue for the interpretation of local APE budgets, but components of the budget unaffected by discontinuities were successfully used to investigate TC energetics, as will be discussed more in the context of Aim (2).

An outstanding issue in local APE theory was the appropriate choice of reference state. Various reference states had been suggested but not systematically assessed. The clearest existing guidance was the suggestion of Wong et al. (2016) to choose the reference state minimising the storage of APE, but this had not been widely accepted. The method developed in Chapter 6 permitted the objective assessment of reference states in the axisymmetric model by comparing the domain-integrated rate of positive APE production to the domain-integrated rate of positive kinetic energy generation, which is independent of reference state. A reference state was deemed more suitable for studying available energetics if the APE and kinetic energy production rates matched more closely, since any APE production ought to feed through to kinetic energy production if the energy is truly “available”. The advice of Wong et al. (2016) was borne out: computing the APE production using a balanced vortex reference state, which is very similar to the actual atmospheric state throughout the model run and therefore stores very little APE, resulted in the closest match to the kinetic energy production in the model.

The assessment of reference states also provided even further reason to recommend against the use of sorting algorithms. The APE production rate calculated using com-

putationally expensive 2D sorting algorithms gave worse estimates of the kinetic energy production than the local APE framework with simple single-sounding reference states.

Although the vortex reference state was found to best predict the TC's instantaneous generation of kinetic energy, it may not be the most suitable reference state for every application. The total APE stored in the TC is better accounted for by the initial or mean reference states, so these might be more useful for a study of the complete life cycle of a TC, which would include the ultimate dissipation of the vortex and the release of its APE. The vortex reference state is also more difficult to construct than the initial or mean reference states, since it requires iterating the thermodynamic fields to thermal wind balance; this may not be possible or may not produce satisfactory results if the spatial resolution of available data is poor. Chapter 7 showed that the initial, mean and vortex reference states all predicted similar values of potential intensity from APE theory, implying that they are all appropriate for this purpose. This highlights that the suitability of a reference state can be dependent on context; it is not always necessary or preferable to strictly choose the reference state with minimal APE storage.

Future studies using local APE should endeavour to discuss the suitability of a chosen reference state with respect to the aim of that particular study. This can be done using a relevant reference-state-independent metric, such as the maximum wind speed or kinetic energy generation rate, to verify that the predictions of APE theory are compatible with the actual evolution of the system when using a particular reference state.

The three main findings of the work fulfilling Aim (1) can be summarised as:

- It is possible to construct an approximately closed budget of moist APE density for a numerical model of the atmosphere, moving away from the less physically meaningful APE sorting algorithms.
- APE density may behave discontinuously when multiple levels of neutral buoyancy exist.
- The suitability of a reference state for studying available energetics can be verified objectively, for example by comparing the rate of positive kinetic energy generation, which is independent of reference state, to the rate of positive APE production relative to the reference state.

Aim (2): To understand TC intensification and maintenance in terms of APE theory.

The work presented in Chapters 5–7 demonstrated the utility of a moist APE framework over TPE or dry APE approaches to studying TC energetics. TPE is imported into the TC core in the low-level inflow and exported at upper levels, with latent heat release in the eyewall leading to a net export. This means that it is difficult to link the total import and local production of TPE in the core to intensification, since much of the TPE is exported rather than converted into kinetic energy; this occurs because a large portion of the TPE generated by diabatic processes cannot be reversibly converted into kinetic energy, so it does not undergo any energy transfer contributing to the intensification.

In contrast, APE is also imported at low levels, but there is very little export of APE by the upper level circulation. Since APE is by definition reversibly convertible to kinetic energy, almost all the APE imported to the core (as well as the APE production within the core) undergoes a transfer to kinetic energy (via buoyancy fluxes), contributing to the intensification of the TC and leaving very little APE to be exported back out of the core. This difference in export can also be understood by observing that the air leaving the core in the upper level outflow contains a lot more TPE than the upper-level far-field environment, because its temperature is higher, but very little APE, because the high static stability at upper levels means that it cannot be displaced far by buoyancy forces.

This is verified by the complete moist APE budget using the model’s initialisation sounding as a reference state, which shows that, in the steady state, the sum of the flux of APE into the $r < 300$ km region and the local APE production in that region is approximately balanced by the conversion of APE to kinetic energy via the buoyancy flux. In the cases analysed in Chapter 5, the import of APE dominates over the local production. This is expected to be a general result, since the main source of APE is latent heating due to surface moisture fluxes, and the convergence of moisture has been widely shown to dominate over local surface evaporation in moisture budgets of the TC core.

An additional advantage of using the moist APE framework arises from its treatment of the original energy source for the TC. Whereas the main source of TPE or dry APE is latent heat release in the mid-troposphere, the main source of moist APE is the ocean-atmosphere surface flux; this result was robust to the choices of reference state tested in this thesis. The latent heating of near-surface air parcels produces APE less efficiently than sensible heating, because the addition of moisture to parcels also increases the effects of water loading and the Gibbs penalty, which act to reduce efficiency slightly. However,

the energy supplied by the latent surface heat flux is much larger than energy supplied by the sensible heat flux, so the latent surface heat flux dominates the production of APE even with this reduced efficiency.

The surface flux has been known as the source of a TC's energy for many decades (Riehl, 1950; Kleinschmidt, 1951). Treating it as such by using a moist APE framework means that boundary layer processes can directly impact the available energy generation, unlike in TPE or dry APE frameworks where the majority of the generation occurs well above the boundary layer. The intensity of TCs in NWP models is known to be affected by the parameterisations of both surface flux and boundary layer mixing (Green and Zhang, 2013; Zhang et al., 2017). An energy budget that includes the role of the boundary layer is therefore preferable to one that does not, because it could be used to diagnose links between the choices made in these parameterisations and the ultimate generation of kinetic energy.

Moist APE theory also has the ability to link the concept of energetic efficiency to the entropy-based Carnot heat engine efficiency commonly used to predict the potential intensity of TCs. Chapter 7 showed how local moist APE theory can be used to easily obtain the usual expression for PI. In contrast, the efficiencies arising from TPE and dry APE theory are much too small to correspond to the Carnot efficiency, and these theories are not concerned with surface or boundary layer processes at all, when the potential intensity is known to depend strongly on the surface or boundary layer temperature.

The exploration of the complete local moist APE budget was limited to the inner regions of the modelled TCs in their mature stage due to the difficulty of handling discontinuities. However, the theoretical advantages of the moist APE approach summarised above mean that it could still be worth pursuing for some applications even though the full budget is much more difficult to construct and analyse than the TPE budget. Chapters 6 and 7 were able to investigate TC development using diagnostics that are unaffected by the discontinuous behaviour of moist APE density, demonstrating that important insights can still be gained if the correct approach is taken to avoid the occurrence of discontinuities.

Using a vortex in thermal wind balance as a reference state enabled the prediction of the positive production rate of kinetic energy by equating it with the rate of positive diabatic APE production. This meant that the APE budget could be used to break down the contributions of individual diabatic processes to the positive production rate of kinetic energy. The chief contributor to APE production was found to be the surface

flux, demonstrating that the surface flux's role as the main energy source is consistent between the APE defined relative to the initial environment and defined relative to a balanced vortex. Non-negligible contributions were also made to the APE production by precipitation and subgrid mixing. This could provide an energetic explanation for why Kim et al. (2018) found that models that generate more inner-core precipitation (for a given value of precipitable water) produce more intense TCs: the precipitation generates additional APE, which can be converted into kinetic energy in the core.

With respect to the vortex reference state, APE is mostly generated in boundary layer parcels that are buoyant relative to the balanced vortex. When using the initial or mean environment reference states, the APE production is much more widespread throughout the troposphere, because most parcels in the warm core of the TC are buoyant relative to the far-field environment. Where possible, future studies attempting to use a moist APE framework to investigate TC development should employ a balanced vortex reference state, since this was shown to give the most direct link between APE production and kinetic energy production. A budget based on the initial reference state can still be useful—the budget in Chapter 5 shows a clear link between the import of APE to the inner region and its conversion to kinetic energy, and Chapter 7 showed that the initial reference state can be used in the estimation of potential intensity—but it must be qualified by the fact that not all of the APE production in the TC will lead to the generation of kinetic energy during the intensification or maintenance stages.

Chapter 7 showed that TC intensification in the axisymmetric model, as measured by the total power dissipation rate, coincides with an increase in the overall efficiency of APE production by surface fluxes, with respect to the vortex reference state. This supports the TPE-based theory of Schubert and Hack (1982) that periods of rapid intensification could be caused by increases in efficiency, since a higher surface APE efficiency will result in higher APE production—and therefore higher kinetic energy generation—for a fixed energy input by surface fluxes. This could lead to a non-WISHE feedback mechanism. Future work investigating the temporal variation of efficiency in TCs should favour the use of the surface APE efficiency over TPE efficiency, because surface APE efficiency can account for the near-surface/boundary layer processes that are crucial for intensification, and can also be linked to the potential intensity of the TC.

The main result of Chapter 7 was the proposal of a two-part WISHE-efficiency feedback for TC intensification, when intensification is considered in terms of the increase in total power dissipation. In addition to the WISHE feedback increasing APE production,

increases in the surface APE efficiency boost APE production even further. Increases in APE production due to both factors lead in turn to a higher power dissipation. The increase in efficiency is not dependent on the WISHE feedback, since it still occurs when the wind speed is capped in the surface flux equations.

The results here agree with previous conclusions that WISHE is important for intensification, but not the only mechanism playing a role (e.g. Zhang and Emanuel, 2016). Slower intensification and a lower final intensity are seen when the surface flux is capped, but efficiency increases and intensification do still occur. Since the APE efficiency is purely a diagnostic rather than appearing anywhere in the model code, it was not possible to run an experiment capping the efficiency to ascertain whether intensification could still occur in the absence of both parts of the WISHE-efficiency feedback.

The processes leading to increasing APE efficiency in the absence of the WISHE feedback are not clear. One possibility is that since the frictional drag at the surface increases with wind speed, boundary layer parcels could be pushed further out of thermal wind balance, increasing the APE efficiency with respect to a balanced vortex. This would result in an increased APE production rate, and hence a higher rate of kinetic energy production and ultimate frictional dissipation at the surface, further increasing the efficiency. A feedback between efficiency and surface wind speed would therefore result. Further work investigating the role of friction in local available TC energetics will be suggested in Section 8.2; this would permit a better understanding of how APE theory is linked to TC intensification theories that rely on surface friction effects, such as CISK or cooperative intensification. Based the present work, however, the WISHE mechanism is preferred as a theory of intensification, since surface fluxes are the key source of APE and the feedback between surface fluxes and wind speed greatly enhances APE production.

Since this thesis only used an axisymmetric model, the relationship between APE theory and the rotating convection paradigm of intensification could not be studied, because the paradigm depends on asymmetric effects. A hypothesis that could link the two theories is that vortical hot towers (VHTs), which are highly buoyant, act as patches of enhanced APE efficiency, increasing the overall efficiency of the TC. However, a study in a 3D model would be necessary to investigate this.

The main findings addressing Aim (2) are:

- Measured relative to the initial environmental sounding, the main source of APE in a steady-state TC is the surface latent heat flux in the outer inflow, in parcels that are positively buoyant with respect to the environment. This APE is then

transported into the TC core by the low-level inflow, where it is converted into kinetic energy.

- If APE is measured relative to a vortex in thermal wind balance, derived from the azimuthal wind field of the TC, the surface latent heat flux remains the main source of APE. Using this vortex reference state, the rate of positive APE production matches the rate of positive kinetic energy production when integrated over the whole TC. Precipitation and turbulent mixing also make non-negligible contributions to the production of kinetic energy.
- Tropical cyclone intensification, in terms of total power dissipation, is caused by a two-part WISHE-efficiency feedback. As surface wind speeds increase the surface enthalpy flux, the APE efficiency with respect to a balanced vortex can also increase. Both of these factors act to increase the surface APE production and hence the kinetic energy generation rate, raising surface wind speeds further. The efficiency increase can occur independently of the surface enthalpy flux increase.
- The well-known equation for the potential intensity of a TC can be derived directly from local moist APE theory by assuming that the maximum rate of APE production by surface fluxes is balanced by the maximum rate of frictional dissipation.

Aim (3): To identify specific aspects of APE or APE-related quantities that could be usefully applied as process-oriented diagnostics for TCs in NWP or global climate models.

The overall motivation for studying moist APE density in an idealised TC model was to enable the development of APE-based diagnostics, which could assist with the fundamental understanding of the representation of intensification and steady-state intensity in numerical models used for operational forecasts or climate projections. Based on the findings of the rest of the thesis, this section recommends some specific model diagnostics, which have the potential to provide links between choices in model configuration and the resultant intensity of TCs. Research questions associated with each diagnostic are also suggested.

The use of an idealised axisymmetric model meant that the budgets and diagnostics featured in this thesis were not limited by data availability or resolution. When applying APE diagnostics to NWP or GCM data, it becomes necessary to take these into account. Since the APE diagnostics are relatively computationally expensive compared to other

energetic frameworks, it would be sensible to restrict the data under investigation to azimuthally-averaged TC case studies or composites in the first instance, with possible study of asymmetric effects following later.

The APE budget terms for the axisymmetric model were highly customised to the model's thermodynamic approximations (for example, in the derivatives of buoyancy used when defining the APE production coefficients). Whilst it is preferable to account for all of a model's approximations, it could become impractical if comparing results from several models that each employ different thermodynamic approximations and therefore require their own budgeting methods. One possible approach would be to develop diagnostics using exact thermodynamics, but this is likely to lead to unclosed budgets; if it had been done for the axisymmetric model, changes in Π would have led to large unexplained APE generation by unidentified diabatic processes. The best avenue may be to only use APE budgets to compare models within the same family (e.g. only changing the resolution, or convection scheme) to prevent the need to develop many budgets for a single study.

Although the vortex reference state provided highly physically relevant metrics for the axisymmetric model, its construction requires the input of the full azimuthal wind field structure. The azimuthal wind may not be available on all levels for existing model runs, and the vortex integration method described in Chapter 6 has not been tested at the lower resolutions that would be required for GCM data. Additionally, the integration method would not work in 3D, so an azimuthal average of the wind speed would have to be taken. An equivalent to the initial or mean reference state should be relatively simple to construct by taking the average model conditions at some distance far from the TC centre. Therefore, although much physical insight can be gained from the vortex reference state, it might be more feasible to use an environmental sounding reference state for some datasets.

It is also desirable to avoid any diagnostics that might be affected by discontinuities in APE density. Although Chapter 5 showed that there are cases in which discontinuities vanish, the diagnostics should be applicable to numerical model TC data in general, rather than restricted to specific scenarios that are not guaranteed to occur.

Specific ideas for diagnostics, and the aspects of model performance they could be used to examine, are listed below. The diagnostics are suggested in order of computational ambition, beginning with those that only require near-surface data outputs and environmental profiles.

- Radial profiles of APE production by surface fluxes, using the environmental sound-

ing as a reference state. These could be decomposed into profiles of APE production efficiency and the surface fluxes themselves. This kind of diagnostic could be used to investigate whether the changes in TC intensity seen as a result of differences in surface flux or boundary layer parameterisations are due to differences in the production of APE at the surface. For example, differences in vertical mixing in the boundary layer may impact the APE efficiency of boundary layer parcels.

- The flux of APE into the TC core at low levels, measured with respect to the environmental sounding. This is linked to the total conversion of APE to kinetic energy in the core, and so comparing the influx of APE between models could provide a simple energetic explanation for why one model develops more intense TCs than another.
- The integrated conversion of APE to kinetic energy via vertical buoyancy fluxes in the core (again using the environmental reference state). This is likely to be useful for investigating differences caused by convection schemes, since the buoyancy fluxes occur as a result of convection. For example, two models with different convection schemes could produce the same APE through surface fluxes, and import the same amount of APE into the core, but then convert a different amount of this imported APE into kinetic energy, resulting in different intensities.
- If it is feasible to construct a balanced vortex reference state, then the time series of bulk surface APE efficiency with respect to this vortex could be useful for attributing differences in intensification. The under-prediction of temporal increases in efficiency would lead models to forecast slower intensification rates, and could result in poor prediction of rapid intensification events.
- A full budget of the positive production rate of APE with respect to a balanced vortex could provide key insights into the effects of diabatic processes on intensification. This would be particularly helpful if the positive APE production rate could be verified to match the model's rate of positive kinetic energy generation, as was done for the axisymmetric model. Such a budget would require all diabatic processes in the model to be accounted for, and to have full spatial fields of their tendency terms available. The budget could assess, for example, how a change in the microphysics scheme affects the generation of APE by precipitation, or how changes in mixing length alter the contribution from subgrid turbulence.

8.2 Limitations and future work

The main avenue of future work arising from this thesis is the application of the diagnostics suggested under Aim (3) above to output from NWP and global climate models. Comparison between the diagnostics for two models that differ only in one aspect of their configuration (e.g. convection scheme, microphysics scheme, boundary layer mixing parameterisation or resolution) would help identify the physical processes linking these configurations to the TC intensification rates and maximum intensities produced by the models. This final section outlines some additional ideas for future studies, which would build on the understanding of TC APE gained through this work and address some of the shortcomings of the present study.

The use of a simple idealised model in this thesis facilitated the construction of an APE budget, which was able to account for the effects of all modelled processes. The results are expected to be generally applicable to TCs in other models, since the model produces TCs with a similar dynamic and thermodynamic structure to those seen in other models and reality. However, it should be borne in mind that these results are only for a single model, and there are some processes that the model does not represent and therefore could not be investigated here.

The equations of the Rotunno and Emanuel (1987) axisymmetric model do not exactly conserve mass or energy. This was not a barrier to investigating the behaviour of APE density in the model, since the budgets developed are internally consistent, but it should be verified that fundamental results—such as the increase of APE efficiency during intensification—can be replicated by a conservative model, to ensure they do not result from spurious sources of energy. This could be attempted using the idealised Cloud Model 1 (CM1, Bryan and Fritsch, 2002), which uses an equation set that conserves total mass and energy in reversible saturated conditions (although in practice there is still some non-conservation due to the numerical scheme), and can easily be configured to simulate an axisymmetric TC (Bryan and Rotunno, 2009b). The more complicated thermodynamics mean that it would be more challenging to construct a full budget of APE production by diabatic processes (if it is possible at all), but the fact that a first budget has been established in this thesis means that a partial budget for CM1—for example, only looking at the production by surface fluxes—could be verified as reasonable without the need for full closure, by comparison to the results here.

Since the model used in this thesis is axisymmetric, the effects of azimuthal asymmetries were not addressed, although they are known to be able to aid intensification

(Persing et al., 2013). Assessing the characteristics of three-dimensional features in terms of APE would be more computationally expensive than the axisymmetric approach, but could yield important insight into how the energetics differ from the axisymmetric case. This would allow the rotating convection theory for intensification to be evaluated from an APE viewpoint and hence linked to the WISHE-efficiency theory established here. CM1 would serve as a useful test bed for comparing APE in equivalent axisymmetric and 3D simulations; NWP models and GCMs can only provide 3D TC data, which can be subsequently azimuthally averaged but is not representative of an axisymmetric simulation.

Dissipative heating was neglected by the Rotunno and Emanuel (1987) axisymmetric model but its effect on the APE budget could be investigated either using CM1 or NWP model data. It is expected that dissipative heating would provide an additional source of APE near the surface, since the APE efficiency with respect to entropy or θ_e is generally positive here.

Boundary layer processes (other than surface fluxes) were also not investigated in this thesis, because there is no boundary layer scheme implemented in the Rotunno and Emanuel (1987) model. There was no obvious way to diagnose a boundary layer top and the vertical resolution was relatively coarse (625 m), so the lowest model level was simply taken to represent the boundary layer air. It would therefore be worthwhile to undertake a more thorough investigation of APE properties in a model with a more realistic boundary layer. This would enable the study of differences in APE properties between the surface and the boundary layer top as well as the exploration of the energetics of the boundary layer spin-up mechanism of intensification. Such a study could be performed using CM1, which includes a choice of boundary layer schemes and the option to use a stretched grid to allow for finer resolution of the boundary layer, or using an NWP model with a well-resolved boundary layer.

The construction of a Lagrangian APE budget would resolve some questions about the relevance of discontinuities in APE density to intensification. CM1 includes parcel-tracking capabilities, which could be used to investigate Lagrangian APE budgets for parcels travelling through the inflow and eyewall. Spatial discontinuities in APE density would disappear in the Lagrangian form of the budget and it would be possible to assess whether parcels undergoing temporal discontinuities exhibited a subsequent associated change in their kinetic energy. It would also be worth investigating whether there is a way to eliminate discontinuities by using an exactly neutral reference state, so that

separated LNBS do not occur. Attempts at this were not successful for the axisymmetric model, but it might be feasible for a setup with exact thermodynamics.

It would be of interest to investigate whether moist APE theory could be used to derive a TC intensification timescale similar to the linear growth rates predicted by Eady (1949) for disturbances in a baroclinic atmosphere, or by Charney and Eliassen (1964) for tropical depressions (based on the CISK theory). It seems likely that a timescale resulting from the consideration of local APE theory would show similarities with the axisymmetric TC spin-up timescale found by Emanuel (1989). This timescale is dependent on the vertical mass flux; a local APE-based timescale could plausibly depend on the vertical buoyancy flux (or the buoyancy flux along angular momentum surfaces, for a non-resting reference state), which constitutes the conversion of APE into kinetic energy.

A full understanding of local available energetics with respect to a non-resting reference requires the generalisation of the theory to allow the use of an arbitrary balanced reference state. The present work constructed the reference state from the model's instantaneous azimuthal wind field, which was the simplest approach because it eliminated discussion of terms arising from differences between the actual and reference angular momentum. However, it means that the theory could not be used to describe the evolution of the reference vortex, which would be a useful metric of intensification, because the vortex was already completely determined by construction. This limits the understanding of intensification that occurs slowly and close to balance. Outside the context of axisymmetric vortices (e.g. for zonal flow), the theory could be formulated in terms of potential vorticity in place of angular momentum. A general theory of local available energetics for axisymmetric flow with an arbitrary balanced reference state, restricted to the case of a single-component fluid (e.g. a dry atmosphere) is presented in Tailleux and Harris (2020, Appendix C), but a general theory for the moist atmosphere remains an open problem.

Another key aspect of the energetics that should be investigated further is the production/dissipation of APE by friction, which does not appear in the theory when a resting reference state is used. Chapter 6 found positive frictional APE production near the location of maximum winds, but the physical significance of this in terms of intensification or potential intensity is not clear. Friction also plays a role in determining the departure of the actual state from the balanced reference state, meaning that it influences the efficiency of diabatic APE production. Exploring the relative roles of diabatic and frictional APE production in a generalised theory could help to unify the understanding of intensification theories that rely on the frictional organisation of convection, such as

CISK or cooperative intensification, with those that focus on diabatic heating by surface fluxes, such as WISHE. It might be useful to compare APE production in a frictionless vortex to the APE production found in this thesis, to establish how the absence of friction impacts the diabatic APE production.

Further investigation is also necessary to fully comprehend the processes involved in the WISHE-efficiency feedback, which was postulated in Chapter 7. Although it was demonstrated that the surface APE efficiency can increase in the absence of the WISHE feedback, the mechanism responsible for this increase was not established. Studying the surface APE efficiency in a frictionless vortex would provide a method of determining whether surface friction plays a role in the efficiency increase, as was suggested in Chapter 7.

Calculating the local available energy relative to a non-resting reference state is in essence a method of separating an atmospheric system into a basic state (the reference state) and disturbances acting upon that basic state to study a wave-mean flow interaction. This is also the idea behind concepts such as wave activity, the generalised Lagrangian mean, the Eliassen-Palm flux, pseudoenergy and pseudomomentum (Andrews and McIntyre, 1976, 1978a,b; Haynes, 1988; Methven, 2013). Now that this link has been recognised, it would be valuable to investigate the fundamental links between local available energetics and these theories and to establish whether they may provide any additional insight into the intensification of TCs in a moist atmosphere.

Appendix A:

Sorting Algorithm Runtimes

The most time-consuming stage of each of the algorithms used to compute APE in Chapter 3 is the calculation of the temperatures of air parcels when they are moved reversibly and adiabatically to a given pressure level. For the approximate sorting algorithms, this calculation is required in order to sort the parcels by density (or specific volume, equivalently) at each pressure level of the sorting process. The Emanuel algorithm requires the calculation in order to find the specific volume of lifted parcels for the calculation of CAPE (see Equation (3.3)). For the Munkres algorithm, it is required in order to compute the *cost matrix* \mathbf{C} , where c_{ij} is the enthalpy of the i^{th} parcel if it were moved to the j^{th} pressure level.

The algorithms here are implemented using a vectorised bisection method to calculate the temperatures of many parcels at once (see Langtangen (2016) for details on both vectorisation with NumPy and an example of the bisection method). To illustrate the speed of the algorithms, Figure A.1 shows the time taken for each algorithm to compute APE for a sounding with a varying number of parcels. For each number of parcels n the test sounding is created by taking the ARM Nauru data from 1200 UTC on 1 April 2001 and linearly interpolating it to n pressure levels.

As expected, the exact Munkres procedure is slowest for large numbers of parcels. The bisection method is poorly suited for application to the Lorenz algorithm, since specific volume must be repeatedly calculated for just two parcels at the midpoint between pressure levels. This results in this version of the Lorenz algorithm being slower than previous implementations: it is slower by almost a factor of 10 than the implementation of Stansifer et al. (2017), whereas the other algorithms are similar in speed to their previous implementations. The new Emanuel algorithm is faster than several of the sorting algorithms, showing that its increased physical insight from linking APE with

CAPE does not come at the expense of practicality. The speed of the divide-and-conquer algorithm shown here, combined with the accuracy illustrated in Section 3.4, makes it a good choice amongst sorting algorithms for computing APE.

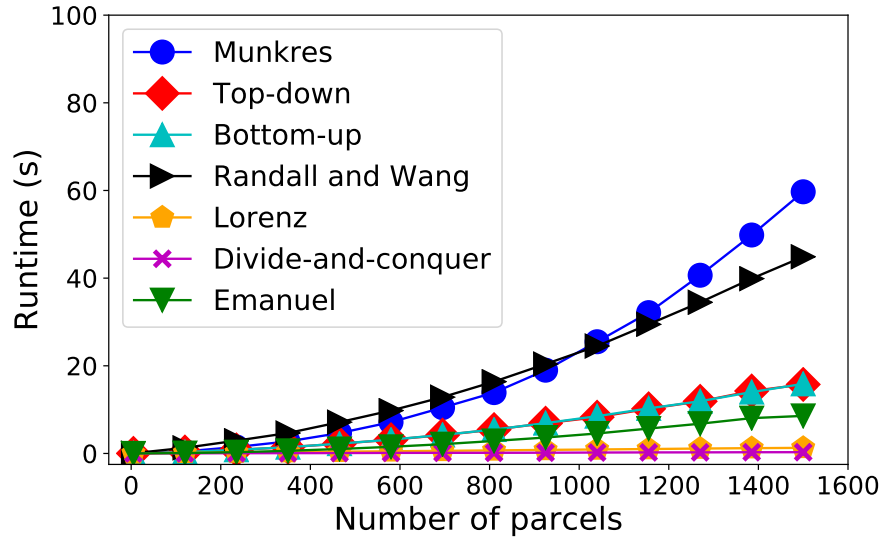


Figure A.1: Time taken for each APE algorithm to compute the APE of an n -parcel sounding linearly interpolated from the data at Nauru on 1 April 2001, 1200 UTC.

Appendix B:

Energy Budget Closures

This appendix provides full details of the finite difference forms used for the energy budgets of the axisymmetric model presented in Chapter 5. It also shows the accuracy of each of the budgets presented in the thesis.

B.1 Finite difference forms of energy budgets

To ensure the closure of the energy budgets, it is necessary to use finite difference forms of the budgets that correspond to the finite difference forms of the model equations. The energy budgets will be obtained using the finite difference identity (4.29), along with the identity

$$\overline{\varphi}^x \delta_x \varphi = \delta_x \left(\frac{\varphi^2}{2} \right) \quad (\text{B.1})$$

and the definition

$$\frac{\widetilde{\psi\psi}^x}{2} = \left(\overline{\psi^x} \right)^2 - \frac{\overline{\psi^2}^x}{2}, \quad (\text{B.2})$$

both given by Lilly (1964). The delta and overbar operators are defined in Equations (4.20) and (4.21) respectively.

B.1.1 Kinetic and elastic energy budgets

The finite difference form of the azimuthal momentum equation (4.3) used in the axisymmetric model is

$$\delta_t (\overline{v^t}) = -\frac{1}{r} \overline{ru\delta_r v^r} - \frac{1}{\overline{\rho}} \overline{\rho w \delta_z v^z} - \left(\frac{v}{r} + f \right) \frac{\overline{ru^r}}{r} + D_v, \quad (\text{B.3})$$

where all symbols are as defined in Chapter 4. Multiplying Equation (B.3) by $\bar{\rho}v$ and using the identities (4.29), (B.1) and (B.2) yields the azimuthal kinetic energy equation

$$\begin{aligned} \delta_t \left(\bar{\rho} \frac{\widetilde{vv^t}}{2} \right) = & -\frac{1}{r} \delta_r \left(\bar{\rho} r u \frac{\widetilde{vv^r}}{2} \right) - \delta_z \left(\bar{\rho} w \frac{\widetilde{vv^z}}{2} \right) + \frac{v^2}{2} \left[\frac{1}{r} \delta_r (\bar{\rho} r u) + \delta_z (\bar{\rho} w) \right] \\ & - \bar{\rho} v \left(\frac{v}{r} + f \right) \frac{\overline{ru^r}}{r} + \bar{\rho} v D_v, \end{aligned} \quad (\text{B.4})$$

which corresponds to the continuous budget equation (5.3).

A similar procedure is followed for the radial and vertical kinetic energy budgets. In these cases, the budgets are re-gridded so that the terms are computed at the v -grid points, to match the azimuthal budget. This is necessary to enable the computation of a total kinetic energy budget. The finite difference form of the radial momentum equation (4.2) is

$$\delta_t (\overline{u^t}) = -\frac{1}{r} \overline{ru^r} \delta_r u^r - \frac{1}{\bar{\rho} r} \overline{\rho r w^r} \delta_z u^z + \left(\frac{v^2}{r} + f v \right) - c_p \bar{\theta}_v \delta_r \pi + D_u, \quad (\text{B.5})$$

leading to a finite difference form of the radial kinetic energy budget (5.4)

$$\begin{aligned} \delta_t \left(\frac{1}{r} \overline{\rho r} \frac{\overline{uu^r}}{2} \right) = & -\frac{1}{r} \delta_r \left(\overline{\rho r u^r} \frac{\overline{uu^r}}{2} \right) - \delta_z \left(\frac{1}{r} \overline{\rho r w^r} \frac{\overline{uu^z}}{2} \right) \\ & + \frac{1}{r} \frac{u^2}{2} \left[\delta_r (\overline{\rho r u^r}) + \delta_z (\overline{\rho r w^r}) \right] - \frac{1}{r} \overline{\rho c_p \theta_v r u} \delta_r \pi \\ & + \frac{1}{r} \overline{\rho r u} \left(\frac{v^2}{r} + f v \right) + \frac{1}{r} \overline{\rho r u} D_u. \end{aligned} \quad (\text{B.6})$$

For the pressure gradient term, the spatial discretisation from the model is used but the effect of the shorter time steps of the semi-implicit scheme is ignored. Instead, u is treated as though it evolves using the leapfrog scheme of the long time steps. This gives a simpler radial kinetic energy budget, but leads to small budget errors, since the budget does not account for the variation of π within the time step. The same approach is applied to terms involving π in the vertical kinetic energy budget and the available elastic energy budget.

When discretising the vertical momentum equation (4.4), the corrected form of the advection operator derived in Equation (4.34) is used:

$$\delta_t (\overline{w^t}) = -\frac{1}{\bar{\rho} r} \overline{\rho r u^z} \delta_r w^r - \frac{1}{\bar{\rho}} \overline{\rho w^z} \delta_z w^z - c_p \bar{\theta}^z (1 + 0.61 \overline{rv^z}) \delta_z \pi + b + D_w, \quad (\text{B.7})$$

where the finite difference form of the buoyancy b is

$$b = g \left[\frac{\overline{\theta}^z}{\overline{\theta}} - 1 + 0.61 (\overline{r_v^z} - \overline{r_v^z}) - \overline{r_l^z} - \overline{r_r^z} - \overline{r_i^z} \right]. \quad (\text{B.8})$$

The vertical kinetic energy budget is then

$$\begin{aligned} \delta_t \left(\frac{\overline{w w^t z}}{\overline{\rho}} \right) &= -\frac{1}{r} \delta_r \left(\frac{\overline{\rho r u^z w w^r z}}{2} \right) - \delta_z \left(\frac{\overline{\rho w^z w w^z z}}{2} \right) \\ &\quad + \frac{w^2}{2} \left[\frac{1}{r} \delta_r (\overline{\rho r u^z}) + \delta_z (\overline{\rho w^z}) \right]^z - \overline{\rho c_p \theta^z} (1 + 0.61 \overline{r_v^z}) w \delta_z \pi \\ &\quad + \overline{\rho b w^z} + \overline{\rho w D_w^z}, \end{aligned} \quad (\text{B.9})$$

which corresponds to the continuous equation (5.6).

The elastic energy budget is obtained from the conservation of mass equation (4.14), which in terms of finite differences is

$$\delta_t (\overline{\pi^t}) = -\frac{\overline{c^2}}{\overline{\rho c_p \theta_v^2}} \left\{ \frac{1}{r} \delta_r (\overline{\rho \theta_v r u}) + \delta_z \left[\overline{\rho \theta^z} (1 + 0.61 \overline{r_v^z}) w \right] \right\} + \frac{\overline{c^2}}{c_p \theta_v^2} \frac{D\theta_v}{Dt}. \quad (\text{B.10})$$

The material derivative $\frac{D\theta_v}{Dt}$ can be easily diagnosed by using Equations (4.7) and (4.8) to write $\frac{D\theta_v}{Dt} = (1 + 0.61 r_v) (M_\theta + D_\theta + R) + 0.61 \theta (M_{r_v} + D_{r_v})$. Multiplying Equation (B.10) by $\frac{\overline{\rho c_p \theta_v^2}}{\overline{c^2}} \pi$ and rearranging using the identity (4.29) yields the finite difference elastic energy budget

$$\begin{aligned} \delta_t \left(\frac{\overline{\rho c_p^2 \theta_v^2} \overline{\pi \pi^t}}{2} \right) &= -\frac{1}{r} \delta_r (\overline{\rho c_p \theta_v r u \overline{\pi^r}}) - \delta_z \left[\overline{\rho c_p \theta^z} (1 + 0.61 \overline{r_v^z}) w \overline{\pi^z} \right] \\ &\quad + \frac{1}{r} \overline{\rho c_p \theta_v r u \delta_r \pi} + \overline{\rho c_p \theta^z} (1 + 0.61 \overline{r_v^z}) w \delta_z \pi + \overline{\rho c_p \pi} \frac{D\theta_v}{Dt}, \end{aligned} \quad (\text{B.11})$$

which is the discretised equivalent of the budget (5.9).

All further budgets involving the kinetic and elastic energies (such as the total kinetic energy budget) are obtained by taking the sums of the budgets from Equations (B.4), (B.6), (B.9) and (B.11) as appropriate.

B.1.2 Available Potential Energy budget

The APE density e_a is computed at v -grid points, and therefore the finite difference forms of the first two terms on the RHS of Equation (5.60) are found by applying the v -grid advection operator of Equation (4.34), multiplying by $\overline{\rho}$ and rearranging using

Equation (4.29), to obtain

$$\begin{aligned} \delta_t (\overline{e_a^t}) = & -\frac{1}{r} \delta_r (\overline{\rho r u \overline{e_a^r}}) - \delta_z (\overline{\rho w \overline{e_a^z}}) + e_a \left[\frac{1}{r} \delta_r (\overline{\rho r u}) + \delta_z (\overline{\rho w}) \right] \\ & + G_{\theta_{ei}} \overline{\rho} \frac{D\theta_{ei}}{Dt} + G_{r_t} \overline{\rho} \frac{Dr_t}{Dt} - \overline{\rho b w^z} + \text{discontinuities.} \end{aligned} \quad (\text{B.12})$$

The term for the conversion between APE and vertical kinetic energy is taken to match the term used in the vertical kinetic energy budget, and the discontinuities are computed using a conditional residual as described in Section 5.2.5.

The diabatic production terms are computed using

$$\overline{\rho} \frac{D\theta_{ei}}{Dt} = \overline{\rho} \frac{D\theta}{Dt} + \frac{L_s}{c_p \overline{\Pi}} \overline{\rho} \frac{Dr_v}{Dt} + \frac{L_f}{c_p \overline{\Pi}} \left(\overline{\rho} \frac{Dr_l}{Dt} + \overline{\rho} \frac{Dr_r}{Dt} \right), \quad (\text{B.13})$$

$$\overline{\rho} \frac{Dr_t}{Dt} = \overline{\rho} \frac{Dr_v}{Dt} + \overline{\rho} \frac{Dr_l}{Dt} + \frac{Dr_r}{Dt} + \overline{\rho} \frac{Dr_i}{Dt}, \quad (\text{B.14})$$

with the material derivatives of each of the thermodynamic variables written in finite difference form as

$$\overline{\rho} \frac{D\theta}{Dt} \rightarrow \delta_t (\overline{\rho \theta^t}) + \frac{1}{r} \overline{\rho r u \delta_r \theta^r} + \overline{\rho w \delta_z \theta^z}, \quad (\text{B.15})$$

$$\overline{\rho} \frac{Dr_j}{Dt} \rightarrow \delta_t (\overline{\rho r_j^t}) + \min \left\{ \frac{1}{r} \overline{\rho r u \delta_r r_j^r} + \overline{\rho w \delta_z r_j^z}, \frac{r_j + Dr_j}{2\Delta t} \right\}, \quad (\text{B.16})$$

for $j = v, l, r, i$. The minimum in the advection term for the water mixing ratios prevents more water content being advected away than is present in the parcel, to prevent negative mixing ratios occurring (this is enforced in the model).

B.2 Budget closures

This section illustrates the accuracy of the budgets used in Chapter 5 of the thesis. All closure plots are of the same format: the solid black line shows the partial time derivative of the appropriate quantity as diagnosed from the model, and the orange dashed line shows the time tendency predicted by the sum of all budget components.

B.2.1 Kinetic and elastic energy budgets

Figure B.1 shows the accuracy of each energy budget from Section 5.1 when integrated over the model domain. In each case, the solid black line is the time tendency $\frac{\partial(\overline{\rho e})}{\partial t}$ of the appropriate energy e , diagnosed from the model, and the orange dashed line shows

the time tendency predicted by the sum of all budget components.

The budgets are well-closed in general; discrepancies arise in the radial and vertical kinetic energy budgets because the effects of the short time step, used by the model to compute the pressure gradient terms and advance u and w , have been neglected. However, when the budgets of e_k^u and e_k^w are considered together, as part of the total kinetic energy budget, these errors cancel out. The budgets are not precisely numerically closed because the small contributions from the Robert time filter have not been included.

B.2.2 Available Potential Energy budget

This section presents results for the accuracy of the APE budget and diabatic APE production budgets used in Section 5.2.

Figure B.2 shows the accuracy of the APE budget integrated over the inner region ($r < 300$ km), which was used to generate Figure 5.19.

The closure of the budget after 150 h, when there are no discontinuities in e_a , is of particular interest. The budget uses a conditional residual to diagnose the contribution by discontinuities, which could lead to an artificially good closure. However, the budget captures the variation in $\frac{\partial(\bar{\rho}e_a)}{\partial t}$ well after 150 h, so we can conclude that the budget is accurate even in the absence of discontinuities and the associated residual calculation.

Before verifying the accuracy of the budget of diabatic APE production, the budgets (5.14) and (5.18) for $\frac{D\theta_{ei}}{Dt}$ and $\frac{Dr_t}{Dt}$ should be inspected, to check that the modified microphysics scheme is behaving as expected. Figure B.3 compares the integral of $\bar{\rho}\frac{D\theta_{ei}}{Dt}$ over the inflow region, diagnosed directly from the model output, with the integral of the sum of the budget terms in (5.14) (multiplied by $\bar{\rho}$). This makes it clear that the budget of the diabatic processes contributing to changes in θ_{ei} is correct and capturing all relevant processes.

Figure B.4 shows the equivalent result for the model-diagnosed $\bar{\rho}\frac{Dr_t}{Dt}$ and the sum of the budget terms in Equation (5.18) integrated over the inflow region. Again we see that the budget of r_t is valid for the modified microphysics scheme. The verification presented here integrates the terms over the inflow region, which does not contain any ice, but has also been tested for the whole domain to ensure the budgets remain valid in the presence of ice.

Now it has been established that the budgets of diabatic processes are closed, the budget of diabatic APE production in the inflow region can be verified; this was presented

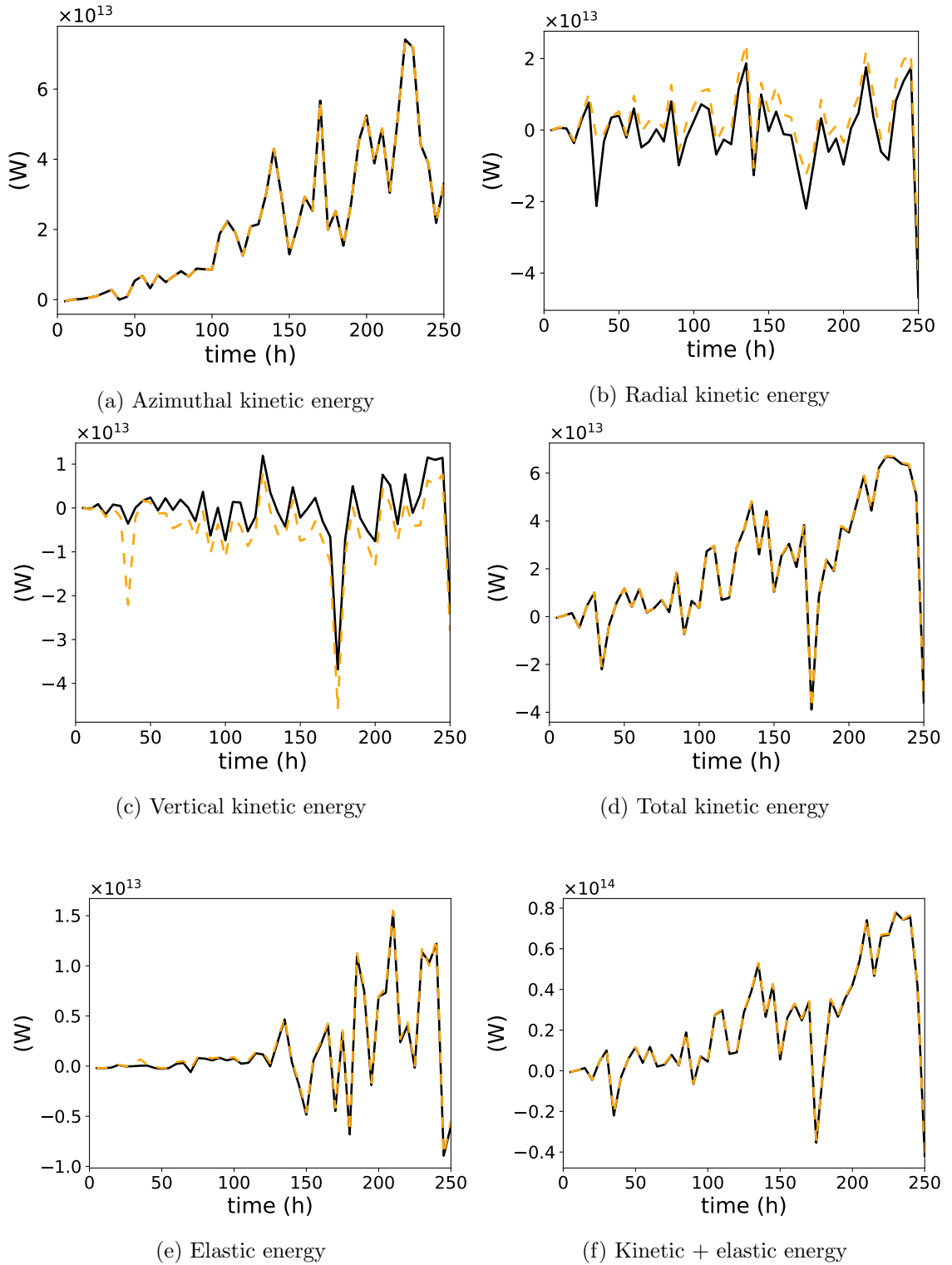


Figure B.1: Accuracy of kinetic and elastic energy budgets analysed in Section 5.1. For each subfigure, the solid black line shows the value of $\frac{\partial(\rho e)}{\partial t}$ diagnosed from the axisymmetric model at 5 h intervals, where e is the appropriate energy density. The dashed orange line shows the tendency predicted by taking the sum of all budget components at that time step.

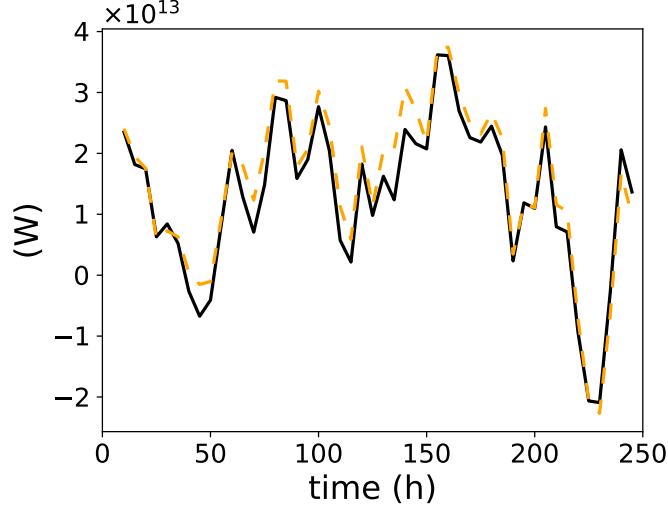


Figure B.2: Accuracy of the APE budget integrated over the inner 300 km of the domain. The solid black line shows the diagnosed $\frac{\partial(\bar{p}e_a)}{\partial t}$ from the model, and the dashed orange line shows the sum of the APE budget components.

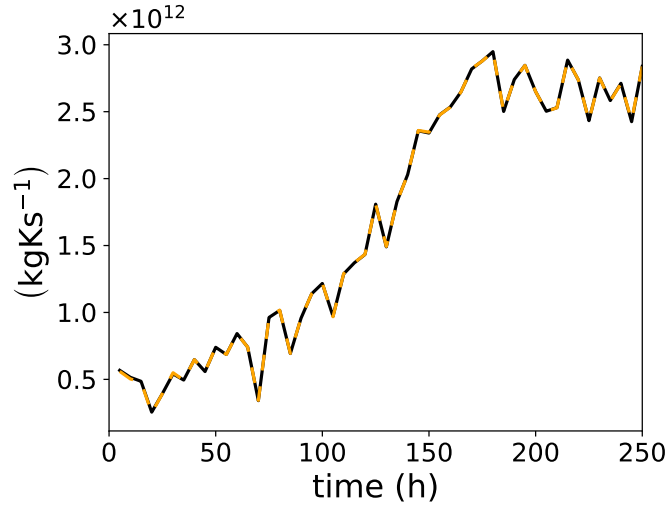


Figure B.3: Accuracy of θ_{ei} budget integrated over inflow region. The solid black line is the model-diagnosed value of $\bar{\rho}\frac{D\theta_{ei}}{Dt}$. The orange dashed line is the sum of the budget components on the RHS of Equation (5.14) (multiplied by $\bar{\rho}$).

in Figure 5.22. The black solid line in Figure B.5 is the value of $\bar{\rho}G_{\theta_{ei}}\frac{D\theta_{ei}}{Dt} + \bar{\rho}G_{r_t}\frac{Dr_t}{Dt}$ found using material derivatives diagnosed from the model. The orange dashed line is the diabatic APE production computed by the APE budget, which employs the domain-averaged $\tilde{\Pi}$ to compute θ_{ei} and hence $\frac{D\theta_{ei}}{Dt}$, in order to account for the neglect of variations in Π in the model's Lagrangian derivative of θ_{ei} . Figure B.5 demonstrates that the production calculated by the two methods is similar; the APE budget provides an overestimate of production towards the end of the model run, but the overall trend is consistent with the APE production by surface fluxes increasing until it dominates over the loss due to mixing.

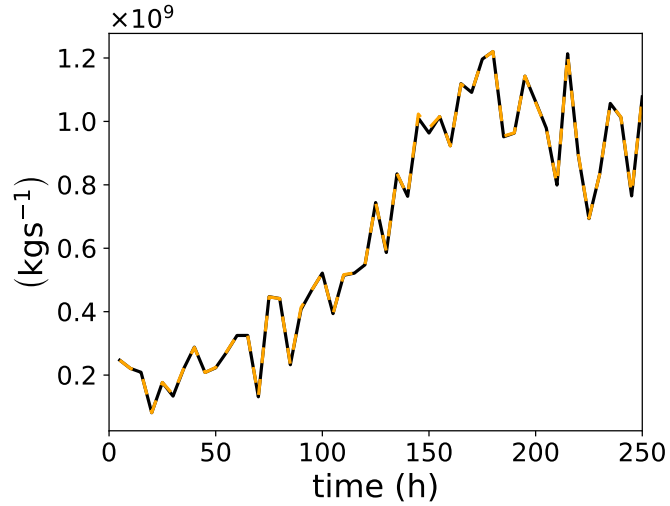


Figure B.4: Accuracy of r_t budget integrated over inflow region. The solid black line is the model-diagnosed value of $\bar{\rho} \frac{Dr_t}{Dt}$. The orange dashed line is the sum of the budget components on the RHS of Equation (5.18) (multiplied by $\bar{\rho}$).

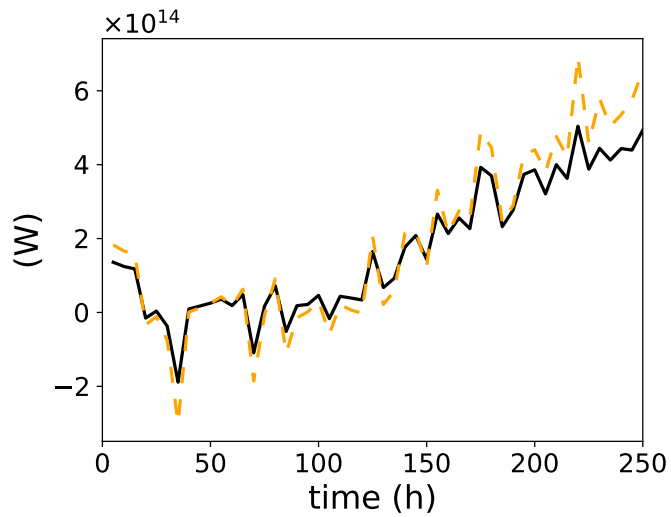


Figure B.5: Accuracy of diabatic APE production budget integrated over inflow region. The solid black line is the production computed using the model-diagnosed Lagrangian derivatives of θ_{ei} and r_t . The orange dashed line is the diabatic production computed as part of the APE budget.

Appendix C:

The generalised buoyancy/inertial forces and available energy of axisymmetric compressible stratified vortex motions

This appendix presents a paper submitted to the *Journal of Fluid Mechanics* (currently in review), which develops a generalised theory of available energetics in axisymmetric vortices in single-component compressible stratified fluids. This work is not included in the main thesis since it was not led by BLH and it focuses on energetics in the dry atmosphere rather than the full moist TC model studied in the main thesis. The work was motivated by the results of Chapter 6, which demonstrated the ability of a balanced vortex reference state to predict the kinetic energy generation in a numerically modelled TC.

RT led the development of the theory and writing of the manuscript. The main contributions of BLH to the work are: recognising that available energetics relative to an axisymmetric vortex can be described in terms of the local buoyancy defined by Smith et al. (2005), as seen in Chapter 6; writing the code for the idealised dry vortex used as an illustration of the theory, and providing all figures; deriving the budget of available energy in the presence of diabatic and frictional effects; and commenting on drafts of the manuscript. The estimated contribution of BLH to the paper is 30%.

The generalised buoyancy/inertial forces and available energy of axisymmetric compressible stratified vortex motions

Rémi Tailleux¹†, and Bethan L. Harris¹

¹Department of Meteorology, University of Reading, Reading, RG6 6BB, United Kingdom

(Received xx; revised xx; accepted xx)

Adiabatic and inviscid axisymmetric perturbations to a stable reference vortex in gradient wind balance gives rise to two kinds of restoring forces: a generalised buoyancy force aligned with the reference pressure gradient, proportional to the perturbation density, and a radial inertial/centrifugal force proportional to the squared angular momentum perturbation. In this paper, it is shown that the concept of available energy for finite amplitude axisymmetric vortex motions, previously constructed by Andrews (2006) and Codoban & Shepherd (2006), is best interpreted as a form of eddy energy that measures the work against such restoring forces required for moving a fluid parcel from its reference balanced vortex equilibrium position to its actual position; it is the sum of available acoustic energy, slantwise available potential energy, and available radial energy. If the reference entropy profile increases with height along surfaces of constant angular momentum and if the squared reference angular momentum increases with radius along isobaric surfaces, then the available energy is positive definite and the reference vortex is stable to all finite amplitude inviscid and adiabatic perturbations. In that case, either non-axisymmetric and/or diabatic/viscous effects are required to cause the available energy to grow with time. Thermodynamic and mechanical efficiencies can be constructed that determine the fraction of the sinks/sources of entropy and angular momentum that respectively modify the eddy available, mean available and background potential energies. When applied to the intensification of a cyclonic vortex by diabatic heating, the new framework vindicates the idea that the sustained creation of positive buoyancy anomalies (defined relative to the reference vortex state) near the eyewall is key for tropical cyclone intensification.

1. Introduction

The concepts of buoyancy and buoyancy forces are central to the theoretical description of most observed phenomena in stratified fluids (Turner 1973). The conventional buoyancy force is generally understood as a purely vertical force due to the restoring effect of gravity that a fluid parcel experiences when it works against the environment. Its magnitude is determined in large part by the background vertical gradient and near material invariance of specific entropy, of which the main relevant measure is the squared buoyancy frequency profile $N_r^2(z)$. The conventional buoyancy force is typically introduced by splitting the total pressure and density fields as perturbations to background reference hydrostatic pressure and density fields $p_r(z)$ and $\rho_r(z)$ that are functions of height z alone. Unless the fluid is close to a state of rest, there is currently no agreement on how these should be defined; as a result, it is generally agreed that

† Email address for correspondence: R.G.J.Tailleux@reading.ac.uk

the conventional buoyancy is non-uniquely defined, as it is dependent on the particular choice of reference state. The energetics counterpart of the conventional buoyancy force is the so-called available potential energy (APE) density, which is a positive definite energy quantity (provided that $N_r^2 > 0$) that measures the work against the buoyancy force needed to move a fluid parcel adiabatically from its equilibrium position in the notional reference state to its actual position (Andrews 1981; Holliday & McIntyre 1981; Tailleux 2013, 2018). The APE density, like the conventional buoyancy, can be defined for arbitrarily specified hydrostatic reference pressure and density fields $p_r(z)$ and $\rho_r(z)$ (which can also be assumed to be time dependent if needed). For a simple fluid whose equation of state depends only on temperature and pressure, the volume integral of APE density is equal to the globally defined APE of Lorenz (1955), provided that the reference state is chosen to coincide with the state of minimum potential energy that can be obtained from the actual state by means of an adiabatic re-arrangement of mass (Andrews 1981; Tailleux 2013). For a general reference state, the integral of APE density usually exceeds the Lorenz APE. In the case of a more complex fluid, such as a moist atmosphere or salty ocean, the issue is considerably more complicated, see Saenz *et al.* (2015); Hieronymus & Nycander (2015); Wong *et al.* (2016); Stansifer *et al.* (2017); Harris & Tailleux (2018) for discussions of some of the issues involved.

In many circumstances of practical importance, however, fluid parcels are so far away from their resting equilibrium position that their conventional buoyancy may differ considerably from their actual acceleration, thus losing all predictive value (Thorpe *et al.* 1989). For this reason, it has been found useful in many applications to define buoyancy relative to more locally defined reference pressure and density fields. This is the case, for example, for the concept of Convective Available Potential Energy (CAPE) (Moncrieff & Miller 1976), which refers to the total work done by the fluid parcel buoyancy — defined relative to a local atmospheric sounding — from its level of free convection (LFC) to an upper level of neutral buoyancy (LNB); in that case, the fluid parcel buoyancy also depends on another material invariant, namely total water content. In an oceanic context, McDougall (1987) proposed a generalisation of the concept of buoyancy valid for lateral displacements $\delta\mathbf{x}$, for which he derived the expression $b = -\mathbf{N} \cdot \delta\mathbf{x}$, where $\mathbf{N} = g(\alpha\nabla\theta - \beta\nabla S)$ is the so-called neutral vector, whose vertical component is equal to the locally defined squared buoyancy frequency. In the context of stratified turbulent mixing, Arthur *et al.* (2017) recently discussed some of the consequences for the estimation of turbulent mixing of using a globally- versus locally-defined reference state. In that case, the issue arises from the difficulty of connecting the study of turbulent mixing in small domains — for which the reference state is naturally defined in terms of a global horizontal average or adiabatically sorted state — with that in the field, which is usually based on the use of a locally-defined reference state, e.g. Thorpe (1977).

Motivated by confusion in the tropical cyclone literature about the role of buoyancy in tropical cyclones — due to the use of different definitions for the term — Smith *et al.* (2005) emphasised the importance of distinguishing between the local buoyancy, defined relative to a reference axisymmetric vortex in gradient wind balance, and the “system” buoyancy of the reference vortex defined relative to a notional state of rest. In terms of energetics, Smith *et al.* (2005)’s approach appears to be closely connected to that underlying the exact partitioning of the local APE density into mean and eddy components by Scotti & White (2014); Novak & Tailleux (2018); Tailleux (2018), in which the eddy and mean APE can be interpreted as related to the work done by the local and system buoyancies respectively, the system then being the mean flow. As shown by Smith *et al.* (2005), the generalised buoyancy force defined relative to a non-resting state is proportional to the local density anomaly times the pressure gradient of the reference

state, so that in addition to the unavoidable vertical component, it also possesses a horizontal component that is lacking in the conventional buoyancy force. In addition to the generalised buoyancy force, fluid parcels displaced adiabatically and inviscidly from a non-resting reference state will in general also experience inertial/centrifugal forces, thus complicating further the understanding of the energetics of displacements with both lateral and vertical components. These additional difficulties are not always recognised, however. For instance, they are neglected in the discussion of the work experienced by lateral displacements in McDougall (1987)’s theory of neutral surfaces. As a result, it is increasingly recognised that adiabatic and isohaline parcel exchanges taking place on neutral surfaces must experience the action of forces (Nycander 2011), and hence that neutral surfaces are in general not energetically optimal for lateral displacements (Tailleux 2016). To what extent such issues matter for our understanding of lateral stirring and mixing in the ocean is currently under active investigation.

As shown by Tailleux (2018), the general expression for the conventional (i.e. defined relative to a state of rest) local APE density for a compressible stratified binary fluid is $\Pi = h(\eta, S, p) - h(\eta, S, p_r(z_r)) + g(z - z_r) + (p_r(z) - p)/\rho$, where h is the specific enthalpy, η the specific entropy, S chemical composition, p pressure, ρ density, and z_r the reference position of the fluid parcel in the reference state. It is easy to see that none of the key features of Π — its positive definite character and the possibility to further partition it as the sum of available acoustic energy (AAE) and the work of the conventional buoyancy force — require that $p_r(z)$ and $\rho_r(z)$ be functions of the vertical coordinate only; they could equally be functions of horizontal coordinates without altering its properties. As a result, it is possible to define an “eddy” form of APE density simply by using a more general reference pressure field $p_m(x, y, z, t)$ in the definition of Π that also depends on horizontal position (and time if needed). In that case, however, the budget for the sum of the kinetic energy and of the eddy APE density thus defined is no longer closed, as a new term in its evolution equation appears that unsurprisingly involves the work against the horizontal pressure gradient $\nabla_h p_m$. The main question addressed in this paper is whether it is possible to achieve a closed budget by incorporating a new form of available energy linked to the work done by the inertial/centrifugal forces. In this paper, we show that this is indeed possible for the particular case of axisymmetric compressible stratified vortex motions around a reference vortex in gradient wind balance. In that case, the construction of a closed energy budget is made possible by the fact that the inertial/centrifugal forces experienced by displaced fluid parcels have the nice property of being purely radial and proportional to the squared angular momentum anomaly, as previously shown and discussed by Rayleigh (1916) and Emanuel (1994). As a result, their energetics is very similar to that of the conventional buoyancy force, which makes it possible to introduce a new form of available radial energy (ARE) as the inertial/centrifugal counterpart of the APE density. The sum of the ARE and APE defines an eddy form of available energy that is formally similar to that previously constructed for a zonal flow by Codoban & Shepherd (2003) and for axisymmetric vortex motions by Codoban & Shepherd (2006) and Andrews (2006) (CSA06 thereafter). Whereas CSA06’s approach emphasises the Energy-Casimir method (Haynes 1988; Shepherd 1993), our approach emphasises a force-based viewpoint of available energetics, which we think is much simpler and more intuitive, as well as much less abstract. This paper is organised as follows. Section 2 describes the model formulation. Section 3 details the construction of the available energy, and provides illustrations of the new energetic concepts for an analytical axisymmetric vortex in a dry atmosphere. Section 4 demonstrates the potential usefulness of the framework by discussing the energetics of the growth and decay of an

axisymmetric vortex due to diabatic heating, in the presence of viscous effects. Section 5 discusses the results.

2. Model formulation

The evolution of compressible vortex motions is most usefully described by writing the Navier-Stokes equations in cylindrical coordinates (r, ϕ, z) :

$$\frac{Du}{Dt} - \left(f + \frac{v}{r}\right)v + \nu \frac{\partial p}{\partial r} = D_u, \quad (2.1)$$

$$\frac{Dv}{Dt} + \left(f + \frac{v}{r}\right)u + \frac{\nu}{r} \frac{\partial p}{\partial \phi} = D_v, \quad (2.2)$$

$$\frac{Dw}{Dt} + \nu \frac{\partial p}{\partial z} = -g + D_w, \quad (2.3)$$

$$\frac{D\eta}{Dt} = \frac{\dot{q}}{T}, \quad (2.4)$$

$$\frac{\partial \rho}{\partial t} + \frac{1}{r} \frac{\partial(\rho r u)}{\partial r} + \frac{1}{r} \frac{\partial(\rho v)}{\partial \phi} + \frac{\partial(\rho w)}{\partial z} = 0, \quad (2.5)$$

$$\frac{D}{Dt} = \frac{\partial}{\partial t} + u \frac{\partial}{\partial r} + \frac{v}{r} \frac{\partial}{\partial \phi} + w \frac{\partial}{\partial z}, \quad (2.6)$$

where (u, v, w) is the velocity field, p is pressure, ρ is the density, $\nu = 1/\rho$ is the specific volume, η is the specific entropy, g is the acceleration of gravity, r is the radial coordinate increasing outward, z is height increasing upward. The terms D_i , $i = u, v, w$ denote dissipative terms for momentum, while \dot{q} denotes diabatic heating. The thermodynamic equation of state is assumed in the form $\rho = \rho(\eta, p)$ or $\nu = \nu(\eta, p)$. For the developments that follow, it is useful to rewrite Eq. (2.2) for the azimuthal motion in terms of the specific angular momentum $M = rv + fr^2/2$ as

$$\frac{DM}{Dt} = rD_v - \frac{1}{\rho} \frac{\partial p}{\partial \phi}. \quad (2.7)$$

As expected, M is materially conserved for purely axisymmetric motions ($\partial p/\partial \phi = 0$) in the absence of the dissipative term D_v . The following relations expressing various quantities in terms of M will prove useful:

$$v = \frac{M}{r} - \frac{fr}{2}, \quad (2.8)$$

$$\frac{v^2}{2} = \frac{M^2}{2r^2} + \frac{f^2 r^2}{8} - \frac{fM}{2} = \mu\chi + \frac{f^2}{16\chi} - \frac{f\sqrt{\mu}}{2}, \quad (2.9)$$

$$\left(f + \frac{v}{r}\right)v = \frac{M^2}{r^3} - \frac{f^2 r}{4} = -\left(\mu - \frac{f^2}{16\chi^2}\right) \frac{\partial \chi}{\partial r}, \quad (2.10)$$

where we have defined $\chi = 1/(2r^2)$ and $\mu = M^2$, similarly to Andrews (2006). Note that (2.9) assumes $M > 0$ in order to write $M = \sqrt{\mu}$. Other quantities of importance in the following discussions are the vorticity

$$\xi = -\frac{\partial v}{\partial z} \hat{\mathbf{r}} + \left(\frac{\partial u}{\partial z} - \frac{\partial w}{\partial r}\right) \hat{\phi} + \frac{1}{r} \frac{\partial(rv)}{\partial r} \hat{\mathbf{z}} \quad (2.11)$$

Available energy including momentum constraints and eddy energy 5

and potential vorticity $Q = (\xi + f\hat{\mathbf{z}}) \cdot \nabla\eta/\rho$. It is useful to remark that M and Q are linked through the relation:

$$Q = \frac{1}{\rho r} \frac{\partial(M, \eta)}{\partial(r, z)}. \quad (2.12)$$

Potential vorticity is thus proportional to the Jacobian of the coordinate transformation allowing one to map the physical space (r, z) to the space (M, η) of the materially conserved quantities for axisymmetric motions. As discussed later on, the stability of axisymmetric compressible vortex motions depends crucially on Q being single-signed over the domain considered.

3. Available energetics

3.1. Reference states

Following Andrews (2006), we define the reference state pertaining to the construction of momentum-constrained available energy as an axisymmetric solution of the inviscid form of Eqs. (2.1-2.5). For such a reference state, the azimuthal velocity $v_m(r, z)$, pressure $p_m(r, z)$ and density $\rho_m(r, z)$ are in gradient wind and hydrostatic balances:

$$\frac{1}{\rho_m} \frac{\partial p_m}{\partial r} = \left(f + \frac{v_m}{r}\right) v_m, \quad \frac{1}{\rho_m} \frac{\partial p_m}{\partial z} = -g. \quad (3.1)$$

The corresponding reference profiles $\eta_m(r, z)$ and $M_m(r, z)$ for the specific entropy and angular momentum may then be inferred from the equation of state for density $\rho_m(r, z) = \rho(\eta_m(r, z), p_m(r, z))$, and via the definition of angular momentum $M_m(r, z) = rv_m(r, z) + fr^2/2$. For illustrative purposes, Fig. 1 shows a particular example of azimuthal wind speed associated with the analytic dry atmospheric vortex solution used by Smith *et al.* (2005), whose details can be found in Appendix A. This analytic solution serves as the basis for all subsequent illustrations.

The construction of a reference vortex solution in gradient wind balance from an actual unbalanced vortex is of interest in TC studies. From the viewpoint of available energy theory, the most logical approach is to regard the reference state as the state of minimum potential energy that can be obtained from the actual state by means of a re-arrangement of mass conserving both entropy and angular momentum, as argued by Cullen *et al.* (2015) (Scotti & Passagia (2019) argue for a similar construction but emphasising conservation of potential vorticity instead). In the TC literature, however, existing constructions such as that proposed by Nolan & Montgomery (2002) or Smith (2006) appear to conserve only angular momentum but not entropy. The precise details of how the reference state is constructed are important, because they ultimately determine the sign of the thermodynamic and mechanical efficiencies defined later on that control the fraction of the diabatic and viscous sources of entropy and angular momentum going into the production of mechanical energy. Any construction of reference state should aim to respect the sign of these efficiencies for fear of violating causality, as emphasised by Codoban & Shepherd (2003).

Regardless of how the reference state is constructed, we define the reference position (r_*, z_*) of a fluid parcel as if the reference state were the state of minimum potential energy obtained by means of an adiabatic re-arrangement of mass conserving entropy and angular momentum, which imposes that it be a solution of:

$$M_m(r_*, z_*) = M, \quad \eta_m(r_*, z_*) = \eta. \quad (3.2)$$

Eq. (3.2) generalises the level of neutral buoyancy (LNB) equation introduced in Tailleux

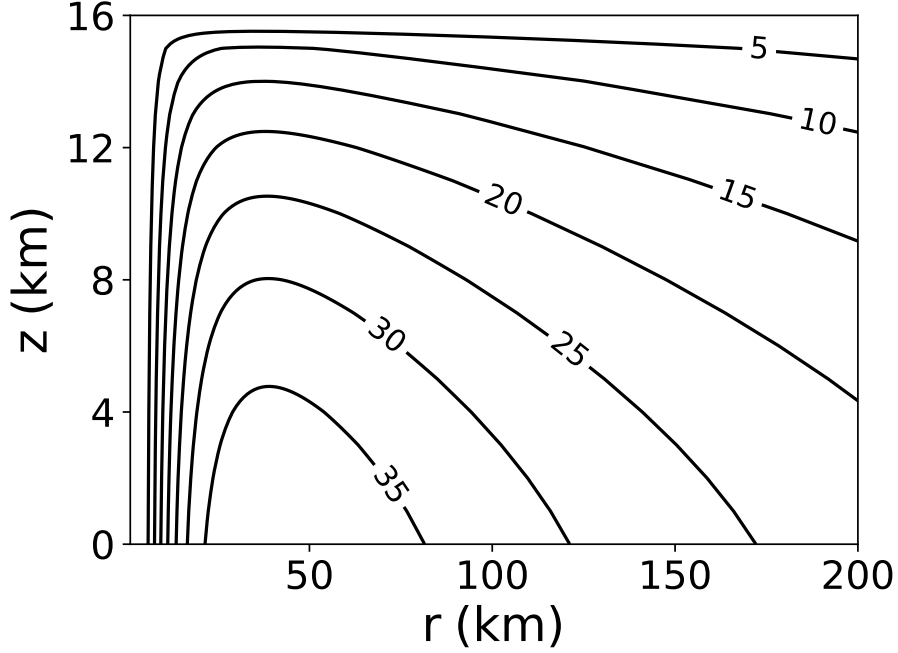


Figure 1: Azimuthal wind speed v_m of the analytic dry vortex from Smith *et al.* (2005) used as a reference state to illustrate the momentum-constrained available energy. Contour labels indicate speed in $\text{m} \cdot \text{s}^{-1}$.

(2013). In the case that the reference state is constructed such that Eq. (3.2) has no solution for some fluid parcels, the reference positions can be arbitrarily imposed to lie at the boundaries of the domain, as discussed by Tailleux (2013). To simplify subsequent derivations, one can rewrite (3.1) as

$$\frac{1}{\rho_m} \nabla p_m = \left(\frac{M_m^2}{r^3} - \frac{f^2 r}{4} \right) \nabla r - \nabla \Phi = - \left(\mu_m - \frac{f^2}{16\chi^2} \right) \nabla \chi - \nabla \Phi, \quad (3.3)$$

where $\Phi = g_0 z$ is the geopotential (g_0 is gravitational acceleration).

To clarify the nature of the links with standard APE theory, we also consider a notional state of rest defined to be a function of height only and in hydrostatic balance only, viz.,

$$\frac{1}{\rho_0} \nabla p_0 = -\nabla \Phi \quad (3.4)$$

where $\rho_0(z) = \rho(\eta_0(z), p_0(z))$. In that case, the reference entropy profile is defined through $\rho_0(z) = \rho(\eta_0(z), p_0(z))$ and the reference angular momentum is a function of radius only: $M_0(r) = fr^2/2$. One may similarly define a reference position (r_R, z_R) in such a reference state via the equations:

$$\eta_0(z_R) = \eta, \quad \frac{fr_R^2}{2} = M. \quad (3.5)$$

Eqs. (3.2) represent constraints similar to those underlying the Generalised Lagrangian Mean (GLM) theory of Andrews & McIntyre (1978) in which the zero mean assumption for the displacements is relaxed (see the recent paper by Gilbert & Vanneste (2018) for a recent revisiting of GLM theory).

3.2. Available energetics

Prior to discussing available energetics, one must start by identifying the appropriate form of total energy conservation pertaining to the system of equations considered. In the present case, the standard form of total energy is $\mathbf{v}^2/2 + e + \Phi = \mathbf{v}^2/2 + h + \Phi - p/\rho$, where e is internal energy. Following the usual procedure, the latter can be shown to satisfy the following evolution equation:

$$\rho \frac{D}{Dt} \left(\frac{\mathbf{v}^2}{2} + h + \Phi - \frac{p}{\rho} \right) + \nabla \cdot (p\mathbf{v}) = \rho\mathbf{v} \cdot \mathbf{D} + \rho\dot{q}. \quad (3.6)$$

For the system of equations considered to be energetically consistent, the viscous and diabatic terms \mathbf{D} and \dot{q} must be such that the right-hand side of Eq. (3.6) is expressible as the divergence of some flux. Following Andrews (1981, 2006), we introduce the following identity:

$$\rho \frac{D}{Dt} \left(\frac{p_m}{\rho} \right) = \frac{\partial p_m}{\partial t} + \nabla \cdot (p_m\mathbf{v}), \quad (3.7)$$

which is valid for any arbitrary pressure field $p_m = p_m(\mathbf{x}, t)$, and add it to (3.6) to obtain the following alternative energy conservation equation:

$$\rho \frac{D}{Dt} \left(\frac{\mathbf{v}^2}{2} + \Pi_1 + h(\eta, p_m) + \Phi(z) \right) + \nabla \cdot [(p - p_m)\mathbf{v}] = \rho\mathbf{v} \cdot \mathbf{D} + \rho\dot{q} + \frac{\partial p_m}{\partial t}, \quad (3.8)$$

where $\Pi_1 = h(\eta, p) - h(\eta, p_m) + (p_m - p)/\rho$ is a positive definite energy quantity usually referred to as Available Acoustic Energy (AAE), e.g. Andrews (1981, 2006), Tailleux (2018). The positive definite character of Π_1 follows from the possibility to write it in the form

$$\Pi_1 = \int_{p_m}^p \int_p^{p'} \nu_p(\eta, p'') dp'' dp' = \int_{p_m}^p \int_{p'}^p \frac{dp'' dp'}{\rho^2 c_s^2} \approx \frac{(p - p_m)^2}{2\rho_m^2 c_{s0}^2}, \quad (3.9)$$

where $c_s^2 = (\partial\rho/\partial p)^{-1}$ is the squared speed of sound (Tailleux 2018). The advantage of using a reference pressure field that also depends on the horizontal coordinates is that it reduces the magnitude of the pressure perturbation p' as compared to standard APE theory, and hence reduces the contribution of AAE to the overall energy budget. Following Andrews (2006) and Codoban & Shepherd (2006), we decompose the total kinetic energy as the sum of the kinetic energies of the secondary (toroidal) and primary (azimuthal) circulations:

$$\frac{\mathbf{v}^2}{2} = \frac{\mathbf{u}_s^2}{2} + \frac{v^2}{2}, \quad (3.10)$$

where $\mathbf{u}_s = (u, 0, w)$ is the velocity of the secondary circulation. Next, we define the vortex dynamic potential energy \mathcal{V} as

$$\mathcal{V} = \frac{v^2}{2} + h(\eta, p_m) + \Phi(z), \quad (3.11)$$

and define the vortex available energy A_e as the difference between the values of \mathcal{V} in the actual and reference states:

$$A_e = \mathcal{V} - \mathcal{V}_\star = \frac{v^2}{2} - \frac{v_\star^2}{2} + h(\eta, p_m) - h(\eta, p_\star) + \Phi(z) - \Phi(z_\star), \quad (3.12)$$

where $p_\star = p_m(r_\star, z_\star, t)$ and $\chi_\star = \chi(r_\star)$. Note that if it were not for the presence of the kinetic energy term $v^2/2 - v_\star^2/2$, A_e would be nearly identical to the eddy APE term introduced by Tailleux (2018), which motivates us to regard A_e as a particular form of

eddy energy. To discuss the properties of A_e , it is more advantageous to express $v^2/2$ and $v_\star^2/2$ in terms of μ by using (2.9) as follows:

$$A_e = \mu(\chi - \chi_\star) + \frac{f^2}{16} \left(\frac{1}{\chi} - \frac{1}{\chi_\star} \right) + h(\eta, p_m) - h(\eta, p_\star) + \Phi(z) - \Phi(z_\star). \quad (3.13)$$

Eq. (3.13) is the starting point for the subsequent derivations.

3.3. Interpretation of A_e in terms of the work of a generalised buoyancy force

As can be seen from (3.13), a key property of A_e is that it is a function of the actual and reference positions only at fixed η and μ (or M). As a result, it is possible to write A_e as the path integral

$$A_e = - \int_{\mathbf{x}_\star}^{\mathbf{x}} \mathbf{b}_e(\mu, \eta, \mathbf{x}', t) \cdot d\mathbf{x}', \quad (3.14)$$

thus allowing A_e to be interpreted as the work against the generalised buoyancy force \mathbf{b}_e defined by

$$\mathbf{b}_e = -\nabla A_e = \underbrace{(\nu_m - \nu_h) \nabla p_m}_{\mathbf{b}_e^T} + \underbrace{(\mu_m - \mu) \nabla \chi}_{\mathbf{b}_e^M}, \quad (3.15)$$

where the derivatives are taken by holding η and μ constant, with $\mathbf{x} = (r, z)$ and $\mathbf{x}_\star = (r_\star, z_\star)$. This result is interesting and important, because it generalises to A_e the possibility first established by Andrews (1981) to interpret the APE density as the work needed to move a fluid parcel from its notional equilibrium position \mathbf{x}_\star in the reference state to its position \mathbf{x} in the actual state. Whether such a possibility also pertained to momentum-constrained available energy had remained unclear so far, as neither Codoban & Shepherd (2006) nor Andrews (2006) had discussed it.

In the following, we regard the part \mathbf{b}_e^T that is proportional to the specific volume anomaly as the thermodynamic component and the part \mathbf{b}_e^M that is proportional to the squared angular momentum anomaly as the mechanical component of the generalised buoyancy force \mathbf{b}_e . The thermodynamic force \mathbf{b}_e^T has been discussed before by Smith *et al.* (2005), who sought to clarify the role played by buoyancy in tropical cyclones. In their paper, they write such a force in the form

$$\mathbf{b}_e^T = \left(1 - \frac{\rho_m}{\rho_h} \right) \frac{1}{\rho_m} \nabla p_m = \left(1 - \frac{\rho_m}{\rho_h} \right) \mathbf{g}_e, \quad (3.16)$$

where \mathbf{g}_e is a generalised acceleration defined by Smith *et al.* (2005) as

$$\mathbf{g}_e = \left(\frac{v_m^2}{r} + f v_m, -g \right) = \frac{1}{\rho_m} \nabla p_m. \quad (3.17)$$

The mechanical force \mathbf{b}_e^M has also been discussed before, for instance in relation to centrifugal waves, e.g. Markowski & Richardson (2010).

3.4. Partitioning of A_e into mechanical and thermodynamic components

The available energy A_e is a two-dimensional function of the radial and vertical displacements $\delta r = r - r_\star$ and $\delta z = z - z_\star$. For small enough displacements, A_e reduces to a quadratic function $A_e \approx 1/2 \delta \mathbf{x}^T H_A \delta \mathbf{x}$, where H_A is the Hessian matrix of A_e 's second derivatives. In that case, the most natural approach to establish the positive definite character of A_e is to compute the (real) eigenvalues of H_A and determine whether they are both positive. Since $\mathbf{b}_e = -\nabla A_e \approx -H_A \delta \mathbf{x}$, the eigenvectors of H_A can be interpreted as the directions along which the restoring buoyancy force \mathbf{b}_e aligns perfectly with the

Available energy including momentum constraints and eddy energy 9

displacement $\delta \mathbf{x}$. The eigenvalues thus represent the squared frequency of the natural oscillation taking place in the eigendirections. In the system of coordinates (x_1, x_2) defined by the eigenvectors, the available energy A_e can be written as the sum of two quadratic terms $A_e \approx \lambda_1 x_1^2/2 + \lambda_2 x_2^2/2$ that most clearly links its sign positive definite character to the sign of the eigenvalues λ_1 and λ_2 . Such an approach is not available, however, for finite-amplitude displacements. In that case, previous authors have showed that A_e can still be decomposed as the sum of two terms whose sign-definiteness can be linked to the sign of the gradients of M_m and η_m . Such a decomposition is not unique in general, however, and different authors have proposed different ones.

Here we propose yet another decomposition $A_e = \Pi_k + \Pi_e$, which differs from previous ones in that it attempts to more cleanly separate the kinetic and potential energy parts of A_e . To that end, we exploit the fact that A_e can be expressed as a path integral. Indeed, such a path can be broken into two components by introducing some yet-to-be-identified intermediate point $\mathbf{x}_\mu = (r_\mu, z_\mu)$, thus allowing one to associate Π_e and Π_k with one of the integration sub-paths as follows:

$$A_e = - \underbrace{\int_{\mathbf{x}_*}^{\mathbf{x}_\mu} \mathbf{b}_e(M, \eta, \mathbf{x}', t) \cdot d\mathbf{x}'}_{\Pi_e} - \underbrace{\int_{\mathbf{x}_\mu}^{\mathbf{x}} \mathbf{b}_e(M, \eta, \mathbf{x}', t) \cdot d\mathbf{x}'}_{\Pi_k}. \quad (3.18)$$

The same intermediate point \mathbf{x}_μ can be similarly used to partition the exact expression (3.13) for A_e , thus yielding the following explicit expressions for Π_e and Π_k :

$$\Pi_e = h(\eta, p_\mu) - h(\eta, p_*) + \Phi(z_\mu) - \Phi(z_*) + \mu(\chi_\mu - \chi_*) + \frac{f^2}{16} \left(\frac{1}{\chi_\mu} - \frac{1}{\chi_*} \right), \quad (3.19)$$

$$\Pi_k = h(\eta, p_m) - h(\eta, p_\mu) + \Phi(z) - \Phi(z_\mu) + \mu(\chi - \chi_\mu) + \frac{f^2}{16} \left(\frac{1}{\chi} - \frac{1}{\chi_\mu} \right), \quad (3.20)$$

where p_μ is shorthand for $p_m(r_\mu, z_\mu)$. In Eq. (3.20), the terms involving the specific enthalpy are clearly of a thermodynamic nature. In order for Π_k to be purely mechanical in nature, these need to be removed. This is possible only if (r_μ, z_μ) is chosen so that $p_\mu = p_m$. To further constrain \mathbf{x}_μ , we further impose that Π_e and Π_k are only contributed to by the thermodynamic and mechanical components of the generalised buoyancy force respectively; mathematically:

$$\Pi_e = - \int_{\mathbf{x}_*}^{\mathbf{x}_\mu} \mathbf{b}_e^T \cdot d\mathbf{x}' = \int_{\mathbf{x}_*}^{\mathbf{x}} (\nu_h - \nu_m) \nabla p_m \cdot d\mathbf{x}' \quad (3.21)$$

$$\Pi_k = - \int_{\mathbf{x}_\mu}^{\mathbf{x}} \mathbf{b}_e^M \cdot d\mathbf{x}' = \int_{\mathbf{x}_*}^{\mathbf{x}} (\mu - \mu_m) \nabla \chi \cdot d\mathbf{x}'. \quad (3.22)$$

For such expressions to hold, the work done by \mathbf{b}_e^M and \mathbf{b}_e^T must vanish on the first and second legs of the overall integration path respectively:

$$\int_{\mathbf{x}_\mu}^{\mathbf{x}} (\nu_h - \nu_m) \nabla p_m \cdot d\mathbf{x}' = 0, \quad \int_{\mathbf{x}_*}^{\mathbf{x}_\mu} (\mu - \mu_m) \nabla \chi \cdot d\mathbf{x}' = 0. \quad (3.23)$$

The most obvious way to fulfill (3.23) is by imposing $\mu_m = \mu$ on the first leg joining \mathbf{x}_* to \mathbf{x}_μ , while imposing to the second leg joining \mathbf{x}_μ to \mathbf{x} that it follows an isobaric surface $\nabla p_m \cdot d\mathbf{x}' = 0$. As a result, the intermediate point $\mathbf{x}_\mu = (r_\mu, z_\mu)$ must lie at the intersection of the surface of constant angular momentum $\mu_m = \mu$ and isobaric surface $p_m = p_m(r, z)$. Its coordinates must therefore be solutions of

$$\mu_m(r_\mu, z_\mu) = \mu, \quad p_m(r_\mu, z_\mu) = p_m(r, z). \quad (3.24)$$

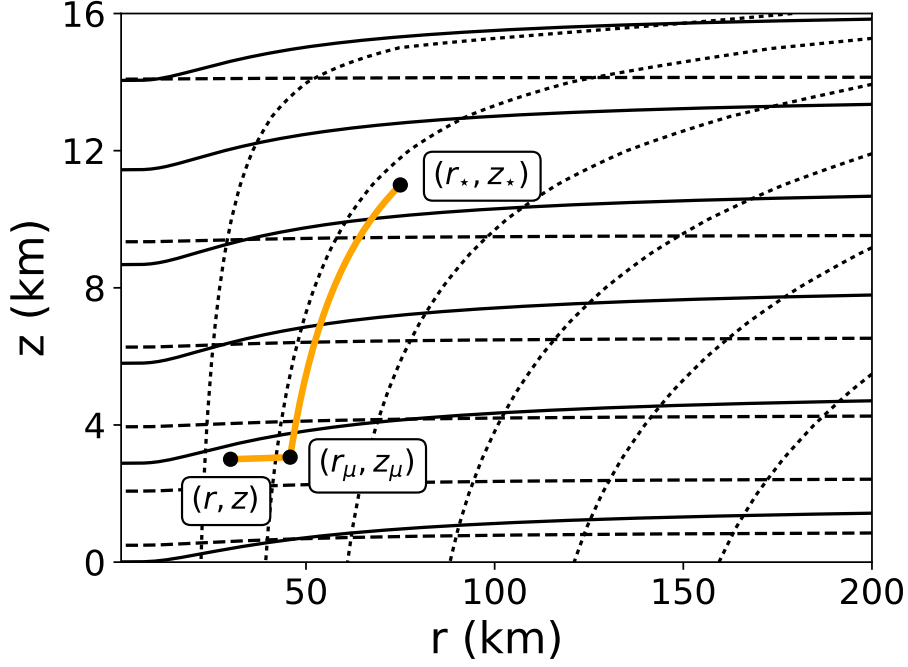


Figure 2: Illustration of a particular pathway linking a fluid parcel reference position (r_*, z_*) to its actual position (r, z) via the intermediate point (r_μ, z_μ) for the analytical vortex state described in Appendix A. The first leg of the path linking \mathbf{x}_* to \mathbf{x}_μ follows a surface of constant angular momentum (denoted by dotted lines). The second leg linking \mathbf{x}_μ to \mathbf{x} follows an isobaric surface (denoted by dashed lines). The thick full lines denote isentropic surfaces, which illustrate the warm core character of such a cyclonic vortex.

Such a construction and the two different integration paths are illustrated in Fig. 2 for the analytical vortex solution detailed in Appendix A. Moreover, Fig. 3 illustrates the superiority, at least visually, of the (μ_m, p_m) representation over the (M_m, η_m) representation to achieve what looks like a near orthogonal finite-amplitude decomposition of available energy.

3.5. Sign definiteness of the eddy available potential energy Π_e

The key role played by isobaric and constant angular momentum surfaces for simplifying the partitioning of A_e motivates us to work in (μ_m, p_m) coordinates. Since $\mu_m = (r^3/\rho_m)\partial p_m/\partial r + f^2 r^4/4$, we have

$$J_{\mu p} = \frac{\partial(\mu_m, p_m)}{\partial(r, z)} = -\rho_m g f^2 r^3 + \frac{\partial}{\partial r} \left(\frac{r^3}{\rho_m} \frac{\partial p_m}{\partial r} \right) \frac{\partial p_m}{\partial z} - \frac{\partial}{\partial z} \left(\frac{r^3}{\rho_m} \frac{\partial p_m}{\partial r} \right) \frac{\partial p_m}{\partial r}. \quad (3.25)$$

Close to a state of rest, $J_{\mu p} \approx -\rho_m g f^2 r^3 < 0$, in which case the coordinate transformation is invertible and well defined, except at the origin $r = 0$. In the following, we assume that this remains the case for a non-resting reference vortex state in gradient wind balance, as can be seen to be the case in Fig. 2 for our example analytical vortex. In the following, a tilde is used to denote functions of (r, z) in their (μ_m, p_m) representation; for instance, $\nu_m(r, z) = \tilde{\nu}_m(\mu_m, p_m)$ and $\chi(r) = \tilde{\chi}(\mu_m, p_m)$.

Using the fact that $\nabla p_m \cdot d\mathbf{x}' = dp'$, where $p' = p_m(r', z')$, it is easily seen that Eq.

Available energy including momentum constraints and eddy energy 11

(3.21) defining Π_e may be rewritten as the following one-dimensional integral in pressure:

$$\Pi_e = \int_{p_\star}^{p_m} [\nu(\eta, p') - \tilde{\nu}_m(\mu, p')] dp' = \int_{p_\star}^{p_m} [\nu(\eta, p') - \nu(\tilde{\eta}_m(\mu, p'), p')] dp', \quad (3.26)$$

where we also used the fact that ν_h in Eq. (3.21) refers to $\nu(\eta, p')$, that $p_m(\mathbf{x}_\star) = p_\star$, that $p_m = p_m(\mathbf{x})$, and that $\nu_m(r', z') = \tilde{\nu}_m(\mu, p') = \nu(\tilde{\eta}_m(\mu, p'), p')$ along the surface of constant angular momentum $\mu_m = \mu$. Physically, Eq. (3.26) can be recognised as being similar to the conventional APE density (compare with Eq. (2.18) of Tailleux (2018)), for a definition of buoyancy defined relative to the horizontally-varying reference specific volume $\tilde{\nu}_m(\mu, p)$ evaluated along a constant angular momentum surface. As a result, Π_e represents a “slantwise” APE density, by analogy with the concept of slantwise convective available potential energy (SCAPE) used in discussions of conditional symmetric instability (Bennetts & Hoskins 1979; Emanuel 1983*b*,*a*). To establish the positive definite character of Π_e , note that (3.26) may be rewritten as

$$\begin{aligned} \Pi_e &= \int_{p_\star}^{p_m} \int_{\tilde{\eta}_m(\mu, p')}^{\eta} \frac{\partial \nu}{\partial \eta}(\eta', p') d\eta' dp' = \frac{\partial \nu}{\partial \eta}(\eta_i, p_i) \int_{p_\star}^{p_m} \int_{\tilde{\eta}_m(\mu, p')}^{\tilde{\eta}_m(\mu, p_\star)} d\eta' dp' \\ &= \frac{\partial \nu}{\partial \eta}(\eta_i, p_i) \int_{p_\star}^{p_m} \int_{p'}^{p_\star} \frac{\partial \tilde{\eta}_m}{\partial p}(\mu, p'') dp'' dp', \end{aligned} \quad (3.27)$$

where we used the mean value theorem to take the adiabatic lapse rate $\partial \nu / \partial \eta = \Gamma = \alpha T / (\rho c_p)$ out of the integral (α is the isobaric thermal expansion and c_p is the isobaric specific heat capacity), where (η_i, p_i) represent some intermediate values of entropy and pressure, and used the fact that $\eta = \tilde{\eta}_m(\mu, p_\star)$ by definition. If the adiabatic lapse rate Γ is positive, as is normally the case, Eq. (3.27) shows that a sufficient condition for Π_e to be positive definite is

$$\frac{\partial \tilde{\eta}_m}{\partial p}(\mu, p'') < 0, \quad (3.28)$$

regardless of p'' ; this states that the specific entropy should increase with height (decrease with pressure) along surfaces of constant angular momentum, as expected. The special case where

$$\frac{\partial \eta_m}{\partial z}(r, z) > 0, \quad \frac{\partial \tilde{\eta}_m}{\partial p}(\mu, p'') > 0, \quad (3.29)$$

would correspond to the so-called conditional symmetric instability (CSI), whereby the entropy profile is stable to upright vertical displacements but not to slantwise displacements. For small amplitude perturbations, a Taylor series expansion shows that (3.27) approximates to

$$\Pi_e \approx -\Gamma_i \frac{\partial \tilde{\eta}_m}{\partial p}(\mu, p_\star) \frac{(p_m - p_\star)^2}{2} \quad (3.30)$$

where Γ_i is shorthand for $\partial \nu / \partial p(\eta_i, p_i)$. Note that this expression is essentially the same as the classical small-amplitude expression $N^2 \delta z^2 / 2$ for the conventional APE density in terms of an appropriate squared buoyancy frequency, where δz is the vertical displacement from the reference height. Note that in Eq. (3.27), we could equally have regarded pressure as a function of entropy to obtain a small amplitude approximation proportional to the squared entropy anomaly $(\tilde{\eta}_m(\mu, p) - \tilde{\eta}_m(\mu, p_\star))^2 / 2$ instead if desired.

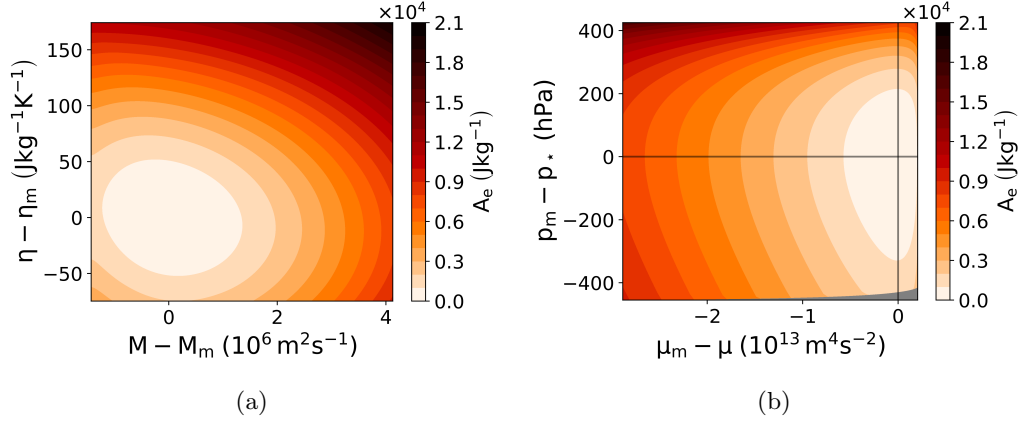


Figure 3: Available energy A_e of a perturbed dry air parcel at $r = 40$ km, $z = 5$ km, in terms of (a) M and η perturbations and (b) μ and p^* perturbations. The grey lines in (b) indicate the horizontal and vertical axes along which Π_k and Π_e change respectively, and the grey shading covers points in the space that are not sampled by the chosen perturbations of M and η .

3.6. Sign definiteness of the mechanical eddy energy Π_k

We now turn to the problem of establishing the conditions for Π_k to be positive definite. Eqs. (3.20), (3.22) and (3.23) show that Π_k may be equivalently written as:

$$\Pi_k = \Phi(z) - \Phi(z_\mu) + \mu(\chi - \chi_\mu) + \frac{f^2}{16} \left(\frac{1}{\chi} - \frac{1}{\chi_\mu} \right) = \int_{\mathbf{x}_\mu}^{\mathbf{x}} (\mu - \mu_m) \nabla \chi \cdot d\mathbf{x}'. \quad (3.31)$$

As for Π_e , we find it useful to keep working in (μ_m, p_m) coordinates. To that end, we use the mathematical identity $(\mu - \mu_m) \nabla \chi = \nabla[(\mu - \mu_m)\chi] + \chi \nabla \mu_m$ (recall that μ is treated like a constant in such calculations), and the fact that by construction $p_\mu = p_m$, to rewrite Π_k in the following equivalent ways:

$$\Pi_k = (\mu - \mu_m)\chi + \int_{\mathbf{x}_\mu}^{\mathbf{x}} \tilde{\chi}(\mu_m, p_m) \nabla \mu_m \cdot d\mathbf{x}' = \int_{\mu}^{\mu_m} [\tilde{\chi}(\mu', p_m) - \tilde{\chi}(\mu_m, p_m)] d\mu'. \quad (3.32)$$

Eq. (3.33) is very similar to the expression Eq. (3.21) for Π_e . It can be similarly expressed as a double integral,

$$\Pi_k = \int_{\mu}^{\mu_m} \int_{\mu_m}^{\mu'} \frac{\partial \tilde{\chi}}{\partial \mu}(\mu'', p_m) d\mu'' d\mu', \quad (3.33)$$

which makes it clear that a sufficient condition for Π_k to be positive definite is

$$\frac{\partial \tilde{\chi}}{\partial \mu}(\mu'', p_m) < 0. \quad (3.34)$$

Physically, Eq. (3.34) corresponds to the condition that the reference squared angular momentum distribution increase with radius along isobaric surfaces. The violation of this condition corresponds to centrifugal instability, e.g. Drazin & Reid (1981). It is useful to remark that the partial derivative $\partial \tilde{\chi} / \partial \mu$ can be expressed in terms of the Jacobian $J_{\mu p}$ of the coordinate transformation from (r, z) to (μ_m, p_m) coordinates as

$$\frac{\partial \tilde{\chi}}{\partial \mu} = \frac{\partial(\tilde{\chi}, p_m)}{\partial(r, z)} \left(\frac{\partial(\mu_m, p_m)}{\partial(r, z)} \right)^{-1} = \frac{\rho_m g}{r^3} \left(\frac{\partial(\mu_m, p_m)}{\partial(r, z)} \right)^{-1}, \quad (3.35)$$

Available energy including momentum constraints and eddy energy

13

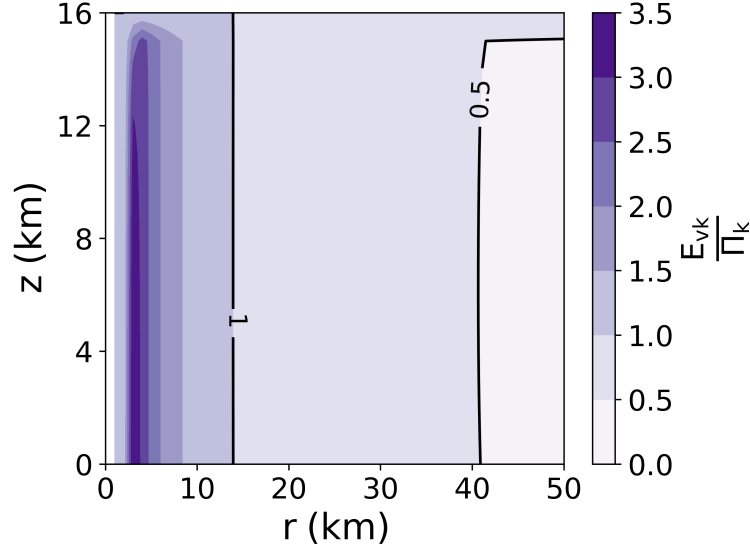


Figure 4: Estimate of the ratio $1/K_i$ as defined by Eq. (3.38) for the analytical vortex state described in Appendix A, assuming $M \approx M_m$.

which shows that the condition (3.34) is actually equivalent to the condition $J_{\mu p} < 0$, and hence to the requirement that the coordinates transformation from (μ_m, p_m) to (r, z) be invertible.

By using the mean value theorem, it is possible to write

$$\Pi_k = -\frac{\partial \tilde{\chi}}{\partial \mu}(\mu_i, p_m) \frac{(\mu - \mu_m)^2}{2} \quad (3.36)$$

where μ_i is some intermediate value of μ within the interval $[\min(\mu, \mu_m), \max(\mu, \mu_m)]$. On the other hand, the Eulerian eddy kinetic energy $E_{vk} = (v - v_m)^2/2$ may be written as

$$E_{vk} = \frac{(v - v_m)^2}{2} = \frac{1}{r^2(M_m + M)^2} \frac{(\mu_m - \mu)^2}{2} \quad (3.37)$$

by using the relations $v = M/r - fr/2$, $v_m = M_m/r - fr/2$, $(v - v_m)^2 = (M - M_m)^2/r^2$ and $(\mu_m - \mu)^2 = (M_m + M)^2(M - M_m)^2$. The two quantities are therefore proportional to each other, i.e., $\Pi_k = K_i E_{vk}$, with the proportionality factor

$$K_i = -r^2(M_m + M)^2 \frac{\partial \tilde{\chi}}{\partial \mu}(\mu_i, p_m). \quad (3.38)$$

Near a state of rest, $M_m \approx M \approx fr^2/2$, then $\partial \tilde{\chi}/\partial \mu \approx -1/(f^2 r^6)$, so that $K_i \approx 1$, and the two quantities are equivalent. In general, however, $K_i \neq 1$ but we were not able to develop a mathematical theory for its value. For illustrative purposes, Fig. 4 shows a particular estimate of the ratio $1/K_i$ for the particular example of the analytical reference vortex state described in Appendix A, where the approximation $\mu_i \approx \mu_m$ was used.

3.7. Mean “system” energies

The reference vortex state in gradient wind balance possesses conventional APE and KE relative to a notional state of rest characterised by the reference hydrostatic pressure and density fields $p_0(z)$ and $\rho_0(z)$. The conventional APE density — denoted Π_m here

— is naturally defined as

$$\Pi_m = h(\eta, p_\star) - h(\eta, p_R) + \Phi(z_\star) - \Phi(z_R) = \int_{p_R}^{p_\star} [\nu(\eta, p') - \nu_0(p')] dp', \quad (3.39)$$

and is equivalent to the APE density denoted by Π_2 in Tailleux (2018). The reference pressure $p_R = p_0(z_R)$ at the reference depth z_R satisfies the level of neutral buoyancy (LNB) equation $\nu(\eta, p_R) = \nu_0(p_R)$ originally introduced in Tailleux (2013), which is key to ensuring that Π_m is positive definite.

The mean kinetic energy of the reference vortex is simply equal to $v_\star^2/2$. In contrast to the case $f = 0$ considered by Andrews (2006), the case of a finite rotation rate $f \neq 0$ considered in this paper gives rise to a background radial distribution of angular momentum $M_R(r) = fr^2/2$ that introduces a radial restoring inertial force, in the same way that a statically stable vertical gradient of entropy introduces a vertical restoring buoyancy force. As mentioned previously, a reference equilibrium radius r_R (for which $v_R = 0$) can then be defined as the solution of $M = fr_R^2/2$. As a result, we may write v_\star as

$$v_\star = \frac{M}{r_\star} - \frac{fr_\star}{2} = \frac{fr_R^2}{2r_\star} - \frac{fr_\star}{2} = \frac{f(r_R + r_\star)(r_R - r_\star)}{2r_\star}, \quad (3.40)$$

which in turn implies for the kinetic energy $v_\star^2/2$

$$\frac{v_\star^2}{2} = \frac{f^2(r_R + r_\star)^2(r_R - r_\star)^2}{8r_\star^2}. \quad (3.41)$$

Eq. (3.41) shows that $v_\star^2/2$ is quadratic in the displacement amplitude $\delta r = r_\star - r_R$ from the equilibrium position r_R even for finite amplitude δr . Moreover, Eq. (3.40) shows that creating a cyclonic circulation ($v_\star > 0$ if $f > 0$) requires $r_R > r_\star$, and hence the compression of the equilibrium constant angular momentum surfaces. In order to express $v_\star^2/2$ as the work against the inertial restoring force, we may use (2.9) to write it in the form:

$$\frac{v_\star^2}{2} = \frac{v_\star^2}{2} - \frac{v_R^2}{2} = \mu(\chi_\star - \chi_R) + \frac{f^2}{16} \left(\frac{1}{\chi_\star} - \frac{1}{\chi_R} \right). \quad (3.42)$$

making use of the fact that $v_R^2 = \mu\chi_R + f^2/(16\chi_R) - f\sqrt{\mu}/2 = 0$, which in turn may be written as the following integrals:

$$\frac{v_\star^2}{2} = \int_{r_R}^{r_\star} (\mu - \mu_R(r')) \frac{\partial \chi}{\partial r}(r') dr' = \int_{\chi_R}^{\chi_\star} (\mu - \mu_R(\chi')) d\chi'. \quad (3.43)$$

We propose to call the right-hand side of (3.41) and its integral expression (3.43) the available radial energy (ARE). Eq. (3.43) makes it clear that the restoring inertial force experienced by the fluid parcel as it experiences a radial displacement is $-(\mu - \mu_r)\partial\chi/\partial r = (\mu - \mu_R)/r^3$, consistent with Emanuel (1994). For small displacements δr , so that $r_R \approx r_\star$, the above expression approximates to $v_\star^2/2 \approx f^2(r_\star - r_R)^2/2$, which suggests that the natural frequency of the radial waves is f , as would be the case for standard inertial waves. These results clearly establish that Π_k and Π_e are the natural generalisations of $v_\star^2/2$ and Π_m for constructing the actual state from a non-resting reference state instead of a resting one.

4. Energetics of vortex growth and decay due to diabatic effects

For a stable reference vortex state, the above results show that the total eddy energy $\mathbf{u}_s^2/2 + \Pi_1 + \Pi_k + \Pi_e$ is globally conserved for purely adiabatic and inviscid axisymmetric

Available energy including momentum constraints and eddy energy 15

disturbances. In that case, \mathbf{b}_e acts a restoring force giving rise to a complex combination of internal and inertial/centrifugal waves, as discussed by Emanuel (1994) for instance. As long as the conditions for symmetric stability (3.28) and (3.34) are met, any transfer between the eddy and mean energies is forbidden, so that there cannot be any net growth or decay of the azimuthal circulation unless non-axisymmetric or diabatic/viscous effects are also considered. As an example of application of our framework, we show in the following how to use it to shed light on the issue of how diabatic/viscous effects may lead to the intensification of a cyclonic vortex, a central issue in the study of tropical cyclones. The discussion of non-axisymmetric effects, which is significantly more involved, is left to a future study.

4.1. Standard energetics viewpoint

Our aim in the following is to establish the conditions under which sinks and sources of specific entropy and angular momentum can lead to the intensification of an incipient cyclonic seed vortex. To that end, we place ourselves in a Northern Hemisphere-like situation ($v > 0, f > 0$). A standard viewpoint in the tropical cyclone literature, e.g., Smith *et al.* (2018), is to consider separate evolution equations for the azimuthal kinetic energy $v^2/2$ and the rest of the flow as follows:

$$\rho \frac{D}{Dt} \left(\frac{\mathbf{u}_s^2}{2} + \Phi + h - \frac{p}{\rho} \right) + \nabla \cdot (p\mathbf{u}_s) = \rho \mathbf{u}_s \cdot \mathbf{D}_s + \rho \dot{q} + \left(f + \frac{v}{r} \right) \rho uv, \quad (4.1)$$

$$\rho \frac{D}{Dt} \frac{v^2}{2} = - \left(f + \frac{v}{r} \right) \rho uv + \rho v D_v, \quad (4.2)$$

Since the dissipation term vD_v presumably acts as a brake on v , Eq. (4.2) demonstrates that because $v > 0$ by design, the radial velocity must be negative ($u < 0$) in order for v to intensify. This is the only way that the energy conversion term $-(f + v/r)uv$ can be positive and hence act as a source of energy for v . This condition is of course well known and observed in numerical simulations of TCs. What the existing literature appears to be lacking, however, is a clear explanation for how the required radially inward motion is actually driven. Indeed, the emphasis tends to be on vertical motion associated with cumulus convection and the generation of strong updrafts by the release of latent heat. While in an axisymmetric model, mass conservation imposes that a low level radial inward motion should exist to replenish the mass lost by strong vertical motion near the TC centre, such an argument is not a physical explanation. While it suggests that radial forces of the correct sign must exist to do the job, it does not in itself explain what such forces are.

An alternative and purely Eulerian argument that calls for both $u < 0$ and $w > 0$ can be made from the angular momentum conservation equation (2.7) — which has essentially the same information content as (4.2) — written in the form:

$$\frac{\partial M}{\partial t} = -u \frac{\partial M}{\partial r} - w \frac{\partial M}{\partial z} + r D_v. \quad (4.3)$$

If the distribution of M is such that $\partial M/\partial r > 0$ and $\partial M/\partial z < 0$ as is seen to be the case for the analytical reference vortex case described in Appendix A and illustrated in Fig. 2, Eq. 4.3 makes it clear that both $u < 0$ and $w > 0$ will contribute to the local intensification of M and hence of v . The understanding of axisymmetric TC intensification therefore boils down to understanding how viscous and diabatic effects cooperate to drive an upward and radially inward secondary circulation at low levels near the eyewall.

4.2. Generalised buoyancy/inertial force viewpoint

We now regard the azimuthal circulation as the sum of balanced and unbalanced parts $v = v_\star + v''$ (Lagrangian viewpoint) or $v = v_m + v'$ (Eulerian viewpoint). In this view, the observed intensification of v may *a priori* be due to the intensification of either v_m or v' (equivalently v_\star or v'') or both, depending on how v_m is defined. Because there is some freedom in the specification of v_m in the present framework (for instance, it could be imposed to be time independent), we first discuss the case where the intensification of v may be primarily attributed to that of v' (restricting ourselves to the Eulerian viewpoint in the following). Evidence that such a case is relevant for the understanding of actual TC intensification is provided by the study of Bui *et al.* (2009), which suggests that the degree of unbalance of TCs is likely significant, especially in the boundary layer. Now, because $v' = v - v_m = (M - M_m)/r = (\mu - \mu_m)/(r(M + M_m))$, any increase in v' must result from the creation of a positive anomaly $\mu' = \mu - \mu_m > 0$ and hence from an increase in the mechanical energy reservoir Π_k , the only one that increases when $|\mu - \mu_m|$ increases.

Prior to discussing energetics, it is useful to first discuss the forces at work in the system as this is what is most helpful to establish causal relationships. To that end, let us consider the form of the momentum equation for the secondary circulation \mathbf{u}_s that makes apparent the role of the generalised inertial/buoyancy force \mathbf{b}_e , viz.,

$$\frac{D\mathbf{u}_s}{Dt} = \mathbf{b}_e - \frac{1}{\rho}\nabla p' - v'\nabla p_m + \mathbf{D}_s, \quad (4.4)$$

where from (3.15), the radial and vertical components of \mathbf{b}_e may be written explicitly as follows:

$$b_e^{(r)} = -(\nu_h - \nu_m)\frac{\partial p_m}{\partial r} + \frac{(\mu - \mu_m)}{r^3} = -\rho_m(\nu_h - \nu_m)\left(f + \frac{v_m}{r}\right)v_m + \frac{(\mu - \mu_m)}{r^3}, \quad (4.5)$$

$$b_e^{(z)} = -(\nu_h - \nu_m)\frac{\partial p_m}{\partial z} = \rho_m g(\nu_h - \nu_m). \quad (4.6)$$

One of the expected advantages of introducing a non-resting reference state is to minimise the role of $\nabla p'$ in (4.4) and hence to maximise the ability of \mathbf{b}_e to predict the actual acceleration $D\mathbf{u}_s/Dt$. Assuming this to be the case, and recalling that $(\mu - \mu_m)/r^3 > 0$, Eq. (4.5) shows that a necessary condition for the radial component of \mathbf{b}_e to point towards the centre of the cyclone is that the fluid parcels be positively buoyant,

$$\nu_h - \nu_m > 0, \quad (4.7)$$

in which case (4.6) shows that $b_e^{(z)}$ will also point upward, as is expected physically. By definition, $\nu_h = \nu(\eta, p_m(r, z))$ and $\nu_m = \nu(\eta_m(r, z), p_m(r, z))$ so that

$$\nu_h - \nu_m \approx \Gamma(\eta(r, z, t) - \eta_m(r, z)) \quad (4.8)$$

is proportional to the local entropy anomaly $\eta' = \eta - \eta_m$ (we have neglected the time variation of the reference variables, but these can be retained if desired). Since $\Gamma > 0$ in general, the creation of a positive specific volume anomaly requires a sustained diabatic source of entropy to increase η . As discussed by Smith *et al.* (2005), whether (4.7) is satisfied depends critically on the choice of reference state used to define buoyancy. For instance, Brown (2002) found such a condition to be met for buoyancy defined relative to a relatively elaborate reference vortex state including even some degree of asymmetry. However, Zhang *et al.* (2000) found the parcels to be negatively buoyant for buoyancy defined relative to a rest state, the desired upward acceleration being then entirely provided by the pressure gradient term $\nabla p'$.

Available energy including momentum constraints and eddy energy

17

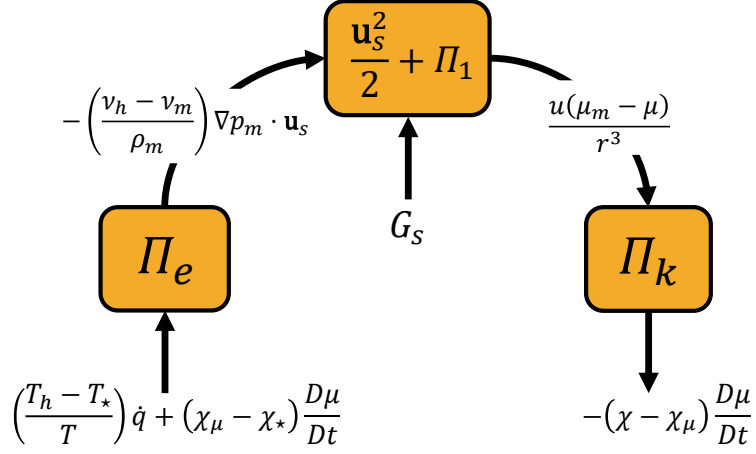


Figure 5: Hypothesised energy pathways associated with the intensification of a cyclonic vortex forced by sources of diabatic heating \dot{q} and angular momentum $D\mu/Dt$.

Even if (4.7) holds, it is not sufficient to ensure that $b_e^{(r)}$ be negative. Indeed, because $(\mu - \mu_m)/r^3 > 0$, (4.5) imposes a further constraint on the magnitude of positive buoyancy anomalies, namely:

$$\nu_h - \nu_m > \left[\rho_m \left(f + \frac{v_m}{r} \right) v_m \right]^{-1} \frac{\mu - \mu_m}{r^3}. \quad (4.9)$$

If specific volume anomalies $\nu_h - \nu_m$ are bounded, as is presumably the case in reality, (4.9) appears to impose an upper limit on the maximum angular momentum anomalies $\mu - \mu_m$ and hence on the maximum intensity that the vortex can reach. This limit is *a priori* different from the maximum potential intensity (MPI) predicted by Emanuel (1986) (see Emanuel (2018) for a recent review on this topic and wider TC research), which is reached when the production of available energy by surface enthalpy fluxes balances dissipation by surface friction in the region of maximum winds. Whether such a condition could account for why the intensity of many observed TCs remain significantly below their theoretical maximum intensity (Emanuel 2000) is left for future study.

4.3. Energy cycle

The generalised buoyancy/inertial force \mathbf{b}_e and other forces that drive the secondary circulation do work and cause energy transfers between the different existing energy reservoirs, for which sources and sinks must exist in order for the system to achieve a steady state. In the following, we discuss the energy cycle associated with an intensifying cyclonic vortex whose intensification is dominated by the intensification of v' . To that end, we find that the simplest and most economical description of the local energy cycle is one based on separate evolution equations for: the sum of the kinetic energy of the secondary circulation plus the AAE, $\mathbf{u}_s^2/2 + \Pi_1$; the eddy slantwise APE Π_e ; and the eddy mechanical energy Π_k . This leads to the following set of equations:

$$\rho \frac{D}{Dt} \left(\frac{\mathbf{u}_s^2}{2} + \Pi_1 \right) + \nabla \cdot (p' \mathbf{u}_s) = \rho (\mathbf{b}_e^T \cdot \mathbf{u}_s + \mathbf{b}_e^M \cdot \mathbf{u}_s) + \rho G_s, \quad (4.10)$$

18

Tailleux & Harris

$$G_s = \left(\frac{T - T_h}{T} \right) \dot{q} + \nu' \left(\frac{\partial p_m}{\partial t} + \mathbf{u}_s \cdot \nabla p_m \right), \quad (4.11)$$

$$\frac{D\Pi_e}{Dt} = -\mathbf{b}_e^T \cdot \mathbf{u}_s + \left(\frac{T_h - T_\star}{T} \right) \dot{q} + (\chi_\mu - \chi_\star) \frac{D\mu}{Dt} + \nu_h \frac{\partial p_m}{\partial t} - \nu_\star \frac{\partial p_\star}{\partial t}, \quad (4.12)$$

$$\frac{D\Pi_k}{Dt} = -\mathbf{b}_e^M \cdot \mathbf{u}_s + (\chi - \chi_\mu) \frac{D\mu}{Dt}. \quad (4.13)$$

For an intensifying vortex resulting from an increase in ν' , we established in the previous section that $\nu_h - \nu_m > 0$ and $\mu - \mu_m > 0$. The implications for the work against the generalised inertial and buoyancy forces \mathbf{b}_e^T and \mathbf{b}_e^M by the secondary circulation are:

$$-\mathbf{b}_e^M \cdot \mathbf{u}_s = (\mu - \mu_m) \nabla \chi \cdot \mathbf{u}_s = -\frac{u(\mu - \mu_m)}{r^3} > 0, \quad (4.14)$$

$$-\mathbf{b}_e^T \cdot \mathbf{u}_s = (\nu_h - \nu_m) \nabla p_m \cdot \mathbf{u}_s = (\nu_h - \nu_m) \left[u \frac{\partial p_m}{\partial r} - \rho_m g w \right] < 0. \quad (4.15)$$

The sign of such energy conversions suggest that the flow of energy follows the paths

$$\Pi_e \rightarrow \frac{\mathbf{u}_s^2}{2} + \Pi_1 \rightarrow \Pi_k, \quad (4.16)$$

as illustrated in Fig. 5. If we neglect the terms related to the time-dependence, the following term needs to be positive

$$\left(\frac{T_h - T_\star}{T} \right) \dot{q} + (\chi_\mu - \chi_\star) \frac{D\mu}{Dt} > 0. \quad (4.17)$$

If $D\mu/Dt < 0$ acts as a retarding effect, Fig. 2 shows that $(r_\star - r_\mu) > 0$ and hence that $(\chi_\mu - \chi_\star) > 0$, suggesting that the sink of angular momentum is of the wrong sign. Therefore, for (4.17) to act as a source term, the diabatic term must be positive and larger than the term proportional to the angular momentum sink term, viz.,

$$\left(\frac{T_h - T_\star}{T} \right) \dot{q} > \left| (\chi_\mu - \chi_\star) \frac{D\mu}{Dt} \right| > 0. \quad (4.18)$$

By definition, $T_h = T(\eta, p_m)$ and $T_\star = T(\eta, p_\star)$, so again from Fig. 2, $p_m - p_\star > 0$ and therefore $T_h - T_\star > 0$. Now, if we regard $p_m = \hat{p}_m(\eta_m, \mu_m)$ as a function of the reference entropy and squared angular momentum, we have

$$\frac{(T_h - T_\star)}{T} \approx \frac{1}{T} \frac{\partial T}{\partial p} (p_m - p_\star) \approx -\frac{1}{T} \frac{\partial T}{\partial p} \left\{ \frac{\partial \hat{p}_m}{\partial \eta_m} (\eta - \eta_m) + \frac{\partial \hat{p}_m}{\partial \mu_m} (\mu - \mu_m) + \dots \right\}. \quad (4.19)$$

Since in general pressure varies little with μ_m , it follows that the term is dominated by the entropy anomaly, which needs to be positive as $\partial \hat{p}_m / \partial \eta_m < 0$. For the intensification of ν' to proceed, a finite amplitude entropy anomaly η' needs to be produced in order for making the thermodynamic efficiency $(T_h - T_\star)/T$ large enough to satisfy the threshold relation (4.18).

4.4. Evolution of the reference state and reference state variables

As in all theories of available energy, there is some freedom in choosing the reference state. In this paper, we assumed it to be constant, thus allowing us to ascribe the intensification of a cyclonic vortex to the intensification of ν' . A theoretically important choice is to regard the reference state at any given time as the state of minimum energy that can be obtained by means of a re-arrangement of mass conserving entropy and angular momentum (alternatively potential vorticity) advocated by some authors

Available energy including momentum constraints and eddy energy 19

Cullen *et al.* (2015); Methven & Berrisford (2015); Scotti & Passagia (2019). Methven & Berrisford (2015) applied such an idea to the atmosphere using real data, and found the reference state to evolve only slowly. Whether this could be shown to be the case for tropical cyclones remains to be demonstrated, as the method to compute such a reference state is technically challenging. Existing methods for estimating a balanced reference state such as Smith (2006) or Nolan & Montgomery (2002) are consistent with angular momentum conservation, but inconsistent with an adiabatic re-arrangement.

Regardless of whether the reference state depends on time or not, Eq. (3.2) shows that the diabatic and frictional effects $D\eta/Dt$ and DM/Dt must in general cause the fluid parcel's reference position (r_*, z_*) to drift with time. Such a drift impacts some of the quantities that play a key role in the discussion of the energy cycle described above, such as the thermodynamic efficiency $(T_h - T_*)/T$, so that its importance needs to be assessed. Evolution equations for $Dr_*/Dt = u_*$ and $Dz_*/Dt = w_*$ can be obtained by taking the material derivative of (3.2), which yields:

$$u_* \frac{\partial \eta_m}{\partial r} + w_* \frac{\partial \eta_m}{\partial z} = \frac{D\eta}{Dt} - \frac{\partial \eta_m}{\partial t}, \quad (4.20)$$

$$u_* \frac{\partial M_m}{\partial r} + w_* \frac{\partial M_m}{\partial z} = \frac{DM}{Dt} - \frac{\partial M_m}{\partial t}. \quad (4.21)$$

If the Jacobian $J_0 = \partial(M_m, \eta_m)/\partial(r, z)$ differs from zero, the above system can be inverted for u_* and w_* :

$$u_* = \frac{Dr_*}{Dt} = \frac{1}{J_0} \left\{ \frac{\partial \eta_m}{\partial z} \left(\frac{DM}{Dt} - \frac{\partial M_m}{\partial t} \right) - \frac{\partial M_m}{\partial z} \left(\frac{D\eta}{Dt} - \frac{\partial \eta_m}{\partial t} \right) \right\} \quad (4.22)$$

$$w_* = \frac{Dz_*}{Dt} = \frac{1}{J_0} \left\{ -\frac{\partial \eta_m}{\partial r} \left(\frac{DM}{Dt} - \frac{\partial M_m}{\partial t} \right) + \frac{\partial M_m}{\partial r} \left(\frac{D\eta}{Dt} - \frac{\partial \eta_m}{\partial t} \right) \right\}. \quad (4.23)$$

For the particular idealised reference vortex considered in this paper, $J_0 > 0$ everywhere, so that (4.20-4.21) is invertible. Moreover, the partial derivatives are such that $\partial \eta_m / \partial z > 0$, $\partial M_m / \partial z < 0$, $\partial \eta_m / \partial r < 0$ and $\partial M_m / \partial r > 0$. As a result, for a time-independent reference state, a positive diabatic entropy source $D\eta/Dt > 0$ and negative angular momentum sink $DM/Dt < 0$ have opposing effects on u_* and w_* .

5. Discussion and conclusions

The conventional local APE density (Andrews 1981; Holliday & McIntyre 1981; Tailleux 2018) has long been known to be interpretable as the work against the conventional buoyancy force that is needed to move a fluid parcel from its notional resting position to its actual position. The arbitrariness of the reference state in the local APE theory appears therefore to reflect the well known non-unique character of the definition of the conventional buoyancy force that pervades the literature about stratified fluids (Turner 1973). The possibility of similarly interpreting the local available energy including momentum constraints for axisymmetric zonal and vortex motions derived by Codoban & Shepherd (2003, 2006); Andrews (2006) in terms of the work done against suitably defined forces had been lacking so far, however. The demonstration that such an interpretation is possible, and that the forces involved are the generalised buoyancy and inertial/centrifugal forces discussed by Smith *et al.* (2005) and Rayleigh (1916); Emanuel (1994) respectively, is one of the main achievements of the present paper. To formalise the fact that a radial gradient of angular momentum plays the same role as the vertical gradient of entropy in giving rise to an inertial/centrifugal restoring force that

is the direct counterpart of the conventional buoyancy force, we introduced a new form of available energy density associated with the radial distribution of squared angular momentum, baptized Available Radial Energy (ARE) density. When it is estimated relative to a reference angular momentum distribution of a resting rotating state, the ARE coincides with the vortex kinetic energy $v^2/2$.

Because it is defined relative to a non-resting reference state, the available energy including momentum constraints is best interpreted as a form of eddy energy related to the local buoyancy. In contrast, the available energy of the reference vortex state can be regarded as the system buoyancy, to use the terminology of Smith *et al.* (2005). In this paper, the eddy form of ARE is denoted by Π_k and the eddy form of the conventional APE density is denoted by Π_e . Physically, Π_e is naturally defined as a slantwise APE that has been extensively discussed in the literature, e.g., Bennetts & Hoskins (1979); Emanuel (1983*b*). On the other hand, we are not aware that either ARE or its eddy form Π_k has been previously discussed. For a symmetrically stable reference vortex, the sum of the available energy and kinetic energy is conserved for adiabatic and inviscid motions. In this paper, only two conditions are found to be sufficient to ensure symmetric stability: 1) that the squared angular momentum increases with radius along isobaric surfaces; 2) that the entropy increases vertically along surfaces of constant angular momentum. Although these cannot be regarded as new, they are given here in a significantly clearer and more explicit way than Andrews (2006) and Ilin (1991), for instance.

As in previous discussions of local available energetics and of the concept of buoyancy, we are unable to reach firm conclusions about the optimal strategy, provided there is one, for specifying the reference state in the present theory. Some key practical considerations seem worth noting, however. First, it is clear that one of the most desirable features of the reference state is that it minimises the role of the pressure gradient term $\nabla p'$ relative to that of the generalised buoyancy/inertial force \mathbf{b}_e in the momentum equation for the secondary circulation \mathbf{u}_s . Second, it is important to note that, as emphasised by Codoban & Shepherd (2003), the choice of reference state impacts the sign and magnitude of the thermodynamic $(T_h - T_\star)/T$ and mechanical $(\chi - \chi_\star)$ efficiencies, which determine the relative fraction of the diabatic heating/cooling and friction contributing to the production/destruction of the available energy. This is of key importance for discussing causality in the considered system. There is some sense that the latter should be defined as the state of minimum energy obtainable by means of a re-arrangement of mass conserving both entropy and angular momentum, as suggested by Cullen *et al.* (2015) and Scotti & Passagia (2019) for instance.

We also derived evolution equations for the different energy reservoirs, accounting for the effects of sources/sinks of entropy and angular momentum, and applied the resulting framework to develop some understanding of how diabatic forcing may lead to the intensification of a cyclonic vortex and of the associated energy cycle. In the case where the vortex reference state can be assumed constant or slowly varying, our framework shows that intensification can only occur where positive buoyancy anomalies (defined relative to the non-resting reference vortex state) are created, in order for the generalised buoyancy force discussed by Smith *et al.* (2005) to be able to drive an inward and vertically directed secondary circulation. Creating such a positive buoyancy anomaly requires a source of diabatic heating. This makes it *a priori* possible for TC-like vortices to exist in a dry or semi-dry atmosphere provided that suitable sources can be shown to exist in such a case, as appears to be the case in Mrowiec *et al.* (2011); Cronin & Chavas (2019). In a moist atmosphere, however, there seems to be little choice but for the required source of diabatic heating to result from the release of latent heat associated with condensation, as is widely recognised. Our framework suggests an amplification mechanism that requires

Available energy including momentum constraints and eddy energy 21

the creation of a sufficiently large positive buoyancy anomaly that will in turn increase the thermodynamic efficiency of the system, thus initiating the creation of slantwise APE Π_e , which is then converted into Π_k . Demonstrating the relevance of such a mechanism for actual tropical cyclones requires generalising the present framework to account for humidity; this is beyond the scope of this paper and will be addressed in a forthcoming study.

Acknowledgements

BLH acknowledges support from NERC as part of the SCENARIO Doctoral Training Partnership (NE/L002566/1). The code used to produce the illustrations of the available energetics of an axisymmetric vortex in a dry atmosphere is available at <https://github.com/bethanharris/vortex-available-energy>.

Appendix A. Analytical expression for vortex motions

Many of the illustrations of this paper are based on a dry idealised tropical cyclone axisymmetric vortex taken from Smith *et al.* (2005), the description of which is reproduced here. This idealised TC is defined by its pressure perturbation

$$p(s, z) = (p_c - p_\infty(0)) \left[1 - \exp\left(\frac{-x}{s}\right) \right] \exp\left(\frac{-z}{z^*}\right) \cos\left(\frac{\pi}{2} \frac{z}{z_0}\right), \quad (\text{A } 1)$$

where p_c is the central pressure at the surface, $p_\infty(0)$ is the surface pressure at large radial distance, $s = r/r_m$ and x, r_m, z_0 and z^* are constants. We choose $p_\infty(0) - p_c$ and x so that the maximum tangential wind speed is about $40 \text{ m} \cdot \text{s}^{-1}$ at a radius of about 40 km and declines to zero at an altitude $z_0 = 16 \text{ km}$: specifically $p_\infty(0) - p_c = 50 \text{ mb}$, $z^* = 8 \text{ km}$ and $x = 1.048$. The exponential decay with height approximately matches the decrease in the environmental density with height and is necessary to produce a reasonably realistic tangential wind distribution that decreases in strength with height.

REFERENCES

- ANDREWS, D. G. 1981 A note on potential energy density in a stratified compressible fluid. *J. Fluid Mech.* **107**, 227–236.
- ANDREWS, D. G. 2006 On the available energy density for axisymmetric motions of a compressible stratified fluid. *J. Fluid Mech.* **569**, 481–492.
- ANDREWS, D. G. & MCINTYRE, M. E. 1978 An exact theory of nonlinear waves on a Lagrangian-mean flow. *J. Fluid Mech.* **89** (4), 609–646.
- ARTHUR, R. S., VENAYAGAMOORTHY, S. K., KOSEFF, J. R. & FRINGER, O. B. 2017 How we compute n matters to estimates of mixing in stratified flows. *J. Fluid Mech.* **831**, R2.
- BENNETTS, D. A. & HOSKINS, B. J. 1979 Conditional symmetric instability — A possible explanation for frontal rainbands. *Quart. J. Roy. Meteor. Soc.* **105**, 945–962.
- BROWN, S. A. 2002 A cloud resolving simulation of Hurricane Bob (1991): storm structure and eyewall buoyancy. *Mon. Wea. Rev.* **130**, 1573–1591.
- BUI, H. H., SMITH, R. K., MONTGOMERY, M. T. & CHENG, P. 2009 Balanced and unbalanced aspects of tropical cyclone intensification. *Q. J. Roy. Met. Soc.* **135**, 1715–1731.
- CODOBAN, S. & SHEPHERD, T. G. 2003 Energetics of a symmetric circulation including momentum constraints. *J. Atmos. Sci.* **60**, 2019–2028.
- CODOBAN, S. & SHEPHERD, T. G. 2006 On the available energy of an axisymmetric vortex. *Meteo. Zeitschrift* **15**, 401–407.
- CRONIN, T. W. & CHAVAS, D. R. 2019 Dry and semidry tropical cyclones. *J. Atmos. Sci.* **76**, 2193–2212.

- CULLEN, M. J. P., GANGBO, W. & SEDJRO, M. 2015 A mathematically rigorous analysis of forced axisymmetric flows in the atmosphere. *Q. J. R. Met. Soc.* **141**, 1836–1844.
- DRAZIN, P. G. & REID, W. H. 1981 *Hydrodynamic stability*. Cambridge University Press.
- EMANUEL, K. 1994 *Atmospheric Convection*. Oxford University Press.
- EMANUEL, K. A. 1983a On assessing local conditional symmetric instability from atmospheric soundings. *Mon. Wea. Rev.* **111**, 2016–2033.
- EMANUEL, K. A. 1983b The Lagrangian parcel dynamics of moist symmetric instability. *J. Atmos. Sci.* **40**, 2368–2376.
- EMANUEL, K. A. 1986 An air-sea interaction theory for tropical cyclones. Part I: Steady state maintenance. *J. Atmos. Sci.* **43**, 585–605.
- EMANUEL, K. A. 2000 A statistical analysis of tropical cyclone intensity. *Mon. Wea. Rev.* **128**, 1139–1152.
- EMANUEL, K. A. 2018 Chapter 15. 100 years of research in tropical cyclone research. *Meteorological Monographs* **59**, 15.1–15.68.
- GILBERT, A. D. & VANNESTE, J. 2018 Geometric generalised Lagrangian-mean theories. *J. Fluid Mech.* **839**, 95–134.
- HARRIS, B. L. & TAILLEUX, R. 2018 Assessment of algorithms for computing moist available potential energy. *Q. J. Roy. Met. Soc.* **144**, 1501–1510.
- HAYNES, P. H. 1988 Forced, dissipative generalizations of finite-amplitude wave action conservation relations for zonal and nonzonal basic flows. *J. Atmos. Sci.* **45**, 2352–2362.
- HIERONYMUS, M. & NYCANDER, J. 2015 Finding the minimum potential energy state by adiabatic parcel rearrangements with a nonlinear equation of state: an exact solution in polynomial time. *J. Phys. Oceanogr.* **45**, 1843–1857.
- HOLLIDAY, D. & MCINTYRE, M. E. 1981 On potential energy density in an incompressible, stratified fluid. *J. Fluid Mech.* **107**, 221–225.
- ILIN, K. I. 1991 Stability of a baroclinic vortex. *Izvestiya Atmos. Ocean. Phys.* **27**, 403–406.
- LORENZ, E. N. 1955 Available potential energy and the maintenance of the general circulation. *Tellus* **7**, 138–157.
- MARKOWSKI, P. & RICHARDSON, Y. 2010 *Mesoscale Meteorology in Midlatitudes*. Wiley-Blackwell.
- MCDUGALL, T. J. 1987 Neutral surfaces. *J. Phys. Oceanogr.* **17**, 1950–1964.
- METHVEN, J. & BERRISFORD, P. 2015 The slowly evolving state of the atmosphere. *Q. J. Roy. Met. Soc.* **141**, 2237–2258.
- MONCRIEFF, M. W. & MILLER, M. J. 1976 The dynamics and simulation of tropical cumulonimbus and squall lines. *Q. J. Roy. Met. Soc.* **102**, 373–374.
- MROWIEC, A. A., GARNER, S. T. & PAULUIS, O. M. 2011 Axisymmetric hurricane in a dry atmosphere: theoretical framework and numerical experiments. *J. Atmos. Sci.* **68**, 1607–1618.
- NOLAN, D. S. & MONTGOMERY, M. T. 2002 Nonhydrostatic, three-dimensional perturbations to balanced, hurricane-like vortices. Part I: Linearized formulation, stability, and evolution. *J. Atmos. Sci.* **59** (21), 2989–3020.
- NOVAK, L. & TAILLEUX, R. 2018 On the local view of atmospheric available potential energy. *J. Atmos. Sci.* **75** (6), 1891–1907.
- NYCANDER, J. 2011 Energy conversion, mixing energy, and neutral surfaces with a nonlinear equation of state. *J. Phys. Oceanogr.* **41**, 28–41.
- RAYLEIGH, LORD 1916 On the dynamics of revolving fluids. *Proc. R. Soc. A.* **93**, 148–154.
- SAENZ, J. A., TAILLEUX, R., BUTLER, E. D., HUGHES, G. O. & OLIVER, K. I. C. 2015 Estimating lorenz’s reference state in an ocean with a nonlinear equation of state for seawater. *J. Phys. Oceanogr.* **45**, 1242–1257.
- SCOTTI, A. & PASSAGIA, P. Y. 2019 Diagnosing the diabatic effects on the available energy of stratified flows in inertial and non-inertial frames. *J. Fluid Mech.* **861**, 608–642.
- SCOTTI, A. & WHITE, B. 2014 Diagnosing mixing in stratified turbulent flows with a locally defined available potential energy. *J. Fluid Mech.* **740**, 114–135.
- SHEPHERD, T. G. 1993 A unified theory of available potential energy. *Atmosphere-Ocean* **31**, 1–26.
- SMITH, R. K. 2006 Accurate determination of a balanced axisymmetric vortex in a compressible atmosphere. *Tellus* **58A**, 98–103.

Available energy including momentum constraints and eddy energy 23

- SMITH, R. K., MONTGOMERY, M. T. & KILROY, G. 2018 The generation of kinetic energy in tropical cyclones revisited. *Q. J. Roy. Met. Soc.* **144**, 1–9.
- SMITH, R. K., MONTGOMERY, M. T. & ZHU, H. 2005 Buoyancy in tropical cyclones and other rapidly rotating atmospheric vortices. *Dyn. Atm. Ocean* **40**, 189–208.
- STANSIFER, E. M., O’GORMAN, P. A. & HOLT, J. I. 2017 Accurate computation of moist available potential energy with the Munkres algorithm. *Q. J. Roy. Met. Soc.* **143**, 288–292.
- TAILLEUX, R. 2013 Available potential energy density for a multicomponent boussinesq fluid with a nonlinear equation of state. *J. Fluid Mech.* **735**, 499–518.
- TAILLEUX, R. 2016 Neutrality versus materiality: a thermodynamic theory of neutral surfaces. *Fluids* **1** (32).
- TAILLEUX, R. 2018 Local available energetics of multicomponent compressible stratified fluids. *J. Fluid Mech.* **842** (R1).
- THORPE, A. J., HOSKINS, B. J. & INNOCENTI, V. 1989 The parcel method in a baroclinic atmosphere. *J. Atmos. Sci.* **46**, 1274–1284.
- THORPE, S. 1977 Turbulent and mixing in a scottish loch. *Philos. Trans. R. Soc. London. Ser. A* **286**, 125–181.
- TURNER, J. S. 1973 *Buoyancy effects in fluids*. Cambridge University Press.
- WONG, K. C., TAILLEUX, R. & GRAY, S. L. 2016 The computation of reference state and ape production by diabatic processes in an idealized tropical cyclone. *Q. J. R. Meteorol. Soc.* **142**, 2646–2657.
- ZHANG, D.-L., LIU, Y. & YAU, M. K. 2000 A multiscale numerical study of Hurricane Andrew (1992). Part III. Dynamically induced vertical motion. *Mon. Wea. Rev.* **128**, 3772–3788.

References

- Ahbe, E. and K. Caldeira, 2017: Spatial Distribution of Generation of Lorenz’s Available Potential Energy in a Global Climate Model. *Journal of Climate*, **30**, 2089–2101, doi:10.1175/JCLI-D-15-0614.1.
- Ambaum, M. H. P., 2010: *Thermal Physics of the Atmosphere*. Wiley-Blackwell, Chichester, UK, 239 pp.
- Andreas, E. L. and K. A. Emanuel, 2001: Effects of Sea Spray on Tropical Cyclone Intensity. *Journal of the Atmospheric Sciences*, **58**, 3741–3751, doi:10.1175/1520-0469(2001)058<3741:EOSSOT>2.0.CO;2.
- Andrews, D. G., 1981: A note on potential energy density in a stratified compressible fluid. *Journal of Fluid Mechanics*, **107**, 227, doi:10.1017/S0022112081001754.
- 2006: On the available energy density for axisymmetric motions of a compressible stratified fluid. *Journal of Fluid Mechanics*, **569**, 481–492, doi:10.1017/S0022112006002680.
- Andrews, D. G. and M. E. McIntyre, 1976: Planetary Waves in Horizontal and Vertical Shear: The Generalized Eliassen-Palm Relation and the Mean Zonal Acceleration. *Journal of the Atmospheric Sciences*, **33**, 2031–2048, doi:10.1175/1520-0469(1976)033<2031:PWIHAV>2.0.CO;2.
- 1978a: An exact theory of nonlinear waves on a Lagrangian-mean flow. *Journal of Fluid Mechanics*, **89**, 609–646, doi:10.1017/S0022112078002773.
- 1978b: Generalized Eliassen-Palm and Charney-Drazin Theorems for Waves on Axisymmetric Mean Flows in Compressible Atmospheres. *Journal of the Atmospheric Sciences*, **35**, 175–185, doi:10.1175/1520-0469(1978)035<0175:gepacd>2.0.co;2.
- Anthes, R. A., 1974: The dynamics and energetics of mature tropical cyclones. *Reviews of Geophysics*, **12**, 495, doi:10.1029/RG012i003p00495.
- Anthes, R. A. and D. R. Johnson, 1968: Generation of Available Potential Energy in Hurricane Hilda (1964). *Monthly Weather Review*, **96**, 291–302, doi:10.1175/1520-0493(1968)096<0291:GOAPEI>2.0.CO;2.
- Bacmeister, J. T., K. A. Reed, C. Hannay, P. Lawrence, S. Bates, J. E. Truesdale, N. Rosenbloom, and M. Levy, 2018: Projected changes in tropical cyclone activity under future warming scenarios using a high-resolution climate model. *Climatic Change*, **146**, 547–560, doi:10.1007/s10584-016-1750-x.
- Balaguru, K., G. R. Foltz, L. R. Leung, E. D’Asaro, K. A. Emanuel, H. Liu, and S. E. Zedler, 2015: Dynamic Potential Intensity: An improved representation of the ocean’s impact on tropical cyclones. *Geophysical Research Letters*, **42**, 6739–6746, doi:10.1002/2015GL064822.
- Bannon, P. R., 2003: Hamiltonian Description of Idealized Binary Geophysical Fluids. *Journal of the Atmospheric Sciences*, **60**, 2809–2819, doi:10.1175/1520-0469(2003)060<2809:HDOIBG>2.0.CO;2.
- 2005: Eulerian Available Energetics in Moist Atmospheres. *Journal of the Atmospheric Sciences*, **62**, 4238–4252, doi:10.1175/JAS3516.1.

- Bass, B., J. N. Irza, J. Proft, P. Bedient, and C. Dawson, 2017: Fidelity of the integrated kinetic energy factor as an indicator of storm surge impacts. *Natural Hazards*, **85**, 575–595, doi:10.1007/s11069-016-2587-3.
- Bell, M. M. and M. T. Montgomery, 2008: Observed Structure, Evolution, and Potential Intensity of Category 5 Hurricane Isabel (2003) from 12 to 14 September. *Monthly Weather Review*, **136**, 2023–2046, doi:10.1175/2007MWR1858.1.
- 2010: Sheared deep vortical convection in pre-depression Hagupit during TCS08. *Geophysical Research Letters*, **37**, L06802, doi:10.1029/2009GL042313.
- Bell, M. M., M. T. Montgomery, and K. A. Emanuel, 2012: Air-Sea Enthalpy and Momentum Exchange at Major Hurricane Wind Speeds Observed during CBLAST. *Journal of the Atmospheric Sciences*, **69**, 3197–3222, doi:10.1175/JAS-D-11-0276.1.
- Bell, R., J. Strachan, P. L. Vidale, K. Hodges, and M. Roberts, 2013: Response of Tropical Cyclones to Idealized Climate Change Experiments in a Global High-Resolution Coupled General Circulation Model. *Journal of Climate*, **26**, 7966–7980, doi:10.1175/JCLI-D-12-00749.1.
- Bhalachandran, S., D. R. Chavas, F. D. Marks, S. Dubey, A. Shreevastava, and T. N. Krishnamurti, 2019: Characterizing the Energetics of Vortex-Scale and Sub-Vortex-Scale Asymmetries during Tropical Cyclone Rapid Intensity Changes. *Journal of the Atmospheric Sciences*, doi:10.1175/JAS-D-19-0067.1.
- Bhatia, K., G. Vecchi, H. Murakami, S. Underwood, and J. Kossin, 2018: Projected Response of Tropical Cyclone Intensity and Intensification in a Global Climate Model. *Journal of Climate*, **31**, 8281–8303, doi:10.1175/JCLI-D-17-0898.1.
- Bister, M. and K. A. Emanuel, 1998: Dissipative heating and hurricane intensity. *Meteorology and Atmospheric Physics*, **65**, 233–240, doi:10.1007/BF01030791.
- 2002: Low frequency variability of tropical cyclone potential intensity 1. Interannual to interdecadal variability. *Journal of Geophysical Research*, **107**, 4801, doi:10.1029/2001JD000776.
- Braun, S. A. and W.-K. Tao, 2000: Sensitivity of High-Resolution Simulations of Hurricane Bob (1991) to Planetary Boundary Layer Parameterizations. *Monthly Weather Review*, **128**, 3941–3961, doi:10.1175/1520-0493(2000)129<3941:SOHRSO>2.0.CO;2.
- Bryan, G. H. and J. M. Fritsch, 2002: A Benchmark Simulation for Moist Nonhydrostatic Numerical Models. *Monthly Weather Review*, **130**, 2917–2928, doi:10.1175/1520-0493(2002)130<2917:ABSFMN>2.0.CO;2.
- Bryan, G. H. and R. Rotunno, 2009a: Evaluation of an Analytical Model for the Maximum Intensity of Tropical Cyclones. *Journal of the Atmospheric Sciences*, **66**, 3042–3060, doi:10.1175/2009JAS3038.1.
- 2009b: The Maximum Intensity of Tropical Cyclones in Axisymmetric Numerical Model Simulations. *Monthly Weather Review*, **137**, 1770–1789, doi:10.1175/2008MWR2709.1.
- Bui, H. H., R. K. Smith, M. T. Montgomery, and J. Peng, 2009: Balanced and unbalanced aspects of tropical cyclone intensification. *Quarterly Journal of the Royal Meteorological Society*, **135**, 1715–1731, doi:10.1002/qj.502.

- Camargo, S. J., A. H. Sobel, A. G. Barnston, and K. A. Emanuel, 2007: Tropical cyclone genesis potential index in climate models. *Tellus, Series A: Dynamic Meteorology and Oceanography*, **59 A**, 428–443, doi:10.1111/j.1600-0870.2007.00238.x.
- Camp, J., M. Roberts, C. MacLachlan, E. Wallace, L. Hermanson, A. Brookshaw, A. Arribas, and A. A. Scaife, 2015: Seasonal forecasting of tropical storms using the Met Office GloSea5 seasonal forecast system. *Quarterly Journal of the Royal Meteorological Society*, **141**, 2206–2219, doi:10.1002/qj.2516.
- Cangialosi, J. P., 2019: National Hurricane Center Forecast Verification Report: 2018 Hurricane Season. Technical report, National Oceanic and Atmospheric Administration. URL https://www.nhc.noaa.gov/verification/pdfs/Verification_2018.pdf
- Chan, K. T. and J. C. Chan, 2016: Sensitivity of the simulation of tropical cyclone size to microphysics schemes. *Advances in Atmospheric Sciences*, **33**, 1024–1035, doi:10.1007/s00376-016-5183-2.
- Charney, J. and A. Eliassen, 1964: On the Growth of the Hurricane Depression. *Journal of the Atmospheric Sciences*, **21**, 68–75, doi:10.1175/1520-0469(1964)021<0068:OTGOTH>2.0.CO;2.
- Chen, J.-H. and S.-J. Lin, 2011: The remarkable predictability of inter-annual variability of Atlantic hurricanes during the past decade. *Geophysical Research Letters*, **38**, L11804, doi:10.1029/2011GL047629.
- 2013: Seasonal Predictions of Tropical Cyclones Using a 25-km-Resolution General Circulation Model. *Journal of Climate*, **26**, 380–398, doi:10.1175/JCLI-D-12-00061.1.
- Codoban, S. and T. G. Shepherd, 2003: Energetics of a Symmetric Circulation Including Momentum Constraints. *Journal of the Atmospheric Sciences*, **60**, 2019–2028, doi:10.1175/1520-0469(2003)060<2019:EOASCI>2.0.CO;2.
- 2006: On the available energy of an axisymmetric vortex. *Meteorologische Zeitschrift*, **15**, 401–407, doi:10.1127/0941-2948/2006/0143.
- Craig, G. C., 1995: Radiation and polar lows. *Quarterly Journal of the Royal Meteorological Society*, **121**, 79–94, doi:10.1002/qj.49712152105.
- 1996: Numerical experiments on radiation and tropical cyclones. *Quarterly Journal of the Royal Meteorological Society*, **122**, 415–422, doi:10.1002/qj.49712253006.
- Craig, G. C. and S. L. Gray, 1996: CISK or WISHE as the Mechanism for Tropical Cyclone Intensification. *Journal of the Atmospheric Sciences*, **53**, 3528–3540, doi:10.1175/1520-0469(1996)053<3528:COWATM>2.0.CO;2.
- Cronin, T. W. and D. R. Chavas, 2019: Dry and Semidry Tropical Cyclones. *Journal of the Atmospheric Sciences*, **76**, 2193–2212, doi:10.1175/JAS-D-18-0357.1.
- Cullen, M. J. P., W. Gangbo, and M. Sedjro, 2015: A mathematically rigorous analysis of forced axisymmetric flows in the atmosphere. *Quarterly Journal of the Royal Meteorological Society*, **141**, 1836–1844, doi:10.1002/qj.2487.
- Cengel, Y. A. and M. A. Boles, 2015: *Thermodynamics: an engineering approach*. McGraw-Hill, New York, 8th edition, 1115 pp.

- Davis, C., W. Wang, S. S. Chen, Y. Chen, K. Corbosiero, M. DeMaria, J. Dudhia, G. Holland, J. Klemp, J. Michalakes, H. Reeves, R. Rotunno, C. Snyder, and Q. Xiao, 2008: Prediction of Landfalling Hurricanes with the Advanced Hurricane WRF Model. *Monthly Weather Review*, **136**, 1990–2005, doi:10.1175/2007MWR2085.1.
- Davis, C. A., 2018: Resolving Tropical Cyclone Intensity in Models. *Geophysical Research Letters*, **45**, 2082–2087, doi:10.1002/2017GL076966.
- DeMaria, M. and J. Kaplan, 1994: A Statistical Hurricane Intensity Prediction Scheme (SHIPS) for the Atlantic Basin. *Weather and Forecasting*, **9**, 209–220, doi:10.1175/1520-0434(1994)009<0209:ASHIPS>2.0.CO;2.
- DeMaria, M., C. R. Sampson, J. A. Knaff, and K. D. Musgrave, 2014: Is Tropical Cyclone Intensity Guidance Improving? *Bulletin of the American Meteorological Society*, **95**, 387–398, doi:10.1175/BAMS-D-12-00240.1.
- Didlake, A. C., P. D. Reasor, R. F. Rogers, and W.-C. Lee, 2018: Dynamics of the Transition from Spiral Rainbands to a Secondary Eyewall in Hurricane Earl (2010). *Journal of the Atmospheric Sciences*, **75**, 2909–2929, doi:10.1175/JAS-D-17-0348.1.
- Dudhia, J., 1993: A Nonhydrostatic Version of the Penn State–NCAR Mesoscale Model: Validation Tests and Simulation of an Atlantic Cyclone and Cold Front. *Monthly Weather Review*, **121**, 1493–1513, doi:10.1175/1520-0493(1993)121<1493:ANVOTP>2.0.CO;2.
- Dutton, J. A., 1973: The global thermodynamics of atmospheric motion. *Tellus*, **25**, 89–110, doi:10.3402/tellusa.v25i2.9647.
- Dutton, J. A. and D. R. Johnson, 1967: The Theory of Available Potential Energy and a Variational Approach to Atmospheric Energetics. *Advances in Geophysics*, **12**, 333–436, doi:10.1016/S0065-2687(08)60379-9.
- Eady, E. T., 1949: Long Waves and Cyclone Waves. *Tellus*, **1**, 33–52, doi:10.3402/tellusa.v1i3.8507.
- Edmon Jr, H. J., 1978: A Reexamination of Limited-Area Available Potential Energy Budget Equations. *Journal of the Atmospheric Sciences*, **35**, 1655–1659, doi:10.1175/1520-0469(1978)035<1655:arolaa>2.0.co;2.
- Edmon Jr, H. J. and D. G. Vincent, 1979: Large-Scale Atmospheric Conditions During the Intensification of Hurricane Carmen (1974) II. Diabatic Heating Rates and Energy Budgets. *Monthly Weather Review*, **107**, 295–313, doi:10.1175/1520-0493(1979)107<0295:LSACDT>2.0.CO;2.
- Eliassen, A., 1951: Slow thermally or frictionally controlled meridional circulation in a circular vortex. *Astrophysica Norvegica*, **5**, 19–60.
- Emanuel, K., 1986: An Air-Sea Interaction Theory for Tropical Cyclones. Part I: Steady-State Maintenance. *Journal of the Atmospheric Sciences*, **43**, 585–605, doi:10.1175/1520-0469(1986)043<0585:AASITF>2.0.CO;2.
- 2000: A Statistical Analysis of Tropical Cyclone Intensity. *Monthly Weather Review*, **128**, 1139–1152, doi:10.1175/1520-0493(2000)128<1139:ASAOTC>2.0.CO;2.
- 2003: Tropical Cyclones. *Annual Review of Earth and Planetary Sciences*, **31**, 75–104, doi:10.1146/annurev.earth.31.100901.141259.

- 2012: Self-Stratification of Tropical Cyclone Outflow. Part II: Implications for Storm Intensification. *Journal of the Atmospheric Sciences*, **69**, 988–996, doi:10.1175/JAS-D-11-0177.1.
- 2017: Will Global Warming Make Hurricane Forecasting More Difficult? *Bulletin of the American Meteorological Society*, **98**, 495–501, doi:10.1175/BAMS-D-16-0134.1.
- 2018: 100 Years of Progress in Tropical Cyclone Research. *Meteorological Monographs*, **59**, 1–15, doi:10.1175/AMSMONOGRAPHS-D-18-0016.1.
- Emanuel, K. A., 1987: The dependence of hurricane intensity on climate. *Nature*, **326**, 483–485, doi:10.1038/326483a0.
- 1988: The Maximum Intensity of Hurricanes. *Journal of the Atmospheric Sciences*, **45**, 1143–1155, doi:10.1175/1520-0469(1988)045<1143:TMIOH>2.0.CO;2.
- 1989: The Finite-Amplitude Nature of Tropical Cyclogenesis. *Journal of the Atmospheric Sciences*, **46**, 3431–3456, doi:10.1175/1520-0469(1989)046<3431:TFANOT>2.0.CO;2.
- 1994: *Atmospheric Convection*. Oxford University Press, Oxford.
- 1995: Sensitivity of Tropical Cyclones to Surface Exchange Coefficients and a Revised Steady-State Model Incorporating Eye Dynamics. *Journal of the Atmospheric Sciences*, **52**, 3969–3976, doi:10.1175/1520-0469(1995)052<3969:SOTCTS>2.0.CO;2.
- 1997: Some Aspects of Hurricane Inner-Core Dynamics and Energetics. *Journal of the Atmospheric Sciences*, **54**, 1014–1026, doi:10.1175/1520-0469(1997)054<1014:SAOHIC>2.0.CO;2.
- Emanuel, K. A., J. David Neelin, and C. S. Bretherton, 1994: On large-scale circulations in convecting atmospheres. *Quarterly Journal of the Royal Meteorological Society*, **120**, 1111–1143, doi:10.1002/qj.49712051902.
- Emanuel, K. A. and R. Rotunno, 1989: Polar lows as arctic hurricanes. *Tellus*, **41A**, 1–17, doi:10.3402/tellusa.v41i1.11817.
- Frank, W. M., 1977: The Structure and Energetics of the Tropical Cyclone II. Dynamics and Energetics. *Monthly Weather Review*, **105**, 1136–1150, doi:10.1175/1520-0493(1977)105<1136:TSAEOT>2.0.CO;2.
- Fritz, C. and Z. Wang, 2014: Water Vapor Budget in a Developing Tropical Cyclone and Its Implication for Tropical Cyclone Formation. *Journal of the Atmospheric Sciences*, **71**, 4321–4332, doi:10.1175/JAS-D-13-0378.1.
- Gall, R., J. Franklin, F. Marks, E. N. Rappaport, and F. Toepfer, 2013: The Hurricane Forecast Improvement Project. *Bulletin of the American Meteorological Society*, **94**, 329–343, doi:10.1175/BAMS-D-12-00071.1.
- Garner, S., 2015: The Relationship between Hurricane Potential Intensity and CAPE. *Journal of the Atmospheric Sciences*, **72**, 141–163, doi:10.1175/JAS-D-14-0008.1.
- Gertler, C. G. and P. A. O’Gorman, 2019: Changing available energy for extratropical cyclones and associated convection in Northern Hemisphere summer. *Proceedings of the National Academy of Sciences of the United States of America*, **116**, 4105–4110, doi:10.1073/pnas.1812312116.

- Gettelman, A., D. N. Bresch, C. C. Chen, J. E. Truesdale, and J. T. Bacmeister, 2018: Projections of future tropical cyclone damage with a high-resolution global climate model. *Climatic Change*, **146**, 575–585, doi:10.1007/s10584-017-1902-7.
- Gill, A. E., 1982: *Atmosphere-ocean dynamics*. Academic Press, 662 pp.
- Golding, B. W., 1993: A Numerical Investigation of Tropical Island Thunderstorms. *Monthly Weather Review*, **121**, 1417–1433, doi:10.1175/1520-0493(1993)121<1417:ANIOTI>2.0.CO;2.
- Gouy, G., 1889: Sur l'énergie utilisable. *Journal de Physique Théorique et Appliquée*, **8**, 501–518, doi:10.1051/jphysap:018890080050101.
- Gray, W. M., 1968: A Global View of the Origin of Tropical Disturbances and Storms. *Monthly Weather Review*, **96**, 669–700, doi:10.1175/1520-0493(1968)096<0669:GVOTOO>2.0.CO;2.
- Green, B. W. and F. Zhang, 2013: Impacts of Air-Sea Flux Parameterizations on the Intensity and Structure of Tropical Cyclones. *Monthly Weather Review*, **141**, 2308–2324, doi:10.1175/MWR-D-12-00274.1.
- 2014: Sensitivity of Tropical Cyclone Simulations to Parametric Uncertainties in Air-Sea Fluxes and Implications for Parameter Estimation. *Monthly Weather Review*, **142**, 2290–2308, doi:10.1175/MWR-D-13-00208.1.
- Gualdi, S., E. Scoccimarro, and A. Navarra, 2008: Changes in Tropical Cyclone Activity due to Global Warming: Results from a High-Resolution Coupled General Circulation Model. *Journal of Climate*, **21**, 5204–5228, doi:10.1175/2008JCLI1921.1.
- Hack, J. J. and W. H. Schubert, 1986: Nonlinear Response of Atmospheric Vortices to Heating by Organized Cumulus Convection. *Journal of the Atmospheric Sciences*, **43**, 1559–1573, doi:10.1175/1520-0469(1986)043<1559:NROAVT>2.0.CO;2.
- Hartmann, D. L., J. R. Holton, and Q. Fu, 2001: The heat balance of the tropical tropopause, cirrus, and stratospheric dehydration. *Geophysical Research Letters*, **28**, 1969–1972, doi:10.1029/2000GL012833.
- Hausman, S. A., 2001: *Formulation and Sensitivity Analysis of a Nonhydrostatic, Axisymmetric Tropical Cyclone Model*. Ph.D. thesis, Colorado State University.
URL <https://apps.dtic.mil/sti/pdfs/ADA388258.pdf>
- Hawkins, H. F. and D. T. Rubsam, 1968: Hurricane Hilda, 1964 II. Structure and Budgets of the Hurricane on October 1, 1964. *Monthly Weather Review*, **96**, 617–636, doi:10.1175/1520-0493(1968)096<0617:HH>2.0.CO;2.
- Haynes, P. H., 1988: Forced, Dissipative Generalizations of Finite-Amplitude Wave-Activity Conservation Relations for Zonal and Nonzonal Basic Flows. *Journal of the Atmospheric Sciences*, **45**, 2352–2362, doi:10.1175/1520-0469(1988)045<2352:FDGOFA>2.0.CO;2.
- Held, I. M. and M. Zhao, 2011: The Response of Tropical Cyclone Statistics to an Increase in CO₂ with Fixed Sea Surface Temperatures. *Journal of Climate*, **24**, 5353–5364, doi:10.1175/JCLI-D-11-00050.1.
- Hendricks, E. A., S. A. Braun, J. L. Vigh, and J. B. Courtney, 2019: A Summary of Research Advances on Tropical Cyclone Intensity Change from 2014–2018. *Tropical Cyclone Research and Review*, **8**, 219–225, doi:10.6057/2019TCRR04.02.

- Hendricks, E. A., M. T. Montgomery, and C. A. Davis, 2004: The Role of “Vortical” Hot Towers in the Formation of Tropical Cyclone Diana (1984). *Journal of the Atmospheric Sciences*, **61**, 1209–1232, doi:10.1175/1520-0469(2004)061<1209:TROVHT>2.0.CO;2.
- Hieronymus, M. and J. Nycander, 2015: Finding the Minimum Potential Energy State by Adiabatic Parcel Rearrangements with a Nonlinear Equation of State: An Exact Solution in Polynomial Time. *Journal of Physical Oceanography*, **45**, 1843–1857, doi:10.1175/JPO-D-14-0174.1.
- Hogsett, W. and D.-L. Zhang, 2009: Numerical Simulation of Hurricane Bonnie (1998). Part III: Energetics. *Journal of the Atmospheric Sciences*, **66**, 2678–2696, doi:10.1175/2009JAS3087.1.
- Holliday, D. and M. E. McIntyre, 1981: On potential energy density in an incompressible, stratified fluid. *Journal of Fluid Mechanics*, **107**, 221–225, doi:10.1017/S0022112081001742.
- Holloway, C. E. and J. D. Neelin, 2009: Moisture Vertical Structure, Column Water Vapor, and Tropical Deep Convection. *Journal of the Atmospheric Sciences*, **66**, 1665–1683, doi:10.1175/2008JAS2806.1.
- Houze Jr, R. A., S. S. Chen, B. F. Smull, W.-C. Lee, and M. M. Bell, 2007: Hurricane Intensity and Eyewall Replacement. *Science*, **315**, 1235–1239, doi:10.1126/science.1135650.
- Houze Jr, R. A., W.-C. Lee, and M. M. Bell, 2009: Convective Contribution to the Genesis of Hurricane Ophelia (2005). *Monthly Weather Review*, **137**, 2778–2800, doi:10.1175/2009MWR2727.1.
- Hu, Q., Y. Tawaye, and S. Feng, 2004: Variations of the Northern Hemisphere Atmospheric Energetics: 1948–2000. *Journal of Climate*, **17**, 1975–1986, doi:10.1175/1520-0442(2004)017<1975:VOTNHA>2.0.CO;2.
- Jin, H., M. S. Peng, Y. Jin, and J. D. Doyle, 2014: An Evaluation of the Impact of Horizontal Resolution on Tropical Cyclone Predictions Using COAMPS-TC. *Weather and Forecasting*, **29**, 252–270, doi:10.1175/WAF-D-13-00054.1.
- Johnson, D. R., 1970: The Available Potential Energy of Storms. *Journal of the Atmospheric Sciences*, **27**, 727–741, doi:10.1175/1520-0469(1970)027<0727:tapeos>2.0.co;2.
- Johnson, D. R. and W. K. Downey, 1982: On the energetics of open systems. *Tellus*, **34**, 458–470, doi:10.3402/tellusa.v34i5.10831.
- Jordan, C. L., 1958: Mean Soundings for the West Indies Area. *Journal of Meteorology*, **15**, 91–97, doi:10.1175/1520-0469(1958)015<0091:MSFTWI>2.0.CO;2.
- Judt, F. and S. S. Chen, 2016: Predictability and Dynamics of Tropical Cyclone Rapid Intensification Deduced from High-Resolution Stochastic Ensembles. *Monthly Weather Review*, **144**, 4395–4420, doi:10.1175/MWR-D-15-0413.1.
- Kamieniecki, J. A., M. H. P. Ambaum, R. S. Plant, and S. J. Woolnough, 2018: The Implications of an Idealized Large-Scale Circulation for Mechanical Work Done by Tropical Convection. *Journal of the Atmospheric Sciences*, **75**, 2533–2547, doi:10.1175/JAS-D-17-0314.1.
- Kaplan, J. and M. DeMaria, 2003: Large-Scale Characteristics of Rapidly Intensifying Tropical Cyclones in the North Atlantic Basin. *Weather and Forecasting*, **18**, 1093–1108, doi:10.1175/1520-0434(2003)018<1093:LCORIT>2.0.CO;2.

- Kaplan, J., M. DeMaria, and J. A. Knaff, 2010: A Revised Tropical Cyclone Rapid Intensification Index for the Atlantic and Eastern North Pacific Basins. *Weather and Forecasting*, **25**, 220–241, doi:10.1175/2009WAF2222280.1.
- Karlsson, S., 1990: *Energy, entropy and exergy in the atmosphere*. Ph.D. thesis, Chalmers University of Technology.
URL <http://publications.lib.chalmers.se/records/fulltext/175950/175950.pdf>
- Kenney, S. E. and P. J. Smith, 1983: On The Release of Eddy Available Potential Energy in an Extratropical Cyclone System. *Monthly Weather Review*, **111**, 745–755, doi:10.1175/1520-0493(1983)111<0745:OTROEA>2.0.CO;2.
- Kent, J., J. P. Whitehead, C. Jablonowski, and R. B. Rood, 2014: Determining the effective resolution of advection schemes. Part I: Dispersion analysis. *Journal of Computational Physics*, **278**, 485–496, doi:10.1016/j.jcp.2014.01.043.
- Kilroy, G., R. K. Smith, and M. T. Montgomery, 2016: Why Do Model Tropical Cyclones Grow Progressively in Size and Decay in Intensity after Reaching Maturity? *Journal of the Atmospheric Sciences*, **73**, 487–503, doi:10.1175/JAS-D-15-0157.1.
- Kim, D., Y. Moon, S. J. Camargo, A. A. Wing, A. H. Sobel, H. Murakami, G. A. Vecchi, M. Zhao, and E. Page, 2018: Process-Oriented Diagnosis of Tropical Cyclones in High-Resolution GCMs. *Journal of Climate*, **31**, 1685–1702, doi:10.1175/JCLI-D-17-0269.1.
- Kim, D., A. H. Sobel, A. D. Del Genio, Y. Chen, S. J. Camargo, M.-S. Yao, M. Kelley, and L. Nazarenko, 2012: The Tropical Subseasonal Variability Simulated in the NASA GISS General Circulation Model. *Journal of Climate*, **25**, 4641–4659, doi:10.1175/JCLI-D-11-00447.1.
- Kim, H.-S., G. A. Vecchi, T. R. Knutson, W. G. Anderson, T. L. Delworth, A. Rosati, F. Zeng, and M. Zhao, 2014: Tropical Cyclone Simulation and Response to CO₂ Doubling in the GFDL CM2.5 High-Resolution Coupled Climate Model. *Journal of Climate*, **27**, 8034–8054, doi:10.1175/JCLI-D-13-00475.1.
- Klaver, R., R. Haarsma, P. L. Vidale, and W. Hazeleger, 2020: Effective resolution in high resolution global atmospheric models for climate studies. *Atmospheric Science Letters*, 1–8, doi:10.1002/asl.952.
- Kleinschmidt, E., 1951: Grundlagen einer Theorie der tropischen Zyklonen. *Archiv für Meteorologie, Geophysik und Bioklimatologie Serie A*, **4**, 53–72, doi:10.1007/BF02246793.
- Klemp, J. B. and R. B. Wilhelmson, 1978: The Simulation of Three-Dimensional Convective Storm Dynamics. *Journal of the Atmospheric Sciences*, **35**, 1070–1096, doi:10.1175/1520-0469(1978)035<1070:TSOTDC>2.0.CO;2.
- Kossin, J. P., 2015: Hurricane Wind-Pressure Relationship and Eyewall Replacement Cycles. *Weather and Forecasting*, **30**, 177–181, doi:10.1175/WAF-D-14-00121.1.
- Kossin, J. P. and M. Sitkowski, 2012: Predicting Hurricane Intensity and Structure Changes Associated with Eyewall Replacement Cycles. *Weather and Forecasting*, **27**, 484–488, doi:10.1175/WAF-D-11-00106.1.
- Kucharski, F., 1997: On the concept of exergy and available potential energy. *Quarterly Journal of the Royal Meteorological Society*, **123**, 2141–2156, doi:10.1002/qj.49712354317.

- 2001: The interpretation of available potential energy as exergy applied to layers of a stratified atmosphere. *Exergy, An International Journal*, **1**, 25–30, doi:10.1016/S1164-0235(01)00006-1.
- Kucharski, F. and A. J. Thorpe, 2000: Local Energetics of an Idealized Baroclinic Wave Using Extended Exergy. *Journal of the Atmospheric Sciences*, **57**, 3272–3284, doi:10.1175/1520-0469(2000)057<3272:LEOAIB>2.0.CO;2.
- Kurihara, Y., 1975: Budget Analysis of a Tropical Cyclone Simulated in an Axisymmetric Numerical Model. *Journal of the Atmospheric Sciences*, **32**, 25–59, doi:10.1175/1520-0469(1975)032<0025:BAOATC>2.0.CO;2.
- Landau, L. D. and E. M. Lifshitz, 1980: *Statistical Physics*. Pergamon Press, Oxford, 3rd edition.
- Langtangen, H., 2016: *A primer on scientific programming with Python*. Springer, Berlin, 5th edition.
- Lee, C.-Y., M. K. Tippett, A. H. Sobel, and S. J. Camargo, 2016: Rapid intensification and the bimodal distribution of tropical cyclone intensity. *Nature Communications*, **7**, 10625, doi:10.1038/ncomms10625.
- Lee, M. and T. Frisius, 2018: On the role of convective available potential energy (CAPE) in tropical cyclone intensification. *Tellus*, **70A**, 1–18, doi:10.1080/16000870.2018.1433433.
- Li, L., A. P. Ingersoll, X. Jiang, D. Feldman, and Y. L. Yung, 2007: Lorenz energy cycle of the global atmosphere based on reanalysis datasets. *Geophysical Research Letters*, **34**, L16813, doi:10.1029/2007GL029985.
- Lilly, D. K., 1964: Numerical Solutions for the Shape-Preserving Two-Dimensional Thermal Convection Element. *Journal of the Atmospheric Sciences*, **21**, 83–98, doi:10.1175/1520-0469(1964)021<0083:NSFTSP>2.0.CO;2.
- 1965: On the Computational Stability of Numerical Solutions of Time-Dependent Non-Linear Geophysical Fluid Dynamics Problems. *Monthly Weather Review*, **93**, 11–25, doi:10.1175/1520-0493(1965)093<0011:OTCSO>2.3.CO;2.
- Lim, Y.-K., S. D. Schubert, O. Reale, M.-I. Lee, A. M. Molod, and M. J. Suarez, 2015: Sensitivity of Tropical Cyclones to Parameterized Convection in the NASA GEOS-5 Model. *Journal of Climate*, **28**, 551–573, doi:10.1175/JCLI-D-14-00104.1.
- Lin, I.-I., P. Black, J. F. Price, C.-Y. Yang, S. S. Chen, C.-C. Lien, P. Harr, N.-H. Chi, C.-C. Wu, and E. A. D’Asaro, 2013: An ocean coupling potential intensity index for tropical cyclones. *Geophysical Research Letters*, **40**, 1878–1882, doi:10.1002/grl.50091.
- Lord, S. J., H. E. Willoughby, and J. M. Piotrowicz, 1984: Role of a Parameterized Ice-Phase Microphysics in an Axisymmetric, Nonhydrostatic Tropical Cyclone Model. *Journal of the Atmospheric Sciences*, **41**, 2836–2848, doi:10.1175/1520-0469(1984)041<2836:ROAPIP>2.0.CO;2.
- Lorenz, E. N., 1955: Available potential energy and the maintenance of the general circulation. *Tellus*, **7**, 157–167, doi:10.3402/tellusa.v7i2.8796.
- 1978: Available energy and the maintenance of a moist circulation. *Tellus*, **30**, 15–31, doi:10.3402/tellusa.v30i1.10308.

- 1979: Numerical evaluation of moist available energy. *Tellus*, **31**, 230–235, doi:10.3402/tellusa.v31i3.10429.
- MacCready, P. and S. N. Giddings, 2016: The Mechanical Energy Budget of a Regional Ocean Model. *Journal of Physical Oceanography*, **46**, 2719–2733, doi:10.1175/JPO-D-16-0086.1.
- Magnusson, L., J.-R. Bidlot, M. Bonavita, A. R. Brown, P. A. Browne, G. De Chiara, M. Dahoui, S. T. K. Lang, T. McNally, K. S. Mogensen, F. Pappenberger, F. Prates, F. Rabier, D. S. Richardson, F. Vitart, and S. Malardel, 2019: ECMWF Activities for Improved Hurricane Forecasts. *Bulletin of the American Meteorological Society*, **100**, 445–458, doi:10.1175/BAMS-D-18-0044.1.
- Malkus, J. S. and H. Riehl, 1960: On the dynamics and energy transformations in steady-state hurricanes. *Tellus*, **12**, 1–20, doi:10.3402/tellusa.v12i1.9351.
- Manganello, J. V., K. I. Hodges, J. L. Kinter, B. A. Cash, L. Marx, T. Jung, D. Achuthavarier, J. M. Adams, E. L. Altshuler, B. Huang, E. K. Jin, C. Stan, P. Towers, and N. Wedi, 2012: Tropical Cyclone Climatology in a 10-km Global Atmospheric GCM: Toward Weather-Resolving Climate Modeling. *Journal of Climate*, **25**, 3867–3893, doi:10.1175/JCLI-D-11-00346.1.
- Margules, M., 1903: Über die Energie der Stürme. *Jahrbücher der Kaiserlich-Königliche Zentralanstalt für Meteorologie und Erdmagnetismus*, translation by C. Abbe in Smithsonian Miscellaneous Collections, **51**, 1910.
- Marks, F. D., L. K. Shay, and PDT-5, 1998: Landfalling Tropical Cyclones: Forecast Problems and Associated Research Opportunities. *Bulletin of the American Meteorological Society*, **79**, 305–323, doi:10.1175/1520-0477(1998)079<0285:QPFROT>2.0.CO;2.
- Marquet, P., 1991: On the concept of exergy and available enthalpy: Application to atmospheric energetics. *Quarterly Journal of the Royal Meteorological Society*, **117**, 449–475, doi:10.1002/qj.49711749903.
- 1993: Exergy in meteorology: Definition and properties of moist available enthalpy. *Quarterly Journal of the Royal Meteorological Society*, **119**, 567–590, doi:10.1002/qj.49711951112.
- 2015: On the computation of moist-air specific thermal enthalpy. *Quarterly Journal of the Royal Meteorological Society*, **141**, 67–84, doi:10.1002/qj.2335.
- Marquet, P. and J.-F. Geleyn, 2015: Formulations of moist thermodynamics for atmospheric modelling. *Parameterization of Atmospheric Convection, Volume 2: Current Issues and New Theories*, R. S. Plant and J.-I. Yano, eds., World Scientific, Chapter 22, 221–274, doi:10.1142/9781783266913_0026, arXiv:1510.03239.
- Marsooli, R., N. Lin, K. Emanuel, and K. Feng, 2019: Climate change exacerbates hurricane flood hazards along US Atlantic and Gulf Coasts in spatially varying patterns. *Nature Communications*, **10**, 3785, doi:10.1038/s41467-019-11755-z.
- Mendelsohn, R., K. Emanuel, S. Chonabayashi, and L. Bakkensen, 2012: The impact of climate change on global tropical cyclone damage. *Nature Climate Change*, **2**, 205–209, doi:10.1038/nclimate1357.
- Merritt, E. S. and R. Wexler, 1967: Cirrus Canopies in Tropical Storms. *Monthly Weather Review*, **95**, 111–120, doi:10.1175/1520-0493(1967)095<0111:CCITS>2.3.CO;2.

- Methven, J., 2013: Wave Activity for Large-Amplitude Disturbances Described by the Primitive Equations on the Sphere. *Journal of the Atmospheric Sciences*, **70**, 1616–1630, doi:10.1175/JAS-D-12-0228.1.
- Montgomery, M. and R. Smith, 2014: Paradigms for tropical cyclone intensification. *Australian Meteorological and Oceanographic Journal*, **64**, 37–66.
- Montgomery, M. T., M. M. Bell, S. D. Aberson, and M. L. Black, 2006: Hurricane Isabel (2003): New Insights into the Physics of Intense Storms. Part I: Mean Vortex Structure and Maximum Intensity Estimates. *Bulletin of the American Meteorological Society*, **87**, 1335–1347, doi:10.1175/BAMS-87-10-1335.
- Montgomery, M. T., J. Persing, and R. K. Smith, 2015: Putting to rest WISHE-ful misconceptions for tropical cyclone intensification. *Journal of Advances in Modeling Earth Systems*, **7**, 92–109, doi:10.1002/2014MS000362.
- 2019: On the hypothesized outflow control of tropical cyclone intensification. *Quarterly Journal of the Royal Meteorological Society*, **145**, 1309–1322, doi:10.1002/qj.3479.
- Montgomery, M. T., N. V. Sang, R. K. Smith, and J. Persing, 2009: Do tropical cyclones intensify by WISHE? *Quarterly Journal of the Royal Meteorological Society*, **135**, 1697–1714, doi:10.1002/qj.459.
- Montgomery, M. T. and R. K. Smith, 2017: Recent Developments in the Fluid Dynamics of Tropical Cyclones. *Annual Review of Fluid Mechanics*, **49**, 541–574, doi:10.1146/annurev-fluid-010816-060022.
- Moon, Y., D. Kim, S. J. Camargo, A. A. Wing, A. H. Sobel, H. Murakami, K. A. Reed, E. Scoccimarro, G. A. Vecchi, M. F. Wehner, C. M. Zarzycki, and M. Zhao, 2019: Azimuthally Averaged Wind and Thermodynamic Structures of Tropical Cyclones in Global Climate Models and Their Sensitivity to Horizontal Resolution. *Journal of Climate*, doi:10.1175/JCLI-D-19-0172.1.
- Mrowiec, A. A., S. T. Garner, and O. M. Pauluis, 2011: Axisymmetric Hurricane in a Dry Atmosphere: Theoretical Framework and Numerical Experiments. *Journal of the Atmospheric Sciences*, **68**, 1607–1619, doi:10.1175/2011JAS3639.1.
- Munkres, J., 1957: Algorithms for the Assignment and Transportation Problems. *Journal of the Society for Industrial and Applied Mathematics*, **5**, 32–38, doi:10.1137/0105003.
- Murakami, H., R. Mizuta, and E. Shindo, 2012a: Future changes in tropical cyclone activity projected by multi-physics and multi-SST ensemble experiments using the 60-km-mesh MRI-AGCM. *Climate Dynamics*, **39**, 2569–2584, doi:10.1007/s00382-011-1223-x.
- Murakami, H., G. A. Vecchi, S. Underwood, T. L. Delworth, A. T. Wittenberg, W. G. Anderson, J. H. Chen, R. G. Gudgel, L. M. Harris, S. J. Lin, and F. Zeng, 2015: Simulation and Prediction of Category 4 and 5 Hurricanes in the High-Resolution GFDL HiFLOR Coupled Climate Model. *Journal of Climate*, **28**, 9058–9079, doi:10.1175/JCLI-D-15-0216.1.
- Murakami, H., G. A. Vecchi, G. Villarini, T. L. Delworth, R. Gudgel, S. Underwood, X. Yang, W. Zhang, and S.-J. Lin, 2016: Seasonal Forecasts of Major Hurricanes and Landfalling Tropical Cyclones using a High-Resolution GFDL Coupled Climate Model. *Journal of Climate*, **29**, 7977–7989, doi:10.1175/JCLI-D-16-0233.1.

- Murakami, H., Y. Wang, H. Yoshimura, R. Mizuta, M. Sugi, E. Shindo, Y. Adachi, S. Yukimoto, M. Hosaka, S. Kusunoki, T. Ose, and A. Kitoh, 2012b: Future Changes in Tropical Cyclone Activity Projected by the New High-Resolution MRI-AGCM. *Journal of Climate*, **25**, 3237–3260, doi:10.1175/JCLI-D-11-00415.1.
- Nichols, W. E. and R. H. Cuenca, 1993: Evaluation of the evaporative fraction for parameterization of the surface energy balance. *Water Resources Research*, **29**, 3681–3690, doi:10.1029/93WR01958.
- Nolan, D. S. and M. T. Montgomery, 2002: Nonhydrostatic, Three-Dimensional Perturbations to Balanced, Hurricane-like Vortices. Part I: Linearized Formulation, Stability, and Evolution. *Journal of the Atmospheric Sciences*, **59**, 2989–3020, doi:10.1175/1520-0469(2002)059<2989:NTDPTB>2.0.CO;2.
- Nolan, D. S., Y. Moon, and D. P. Stern, 2007: Tropical Cyclone Intensification from Asymmetric Convection: Energetics and Efficiency. *Journal of the Atmospheric Sciences*, **64**, 3377–3405, doi:10.1175/JAS3988.1.
- Novak, L. and R. Tailleux, 2018: On the Local View of Atmospheric Available Potential Energy. *Journal of the Atmospheric Sciences*, **75**, 1891–1907, doi:10.1175/JAS-D-17-0330.1.
- Nystrom, R. G., X. Chen, F. Zhang, and C. A. Davis, 2020: Nonlinear Impacts of Surface Exchange Coefficient Uncertainty on Tropical Cyclone Intensity and Air-Sea Interactions. *Geophysical Research Letters*, 2019GL085783, doi:10.1029/2019GL085783.
- O’Gorman, P. A., 2010: Understanding the varied response of the extratropical storm tracks to climate change. *Proceedings of the National Academy of Sciences of the United States of America*, **107**, 19176–80, doi:10.1073/pnas.1011547107.
- O’Gorman, P. A. and T. Schneider, 2008: Energy of Midlatitude Transient Eddies in Idealized Simulations of Changed Climates. *Journal of Climate*, **21**, 5797–5806, doi:10.1175/2008JCLI2099.1.
- Ooyama, K., 1969: Numerical Simulation of the Life Cycle of Tropical Cyclones. *Journal of the Atmospheric Sciences*, **26**, 3–40, doi:10.1175/1520-0469(1969)026<0003:NSOTLC>2.0.CO;2.
- 1982: Conceptual Evolution of the Theory and Modeling of the Tropical Cyclone. *Journal of the Meteorological Society of Japan*, **60**, 369–380, doi:10.2151/jmsj1965.60.1.369.
- Palmén, E. and C. L. Jordan, 1955: Note on the Release of Kinetic Energy in Tropical Cyclones. *Tellus*, **7**, 186–188, doi:10.3402/tellusa.v7i2.8793.
- Palmén, E. and H. Riehl, 1957: Budget of Angular Momentum and Energy in Tropical Cyclones. *Journal of Meteorology*, **14**, 150–159, doi:10.1175/1520-0469(1957)014<0150:BOAMAE>2.0.CO;2.
- Pauluis, O., 2007: Sources and Sinks of Available Potential Energy in a Moist Atmosphere. *Journal of the Atmospheric Sciences*, **64**, 2627–2641, doi:10.1175/JAS3937.1.
- 2011: Water Vapor and Mechanical Work: A Comparison of Carnot and Steam Cycles. *Journal of the Atmospheric Sciences*, **68**, 91–102, doi:10.1175/2010JAS3530.1.
- Pauluis, O. and I. M. Held, 2002a: Entropy Budget of an Atmosphere in Radiative-Convective Equilibrium. Part I: Maximum Work and Frictional Dissipation. *Journal of the Atmospheric Sciences*, **59**, 125–139, doi:10.1175/1520-0469(2002)059<0125:EBOAAI>2.0.CO;2.

- 2002b: Entropy Budget of an Atmosphere in Radiative-Convective Equilibrium. Part II: Latent Heat Transport and Moist Processes. *Journal of the Atmospheric Sciences*, **59**, 140–149, doi:10.1175/1520-0469(2002)059<0140:EBOAAI>2.0.CO;2.
- Pauluis, O. M., 2016: The Mean Air Flow as Lagrangian Dynamics Approximation and Its Application to Moist Convection. *Journal of the Atmospheric Sciences*, **73**, 4407–4425, doi:10.1175/JAS-D-15-0284.1.
- Pauluis, O. M. and F. Zhang, 2017: Reconstruction of Thermodynamic Cycles in a High-Resolution Simulation of a Hurricane. *Journal of the Atmospheric Sciences*, **74**, 3367–3381, doi:10.1175/JAS-D-16-0353.1.
- Pearce, R. P., 1978: On the concept of available potential energy. *Quarterly Journal of the Royal Meteorological Society*, **104**, 737–755, doi:10.1002/qj.49710444115.
- Peduzzi, P., B. Chatenoux, H. Dao, A. De Bono, C. Herold, J. Kossin, F. Mouton, and O. Nordbeck, 2012: Global trends in tropical cyclone risk. *Nature Climate Change*, **2**, 289–294, doi:10.1038/nclimate1410.
- Peng, J., L. Zhang, and Y. Zhang, 2015: On the Local Available Energetics in a Moist Compressible Atmosphere. *Journal of the Atmospheric Sciences*, **72**, 1551–1561, doi:10.1175/JAS-D-14-0181.1.
- Persing, J. and M. T. Montgomery, 2003: Hurricane Superintensity. *Journal of the Atmospheric Sciences*, **60**, 2349–2371, doi:10.1175/1520-0469(2003)060<2349:HS>2.0.CO;2.
- 2005: Is Environmental CAPE Important in the Determination of Maximum Possible Hurricane Intensity? *Journal of the Atmospheric Sciences*, **62**, 542–550, doi:10.1175/JAS-3370.1.
- Persing, J., M. T. Montgomery, J. C. McWilliams, and R. K. Smith, 2013: Asymmetric and axisymmetric dynamics of tropical cyclones. *Atmospheric Chemistry and Physics*, **13**, 12299–12341, doi:10.5194/acp-13-12299-2013.
- Pielke, R. A., J. Gratz, C. W. Landsea, D. Collins, M. A. Saunders, and R. Musulin, 2008: Normalized Hurricane Damage in the United States: 1900–2005. *Natural Hazards Review*, **9**, 29–42, doi:10.1061/(ASCE)1527-6988(2008)9:1(29).
- Powell, M. D. and T. A. Reinhold, 2007: Tropical Cyclone Destructive Potential by Integrated Kinetic Energy. *Bulletin of the American Meteorological Society*, **88**, 513–526, doi:10.1175/BAMS-88-4-513.
- Randall, D. A. and J. Wang, 1992: The Moist Available Energy of a Conditionally Unstable Atmosphere. *Journal of the Atmospheric Sciences*, **49**, 240–255, doi:10.1175/1520-0469(1992)049<0240:TMAEOA>2.0.CO;2.
- Rappaport, E. N., J. L. Franklin, L. A. Avila, S. R. Baig, J. L. Beven, E. S. Blake, C. A. Burr, J.-G. Jiing, C. A. Juckins, R. D. Knabb, C. W. Landsea, M. Mainelli, M. Mayfield, C. J. McAdie, R. J. Pasch, C. Sisko, S. R. Stewart, and A. N. Tribble, 2009: Advances and Challenges at the National Hurricane Center. *Weather and Forecasting*, **24**, 395–419, doi:10.1175/2008WAF2222128.1.
- Rappaport, E. N., J. G. Jiing, C. W. Landsea, S. T. Murilla, and J. L. Franklin, 2012: The Joint Hurricane Test Bed: Its First Decade of Tropical Cyclone Research-To-Operations Activities Reviewed. *Bulletin of the American Meteorological Society*, **93**, 371–380, doi:10.1175/BAMS-D-11-00037.1.

- Rathmann, N. M., S. Yang, and E. Kaas, 2014: Tropical cyclones in enhanced resolution CMIP5 experiments. *Climate Dynamics*, **42**, 665–681, doi:10.1007/s00382-013-1818-5.
- Raymond, D. J. and K. A. Emanuel, 1997: The Kuo Cumulus Parameterisation. *The Representation of Cumulus Convection in Numerical Models*, K. A. Emanuel and D. J. Raymond, eds., Meteorological Monograph No. 46, American Meteorological Society, Boston, MA, Chapter 12, 145–47, doi:10.1007/978-1-935704-13-3_12.
- Raymond, D. J. and C. López Carrillo, 2011: The vorticity budget of developing typhoon Nuri (2008). *Atmospheric Chemistry and Physics*, **11**, 147–163, doi:10.5194/acp-11-147-2011.
- Reasor, P. D., M. T. Montgomery, and L. F. Bosart, 2005: Mesoscale observations of the genesis of Hurricane Dolly (1996). *Journal of the Atmospheric Sciences*, **62**, 3151–3171, doi:10.1175/JAS3540.1.
- Reed, K. A., J. T. Bacmeister, N. A. Rosenbloom, M. F. Wehner, S. C. Bates, P. H. Lauritzen, J. E. Truesdale, and C. Hannay, 2015: Impact of the dynamical core on the direct simulation of tropical cyclones in a high-resolution global model. *Geophysical Research Letters*, **42**, 3603–3608, doi:10.1002/2015GL063974.
- Reed, K. A. and C. Jablonowski, 2011: Impact of physical parameterizations on idealized tropical cyclones in the Community Atmosphere Model. *Geophysical Research Letters*, **38**, L04805, doi:10.1029/2010GL046297.
- Riehl, H., 1950: A Model of Hurricane Formation. *Journal of Applied Physics*, **21**, 917–925, doi:10.1063/1.1699784.
- 1954: *Tropical Meteorology*. McGraw-Hill, New York, 392 pp.
- Riehl, H. and J. Malkus, 1961: Some Aspects of Hurricane Daisy, 1958. *Tellus*, **13**, 181–213, doi:10.3402/tellusa.v13i2.9495.
- Robert, A. J., 1966: The Integration of a Low Order Spectral Form of the Primitive Meteorological Equations. *Journal of the Meteorological Society of Japan*, **44**, 237–245, doi:10.2151/jmsj1965.44.5_237.
- Roberts, M. J., J. Camp, J. Seddon, P. L. Vidale, K. Hodges, B. Vanniere, J. Mecking, R. Haarsma, A. Bellucci, E. Scoccimarro, L.-P. Caron, F. Chauvin, L. Terray, S. Valcke, M.-P. Moine, D. Putrasahan, C. Roberts, R. Senan, C. Zarzycki, and P. Ullrich, 2020: Impact of model resolution on tropical cyclone simulation using the HighResMIP-PRIMAVERA multi-model ensemble. *Journal of Climate*, 19–0639, doi:10.1175/JCLI-D-19-0639.1.
- Roberts, M. J., P. L. Vidale, M. S. Mizielinski, M.-E. Demory, R. Schiemann, J. Strachan, K. Hodges, R. Bell, and J. Camp, 2015: Tropical Cyclones in the UPSCALE Ensemble of High-Resolution Global Climate Models. *Journal of Climate*, **28**, 574–596, doi:10.1175/JCLI-D-14-00131.1.
- Rodgers, E. B., S. W. Chang, and H. F. Pierce, 1994: A Satellite Observational and Numerical Study of Precipitation Characteristics in Western North Atlantic Tropical Cyclones. *Journal of Applied Meteorology*, **33**, 129–139, doi:10.1175/1520-0450(1994)033<0129:ASOANS>2.0.CO;2.
- Rodgers, E. B., W. S. Olson, V. M. Karyampudi, and H. F. Pierce, 1998: Satellite-Derived Latent Heating Distribution and Environmental Influences in Hurricane Opal (1995). *Monthly Weather Review*, **126**, 1229–1247, doi:10.1175/1520-0493(1998)126<1229:SDLHDA>2.0.CO;2.

- Roll, H. V., 1965: *Physics of the Marine Atmosphere*. Academic Press, New York, 426 pp.
- Rotunno, R. and K. Emanuel, 1987: An Air-Sea Interaction Theory for Tropical Cyclones. Part II: Evolutionary Study Using a Nonhydrostatic Axisymmetric Numerical Model. *Journal of the Atmospheric Sciences*, **44**, 542–561, doi:10.1175/1520-0469(1987)044<0542:AAITFT>2.0.CO;2.
- Rousseau-Rizzi, R. and K. Emanuel, 2019: An Evaluation of Hurricane Superintensity in Axisymmetric Numerical Models. *Journal of the Atmospheric Sciences*, **76**, 1697–1708, doi:10.1175/JAS-D-18-0238.1.
- Sabuwala, T., G. Gioia, and P. Chakraborty, 2015: Effect of rainpower on hurricane intensity. *Geophysical Research Letters*, **42**, 3024–3029, doi:10.1002/2015GL063785.
- Saenz, J. A., R. Tailleux, E. D. Butler, G. O. Hughes, and K. I. C. Oliver, 2015: Estimating Lorenz’s Reference State in an Ocean with a Nonlinear Equation of State for Seawater. *Journal of Physical Oceanography*, **45**, 1242–1257, doi:10.1175/JPO-D-14-0105.1.
- Schmidt, C. W. and R. K. Smith, 2016: Tropical cyclone evolution in a minimal axisymmetric model revisited. *Quarterly Journal of the Royal Meteorological Society*, **142**, 1505–1516, doi:10.1002/qj.2753.
- Schneider, T. and C. C. Walker, 2008: Scaling Laws and Regime Transitions of Macro-turbulence in Dry Atmospheres. *Journal of the Atmospheric Sciences*, **65**, 2153–2173, doi:10.1175/2007JAS2616.1.
- Schubert, W. H. and J. J. Hack, 1982: Inertial Stability and Tropical Cyclone Development. *Journal of the Atmospheric Sciences*, **39**, 1687–1697, doi:10.1175/1520-0469(1982)039<1687:ISATCD>2.0.CO;2.
- Scoccimarro, E., G. Villarini, S. Gualdi, A. Navarra, G. Vecchi, K. Walsh, and M. Zhao, 2017: Tropical Cyclone Rainfall Changes in a Warmer Climate. *Hurricanes and Climate Change*, J. M. Collins and K. Walsh, eds., Springer International Publishing, volume 3, Chapter 10, 243–255, doi:10.1007/978-3-319-47594-3_10.
- Scotti, A., R. Beardsley, and B. Butman, 2006: On the interpretation of energy and energy fluxes of nonlinear internal waves: an example from Massachusetts Bay. *Journal of Fluid Mechanics*, **561**, 103–112, doi:10.1017/S0022112006000991.
- Scotti, A. and B. White, 2014: Diagnosing mixing in stratified turbulent flows with a locally defined available potential energy. *Journal of Fluid Mechanics*, **740**, 114–135, doi:10.1017/jfm.2013.643.
- Shaevitz, D. A., S. J. Camargo, A. H. Sobel, J. A. Jonas, D. Kim, A. Kumar, T. E. LaRow, Y.-K. Lim, H. Murakami, K. A. Reed, M. J. Roberts, E. Scoccimarro, P. L. Vidale, H. Wang, M. F. Wehner, M. Zhao, and N. Henderson, 2014: Characteristics of tropical cyclones in high-resolution models in the present climate. *Journal of Advances in Modeling Earth Systems*, **6**, 1154–1172, doi:10.1002/2014MS000372.
- Shen, W., 2004: Hurricane potential intensity from an energetics point of view. *Quarterly Journal of the Royal Meteorological Society*, **130**, 2629–2648, doi:10.1256/qj.03.65.
- Shepherd, T. G., 1993: A unified theory of available potential energy. *Atmosphere-Ocean*, **31**, 1–26, doi:10.1080/07055900.1993.9649460.

- Sippel, J. A., J. W. Nielsen-Gammon, and S. E. Allen, 2006: The Multiple-Vortex Nature of Tropical Cyclogenesis. *Monthly Weather Review*, **134**, 1796–1814, doi:10.1175/MWR3165.1.
- Smith, P. J., 1970: A Note on Energy Conversions in Open Atmospheric Systems. *Journal of the Atmospheric Sciences*, **27**, 518–521, doi:10.1175/1520-0469(1970)027<0518:ANOECI>2.0.CO;2.
- Smith, P. J., D. G. Vincent, and H. J. Edmond Jr, 1977: The time dependence of reference pressure in limited region available potential energy budget equations. *Tellus*, **29**, 476–480, doi:10.3402/tellusa.v29i5.11381.
- Smith, R. K., 1997: On the theory of CISK. *Quarterly Journal of the Royal Meteorological Society*, **123**, 407–418, doi:10.1002/qj.49712353808.
- Smith, R. K. and M. T. Montgomery, 2016: The efficiency of diabatic heating and tropical cyclone intensification. *Quarterly Journal of the Royal Meteorological Society*, **142**, 2081–2086, doi:10.1002/qj.2804.
- Smith, R. K., M. T. Montgomery, and G. Kilroy, 2018: The generation of kinetic energy in tropical cyclones revisited. *Quarterly Journal of the Royal Meteorological Society*, **144**, 2481–2490, doi:10.1002/qj.3332.
- Smith, R. K., M. T. Montgomery, and N. Van Sang, 2009: Tropical cyclone spin-up revisited. *Quarterly Journal of the Royal Meteorological Society*, **135**, 1321–1335, doi:10.1002/qj.428.
- Smith, R. K., M. T. Montgomery, and H. Zhu, 2005: Buoyancy in tropical cyclones and other rapidly rotating atmospheric vortices. *Dynamics of Atmospheres and Oceans*, **40**, 189–208, doi:10.1016/J.DYNATMOCE.2005.03.003.
- Smith, R. K. and S. Vogl, 2008: A simple model of the hurricane boundary layer revisited. *Quarterly Journal of the Royal Meteorological Society*, **134**, 337–351, doi:10.1002/qj.216.
- Stan, C., 2012: Is cumulus convection the concertmaster of tropical cyclone activity in the Atlantic? *Geophysical Research Letters*, **39**, L19716, doi:10.1029/2012GL053449.
- Stansifer, E. M., P. A. O’Gorman, and J. I. Holt, 2017: Accurate computation of moist available potential energy with the Munkres algorithm. *Quarterly Journal of the Royal Meteorological Society*, **143**, 288–292, doi:10.1002/qj.2921.
- Stokes, G. M. and S. E. Schwartz, 1994: The Atmospheric Radiation Measurement (ARM) Program: Programmatic Background and Design of the Cloud and Radiation Test Bed. *Bulletin of the American Meteorological Society*, **75**, 1201–1221, doi:10.1175/1520-0477(1994)075<1201:TARMPP>2.0.CO;2.
- Tailleux, R., 2010: Entropy versus APE production: On the buoyancy power input in the ocean’s energy cycle. *Geophysical Research Letters*, **37**, L22603, doi:10.1029/2010GL044962.
- 2013a: Available Potential Energy and Exergy in Stratified Fluids. *Annual Review of Fluid Mechanics*, **45**, 35–58, doi:10.1146/annurev-fluid-011212-140620.
- 2013b: Available potential energy density for a multicomponent Boussinesq fluid with arbitrary nonlinear equation of state. *Journal of Fluid Mechanics*, **735**, 499–518, doi:10.1017/jfm.2013.509.

- 2018: Local available energetics of multicomponent compressible stratified fluids. *Journal of Fluid Mechanics*, **842**, R1, doi:10.1017/jfm.2018.196.
- Tailleux, R. and J.-Y. Grandpeix, 2004: On the seemingly incompatible parcel and globally integrated views of the energetics of triggered atmospheric deep convection over land. *Quarterly Journal of the Royal Meteorological Society*, **130**, 3223–3243, doi:10.1256/qj.03.140.
- Tailleux, R. and B. L. Harris, 2020: The generalised buoyancy/inertial forces and available energy of axisymmetric compressible stratified vortex motions. *Journal of Fluid Mechanics*, **submitted**, arXiv:1911.10333v1.
- Tang, B. and K. Emanuel, 2012: Sensitivity of Tropical Cyclone Intensity to Ventilation in an Axisymmetric Model. *Journal of the Atmospheric Sciences*, **69**, 2394–2413, doi:10.1175/JAS-D-11-0232.1.
- Tang, B. H., 2010: *Midlevel Ventilation's Constraint on Tropical Cyclone Intensity*. Ph.D. thesis, Massachusetts Institute of Technology.
URL <https://dspace.mit.edu/bitstream/handle/1721.1/62321/712176836-MIT.pdf>
- Tang, B. H., R. Rios-Berrios, J. J. Alland, J. D. Berman, and K. L. Corbosiero, 2016: Sensitivity of Axisymmetric Tropical Cyclone Spinup Time to Dry Air Aloft. *Journal of the Atmospheric Sciences*, **73**, 4269–4287, doi:10.1175/JAS-D-16-0068.1.
- Trenberth, K. E., C. A. Davis, and J. Fasullo, 2007: Water and energy budgets of hurricanes: Case studies of Ivan and Katrina. *Journal of Geophysical Research*, **112**, D23106, doi:10.1029/2006JD008303.
- Tseng, Y.-h. and J. H. Ferziger, 2001: Mixing and available potential energy in stratified flows. *Physics of Fluids*, **13**, 1281–1293, doi:10.1063/1.1358307.
- Tuleya, R. E. and Y. Kurihara, 1975: The Energy and Angular Momentum Budgets of a Three-Dimensional Tropical Cyclone Model. *Journal of the Atmospheric Sciences*, **32**, 287–301, doi:10.1175/1520-0469(1975)032<0287:TEAAMB>2.0.CO;2.
- Turner, M. R. and J. Norbury, 2020: Nonuniqueness in a Single-Column Model for Moist Convection. *Journal of the Atmospheric Sciences*, **77**, 1001–1018, doi:10.1175/JAS-D-19-0045.1.
- Van Sang, N., R. K. Smith, and M. T. Montgomery, 2008: Tropical-cyclone intensification and predictability in three dimensions. *Quarterly Journal of the Royal Meteorological Society*, **134**, 563–582, doi:10.1002/qj.235.
- Vecchi, G. A., T. Delworth, R. Gudgel, S. Kapnick, A. Rosati, A. T. Wittenberg, F. Zeng, W. Anderson, V. Balaji, K. Dixon, L. Jia, H. S. Kim, L. Krishnamurthy, R. Msadek, W. F. Stern, S. D. Underwood, G. Villarini, X. Yang, and S. Zhang, 2014: On the Seasonal Forecasting of Regional Tropical Cyclone Activity. *Journal of Climate*, **27**, 7994–8016, doi:10.1175/JCLI-D-14-00158.1.
- Vecchi, G. A., T. L. Delworth, H. Murakami, S. D. Underwood, A. T. Wittenberg, F. Zeng, W. Zhang, J. W. Baldwin, K. T. Bhatia, W. Cooke, J. He, S. B. Kapnick, T. R. Knutson, G. Villarini, K. van der Wiel, W. Anderson, V. Balaji, J. . Chen, K. W. Dixon, R. Gudgel, L. M. Harris, L. Jia, N. C. Johnson, S. J. Lin, M. Liu, C. H. J. Ng, A. Rosati, J. A. Smith, and X. Yang, 2019: Tropical cyclone sensitivities to CO₂ doubling: roles of atmospheric resolution, synoptic variability and background climate changes. *Climate Dynamics*, **53**, 5999–6033, doi:10.1007/s00382-019-04913-y.

- Veiga, J. A. P. and T. Ambrizzi, 2013: A Global and Hemispherical Analysis of the Lorenz Energetics Based on the Representative Concentration Pathways Used in CMIP5. *Advances in Meteorology*, **2013**, 485047, doi:10.1155/2013/485047.
- Vidale, P. L., K. Hodges, M. J. Roberts, K. Strommen, P. Davini, A. Weisheimer, and S. Corti, 2019: The future of Tropical Cyclones in AGCM simulations: the role of Stochastic Physics and model resolution. *AGU Fall Meeting Abstracts*, A11Q-2738. URL <https://ui.adsabs.harvard.edu/abs/2019AGUFM.A11Q2738V>
- Vigh, J. L. and W. H. Schubert, 2009: Rapid Development of the Tropical Cyclone Warm Core. *Journal of the Atmospheric Sciences*, **66**, 3335–3350, doi:10.1175/2009JAS3092.1.
- Walsh, K. J., J. L. McBride, P. J. Klotzbach, S. Balachandran, S. J. Camargo, G. Holland, T. R. Knutson, J. P. Kossin, T.-c. Lee, A. Sobel, and M. Sugi, 2016: Tropical cyclones and climate change. *Wiley Interdisciplinary Reviews: Climate Change*, **7**, 65–89, doi:10.1002/wcc.371.
- Wang, Y., 2009: How Do Outer Spiral Rainbands Affect Tropical Cyclone Structure and Intensity? *Journal of the Atmospheric Sciences*, **66**, 1250–1273, doi:10.1175/2008JAS2737.1.
- Warner, C., 2005: Entropy Sources in Equilibrium Conditions over a Tropical Ocean. *Journal of the Atmospheric Sciences*, **62**, 1588–1600, doi:10.1175/JAS3422.1.
- Wehner, M., Prabhat, K. A. Reed, D. Stone, W. D. Collins, and J. Bacmeister, 2015: Resolution Dependence of Future Tropical Cyclone Projections of CAM5.1 in the U.S. CLIVAR Hurricane Working Group Idealized Configurations. *Journal of Climate*, **28**, 3905–3925, doi:10.1175/jcli-d-14-00311.1.
- Wing, A. A., S. J. Camargo, A. H. Sobel, D. Kim, Y. Moon, H. Murakami, K. A. Reed, G. A. Vecchi, M. F. Wehner, C. Zarzycki, and M. Zhao, 2019: Moist Static Energy Budget Analysis of Tropical Cyclone Intensification in High-Resolution Climate Models. *Journal of Climate*, **32**, 6071–6095, doi:10.1175/JCLI-D-18-0599.1.
- Winters, K. B. and R. Barkan, 2013: Available potential energy density for Boussinesq fluid flow. *Journal of Fluid Mechanics*, **714**, 476–488, doi:10.1017/jfm.2012.493.
- Wong, K. C., 2014: *The energetics of tropical cyclone intensification*. Ph.D. thesis, University of Reading.
- Wong, K. C., R. Tailleux, and S. L. Gray, 2016: The computation of reference state and APE production by diabatic processes in an idealized tropical cyclone. *Quarterly Journal of the Royal Meteorological Society*, **142**, 2646–2657, doi:10.1002/qj.2854.
- Xue, M. and S.-J. Lin, 2001: Numerical Equivalence of Advection in Flux and Advective Forms and Quadratically Conservative High-Order Advection Schemes. *Monthly Weather Review*, **129**, 561–565, doi:10.1175/1520-0493(2001)129<0561:NEOAIIF>2.0.CO;2.
- Yamaguchi, M., J. Ishida, H. Sato, and M. Nakagawa, 2017: WGNE Intercomparison of Tropical Cyclone Forecasts by Operational NWP Models: A Quarter Century and Beyond. *Bulletin of the American Meteorological Society*, **98**, 2337–2349, doi:10.1175/BAMS-D-16-0133.1.
- Yoshida, K., M. Sugi, R. Mizuta, H. Murakami, and M. Ishii, 2017: Future Changes in Tropical Cyclone Activity in High-Resolution Large-Ensemble Simulations. *Geophysical Research Letters*, **44**, 9910–9917, doi:10.1002/2017GL075058.

- Zarzycki, C. M., 2016: Tropical Cyclone Intensity Errors Associated with Lack of Two-Way Ocean Coupling in High-Resolution Global Simulations. *Journal of Climate*, **29**, 8589–8610, doi:10.1175/JCLI-D-16-0273.1.
- Zemskova, V. E., B. L. White, and A. Scotti, 2015: Available Potential Energy and the General Circulation: Partitioning Wind, Buoyancy Forcing, and Diapycnal Mixing. *Journal of Physical Oceanography*, **45**, 1510–1531, doi:10.1175/JPO-D-14-0043.1.
- Zhang, F. and K. Emanuel, 2016: On the Role of Surface Fluxes and WISHE in Tropical Cyclone Intensification. *Journal of the Atmospheric Sciences*, **73**, 2011–2019, doi:10.1175/JAS-D-16-0011.1.
- Zhang, J. A., R. F. Rogers, and V. Tallapragada, 2017: Impact of Parameterized Boundary Layer Structure on Tropical Cyclone Rapid Intensification Forecasts in HWRF. *Monthly Weather Review*, **145**, 1413–1426, doi:10.1175/MWR-D-16-0129.1.
- Zhao, M., I. M. Held, and S.-J. Lin, 2012: Some Counterintuitive Dependencies of Tropical Cyclone Frequency on Parameters in a GCM. *Journal of the Atmospheric Sciences*, **69**, 2272–2283, doi:10.1175/JAS-D-11-0238.1.
- Zhu, T. and D.-L. Zhang, 2006: Numerical Simulation of Hurricane Bonnie (1998). Part II: Sensitivity to Varying Cloud Microphysical Processes. *Journal of the Atmospheric Sciences*, **63**, 109–126, doi:10.1175/JAS3599.1.